CARBON NANOTUBES FOR THERMAL INTERFACE MATERIALS IN MICROELECTRONIC PACKAGING

A Ph. D Thesis
Presented to
The Academic Faculty

by

Wei Lin

In Partial Fulfillment
of the Requirements for the Degree
on Polymer Textile & Fiber Engineering in the
School of Materials Science & Engineering

Georgia Institute of Technology
December 2011

CARBON NANOTUBES FOR THERMAL INTERFACE MATERIALS IN MICROELECTRONIC PACKAGING

Approved by:

Dr. Wong, C. P., Advisor
School of Materials Science & Engineering
Georgia Institute of Technology

Dr. Jacob, Karl
School of Materials Science & Engineering
Georgia Institute of Technology

Dr. Graham, Samuel
School of Mechanical Engineering
Georgia Institute of Technology

Dr. Yao, Dong
School of Materials Science & Engineering
Georgia Institute of Technology

Dr. Hess, Dennis W.
School of Chemical & Biomolecular Engineering
Georgia Institute of Technology

Dr. Wang, Z. L.
School of Materials Science & Engineering
Georgia Institute of Technology

Date Approved: Nov. 4, 2011

ACKNOWLEDGEMENTS

I thank Prof. C. P. Wong, my advisor for leading me to the project, which well suits my interests and broadens my knowledge, offering me lots of help and advice, and giving me much freedom to direct my progress. I truly appreciate my thesis committee members, Prof. Zhonglin Wang, Prof. Dennis W. Hess, Prof. Karl Jacob, Prof. Dong Yao, and Prof. Samuel Graham, for their involvement in my research, their invaluable discussion and advice.

I am grateful to Prof. Xiansu Cheng (Fuzhou University, China), Prof. Chang-an Wang (Tsinghua University), Prof. Liming Dai (Case Western Reserve University), Prof. Zhuomin Zhang (Georgia Institute of Technology, Mechanical Engineering), Prof. Seung-Soon Jang (Georgia Institute of Technology, Materials Science & Engineering), Prof. Jianmin Qu (Northwestern University), Prof. Matthew Yuen (Hongkong University of Science and Technology), and Prof. Anselm Griffin (Georgia Institute of Technology, Materials Science & Engineering), as well as the thesis committee members, for their guidance and support on me toward my future career.

I thank Dr. Shanju Zhang (Yale University), Dr. Jake Sober (Georgia Institute of Technology, Chemistry), Dr. Fuhan Liu (Georgia Institute of Technology, Packaging Research Center), Dr. Yong Ding (Georgia Institute of Technology, Materials Science & Engineering), Dr. Jintang Shang (Southeast University, China), Dr. Dajun Yuan (Georgia Institute of Technology), Dr. Cheng Yang (Hongkong University of Science and Technology), Mr. Owen Hildreth (Georgia Institute of Technology, Materials Science & Engineering), Prof. Vesselin Shanov (University of Cincinnati), Prof. Cewen Nan (Tsinghua University), Dr. Bo Xu (Milliken Corporation), Dr. Jung-Il Hong (Georgia Institute of Technology, Materials Science & Engineering), Mr. Chen Xu (Georgia Institute of Technology, Materials Science & Engineering), Dr. Liang Guo (Massachusetts Institute of Technology, Biomedical Engineering), and Mr. Robert Campbell (NETZSCH Instruments, Inc.) for their collaboration, discussion, and help in the past few years.

I am indebted to Dr. Kyoung-Sik Moon, who always offers me lots of help. I appreciate the discussion and help from other group members and my friends, especially from Dr. Yonghao Xiu, Dr. Lingbo Zhu, Dr. Hongjin Jiang, and my close friend—Dr. Rongwei Zhang. Finally, I would like to thank my parents and my wife for their support.

TABLE OF CONTENTS

LIST OF TABLES

LIST OF FIGURES

LIST OF SYMBOLS AND ABBREVIATIONS

< >	spatial average
1D	one-dimensional
2D	two-dimensional
3D	three-dimensional
a	activity
$a_{c\text{-}c}$	carbon–carbon bond length
AFM	atomic force microscopy
Ag	silver
a_K	Kapitza radius
Al	aluminum
Al_2O_3	aluminum oxide
ALD	atomic layer deposition
Ar	argon
Au	gold
BEOL	back-end-of-line
Bi	bismuth
BN	boron nitride
c	concentration of solution
C_2H_4	ethylene
Cd	cadmium
C_h	chiral vector
CHF_3	trifluoromethane

CNT(s)	carbon nanotube(s)
Co	colbalt
C_p	specific heat at constant pressure
Cr	chromium
CTE	coefficient of thermal expansion
Cu	copper
C_v	specific heat at constant volume
$C_{v,e}$	specific heat of electrons
CVD	chemical vapor deposition
d	diameter
d_i	inner diameter
DMA	dynamical mechanical analysis (analyzer)
DMF	dimethylformamide
d_o	outer diameter
DSC	differential scanning calorimeter
DWNT(s)	double-walled carbon nanotube(s)
e	electron charge
E_g	band gap width
EMT	effective medium theory
EP	epoxy
f	packing density
f	filler loading
FCCVD	floating catalyst chemical vapor deposition
f-CNT(s)	in situ functionalized carbon nanotube(s)
Fe	iron

FEOL	front-end-of-line
FT-IR	Fourier-transform infrared spectroscopy
G'	storage modulus
G_0	quantum conductance
GNS	graphite nanosheets
GO	graphene oxide
h	Plank constant
H_2	hydrogen
H_2O	water
H_2O_2	hydrogen peroxide
HFCVD	hot filament chemical vapor deposition
Hg	mercury
HRTEM	high-resolution transmission electron microscopy
I	unit tensor
IC(s)	integrated circuit(s)
I_D	integrated intensity of D band in Raman spectra
I_G	integrated intensity of G band in Raman spectra
$I_{G'}$	integrated intensity of G' band in Raman spectra
k	wave vector
K	physical transport property in effective medium theory
k_B	Boltzmann's constant
K_e	effective thermal conductivity
K_f	thermal conductivity of filler
K_m	thermal conductivity of matrix
l	thickness

LFA	laser flash analysis
m	number of steps along α_1
*m**	effective mass of electrons
MBA	4-mercaptobenzoic acid
MCOM	composite by the VFM-assisted curing
MEP	microwave-assisted-cured epoxy
Mo	molebdenum
MPC	molecular phonon coupler
m-SWNT	metallic single-walled carbon nanotube
MWNT(s)	multi-walled carbon nanotube(s)
n	number of steps along α_2
N_2	nitrogen
Ni	nickel
NMR	nuclear magnetic resonance
NP(s)	nano particle(s)
O_2	oxygen
OAR	organic aqua regia
p	partial pressure
p	aspect ratio
Pb	lead
PCM(s)	phase change material(s)
p-CNT(s)	pristine carbon nanotube(s)
Pd	paladium
PECVD	plasma enhanced chemical vapor deposition
PEG	polyethyelen glycol

PGS	pyrolytic graphite sheet
p^s	saturated vapor pressure of pure water
Pt	platinum
p^t	total pressure
py	pyridine
r	radius of a carbon nanotube
R_a	average roughness
RF	radio frequency
R_i	interfacial thermal resistance between two adjacent VACNT layers
R_K	Kapitza resistance
R_Q	quantum resistance
R_{TIM}	overall thermal resistance of the thermal interface material
R_z	peak-to-valley height (roughness)
sccm	standard cubic cm per min
SDL	screw-dislocation-like
SEM	scanning electron microscopy
Si	silicon
SiC	silicon carbide
SiO_2	silicon dioxide
SMT	surface mount technology
Sn	tin
$SOCl_2$	thionyl chloride
sp^2	a hybridization mode of carbon atoms
sp^3	a hybridization mode of carbon atoms
s-SWNT	semiconducting single-walled carbon nanotube

SWNT(s)	single-walled carbon nanotube(s)
T	temperature
t	time
T	transition matrix in effective medium theory
Ta	tantalum
TCOM	composite by thermal curing
TCVD	thermal chemical vapor deposition
TEM	transmission electron microscopy
TEP	thermally cured epoxy
T_g	glass transition temperature
TGA	thermogravimetric analysis (analyzer)
Ti	titanium
TIM(s)	thermal interface material(s)
TMA	trimethyl aluminum
TMA	thermal mechanical analysis (analyzer)
TMS	Trimethoxysilane
UBM	under-bump metallurgy
UV	ultra violet
v_a	acoustic velocity of sound
VACNT(s)	vertically aligned cabron nanotube(s)
v_F	Fermi velocity
VFM	variable frequency microwave
VLS	vapor-liquid-solid
W	tungsten
x_2	mole fraction of argon dissolved in water

XPS	X-ray photoelectron spectroscopy
y_1	mole fraction of water vapor in the Ar carrier gas
Zn	zinc
α	thermal diffusivity
α_1	unit vector
α_2	unit vector
α_e	effective thermal diffusivity
α_N	through-thickness coefficient of thermal expansion
α_P	in-plane coefficient of thermal expansion
γ	interfacial energy
ΔG	Gibbs free energy change
ΔH	enthalpy change
Δp	pressure difference
ΔS	entropy change
ΔT	temperature drop across an interface
ε_c	critical strain
θ	contact angle
θ	chiral angle
θ	orientation angle
κ	thermal conductivity
Λ	interfacial thermal conductance
Λ	electrical conductivity of a solution
Λ_e	mean free path of electrons
Λ_{ph}	mean free path of phonons
π	mathematical constant, pi

ρ	mass density
ρ_e	mass of electrons per unit volume
$\sigma(\omega)$	frequency dependent electrical conductivity
τ	pulse duration
ω	angular frequency of microwave

SUMMARY

As the integration scale of transistors/devices in a chip/system keeps increasing, effective cooling has become more and more important in microelectronics. To address the thermal dissipation issue, one important solution is to develop thermal interface materials with higher performance. Carbon nanotubes, given their high intrinsic thermal and mechanical properties, and their high thermal and chemical stabilities, have received extensive attention from both academia and industry as a candidate for high-performance thermal interface materials.

The thesis is devoted to addressing some challenges related to the potential application of carbon nanotubes as thermal interface materials in microelectronics. These challenges include: 1) controlled synthesis of vertically aligned carbon nanotubes on various bulk substrates via chemical vapor deposition and the fundamental understanding involved; 2) development of a scalable annealing process to improve the intrinsic properties of synthesized carbon nanotubes; 3) development of a state-of-art assembling process to effectively implement high-quality vertically aligned carbon nanotubes into a flip-chip assembly; 4) a reliable thermal measurement of intrinsic thermal transport property of vertically aligned carbon nanotube films; 5) improvement of interfacial thermal transport between carbon nanotubes and other materials.

The major achievements are summarized.

1. Based on the fundamental understanding of catalytic chemical vapor deposition processes and the growth mechanism of carbon nanotube, fast synthesis of high-quality vertically aligned carbon nanotubes on various bulk substrates (*e.g.*, copper, quartz,

silicon, aluminum oxide, *etc.*) has been successfully achieved. The synthesis of vertically aligned carbon nanotubes on the bulk copper substrate by the thermal chemical vapor deposition process has set a world record. In order to functionalize the synthesized carbon nanotubes while maintaining their good vertical alignment, an in situ functionalization process has for the first time been demonstrated. The in situ functionalization renders the vertically aligned carbon nanotubes a proper chemical reactivity for forming chemical bonding with other substrate materials such as gold and silicon.

2. An ultrafast microwave annealing process has been developed to reduce the defect density in vertically aligned carbon nanotubes. Raman and thermogravimetric analyses have shown a distinct defect reduction in the CNTs annealed in microwave for 3 min. Fibers spun from the as-annealed CNTs, in comparison with those from the pristine CNTs, show increases of ~35% and ~65%, respectively, in tensile strength (~0.8 GPa) and modulus (~90 GPa) during tensile testing; an ~20% improvement in electrical conductivity (~80000 S m^{-1}) was also reported. The mechanism of the microwave response of CNTs was discussed. Such a microwave annealing process has been extended to the preparation of reduced graphene oxide.

3. Based on the fundamental understanding of interfacial thermal transport and surface chemistry of metals and carbon nanotubes, two major transfer/assembling processes have been developed: molecular bonding and metal bonding. Effective improvement of the interfacial thermal transport has been achieved by the interfacial bonding.

4. The thermal diffusivity of vertically aligned carbon nanotube (VACNT, multi-walled) films was measured by a laser flash technique, and shown to be ~30 mm^2 s^{-1}

along the tube-alignment direction. The calculated thermal conductivities of the VACNT film and the individual CNTs are ~27 and ~540 W m^{-1} K^{-1}, respectively. The technique was verified to be reliable although a proper sampling procedure is critical. A systematic parametric study of the effects of defects, buckling, tip-to-tip contacts, packing density, and tube-tube interaction on the thermal diffusivity was carried out. Defects and buckling decreased the thermal diffusivity dramatically. An increased packing density was beneficial in increasing the collective thermal conductivity of the VACNT film; however, the increased tube-tube interaction in dense VACNT films decreased the thermal conductivity of the individual CNTs. The tip-to-tip contact resistance was shown to be ~1×10^{-7} m^2 K W^{-1}. The study will shed light on the potential application of VACNTs as thermal interface materials in microelectronic packaging.

5. A combined process of in situ functionalization and microwave curing has been developed to effective enhance the interface between carbon nanotubes and the epoxy matrix. Effective medium theory has been used to analyze the interfacial thermal resistance between carbon nanotubes and polymer matrix, and that between graphite nanoplatlets and polymer matrix.

CHAPTER 1

INTRODUCTION

At the beginning of the chapter, I present the justification for the potential applications of carbon nanotubes (CNTs) in "electronic packaging", namely as electrical interconnects and thermal interface materials (TIMs). Then I give a brief review of CNT structure, electrical and thermal properties, and syntheses. At the end of the chapter, challenges and research objects are discussed, as a transition to the next chapters. Before I start, I would like to clarify the levels of "electronic packaging" that CNTs may potentially fit: such a definition—unfortunately not found in literature—is aimed at bridging the knowledge gap between packaging engineers and CNT researchers. Today, "electronic packaging" has developed far beyond the traditional "surface mount technology (SMT)"; it is now a system-like integration of hierarchical structures consisting of different levels after front-end-of-line (FEOL), including back-end-of-line (BEOL, level 0), chip bonding/attachment (level 1), and other package levels (carrier/interposer level, board level…). There are three levels that CNTs might fit as advanced materials: 1) as the building block for fine-pitch transistors in the FEOL level;[1,2] 2) as the fine-pitch horizontal/vertical interconnects in the BEOL level;[3-5] 3) in the package level, *e.g.*, as TIMs.[6-8]

In the past 60 years, we have been experiencing constant scaling-down (miniaturization) of electronic devices with better performance, lower cost, and higher reliability. Such a success is mainly attributed to the increased transistor density in a semiconductor chip. As originally proposed, Moore's law stated that the number of transistors in semiconductor devices or integrated circuits (ICs) would double in every 18 months.[9] Moore's law has been realized based on several key technologies, including the shrinkage of transistor node size in the FEOL level (23-nm foundry is being built by

Intel; 14-nm node size is being intensively studied by leading semiconductor companies), and copper/high-K (introduced in 1998) technology in the BEOL level. Further scaling down the transistors is becoming very challenging or theoretically unfavorable partially because of the intrinsic limitations of the properties of the integration materials. For example, the electrical resistivity of pure copper (Cu) interconnects increases with the decreased dimension because of grain-boundary and surface scattering.[10] In the mean time, hot spot and electromigration issues for metal interconnects will become more severe. In these regards, CNTs have been proposed as a potential candidate for future ultra-fine pitch interconnects based on their ultra-high current carrying capacity (10^9 A cm^{-2}), excellent thermal stability, and high resistance to electromigration.[3-5,11-16]

In spite of electrical performance, increasing microprocessor performance is associated with an increased cooling demand; in other words, more effective heat dissipation is required. Effective heat dissipation has become a key issue for the development of high performance semiconductor devices. Efforts on improving thermal management have led to intensive researches in the following two directions: 1) new cooling technology developments, including turbulator-enhanced air cooling, hybrid air-water cooling, water cooling, direct liquid cooling, and thermal ground plane, *etc*.[17]; 2) high-performance TIMs. Figure 1.1 shows the thermal ground plane technology as an example, which can potentially enhance the thermal performance of the device by introducing nano-vapor chamber spreader. Whereas, in many cases of the advanced cooling technologies, the thermal resistance/contact at the solid/solid interfaces still needs to be addressed by using TIM. TIM is a layer of material between two solid blocks to reduce the interfacial thermal resistance due to the surface waviness and roughness, and provide certain adhesion strength. In a simple flip-chip package (Figure 1.2), TIM1 is the thermal interface material between the backside of the chip and the heat spreader/cap, and TIM2 between the heat spreader and the heat sink. The topic of the thesis focuses on TIM1 only as most researchers do.

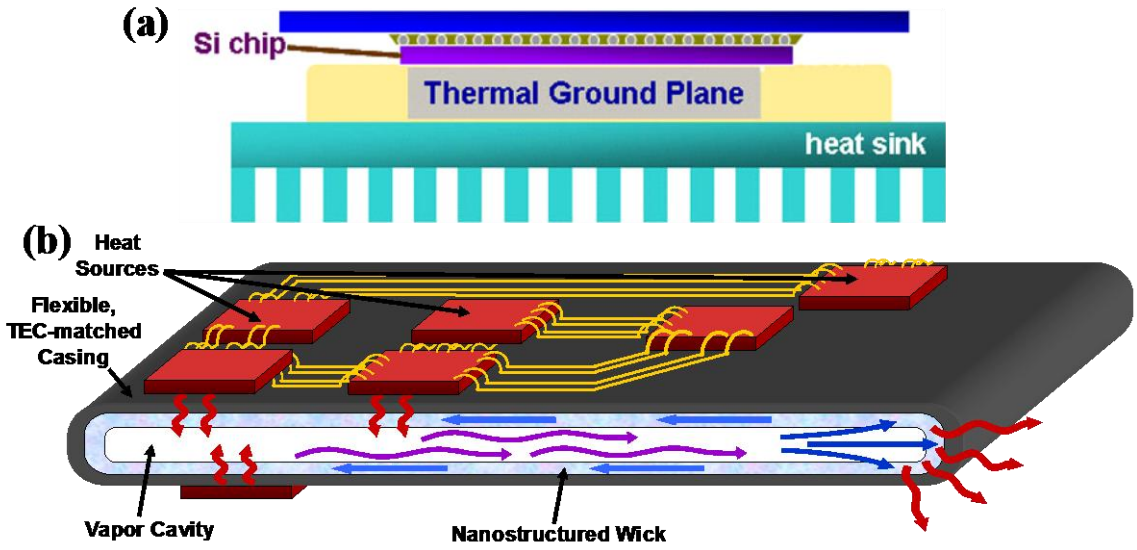

Figure 1.1 (a) Schematic illustration of combined technologies for thermal dissipation; (b) 2-D structure of a thermal ground plane supporting multi-chip modules.[18]

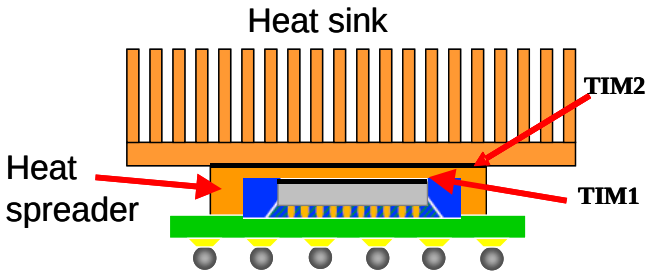

Figure 1.2 Schematic illustration of TIM architecture in flip-chip technology.

TIMs have been extensively used in microelectronic industry for decades. However, the conventional TIMs and related technologies have more or less reached their limits. Development of high-performance TIMs for next-generation electronic packaging is highly desired. High-performance TIMs are expected to possess at least the following properties: 1) high thermal conductivity; 2) low contact thermal resistance with the mating substrate (such as copper and silicon); 3) small coefficient of thermal expansion; 4) proper modulus; 5) chemically and thermally stable; 6) processing-wise, compatible

with the thermal budget from FEOL and BEOL. CNTs, given their high axial thermal conductivity, high thermal stability, high chemical stability, and combined elasticity and flexibility, have been proposed as a promising candidate for the future TIM application.

1.1 Carbon Nanotube Structure

CNTs are carbon allotropes, with cylindrical hollow structures and extremely high length-to-diameter aspect ratio. Generically, CNTs can be divided into two distinct types—single-walled CNT (SWNT) and multi-walled CNT (MWNT), depending on the number of their walls. A SWNT has only one shell with a small diameter (typically <2 nm). MWNT diameters are typically in the range of 2-40 nm.

A SWNT is conveniently illustrated by rolling a two-dimensional (2D) graphene sheet of honeycomb structure along a chiral vector, C_h.[19,20] The circumference of any SWNT can be described as:

$$C_h = m\alpha_1 + n\alpha_2 \tag{1.1}$$

where α_1 and α_2 are unit vectors; m and n are numbers of steps along the corresponding unit vectors. The chiral angle, θ, determined relative to the direction defined by α_1 uniquely defines a SWNT structure. Chiral nanotubes have general (n, m) values and a chiral angle between 0° and 30°. Zigzag nanotubes correspond to (m, 0) or (0, n) and have a chiral angle of 0°, armchair nanotubes have (n, n) and a chiral angle of 30°. Both zigzag and armchair SWNTs have a mirror plane and thus are considered as achiral. The diameter of the a SWNT is given by

$$d = \frac{|C_h|}{\pi} = \frac{\sqrt{3}a_{c-c}\sqrt{m^2 + mn + n^2}}{\pi} \tag{1.2}$$

where $a_{c\text{-}c}$ is the carbon–carbon bond length (1.42 Å). Figure 1.3 shows the vector C_h constructed for (m, n) = (3, 1). The most effective characterization technique for identifying SWNT structure is Raman spectroscopy mainly on the basis that one characteristic radial breathing modes represents one specific SWNT structure.[21]

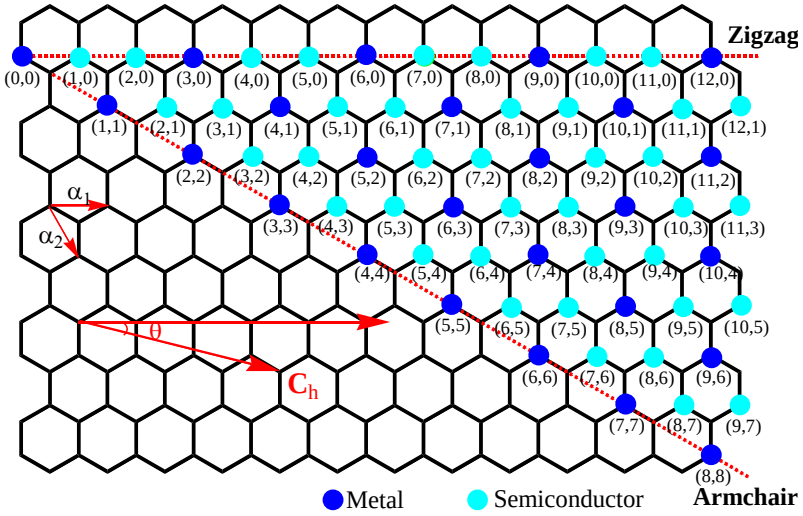

Figure 1.3 Formation of a CNT from a 2D graphene sheet along the vector that specifies a chiral nanotube.

MWNT structures can be extremely complicated. Most people believe that a MWNT is basically similar to a SWNT in the individual wall structure and consists of two or more concentric cylindrical shells of rolled graphene sheets coaxially arranged around a central hollow with a constant separation (~3.4 Å) between the layers.[22] However, the real structure of MWNT has still been open to question to date; techniques to identify the wall structure of each layer in a MWNT are, as far as I know, still lacking except for certain cases of double-walled CNTs. In fact, a scroll tubule structure (Figure 4), rather than a concentric tubule structure, has been proposed based on the relatively large radial thermal expansion observed from X-ray diffraction studies of MWNTs.[23-26] It is worth pointing out that in literature, researchers tend to use "CNT" to extensively represent any one-dimensional (1D) carbon nano structure, including bamboo-structured carbon fibers synthesized by plasma-enhanced chemical vapor deposition,[27] and carbon filaments prepared using anodic aluminum oxide as a template.[28]

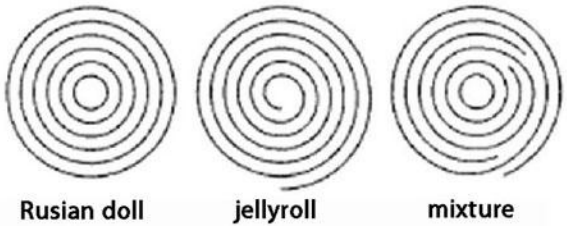

Figure 1.4 Cross sections of concentric (Russian doll) MWNT, scroll (jellyroll) MWNT and mixed MWNT of Russian doll and jellyroll structures.[25]

1.2 Electronic Structure and Electrical Properties

A simple approximation based on a tight-binding calculation for the electronic structure of a 2D graphene sheet is expressed as:[29]

$$E_{2D}(k_x, k_y) = \pm\gamma_0 \left\{ 1 + 4\cos\left(\frac{\sqrt{3}k_x a}{2}\right)\left(\frac{\sqrt{3}k_y a}{2}\right) + 4\cos^2\left(\frac{k_y a}{2}\right) \right\}^{\frac{1}{2}} \tag{1.3}$$

where k_x, k_y and γ_0 are wave vectors and the nearest-neighbor overlap integral, respectively; a=0.246 nm is the in-plane lattice constant. Based on this calculation, the valence and conductance bands touch and are degenerated at the six K (k_F) points at the 2D Brillouin zone corner where the Fermi level in reciprocal space is located. Therefore, graphene is a zero-gap semiconductor (when no other effects interfere). When graphene is rolled over to form a CNT, the periodic boundary condition "$C_h \cdot k = 2\pi q$" is imposed.[19] From tight-binding approximations, all CNTs are conductive, but have different band gap width (E_g). As such, SWNTs can be classified into metallic (m-SWNT, with E_g as small as a few meV) and semiconducting (s-SWNT). E_g of a 1-nm s-SWNT, for example, is between 0.7 and 0.9 eV.[30,31] The natural abundance of m-SWNT relative to s-SWNT is 1:2. MWNTs, if purely concentrical, can also be metallic or semiconducting, analogous to SWNTs. Smaller MWNTs show lower carrier density and greater average carrier localization due to the increasing curvature. Therefore, MWNTs, which usually have large diameters, are metallically conductive.

Owing to the strong C–C bond and the rolled graphitic structure, CNTs with even extremely small diameters as 1 nm do not show the Peierls instability—a metal-to-insulator transition for most 1D materials when they are sized to nano scale.[32] It is such a peerless advantage that makes SWNTs a potential building block for ultra-fine interconnects. Besides, when the length of a CNT is smaller than the mean free path of electron in it, the electron transport is ballistic. This has become an important property for CNTs. For a perfect metallic SWNT with 100% transparent contacts, low-bias transport (*e.g.*, V_b<0.1 V) is ballistic over length scales that can reach micrometers, due to extremely weak acoustic phonon scattering along the axis. For ballistic transport, neglecting electron spin and sublattice degeneracy, the quantum resistance for a single channel is a constant, $R_Q=h/e^2$, where h is the Plank constant, and e the electron charge. Taking into account electron spin and sublattice degeneracy, the corresponding conductance is $G_0=2e^2/h$, which is frequently referred in literature. At high bias, however, strong excitation of optical phonons by electrons leads to energy dissipation in the tube and current saturation.

A single metallic SWNT can carry up to 25 μA of current, which corresponds to a current density of 10^9 A cm^{-2}.[33,34] MWNTs have similar conductance and current density when only the outer wall/shell contributes to the current transport.[35-37] However, multichannel quasiballistic conduction with extremely high conductance of 460 G_0 and large current-carrying capacity was found in an open-ended MWNT.[38] This implies that CNT conductance and current-carrying capacity will be dramatically improved by integrating open-ended MWNTs which have multichannels in metallic contact with the electrodes.

A SWNT rope or MWNT can be viewed as a parallel assembly of individual SWNTs. Naeemi *et al.* derived physical models for the conductivity of MWNT interconnects.[39] The results indicate that for long interconnects (hundreds of micrometers) MWNTs may have conductivities several times larger than that of Cu or

even SWNT bundles. However, a real CNT (by synthesis) is not perfect in structure. When a few local defects are present, electron scattering can be increased.[40-44] In reality, electrical conductance may be even lower due to intershell/interwall coupling,[45, 46], tube-tube contact resistance,[47] and contact resistance at the hetero-junctions between CNTs and other materials.[48,49] Therefore, it is considered necessary to use nanotube bundles/arrays aligned in parallel for interconnects.

Today, the main challenges for CNT interconnects (circuits) are: 1) purification/separation of m-SWNTs from s-SWNTs if SWNTs are used; 2) CNT defect reduction; 3) selective positioning of CNTs; 4) effective and reliable contacts at tube-tube junctions and hetero-junctions between CNTs and other materials.[50,51] Although the SWNT purification/separation issue has almost been addressed by recent development of various CNT separation methods,[52-69] CNT defect reduction/control, selective positioning and contact reliability issues are still unaddressed. Similar issues also exist for CNT transistors, with the difference being that separation of s-SWNT from m-SWNT, or position-selective chirality-controllable synthesis of s-SWNTs is desired. Therefore, it is predicted that applications of CNTs in the FEOL and BEOL won't be possible within the next 25 years.[70]

1.3 Thermal Transport

High thermal conductivity (κ) is one of the most attractive intrinsic properties of CNTs.[71] There are many theoretical and experimental studies on the thermal transport property of CNTs.[72-98]

For CNTs, κ is given by the sum of contributions from electrons and phonons:

$$\kappa = \kappa_{ph} + \kappa_e \tag{1.4}$$

where κ_{ph} and κ_e are the contributions from phonons and electrons, respectively.

Simple kinetic theory gives:

$$\kappa_e = \frac{1}{3}\rho_e C_{v,e} v_F \Lambda_e \tag{1.5}$$

$$\kappa_{ph} = \frac{1}{3}\rho C_v v_a \Lambda_{ph} \tag{1.6}$$

where ρ_e is the mass of electrons per unit volume, $C_{v,e}$ the specific heat of electrons, v_F the Fermi velocity of the material (~10^6 m s^{-1}), Λ_e the mean free path of electrons, ρ the mass density, C_v the specific heat, v_a the acoustic velocity of sound in the material (~10^4 m s^{-1}), and Λ_{ph} the mean free path of phonons.[83]

For s-SWNTs, due to the large band gap, the heat carried by free electrons is negligible compared with that by phonons at moderate temperatures. For m-SWNTs, both electrons and phonons carry heat, and contribute to κ. However, the mean free pathes (scattering rates) of electorns and phonons have different susceptibilities to different structural defects at different temperatures.[84] Therefore, the percentage of contribution to κ from electrons/phonons depends on the structure of CNTs, and temperature.

By molecular dynamics simulations, Berber *et al*.[79] determined κ of an isolated defect-free (10, 10) s-SWNT at room temperature to be ~ 6600 W m^{-1} K^{-1} based on molecular dynamics simulations. Such a high κ is mainly attributed to the large Λ_{ph} in a CNT, *i.e.*, on the order of micron at low temperatures.[74,76,78] Experiments showed a linear increment of thermal conductivity of m-SWNTs with increased temperature at low temperatures, in line with the Wiedemann-Franz law;[74,94,95] however, at high temperatures, *e.g.*, from 300 to 800 K, the thermal conductivity decays with temperature due to strong scattering. Experimental κ values of individual CNTs fall in the range of 42-3000 W m^{-1} K^{-1},[72,73,78,81,86,91,92] depending on tube diameter,[79,87] length,[76,82] chirality,[85] defect,[89,90,92] and temperature,[74,75,77] *etc*.

For MWNTs, heat transport is very complex. The strong intershell interaction and, therefore, phonon coupling between the MWNT shells, is supposed to cause a behavior similar to that of graphite. A thermal relaxation technique has been used to measure the specific heat of MWNTs from 0.6 to 210 K; the results indicate that an

individual MWNT has a similar specific heat to that of SWNT ropes and graphite.[96] In a SWNT rope, phonons propagate along individual tube axes as well as between parallel tubes, leading to phonon dispersion in both the longitudinal and transverse directions. The net effect of dispersion is a significant reduction of the specific heat at low temperatures compared to an isolated nanotube.[98] Yang *et al*. investigated the thermal conductivity of MWNT films using a pulsed photothermal reflectance technique.[97] The average thermal conductivity of CNT films, with the film thickness from 10 to 50 μm, was ~15 W m^{-1} K^{-1} at room temperature and independent of tube length. However, in contrast, Kim *et al.* fabricated a device with suspended MWNTs (~1 μm) to allow the study of thermal transport where no substrate contact was involved,[86] and found the observed thermal conductivity of individual MWNTs was >3,000 W m^{-1} K^{-1} at room temperature. Choi *et al.* obtained the thermal conductivity of individual MWNTs (outer diameter of ~45 nm) by employing a 3ω method.[91,97] The thermal conductivity was reported to be 650-830 W m^{-1} K^{-1} at room temperature, lower than that of individual SWNTs. The results by Kim *et al.* and Choi *et al.* are obviously against prediction and the result by Yang *et al*. In fact, we should be very cautious about the reported values in literature, because the measurement techniques and the CNTs (in terms of structure and defect, *etc.*) are completely different. We should note that besides the intershell coupling and tube-tube interaction, the influence of structural defects on the heat transport in the 1D structure of CNTs could be anomalously high, much larger than in bulk materials. Yi *et al.* measured the thermal conductivity of millimeter-long aligned MWNTs.[99] At room temperature, the thermal conductivity of these samples was only ~25 W m^{-1} K^{-1} , due to a large number of CNT defects. The thermal conductivity recovered to a high value after the aligned MWNTs were annealed at 3,000 °C.

For practical applications such as TIMs, collective thermal transport properties of CNT arrays (carpet, mat, yarn…) are of more interest than the intrinsic κ of individual CNTs and collective thermal transport properties of 2D and three-dimensional (3D)

random CNT networks.[100] A brief literature review on the thermal transport property of vertically aligned CNTs will be given in Chapter 4. Given that MWNTs are more easily synthesized and assembled and possess higher rigidity, MWNTs have been considered more promising than SWNTs, to be applied as TIMs in electronic packaging. The thesis focuses on MWNTs as TIM1.

1.4 CNT Syntheses

Reliable synthesis techniques capable of yielding high-purity high-quality CNTs of desirable quantities at selective positions on synthesis substrates are critical to realizing CNT's applications in electronic packaging. Till now, various synthesis techniques have been developed to produce CNTs for specific research uses or applications, mainly including arc-discharge, laser ablation, and various chemical vapor deposition (CVD) processes, each of them having its own advantages and disadvantages. Since there are thousands of publications dealing with various CNT syntheses, I would like to give only a broad picture of the most commonly used techniques for CNT synthesis.

1.4.1 Arc-Discharge and Laser Ablation Methods

In 1992, Ebbesen and Ajayan adapted the standard arc-discharge technique used for fullerene synthesis to a gram-level synthesis of MWNTs under a helium atmosphere.[101] In this process, carbon atoms are evaporated with inert gas plasma characterized by high electric currents passing between opposing carbon electrodes (cathode and anode). Usually the carbon anode contains a small percentage of metal catalyst such as cobalt (Co), nickel (Ni) or iron (Fe). The results show that the purity and yield depend sensitively on the gas pressure in the reaction vessel. The length of the synthesized MWNTs is several micrometers with diameters ranging from 2 to 20 nm. However, such synthesized CNTs are inevitably accompanied by the formation of a large

amount of carbon particles that are attached to the nanotube walls. In 1993, Bethune and coworkers reported a large-scale synthesis of SWNTs by an arc-discharge method using a carbon electrode that contained ~2 atom% Co.[102] At high temperatures, carbon and metal catalysts are co-vaporized into the arc, leading to the formation of CNTs with very uniform diameter (~1.2 nm). However, fullerenes (by-products of the arc-discharge process) also form readily in this process. In order to obtain high-purity SWNTs, a purification process is therefore necessary. In 1996, the Smalley group reported the synthesis of high-quality SWNTs with yields >70% using a laser ablation method.[103] This method utilized double pulse lasers to evaporate graphite rods doped with 1.2 atomic% of a 50:50 mixture of Co and Ni powder, which was placed in a tube-furnace heated to 1200 °C in flowing argon (Ar) at 500 Torr; this process was followed by heat treatment in vacuum at 1000 °C to sublime C_{60} and other small fullerenes. The resulting SWNTs were quite uniform, had a diameter of ~1.38 nm, and formed ropes consisting of tens of individual SWNTs closely-packed into hexagonal crystal structures that were stabilized through van der Waals forces.

The success in producing large quantities of CNTs offers wide availability of CNTs for fundamental studies and exploration of potential applications. However, there are several concerns associated with these two synthesis methods: first, energy consumption is large; second, only powder-like samples with bundled/tangled CNT bundles are produced; third, by-products are usually unavoidable, including fullerenes, graphitic polyhedrons, and amorphous carbon in the form of particles or over-coats on nanotubes; fourth, patterned synthesis of CNTs is a great challenge.[104] These make purification, manipulation, positioning and assembly of the CNTs extremely difficult.

1.4.2 Chemical Vapor Deposition (CVD)

CVD is the only route toward the synthesis of vertically aligned CNTs (VACNTs). Both vertically-aligned MWNTs and SWNTs have been synthesized successfully using

CVD processes. CVD processes have the great advantages in controllable tuning of CNT length, packing density, diameter, morphology, alignment, doping, position and adhesion on substrates. This is why CVD is the most attractive synthesis route toward various CNT applications. There are many critical parameters in the CVD syntheses of CNTs, including carbon precursor (*e.g.*, methane, acetylene, ethylene, benzene, xylene…), carrier gas (*e.g.*, hydrogen, argon, helium, nitrogen…), reduction gas (*e.g.*, ammonium, hydrogen), catalyst recipe (*e.g.*, Fe/Al, Fe/Al_2O_3, Ni/Al, Fe-Mo/Al_2O_3, Co-Mo…), catalyst preparation (*e.g.*, sputtering, atomic layer deposition, e-beam evaporation, sol-gel…), catalyst pretreatment (*e.g.*, fast heating/cracking, oxidative annealing…), reactor design, synthesis temperature and pressure, to name a few. The effects of the parameters on the CNT syntheses have been investigated extensively in literature.

Various CVD processes have been developed, including common thermal CVD (TCVD),[105,106] plasma enhanced CVD (PECVD),[107,108] floating catalyst CVD (FCCVD),[109,110] and hot filament CVD (HFCVD),[111] *etc*.

Generally, PECVD has the particular advantage in obtaining a good alignment of a CNT array.[112] PECVD can also lower the synthesis temperature, compared to TCVD, because plasma dissociates hydrocarbon molecules more efficiently and promotes surface diffusion of carbon on the catalyst droplet, thereby allowing CNT synthesis to occur at lower temperatures than are possible with TCVD.[108,113] Interestingly, a TCVD process for CNT synthesis at as low as 450 °C was recently reported.[114] However, the quality of the as-synthesized CNTs may be poor. The advantage of FCCVD over TCVD and PECVD is to grow VACNT arrays with a higher packing density.[110,115,116] FCCVD doesn't need a catalyst layer on the substrate; instead, the catalyst is generated in situ in the reaction chamber by the decomposition of a metal catalyst precursor such as ferrocene dissolved in xylene, which is delivered/floated to the synthesis zone. The average metal content in the CNTs arrays synthesized by FCCVD is typically 10-15

wt%.[116,117] Recently, helical CNT arrays were synthesized by FCCVD, indicating more flexibility of FCCVD in controlling CNT morphology.[118]

1.5 Challenges and Research Objectives

My Ph. D thesis will be focusing on TCVD-synthesized vertically-aligned MWNTs for TIM application. There are two important reaons why I focus on TCVD instead of PECVD or FCCVD. First, the quality of the VACNTs by TCVD is known to be better than that by PECVD or FCCVD. Second, transfer of the synthesized VACNTs by TCVD, in general, is easier than that by PECVD and FCCVD. The importance of a high quality of synthesized VACNTs has been mentioned in Section 1.3, and will be discussed in details in Chapters 3 and 4. The importance of a good transferability of a synthesized VACNT film/arry on a growth substrate is justrified as follows.

Taking a look at Figure 1.2, we can think of only four basic scenarios to incorporate a VACNT film as the TIM1 to a typical package: 1) synthesizing the VACNT film on the backside of the silicon (Si) chip; 2) synthesizing the VACNT film on the heat spreader/cap (or on the heat sink if no heat spreader is used as in the package structure); 3) transferring the synthesized VACNT film from its sacrificial growth substrate (such as Si or quartz) to the backside of the Si chip or the heat spreader (or heat sink) via a transfer technique; 4) synthesizing a free-standing VACNT (with or without a carrier sheet such as aluminum or copper).

I would like to say that the first scenario, *i.e.*, direct synthesis of VACNTs on the Si chip, is not wise. There are three possible subscenarios to incorporate the VACNT-on-chip to a flip-chip package: VACNT-first (*i.e.*, TIM-first), VACNT-middle (*i.e.*, TIM-middle), and VACNT-last (*i.e.*, TIM-last). The definitions are analogous to those for through-silicon-via in terms of the fabrication sequence. VACNT-first refers to the process where the VACNT TIM layer is synthesized on the back side of the Si chip before FEOL; VACNT-middle means the VACNT TIM synthesis is between FEOL and

BEOL; VACNT-last incorporates the VACNT TIM synthesis in the last step before the next level of packaging, *i.e.*, after FEOL and BEOL. Although VACNT synthesis on Si has been widely investigated, VACNT-middle and VACNT-last are not compatible with the current FEOL or BEOL processes—TCVD synthesis temperature is typically >650 ^{o}C, which is too high for any modern semiconductor logic device to survive. Although PECVD dramatically reduces the synthesis temperature and makes VACNT-middle possible, the relatively low CNT quality (except for SWNTs, PECVD typically gives bamboo-structure) and the contamination issue (catalyst residue, and carbon overcoat) are of great concern, and haven't been addressed yet. Contamination is undoubtedly a more severe issue for FCCVD. VACNT-first and VACNT-middle both encounter the extreme difficulty in sample handling. For example, due to the porous structure, VACNTs will collapse/crush upon compression in the presence of the liquid etchant during the chemical mechanical polishing process. Moreover, a high thermal stress is expected from the Scenario 1.

In comparison, a transfer process can avoid the issue of contamination and high thermal stress, as well as the limitations on the synthesis temperature by thermal budgets from FEOL and BEOL. In conjuction with the advantages of TCVD, Scenario 3 is promising. Scenarios 2 (discussed in Chapter 2 when I talk about the TCVD synthesis of VACNTs on bulk Cu) and 4 (Prof. Samuel Graham's research on VACNT TIMs has been focused on the Scenario 4) are both feasible, too.

1.5.1 Synthesis, Annealing and Characterizations of VACNTs

In most cases, defects in synthesized CNTs tend to degrade the intrinsically excellent properties of CNTs. One solution to this issue is to improve CNT quality by optimizing the catalyst-support recipe and the CVD process for the VACNT synthesis. In chapter 2, based on the fundamental understanding of CNT synthesis, we achieve high quality of the VACNTs by TCVD. The high quality of the synthesized VACNTs can be

seen in the high intrinsic thermal transport property measured in Chapter 4. Other than the synthesis control, an alternative/complimentary solution is post-synthesis annealing of CNTs. Conventionally a high-temperature annealing is needed for CNT defect reduction but has some inhibiting limitations that make it not feasible for practical VACNT applications. In chapter 3, an efficient microwave treatment process is described for CNT annealing. The microwave annealing process can also be extended to fast synthesis of reduced graphene oxide. For TIM applications, an alternative scenario (the aforementioned scenario 2) is to synthesize high-quality VACNTs on various substrates such as bulk Cu, aluminum nitride, silicon nitride and silicon carbide, with a relatively high accommodation of surface roughness. In chapter 2, I present the synthesis of high-quality VACNTs on bulk Cu by TCVD.

1.5.2 VACNT TIM Assembling

Contact resistance in terms of electron and phonon transport is a very important issue for any electronic packaging or nanoscale device. The high contact resistance between VACNTs and a substrate surface has been recognized as a major limitation to the immediate implementation of VACNTs for interconnects or TIMs. Contact resistance is determined by the intrinsic properties of the materials in junction/contact, and the assembling processes, which determines the interfacial status. Therefore, development of an effective VACNT assembling (also named as “transfer” or “anchoring” from here after) process with reduced interfacial contact resistance is significant. In chapter 5, I summarize various VACNT assembling processes that may be implemented into the TIM application.

1.5.3 CNT/Polymer Composite

Till today, the most promising application of CNTs in industry has still been CNT/polymer composite. Thousands of publications are relevant to preparations,

characterizations, properties, and various application prototypes of CNT/polymer composite. The topic of interest in my thesis is the thermal properties of CNT/polymer composite. Thermal transport in CNT/polymer composite has been studied extensively. Unfortunately, it is disappointing that CNT/polymer composites do not show as high a thermal conductivity as expected. What has been proposed to explain such a phenomenon is a large interfacial thermal resistance between CNTs and the surrounding polymer matrix. Chapter 6 discusses an effective approach to enhance the interface between VACNTs and epoxy (EP), based on which thermal and mechanical properties of the VACNT/EP composite are improved. The interface enhancement also results in very interesting phenomena of the thermal expansion of the composite. The interfacial thermal resistance between graphite nanosheets and EP turns out to be better compared with the CNT/EP composite.

CHAPTER 2

SYNTHESIS OF VERTICALLY ALIGNED CARBON NANOTUBES

In this chapter, I present a critical review of the mechanism for CNT synthesis (Section 2.1), and summarize VACNT synthesis by TCVD (Section 2.2)—in particular, with the assistance of water vapor (Section 2.3). Based on the fundamental understanding of thermodynamics and kinetics of TCVD synthesis of CNTs, in Section 2.4, I discuss an in-situ functionalization process of VACNTs during TCVD, which laid an important foundation of much of the research work in the following chapters. In Section 2.5, a record synthesis of VACNTs on bulk Cu is introduced.

2.1 Mechanism for CNT Synthesis

I would like to put certain efforts on a review of the mechanism for CNT synthesis. Pursuing the fundamental understanding of CNT growth is, from my point of view, one of the most important reasons (others are potential applications in transistors, interconnects, and high-performance composites) why CNT has become the hottest research topic in the past 2 decades. Fundamental understanding of CNT synthesis is the basis for the realization of CNT-related applications. There are bunches of Ph. D theses about CNT-related applications; however, few of them give a proper discussion on the mechanism for CNT synthesis. There are thousands of research papers relevant to CNT synthesis; however, very few of them ever touch the synthesis mechanism from a scientific view. There are several review papers and book chapters that cover certain aspects of the mechanistic study; however, recent literature update is not covered, and a critical review/interpretation of the synthesis mechanism can not be found.

In general, CNT synthesis can be classified into non-catalytic processes and catalytic processes, based on the synthesis mechanism of CNTs. For non-catalytic processes, *i.e.*, the original arc-discharge and carbon pyrolysis, it was proposed that the

synthesis of a CNT is due to the extension of a fullerene by adding small carbon unit/cluster from the carbon vapor into the carbon network at the formed cap area, especially at the asymmetric pentagon sites.[119] This is a typical closed-cap synthesis mechanism, consistent with the observations by Ulmer *et al.*[120] and McElvany *et al.*[121], that fullerenes could grow by ingestion of carbon fragments into their completely closed networks. Alternatively, Iijima proposed an open-ended synthesis mechanism.[122] It was thought that a CNT end is open during tube synthesis and it was the open end that was the active site for the upcoming carbon atoms to add in. Synthesis termination was due to polyhedral capping or conical capping, both of which were rapid capping processes. Both synthesis schemes are also consistent with Iijima's observation that, in general, the tubes appear to have their hexagons helically disposed in the tube walls.[123] Both schemes proposed that the multi-shells in a MWNT were not formed simultaneously but rather layer-by-layer with the existed inner shell as a synthesis template. The recent work of in-situ transmission electron microscopy (TEM) observation of CNT cap evolution seems to provide futher proof of the closed-cap mechanism.[124] However, the typical low yield and high impurity level by the non-catalytic processes makes the generalization of such mechanisms difficult.

Catalytic CVD processes seem more complicated and are still open to question. Generally, a catalytic CVD process for CNT synthesis involves decomposition of carbon sources, *e.g.*, gaseous precursors or volatile compounds of carbon, catalyzed by metal nanoparticles (NPs) at high temperatures. The basic mechanism for CNT synthesis has been generally assumed to be a dissociation-diffusion-precipitation process during which elemental carbon is formed on the surface of a catalyst metal particle followed by diffusion and precipitation in the form of cylindrical graphite.[26,125] If we want to know a bit more details about the dissociation-diffusion-precipitation process, we will naturally expect answers to the following questions:

Why and how is a carbon source dissociated by the catalyst particles?

Why and how do the dissociated carbon atoms/clusters diffuse?

Why and how does the diffused carbon precipitate to become cylindrical graphite?

Adsorption and reaction (hydrogenation, oxidation, polymerization, dissociation, reconstruction, and coordination, *etc*.) of molecules on catalyst surface has been the most challenging fundamental question in heterocatalysis. The answer to the first question here involves the interpretation of the chemisorption and dissociation of hydrocarbon on nano-sized metal catalyst surfaces, especially on nano-sized *d*-block metal (I don't use the term: "transition metal") surfaces. In general, the electronic structure of a catalyst particle determines the whole process.[126] Chemisorption is the first step, and takes place by coordination or charge-transfer between the molecular orbitals of the hydrocarbon molecule and the electronic orbitals of the metal surface atoms. "Electronic orbitals of the metal surface" is not the term that is often used. In most cases, we talk about "band structure of metals" when dealing with bulk metals, "electronic orbitals of metal atoms" when dealing with single atoms, or "molecular orbitals" when dealing with transition metal complexes with ligands; however, none of these is close enough to describe the surface coordination chemistry of metal NPs. In general, two processes take place simultaneously regarding the chemisorption: 1) symmetry-allowed coordination or charge transfer from a filled orbital of the adsorbate to an unoccupied orbital of the surface metal atom; 2) the back-donation from a filled *d*-orbital (of π-symmetry with respect to the metal-ligand axis) of the metal atom to the non-filled π^*-orbital of the adsorbate.[127] The dissociation of the hydrocarbon molecule can be explained by the "bond order" theory. The bond order of the hydrocarbon molecule is reduced when the anti-bonding orbital is filled (or partially filled) during the back-donation process; therefore, the overall bond energy within the hydrocarbon molecule is reduced due to the interaction between the molecule and the metal atom. Based on such understanding and the previous experiment results on catalytic CVD synthesis of CNTs, Dupuis stated in his review

paper: “the transition metals have non-filled *d* shells and are for that reason able to interact with hydrocarbons and show catalytic activity.” It was also stated: “Cu, a non-transition metal with its 3*d* shell completely filled, was observed to yield only amorphous carbon.”[127] Such statements have been taken as the principles by many researchers; however, I would like to point out that the statements are not accurate.

First, the IUPAC definition of a transition element is that it is an element that has an incomplete *d* subshell in either the neutral atom or its ions. As such, the Group 12 elements (Zn, Cd, Hg) are members of the *d* block but are not transition elements; the Group 11 elements (Cu, Ag, Au) are transition elements even though their *d* orbitals are completely filled. Dupuis’ statement about “non-filled *d* shells” of transition metals and Cu not belonging to transition metals is not correct.

Second, Dupuis’ statements seem to explain the fact that the most efficient (in terms of synthesis temperature, catalyst loading, and most importantly, CNT yield and quality) catalysts are limited to be based on three mid-transition metals: Fe, Co, and Ni. In fact, the discussion above about the interaction energy is all about thermodynamics; while efficiency is about kinetics rather than thermodynamics. For example, early-transion metals such as Ti has more emply *d* orbitals to accommodate the electron donation from the adsorbed hydrocarbon molecules; however, Ti by itself has very weak catalytic ability.[128]

Third, Dupuis’ statements can’t explain the recent experiment results on CVD synthesis of CNTs using Au,[129,130], Pd,[131], Pt,[132] Ti,[133] Cu,[134] or Zn[135] as the catalyst, or co-catalyst.[128,136] In particular, Zhou *et al.* reported very high catalytic activity of Cu NPs for the growth of both random SWNT networks and horizontally aligned SWNT arrays.[134] Such results are undoubtedly against Dupuis’ statements but should not be against the discussion above about the chemisorption-dissociation mechanism. Now a question arises: how does the metal, say Cu, with full *d* orbitals accommodate/accept the electrons from the hydrocarbon molecule during the

catalytic CVD process? The key is that we shall think about "*d* band" instead of "*d* orbital" of the surface metal atoms of the catalyst particles. Let us do a simple calculation. Take Fe-catalytic synthesis of SWNT as an example. The nominal diameter of Fe in its face center cubic crystal structure is 0.3 nm at room temperature. Two nanocubes of Fe are considered: $3\times3\times3$ nm^3 (large cube), and $0.9\times0.9\times0.9$ nm^3 (small cube). Neglecting the thermal expansion and the surface instability of the Fe nanocubes, the two cubes accommodate 10^3 and 27 Fe atoms, respectively. The energy spread of a band is typically on the order of 1 eV. The energy-level separation between the adjacent levels in a nominal band is approximatvely 1 eV divided by the number of atoms in the particle, which are ~1 and ~37 meV for the large cube and the small cube, respectively. Boltzmann's constant (k_B) in eV units is 8.625×10^{-5} eV K^{-1}. Simply taking $E=k_BT$, and the CVD temperature as 1000 K, the thermal energy is ~86 meV, which makes the energy-level separation indiscernible. For metals, their intrinsic conduction band and valence band are overlapped (or just touch each other). Therefore, it is the *d* band that accommodates the electrons from the hydrocarbon molecule. Given that the chemisorption takes place only at the top surface atoms, the electronic structure of the surface metal atoms should change upon coordination. The simple model proposed by Norskov's research group singles out three surface properties contributing to the ability of the surface to make and break adsorbate (the adsorbed hydrocarbon molecule in our case) bonds: 1) the center of the *d*-bands; 2) the degree of filling of the *d*-bands; 3) the coupling matrix element between the adsorbate states and the metal *d*-states.[126] For pure metal elements, the first and the second properties are intrinsic, and determined by the nature of the elements and temperature. According to molecular orbital theory, the third property, the coupling, is determined by the energy difference and the symmetry of the orbitals involved. Calculation results show the shift in the *d*-band center when the metal is alloyed into the surface of the other or is deposited as a pseudomorphic overlayer.[137] The last thing that calls for our attention is that the surface of the metal

NPs may be intrinsically oxidized; this will be discussed from the view of thermodynamics in Chapter 5 when CNT-solder wettablity is discussed.

To answer the second question, vapor-liquid-solid (VLS) model was proposed and is widely appreciated.[138] VLS model was first used to explain the synthesis of silicon nanowiskers[139] and then to describe the synthesis of carbon nano fibers/filaments.[140] According to the VLS model, dissociated carbon dissolves into the liquid catalyst particle and when the catalyst is supersaturated by the dissolved carbon, carbon precipitates on the particle surface and nucleates the synthesis of CNTs; CNT synthesis is due to a continuous diffusion of carbon from the exposed catalyst surface through the particle.[141] Liquid catalyst particles form at the synthesis temperature due to the melting point depression effect originated from the small particle size. It is generally accepted that the diffusion of carbon through the catalyst particle is the rate-limiting step. However, the nature of the driving force for the carbon diffusion is a subject of debate.

In 1972, Baker *et al.* proposed that a temperature gradient across the catalyst particle was the driving force for the carbon diffusion.[140] It was believed that carbon diffused from the hotter leading surface on which the exothermic pyrolysis of hydrocarbons occurs to the cooler surfaces on which carbon is precipitated endothermically. There is some experimental evidence for the temperature-driven carbon diffusion mechanism;[142,143] nevertheless, the model could not provide a rational explanation for the endothermic pyrolysis of some hydrocarbons such as methane.[143] A recent molecular dynamics simulations showed that such a temperature gradient was not required for SWNT synthesis from small catalyst particles.[144]

As an alternative to the temperature-driven diffusion model, a concentration-driven diffusion model was proposed.[145] This model involves a concentration gradient across the catalyst particle in contact with the hydrocarbon on one side and with a

graphitic precipitation on the other side. However, experimental evidence for this model is lacking.

Are there any other explanations for the carbon diffusion? What if it is not due to bulk diffusion but, rather, due to a surface diffusion (or quasi-surface diffusion) process that drives the dissociated carbon species around the catalytic particle to form graphitic carbon deposit? Actually, against any bulk diffusion model, a surface diffusion model was proposed by Baird in 1974, which was found to be more satisfactory and consistent for both platelet and filamentary graphitic carbon deposit on catalyst surface.[146] This model involves a surface diffusion of "metal-metal hydrocarbon species" (after taking into account the metal diffusion into the carbon precipitate) across the edge of the carbon layer planes. At the beginning stage, a clean "liquid-like" (can be liquid, or at least the surface can be like liquid in properties) catalyst particle formed on the surface of the supporting material as a result of reduction of catalyst oxide by hydrogen (H_2) at elevated temperatures. An association of metal and hydrocarbon species then nucleated on the fresh surface of the liquid catalyst particle and diffuses on the surface and dissociates at the contact angle between the droplet and the wall of the supporting material.[147] The subsequent further precipitation of carbon gives rise to the graphitic shell. In comparison with bulk diffusion of carbon into the catalyst particle, which seems unlikely due to high activation energy, a surface diffusion process seems more feasible.[148,149] Synthesis termination occurs when the catalyst particles are capped.[147,150,151]

Moreover, base-synthesis mode and tip-synthesis mode can also be explained based on the surface diffusion model. Interaction between the metal catalyst particle and the support material is a key factor that influences the CNT synthesis mode. Figure 2.1 is a schematic representation of the two typical CNT synthesis modes, *i.e.*, base-synthesis mode and tip-synthesis mode. If the particle adheres to the surface of support materials strongly, carbon precipitates from the front of the particle and CNT synthesis continues with the particle attached on the substrates. In contrast, when interaction between the

metal catalyst and the support material is weak, carbon precipitates at the opposite surface of the particles and the growing CNT lifts the particles as it grows.

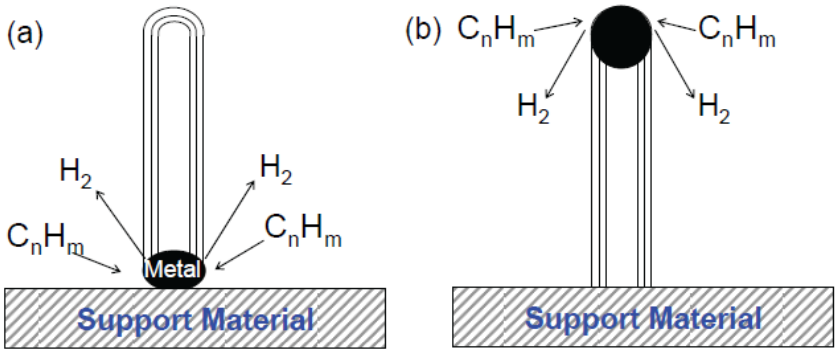

Figure 2.1 Two typical CNT synthesis modes in CVD: (a) base-synthesis mode, and (b) tip-synthesis mode.

Now let us come to the third question: why and how does the carbon deposit precipitate to form a tubular graphitic shell? Some researchers claimed that the active site of the catalyst particle for CNT synthesis could be metal carbide, which decomposes on the surface of the metal, producing graphite layers.[140,152-155] If metal carbide determines CNT precipitation, there must be some relation between the orientation of graphitic shells and the plane index of the carbide at the catalyst particle surface. However, some researchers showed that the carbon shells resulting from carbide decomposition always presented a constant thickness and orientation whatever the Miller indices of the carbide crystal face.[147] Actually, some lattice-resolved images show neither carbide formation,[155] nor extended liquid surface layers.[148] Dynamic reshaping of catalyst particles during CNT synthesis was recently observed,[156] indicating a weak relation between the catalytic synthesis of CNTs and metal carbide formation. In contrast to the theory of carbide-directed formation of graphitic structure, some researchers postulate that the metal carbide formation during a CVD process is the

deactivation mechanism for the metal catalyst. Then how can we explain the hollow graphitic rolls with a constant interlayer distance? I would say it is "spontaneous" when we think about the following three facts: 1) graphite is thermodynamically more stable than any other carbon isotopes at the synthesis temperature; 2) (0002) crystal plane of graphite has the lowest surface energy; 3) interaction with the metal catalyst surface. Recently, the graphitization ability of several transition metals used as catalysts for CNT growth via CVD was investigated via classical molecular dynamics simulation on planar crystalline metal surfaces and metal nanoclusters.[157] Close-packed facets are shown to be a good template for reconstructing graphene structure since they exhibit some degree of epitaxy with hexagonal carbon network. Moreover, the interaction energy between a Fe cluster and graphene sheet was found to be higher than for clusters comprising cobalt or nickel, since the high energy of graphene due to induced defects is stabilized by interaction with surface of Fe cluster. The hollow structure is probably because if an inner shell with an extremely small diameter forms, its strain due to the large curvature will be too high. As a matter of fact, in many cases, a CNT is not hollow but seemingly has some amorphous carbon-like matter partially filled inside. For the carbon precipitation process, a "screw-dislocation-like" (SDL) mechanism has recently been proposed by Ding *et al.* by extending the conventional synthesis model for 1D crystals.[158] SDL mechanism has been experimentally proved by the observation by Marchand *et al.* that SWNT turns during catalytic synthesis.[159] I believe more theoretical and experimental studies will come out to analyze the SDL mechanism.

Finally, let me challenge the VSL mechanism a bit by thinking about the following phenomena observed during our MWNT synthesis. Melting point depression is based on the high surface energy of nano-sized particles. It is known that, as is also observed in my research, the catalyst particles usually grow bigger (>20 nm) during the CVD synthesis probably due to the Oswald ripening process. The corrected melting point for the big catalyst particles is way above the CVD temperature for our MWNT

synthesis. Moreover, when I suspend the MWNT synthesis in purpose—rather than self-termination—and do TEM imaging of the MWNTs, I observe that the big catalyst particles are wrapped by multi layers of graphitic carbon (Figure 2.2). The surface energy of the wrapped catalyst particle is totally different from a pure nano-sized catalyst particle. Therefore, a "liquid-like" catalyst particle is unlikely in our CVD conditions and is not necessary for CNT synthesis. Shall the surface diffusion model be used to modify the VLS model, there is still a shortcoming—is a "liquid-like" catalyst surface required for carbon diffusion? The answer, in my view, is "no". In fact, low-temperature CNT synthesis has been reported,[108,160-162] where the synthesis temperatures were well below the (size-corrected) metal-carbon eutectic temperature.[163] In situ TEM studies showed that the nickel catalyst stayed crystalline throughout the thermal synthesis of CNTs at 540 ^{o}C.[164] All these imply that the catalyst can be completely "solid", in contrast to the VLS model. In addition, it is noteworthy that these wrapped MWNTs can resume growth; it seems that catalyst capping is not the termination mechanism for CNT synthesis. This is consistent with the recent simulation result by Charlier *et al*.[165] Earliest results on open-ended VACNT sysnthesis by Pan *et al*.[166] also challenge such a termination mechanism. About the termination of CNT synthesis, various mechanisms have been proposed but all have, obviously, some shortcomings.[167-173]

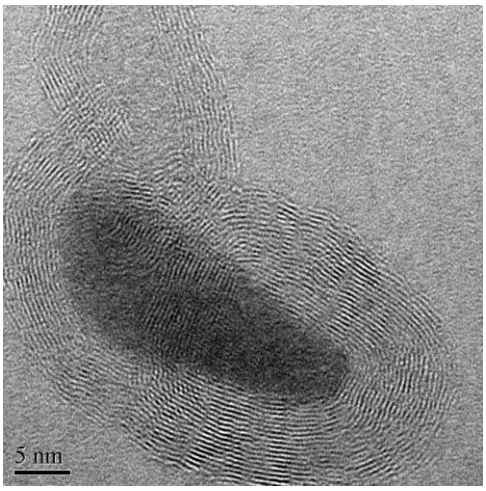

Figure 2.2. A capped CNT with the metal catalyst (Fe) particle enclosed.

2.2 Fast Synthesis of VACNTs by TCVD

Given that PECVD covers a completely different mechanism for VACNT growth,[112] and it typically doesn't promise high quality of VACNTs, this section focuses on TCVD only. Up to date, many researchers have reported successful synsthesis of VACNTs by various TCVD processes. For TCVD processes, in most cases, VACNT growth assumes the base-growth mechanism,[182] which was confirmed by Fan *et al*. via an isotoping process.[150] Mass transport and alignment formation during the VACNT growth were also studied by Fan *et al.* (Figure 2.3).

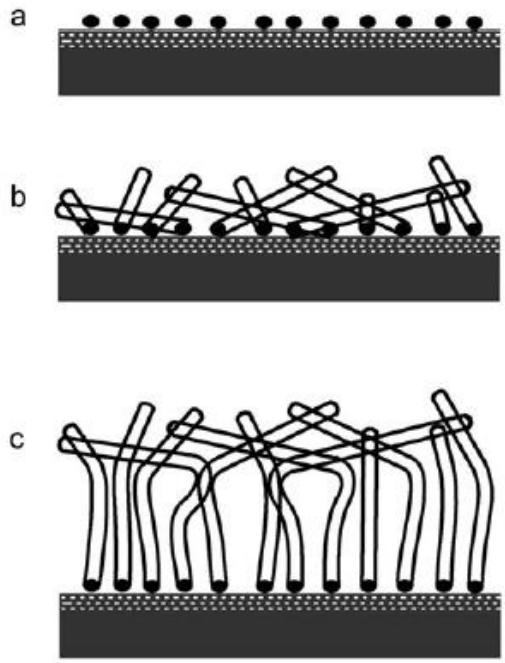

Figure 2.3 Evolution of CNTs into arrays by a weaving model. (a) Porous Si substrate with catalytic particles. (b) The nanotubes begin to grow in random directions and cross each other, weaving a net form. (c) As the nanotubes continue to grow, the entangled layer is lifted upwards and anchors the nanotubes into an aligned array.[150]

In 2009, Bedewy *et al*. reported a mechanistic study of VACNT growth with much more details (Figure 2.4).[174] They proposed that VACNT forest growth

consisted of four stages: 1) self-organization; 2) steady growth with a constant CNT number density; 3) decay with a decreasing number density; 4) abrupt self-termination, which is coincident with a loss of alignment at the base of the forest.

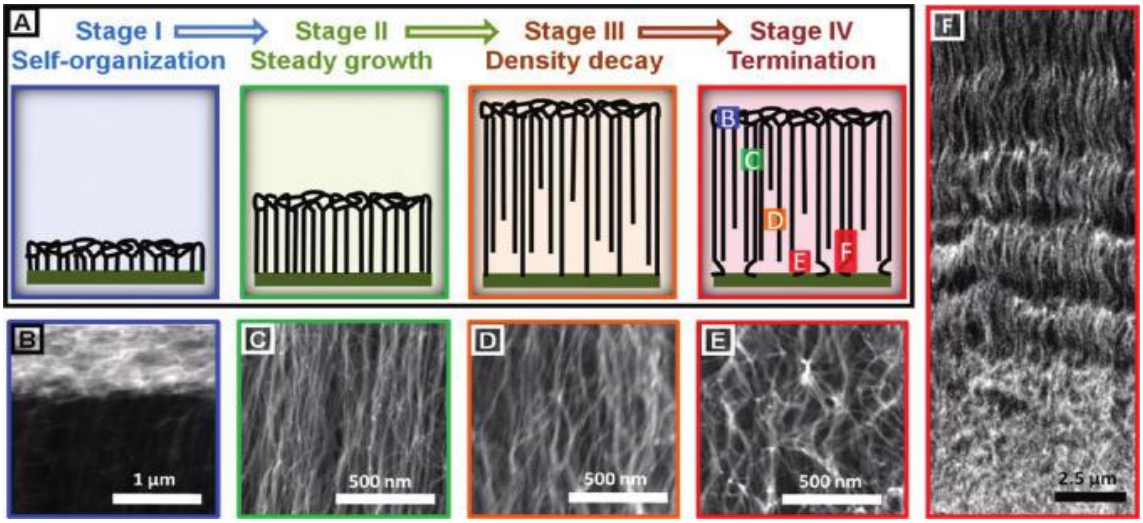

Figure 2.4 The four steps of VACNT growth proposed in Ref. 174.

In general, there are three requirements for successful synthesis of VACNTs: 1) a high number density of active catalyst NPs at the growth temperature;[175] 2) fast initiation and high growth rate;[176] 3) sustainable/competitive growth over the whole growth substrate.[177] To these ends, the control over the catalyst layer (in terms of composition,[178] morphology,[179] thickness,[180] and treatment[181]…) turned out to be the most important, in conjunction with the control over the CVD procedure (in terms of temperature, heating rate, atmosphere, and pressure…). The base-growth mechanism by TCVD necessitates an effective barrier layer against the diffusion of the catalyst to the growth substrate. It was found that synthesis of CNTs on a bare Si surface was not possible; a silicon oxide (SiO_2) barrier layer of a certain thickness was necessary.[154,183-186] Hence, SiO_2 could be used for patterned/selective synthesis of

VACNTs.[187] Actually, before 2004, TCVD processes of VACNT synthesis were limited to quartz substrate, silica-coated (mesoporous or nano-sized) surface, or surface oxidized silicon substrate, however, with relatively unsatisfactory growth rate, thickness uniformity, packing density, and/or quality.[117,166,175,188,189] In 2004, a breakthrough was achieved by Hata *et al*. They synthesized vertically-aligned SWNTs on a Si substrate using a water-vapor-assisted TCVD process, with aluminum oxide (or aluminum) and silicon oxide as the support layer and barrier layer, respectively.[105] Detailed discussion about the roles of the support layer and the barrier layer will be covered in Sections 2.3.3 and 2.5 in the chapter. Following the work by Hata *et al.*, Zhu *et al.* reported fast synthesis of high-qualtiy vertically aligned MWNTs, and multi-layered vertically aligned MWNTs via a water-vapor-assisted TCVD process.[106] It was found that VACNT growth was kinetics-controlled when the temperature was below 740 ^{o}C, but diffusion-controlled above 750 ^{o}C.[190]

2.3 Water-Vapor-Assisted TCVD for VACNT Synthesis

In this section, I present a study of the water-vapor-assisted TCVD process with more details.

2.3.1 Experimental

A Si (single-sided polished) wafer was surface oxidized by a stardard wet oxidation process to form a 200-nm-thick surface oxide. A support layer (Al_2O_3 or Al, or combined) and a layer of Fe catalyst were deposited sequentially onto the substrate. E-beam evaporation of Al_2O_3 and Al was conducted under a vacuum of 7.8×10^{-7}-1.1×10^{-6} Torr, with a deposition rate of 0.4-0.5 Å s^{-1}. Atomic layer deposition (ALD) of Al_2O_3 was carried out using trimethyl aluminum (TMA, Sigma-Aldrich) and distilled water alternatively entrained in nitrogen (N_2, Airgas) carrier flow. Exposure time in the TMA and the water vapors was 10 s each. The chamber pressure and the chamber temperature

were kept at ~1.0 Torr and 250 ^{o}C, respectively. For bimetallic catalyst recipes, the second metal was deposited by e-beam evaporation under a vacuum of ~3×10^{-6} Torr, with a deposition rate of 0.4-0.5 Å s^{-1} before the deposition of the top layer of Fe. For VACNT synthesis, the prepared substrate (with catalyst) was heated to 750 ^{o}C (unless otherwise mentioned) with a heating rate of 25 ^{o}C min^{-1} in a mixed gas of Ar and H_2. The flow rates of Ar and H_2 were 350 and 180 standard cubic cm per min (sccm), respectively. At 750 ^{o}C, ethylene (C_2H_4, 150 sccm) was turned on; a small flow of Ar bubbling through DI water at room temperature was turned on simultaneously. After preset growth duration at 750 ^{o}C, the ethylene flow and the small flow of Ar were turned off. The furnace was cooled to room temperature. The height of the VACNTs was measured under optical microscope. To study the nucleation of the Fe catalyst on the support layer and the surface roughness of the support layer, the substrates with Fe and without Fe, respectively, were heated to 750 ^{o}C with a heating rate of 30 ^{o}C min^{-1} in a mixed gas of Ar (350 sccm) and H_2 (180 sccm); then the substrat was naturally cooled to 200 ^{o}C in Ar only. For the catalyst annealing in oxygen (O_2), the substrate (with catalyst) was heated in a quartz tube from room temperature to 450 ^{o}C within 15 min, and then a 350-sccm Ar flow and a 150-sccm O_2 flow were turned on. After 1-hour annealing at 450 ^{o}C, the the substrat was naturally cooled to 200 ^{o}C in Ar only.

2.3.2 Status of Furnace Tube

Al_2O_3 tubes have been used in our lab for VACNT syntheses for years; however, little attention has been paid to the variation of the tube status. In the presence of the large H_2 flow (180 sccm), H_2-H_2O ratio determines the partial pressure of oxygen in the furnace tube. It will be seen in the Ellingham diagram (discussed in details in Section 2.4) that when the flow rates of the H_2 and the Ar bubbled into the DI water are 180 and 10 sccm, respectively, the partial pressure of O_2 in the furnace tube is ~10^{-25} at 750 ^{o}C. The number is so small that it means the control of the water-assisted VACNT synthesis is

extremely sensitive to the furnace status (sealing and inner-wall contamination). In fact, Al_2O_3 itself decomposes the carbon source at high temperatures, and the carbon deposite accumulates on the inner-wall of the furnace tube. Thus, tube cleaning is needed once every several weeks by purging O_2 at high temperatures. This introduces an issue to the reproducibility of the TCVD process: variation of the status of the furnace tube. In Figure 2.5, we show that the oxygen-rich furnace environment (right after the tube cleaning) and the carbon-rich environment (after 100 batches of TCVD synthesis) give rise to very different growth rates and growth termination points than the normal status (namely between 5 to 100 batches after tube cleaning). To ensure a high reproducibility, from here after, the synthsis is carried out at the normal furnace tube status.

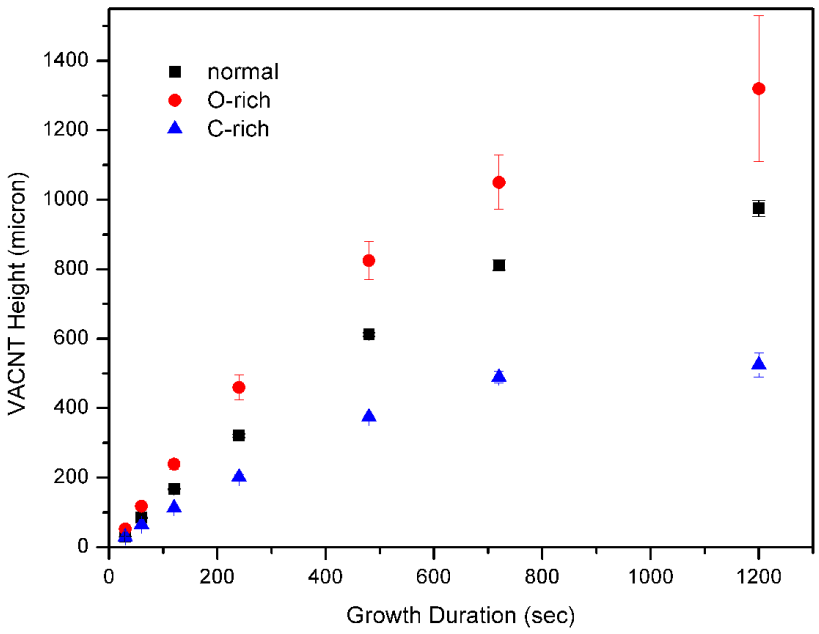

Figure 2.5 VACNT height as a function of growth time at different furnace status. "O-rich" refers to the VACNTs from the first 5 batches of synthesis after tube cleaning (it took one year to collect the O-rich data in the graph); "C-rich" refers to the VACNTs from after the first 100 batches of synthesis; "normal" refers to the VACNTs synthesized between 5 and 100 batches after tube cleaning. Synthesis conditions: 350-sccm Ar, 150-sccm C_2H_4, 180-sccm H_2, 6-sccm Ar bubbled into water, and at 770 ^oC. 15-nm Al_2O_3 by e-beam evaporation is used as the support layer, with a 2.5-nm Fe on top.

2.3.3 The Support Layer

An Al_2O_3 support layer of 10- to 15-nm thick has been used by many researchers for VACNT synthesis.[105,106,190-192] Indeed, Al_2O_3 has for long been used as the most efficient support material for Fe catalyst in hydrocarbon decomposition due to the following advantages: 1) accelerates decomposition of hydrocarbons;[193-197] 2) stable at high temperatures; 3) strong interaction with the Fe catalyst to restrict the surface mobility of Fe;[198,199] 4) Fe diffusion is very slow in Al_2O_3,[200] especially under a reduction atmosphere (*i.e.*, low partial pressure of O_2).[201]. Besides, wetting between Al_2O_3 and SiO_2 is good, even at high temperatures.[202,203]

In our study, we found that different preparation processes of the Al_2O_3 layer gave rise to very different growth rates (determined by the activity of the catalyst) and termination points (determined by the life time of the catalyst) of VACNTs under the same TCVD process, as shown in Figure 2.6. The life time and the growth rate increase in the order: ALD < EB < ALD-O < Al-ALD-O. One possible reason for the difference is the influence of the support layer on the aggregation of the Fe NPs. However, no distinct difference is observed between EB (Figure 2.7c) and ALD-O (Figure 2.7d) in terms of the Fe aggregation, probably because the aggregation is too fast to be discernible.[204] It is very interesting that the average surface roughness (measured by AFM) of the substrate (without Fe) increases in the order: ALD (0.21 nm) < EB (0.23 nm) = ALD-O (0.23 nm) < Al-ALD-O (0.43 nm), roughly in line with the trend on the life time and the growth rate. Recently, Amama *et al.* reported that the activity and lifetime of the catalyst was closely related to Oswald ripening (coarsening) of the catalyst during the TCVD process.[167] They also linked the Oswald ripening of the Fe catalyt to the surface roughness of the support layer,[179] consistent with our experimental results.

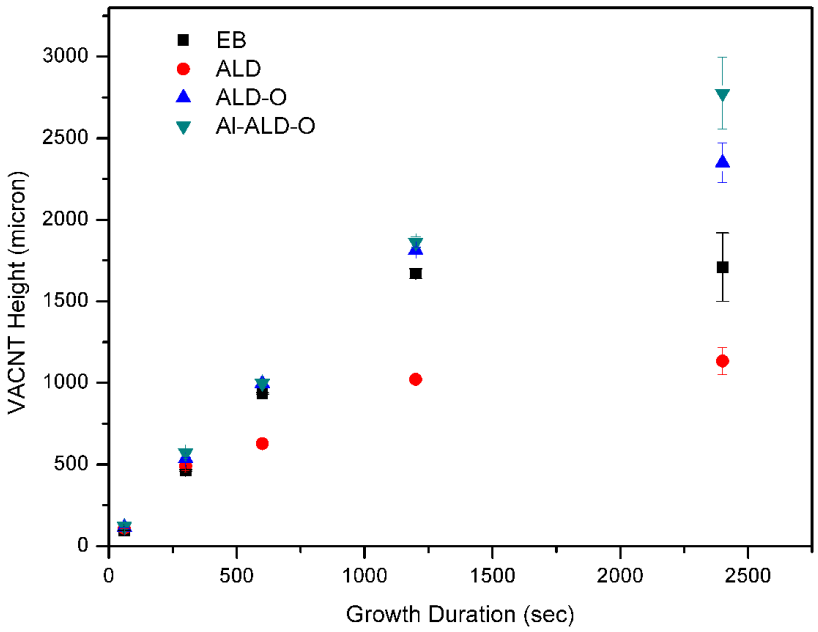

Figure 2.6 Influence of the support layer on water-vapor-assisted VACNT growth. "EB" referes to the catalyst (1.6-nm Fe) with a support layer of 10-nm Al_2O_3 by e-beam evaporation; "ADL": 10-nm Al_2O_3 by ALD; "ALD-O": 10-nm Al_2O_3 by ALD, and the whole substrate (with the deposited Fe catalyst) is annealed in oxygen before the TCVD process; "Al-ALD-O" 8-nm Al by e-beam evaporation plus 1.2-nm Al_2O_3 on top by ALD, and the whole substrate (with Fe) is annealed in oxygen.

2.3.4 The Roles of Water Vapor

The roles of water vapor in the TCVD process may include: 1) improving the synthesis rate of CNTs;[105] 2) etching amorphous carbon at the CVD temperature to generate clean CNT surface;[106] 3) keeping the bottom part of the tubes (where catalyst particle and the tube are in contact) opened to retard the synthesis termination (catalyst deactivation).[191,205,206] Recently, Amama *et al*. studied the Oswald ripening process of Fe catalyst particles during TCVD synthesis, and proposed that water vapor retarded the Ostwald ripening of the Fe catalyst particles due to the ability of oxygen and hydroxyl species to reduce diffusion rates of Fe.[167] In Figure 2.8, we show that the size of the Fe particles on the growth substate (with an EB-Al_2O_3 support layer) exhibits a more

uniform distribution when treated in the presence of water vapor than in the absence of water vapor.

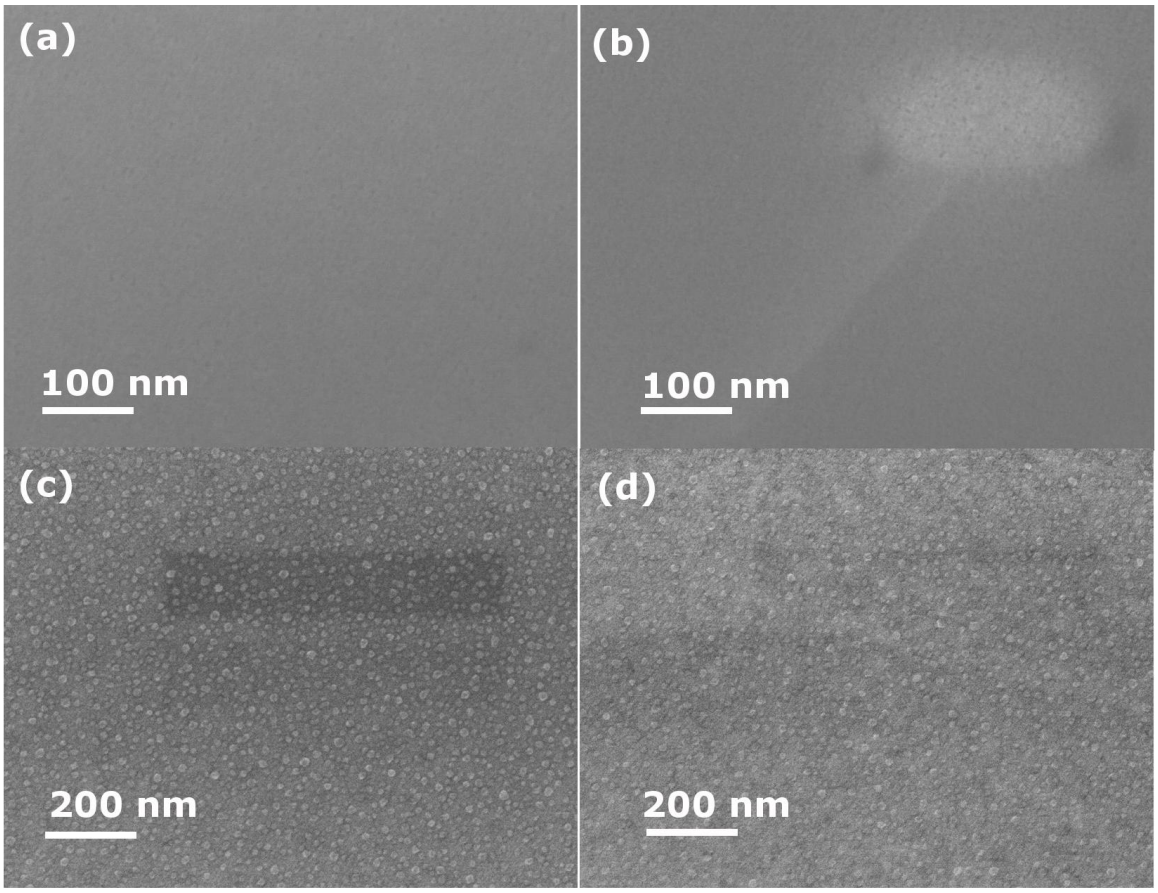

Figure 2.7 Top-view SEM images of the growth substrate with 2.2-nm Fe and a 10-nm Al_2O_3. (A) EB-Al_2O_3 before thermal treatment; (B) ALD-O before thermal treatment; (C) EB-Al_2O_3 after thermal treatment; (D) ALD-O after thermal treatment.

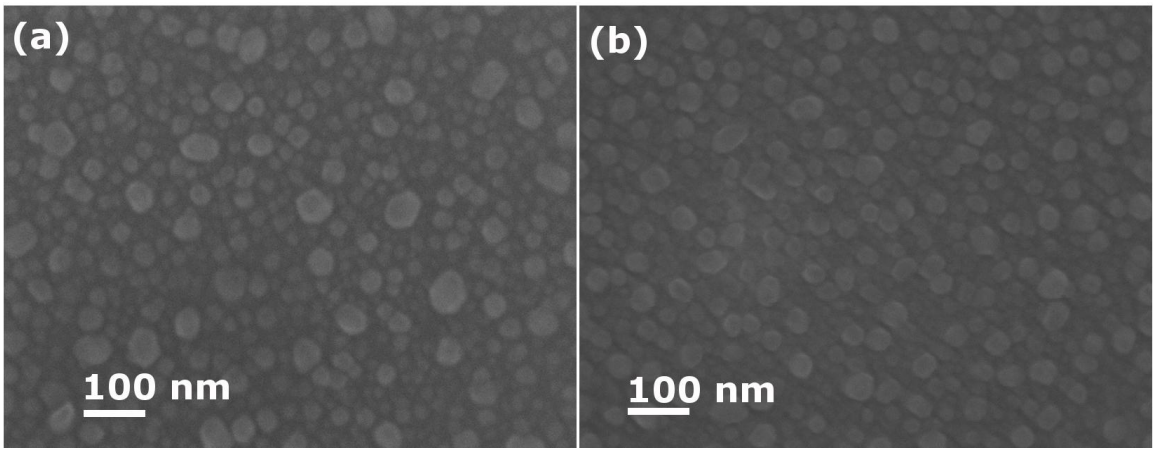

Figure 2.8 Top-view SEM images of the Fe catalyst particles:(a) without water vapor; (b) with water vapor. The treatment was carried out in the absence of C_2H_4, as for Figure 2.7.

2.3.5 Water-Vapor-Assisted TCVD Synthesis of Vertically Aligned Double-Walled CNTs

One general requirement for SWNT or doubled-walled CNT (DWNT) synthesis is to have small enough catalyst NPs on the substrate surface during the initiation process. The key is to retard the aggregation of the catalyst. The following procedures (not necessarily all) are widely used in literature to prohibit/retard the agglomeration of the catalyst to form large NPs upon reduction: 1) a thin catalyst layer (typically <1 nm);[105,107,111,207,208] 2) fast heating of the substrate to the growth temperature;[107,111] 3) addition of a second element in the catalyst recipe such as Mo;[207] 4) low vacuum;[107,207] 5) PECVD.[107,208] Here we demonstrate that at certain conditions vertically aligned DWNTs with relatively large diameters can be synthesized via the water-vapor-assisted TCVD process. There were four major modifications on the aforementioned water-vapor-assisted TCVD process: 1) a thinner Fe layer (0.8 nm) was deposited on the aforementioned Al-ALD-O support layer; 2) after annealed in oxygen, reduced in H2 (at 550 ^{o}C for 5 min), a 1.3-nm-thick Al_2O_3 layer was immediately deposted on top of the catalyst by ALD, followed by the deposition of a second 0.8-nm-thick Fe layer; 3) the H_2 flow was turned on after the furnace reached 700

^{o}C; 4) the flow rate of C_2H_4 was 130 sccm. HRTEM images of the DWNTs are shown in Figure 2.9.

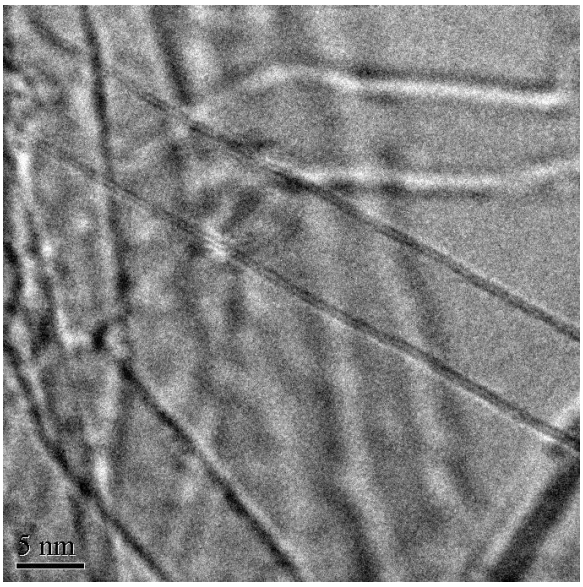

Figure 2.9 HRTEM image of synthesized double-walled CNTs.

As has been shown in Section 2.3.3, oxygen annealing is beneficial for achieving a long life time of catalyst NPs and a high growth rate of CNTs. This is consistent with the result reported by Shanov's group.[181] To single out the influence of the top ALD-Al_2O_3, we studied the aggregation of a 3.5-nm-thick Fe catalyst layer on a regular growth substrate (with 10-nm EB-Al_2O_3) with and without the top 1.3-nm ALD-Al_2O_3. In Figure 2.10, we see that the top ALD-Al_2O_3 layer effectively retards the aggregation of Fe at the growth temperature.

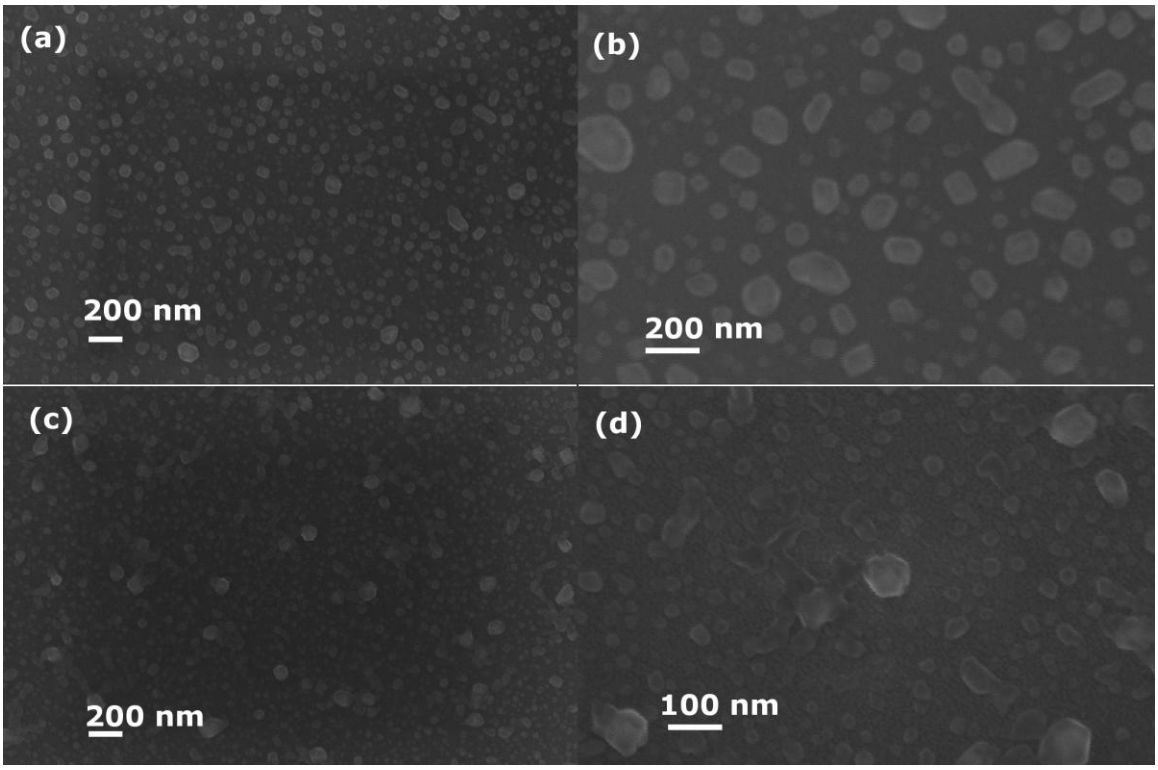

Figure 2.10 Top-view SEM images of the aggregated Fe NPs on a regular growth substrate (with 10-nm EB-Al_2O_3) without (a and b) and with (c and d) the 1.3-nm ALD-Al_2O_3.

2.3.6 Bimetallic Catalyst

In some cases, a good adhesion between the growth substrate and the VACNT film is desired. Titanium (Ti) and chrominum (Cr) are widely used as the adhesion layer in electronics, and have been said to be able to enhance the interface between CNTs and the growth substate by some researchers. In Figures 2.11 and 2.12, we show the preliminary results of VANCT synthesis based on Fe-Cr bimetallic catalyst. We see that the presence of Cr greatly interrupts the VACNT synthsis, resulting in a poor alignment and uniformity, and a high impurity. Even worse results can be seen in the case of Fe-Ti (Figure 2.13). In Figure 2.14, we see that the presence of Ti accelerates the agglomeration of the catalyst particles. Moreover, we didn't find distinct improvement of the interfacial

adhesion between the growth substrate and the VACNT film by introducing Cr or Ti in the catalyst recipe.

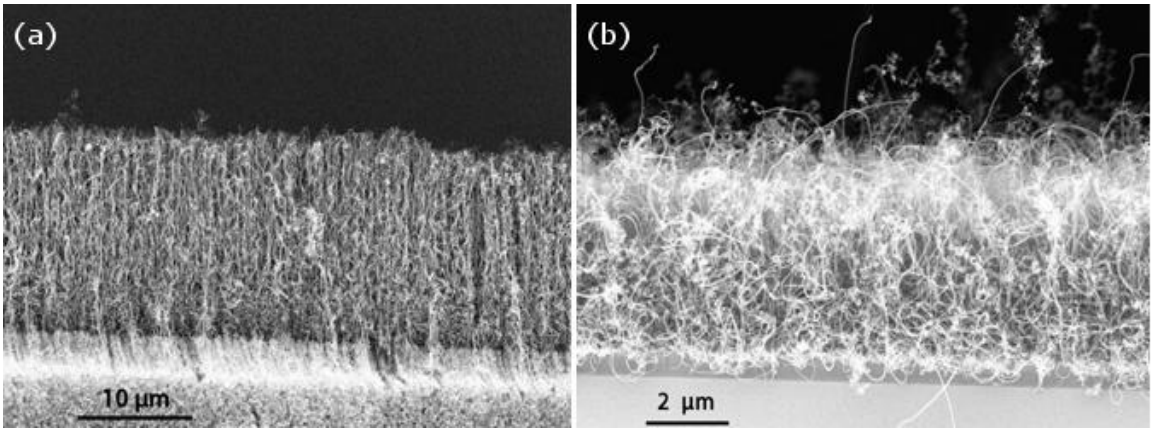

Figure 2.11 Side-view SEM images of the CNT film synthesized using Fe-Cr bimetallic catalyst: (a) 5-nm Fe on 3-nm Cr; (b) 3-nm Fe on 5-nm Cr.

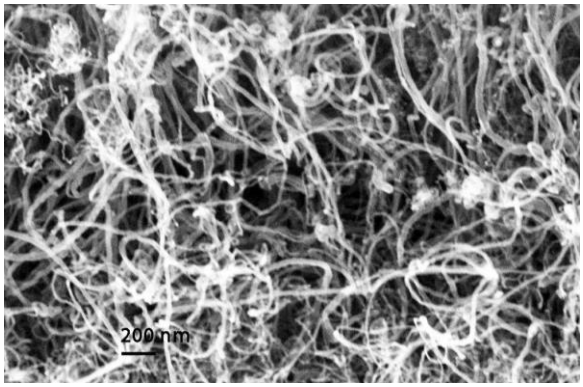

Figure 2.12 A tilt-view SEM image of the synthesized CNTs using Fe-Cr bimetallic catalyst (5-nm Fe on 3-nm Cr).

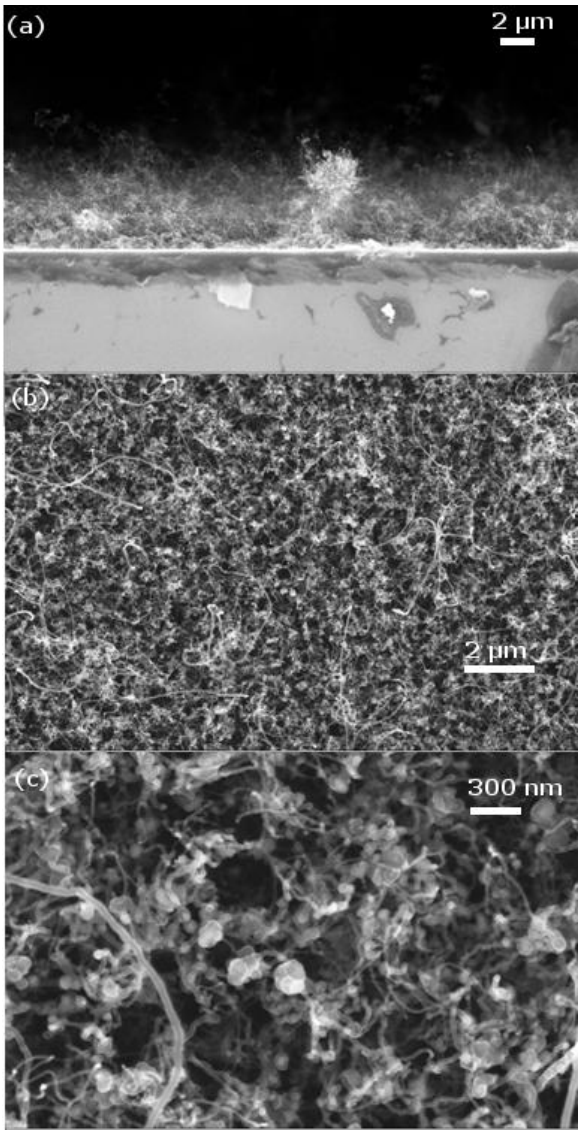

Figure 2.13 SEM images of the synthesized CNTs by Fe-Ti bimetallic catalyst (3-nm Fe on 2-nm Ti): (a) a side view; (b) and (c) top views.

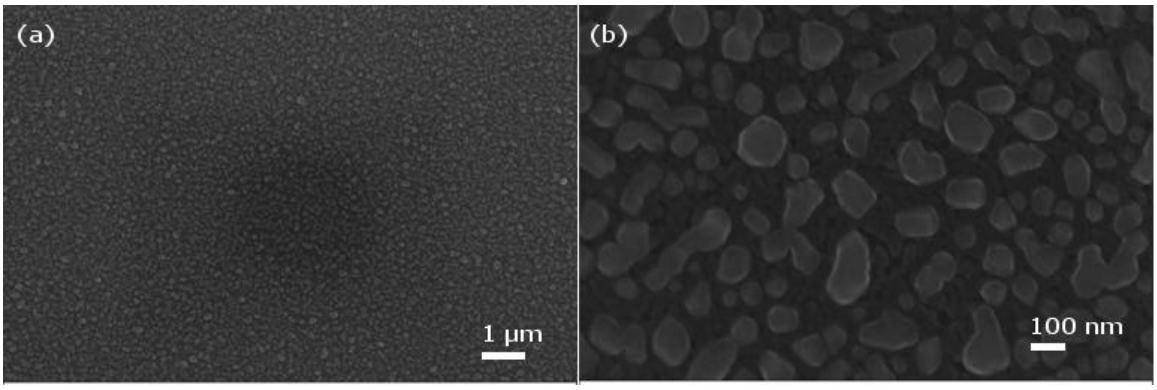

Figure 2.14 Top-view SEM images of catalyst (3-nm Fe on 2-nm Ti) on the growth substrate.

2.4 In Situ Functionalization of VACNTs

Synthesized VACNTs are typically inert. Wet functionalization processes have been developed to introduce functional groups to the CNT surface.[209-211] The wet functionalization processes usually truncate the CNTs randomly and introduce high defect density to the lateral walls of the CNTs, which greatly degrades the intrinsic electrical and thermal properties of the 1D structure of the CNTs. Furthermore, big challenges exist in maintaining the vertical alignment, selective patterning, length control and quality control of functionalized VACNTs. In this section, we explore a novel functionalization process: in situ functionalization, namely, functionalization of VACNTs during the TCVD process.

2.4.1 Experimental

10-nm-thick Al_2O_3 and a 2.2-nm-thick Fe were deposited sequentially on the substrate by e-beam evaporation. The substrate was heated to 750 ^oC with a heating rate of 25 $^oC\ min^{-1}$ in a mixed gas of Ar and H_2. The flow rates of Ar and H_2 were 350 and 180 sccm, respectively. At 750 ^oC, ethylene (150 sccm) was turned on; a small flow (1-3 sccm) of Ar was turned on simultaneously to bubble through a 10 wt.% aqueous solution of hydrogen peroxide (H_2O_2). After preset growth duration at 750 ^oC, the ethylene flow and the small flow of Ar were turned off. The furnace tube was cooled to 300 ^oC. At 300

^{o}C, Ar was turned up to 500 sccm, and 1-sccm Ar flow that was bubbled through the H_2O_2/H_2O solution was turned back on. After 5 min, H_2 and the small Ar flows were turned off. The furnace tube was fastly cooled to room temperature from 220 ^{o}C.

X-ray photoelectron spectroscopy (XPS) was performed on Model 1600 XPS system equipped with a monochromator Al K_α source. High resolution spectra were collected with a passing energy of 46.95 eV. The step size and time were 0.025 eV and 100 ms, respectively. Fourier-transform infrared spectroscopy (FT-IR, Nicolet, Magna IR 560) was used to study the functional groups on the in situ functionalized CNTs (f-CNTs) and their reactions with thionyl chloride ($SOCl_2$). The reaction product of f-CNTs with $SOCl_2$ was designated as s-CNT. The samples were properly dried, mixed with KBr and pressed to form the semi-transparent pellets. Spectra were collected in N_2 at an ambient temperature, by 1000 scans in the wavelength range from 500 to 4000 cm^{-1}, at a resolution of ~4 cm^{-1}.

2.4.2 Results and Discussion

Figure 2.15 shows the side-view SEM images of the as-synthesized f-CNT films, showing a well aligned structure and uniform thickness.

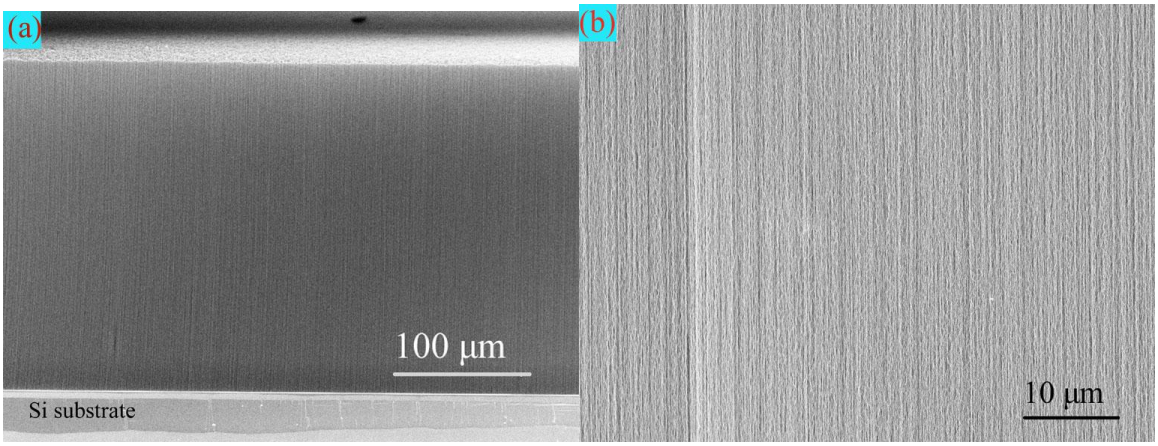

Figure 2.15 Side-view SEM images of an f-CNT film.

XPS scans were carried out on the top of the pristine (non-functionalized) VACNTs (p-CNTs) and the f-CNTs. Figure 2.16a is the spectrum of p-CNTs, where no oxygen peaks were detected. The C1s peak of the p-CNTs is centered at 284.5±0.1 eV, assigned to the sp^2 hybridized carbons in the graphitic structure. In comparison, Figure 2.16b clearly shows the existence of oxygen in f-CNTs. The binding energy of the O1s peak is around 529.6 eV, which means that the oxygen does not come from the dissociated (or adsorbed) H_2O—the binding energy of O1s in H_2O is ~533 eV.[212] The asymmetric C1s peak in f-CNT was deconvoluted after background subtraction by the Shirley's method. The peaks at 286.3±0.2 and 287.3±0.2 both correspond to carbon atoms in C-O.[213] The peaks centered at 285.2±0.2 and 290.0±0.2 eV are attributed to the sp^3 carbon atoms and the carboxylic acid groups on the aromatic ring, respectively.[214] The XPS results indicate that the as-synthesized f-CNT walls were in situ modified with some oxygen-containing functional groups.

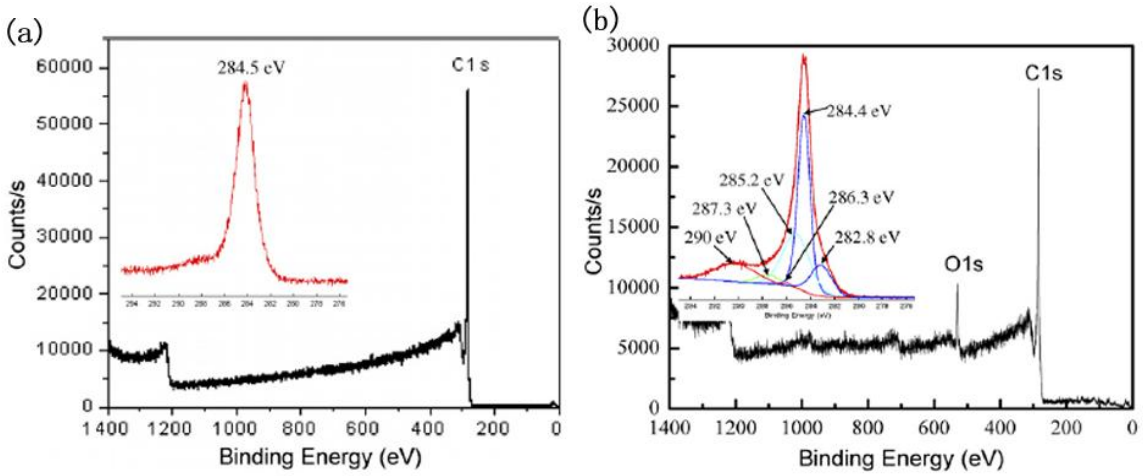

Figure 2.16 XPS spectra of p-CNT (a) and f-CNT (b). Inserted are the corresponding high-resolution C1s spectra.

Figure 2.17 (trace a) shows the FT-IR spectrum of the f-CNTs. The peak at ~1572 cm^{-1} is attributed to the C=C asymmetric stretching in graphite-like CNT structure. Consistent with XPS results, oxygen related functional groups were found in the f-CNTs. The peaks at 3445, 1229, 1179 and 1060 cm^{-1} are attributed to O-H, C-O, C-O-C and

primary C-OH stretchings, respectively. The weak and wide absorption band at ~1730 cm^{-1} is supposed to consist of different carbonyl groups from, for example, carboxylic acid groups and ester groups. The sharp peak at 1647 cm^{-1} is assigned to quinone type units along the side walls of the CNTs.[215] These oxygen involved functional groups, particularly the hydroxyl groups and the carboxylic acid groups, may render the f-CNTs chemically reactive. To prove the reactivity, we use $SOCl_2$ to react with the f-CNTs. Trace b in Figure 2.17 shows the FT-IR spectrum of s-CNTs. Many characteristic peaks in the f-CNTs remain in the s-CNTs, except that the peaks of hydroxyl groups at 3445 and 1060 cm^{-1} disappear. We postulate that the hydroxyl groups on the f-CNTs reacted with $SOCl_2$ to give –C–O–S or even (–C–O–)2S=O groups. Correspondingly, two new peaks at 1338 and 1070 cm^{-1}, both coming from the S=O stretching, appear in the s-CNTs. Another feature in the spectrum of s-CNT is the distinct carbonyl groups at 1797 cm^{-1}, characteristic of carbonyl chloride groups from the reaction between –COOH and $SOCl_2$.

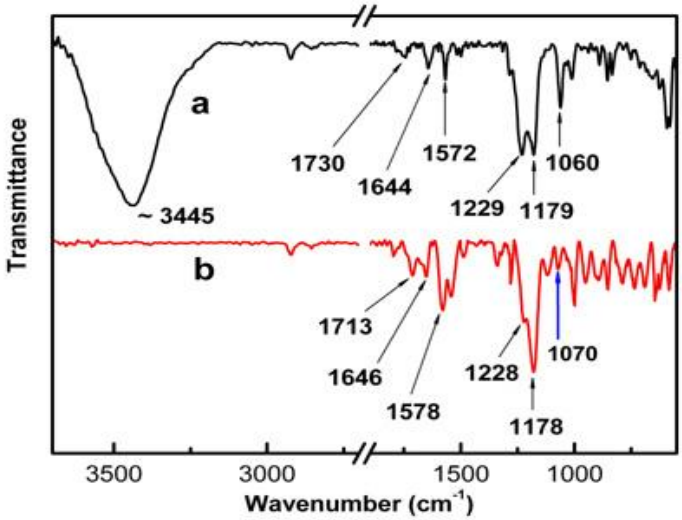

Figure 2.17 FT-IR spectra of f-CNTs (a) and s-CNTs (b)

2.4.3 Thermodynamics and Kinetics Considerations of the In Situ Functionalization

Let us think about the simplest single reaction: functionalizaiton of double bonds in CNTs by O_2 to form epoxide groups, as illustrated in Figure 2.18.

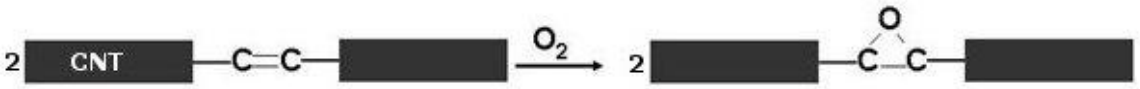

Figure 2.18 Illustration of the functionalization of the double bonds in CNTs by oxygen to form epoxide groups.

Since the experimental conditions ensure a constant temperature and pressure, if the change of Gibbs free energy of the reaction, ΔG, is negative at a particular temperature and total pressure, the reaction can occur. Assuming a small percentage (0.1% by atom) of epoxide functional groups uniformly distributed among the double bonds on an f-CNT, Gibbs free energy can be written as:

$$\Delta G = \Delta G_T^0 + RT \ln Q \tag{2.1}$$

$$Q = \frac{a^2_{f-CNT,epoxide}}{a^2_{CNT} \cdot a_{O_2}} \tag{2.2}$$

where a is the activity, and $a_{f\text{-}CNT,epoxide}=10^{-3}$.

Let us choose pure, stoichiometric CNT and f-CNT, and pure O_2(g), all at 1 atm pressure, as our reference states.

$$Q = \frac{a^2_{f-CNT,epoxide}}{a_{O_2}} \approx \frac{a^2_{f-CNT,epoxide}}{p_{O_2}} \tag{2.3}$$

where p_{O2} is the partial pressure of O_2 in the gas phase.

$$\Delta G_T^0 = -RT \ln K = RT \ln \left[p_{O_2}\right]_{eq} \tag{2.4}$$

Hence,

$$\Delta G = RT \ln \frac{\left[p_{O_2}\right]_{eq} a^2_{f-CNT,epoxide}}{p_{O_2}} \tag{2.5}$$

which means that the oxidative functionalization of CNTs to form the epoxide groups will proceed if:

$$\frac{\left[p_{O_2}\right]_{eq} a^2_{f-CNT,epoxide}}{p_{O_2}} < 1 \tag{2.6}$$

i.e.,

$$p_{O_2} > \left[p_{O_2}\right]_{eq} a^2_{f-CNT,epoxide} = 10^{-6} \cdot \left[p_{O_2}\right]_{eq} \tag{2.7}$$

ΔG can be written as:

$$\Delta G^0_T = \Delta H^0_T - T\Delta S^0_T \tag{2.8}$$

Given that the CNT and the f-CNT are essentially identical in structure, and that the functionalization degree is very low, the difference in entropy between the CNT and the f-CNT is zero. The contribution to entropy change is from oxygen; this is exactly the reason why in the Ellingham diagram (Figure 2.19) we can see that most of the curves exhibit almost the same slope.

Take T=800 K as an example, the absolute entropy value of oxygen at 800 K and 1 atm is 235.8 J mol^{-1} K^{-1}.[216]

$$T\Delta S^0_T = -0.8 \times 235.8 = -188.6 \text{ kJ mol}^{-1} \tag{2.9}$$

Given that enthalpy is a weak function of temperature, the enthalpy change of reaction is approximated by bond enthalpy difference. Enthalpy of the second C–C bond in an aromatic molecule is -170 kJ mol^{-1}; bond enthalpy (the double bond) of O_2 is -479 kJ mol^{-1}; C-O bond enthalpy is -360 kJ mol^{-1}.

$$\Delta_f H^0_{800K} = (-360) \times 4 - \left[-479 + (-170) \times 2\right] = -603 \text{ kJ mol}^{-1} \tag{2.10}$$

Additional contribution from absolute enthalpy change of oxygen is:

$$\Delta H^{800K,O_2}_{298K,O_2} = -(\Delta_f H^0_{298K,O_2} + H_{800K,O_2} - H_{298K,O_2}) = -15.8 \text{ kJ mol}^{-1} \tag{2.11}$$

We can see the effect of temperature on the enthalpy change is <10% that on the entropy change.

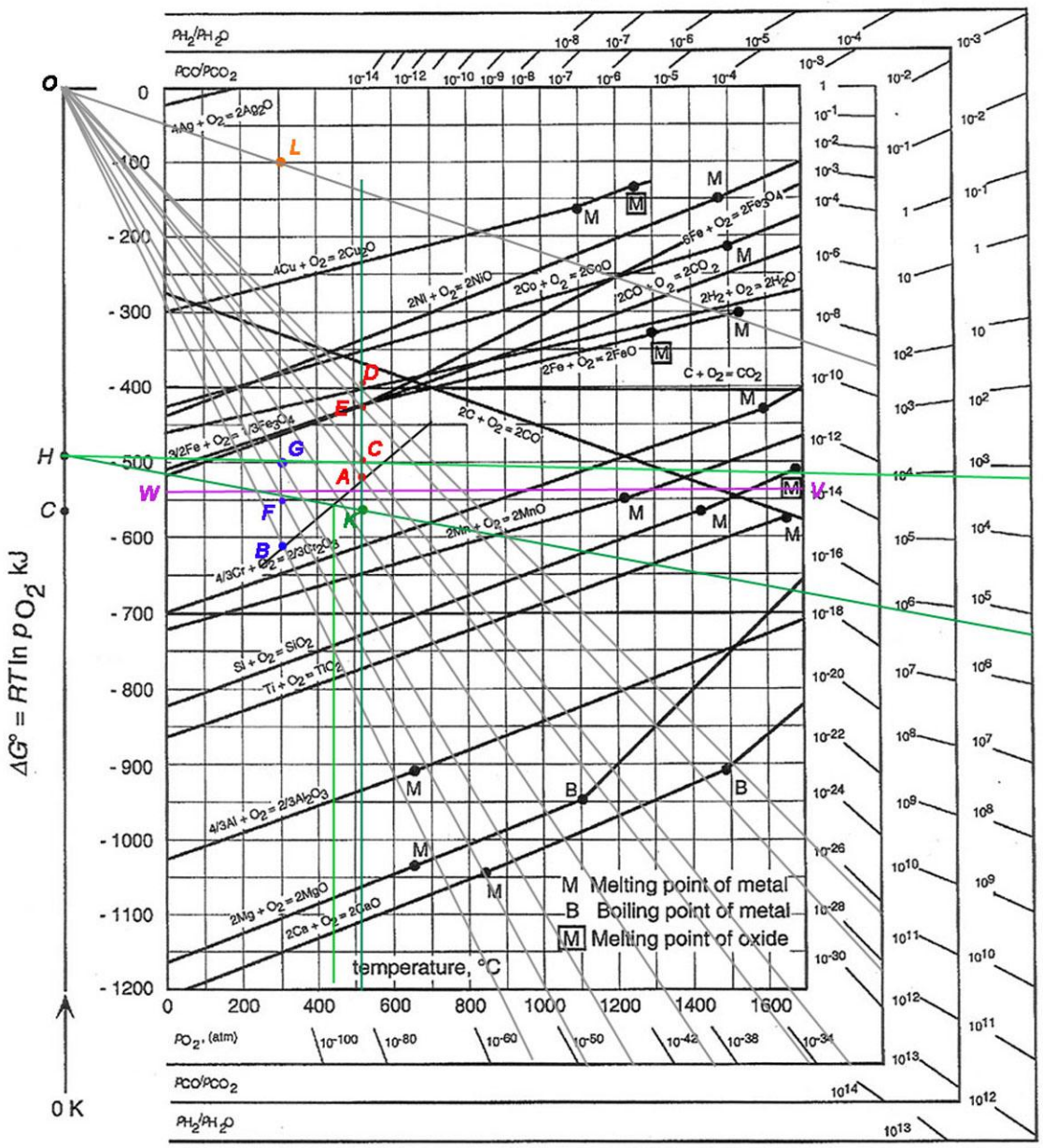

Figure 2.19 Ellingham diagram for the study of in situ functionalization of CNTs.

$$\Delta H^0_{800K} = \Delta_f H^0_{800K} + \Delta H^{800K,O_2}_{298K,O_2} = -618.8 \text{ kJ mol}^{-1} \tag{2.12}$$

$$\Delta G^0_{800K} = \Delta H^0_{800K} - T\Delta S^0_{800K} = -430 \text{ kJ mol}^{-1} \tag{2.13}$$

Hence, at 800K, at equilibrium,

$$\left[p_{O_2}\right]_{eq,800K} = 8\times10^{-29} \tag{2.14}$$

$p_{O_2} > 8\times10^{-35}$ is the criterion for the reaction to proceed at 800K (point A in Figure 2.19) to achieve 0.1% functionalization degree of epoxide groups on the CNTs.

Note that point A is below point D, which states that because the equilibrium partial pressure of O_2 for oxidation reaction of pure graphite to carbon dioxide at 800K (point D) is 5×10^{-27}, it is thermodynamically allowed to have the 0.1% functionalization degree, or even 100% such functionalization (point E) without burning the CNTs.

Let us think about O_2 control by controlling the ratio of the partial pressure of H_2 to the partial pressure of H_2O vapor. The solubility of water in a gas at 1 atm can be calculated from the vapor pressure of the liquid. Raoult's law yields an expression for the mole fraction, y_1:

$$y_1 = \frac{(1-x_2)p^s}{p^t} \tag{2.15}$$

where x_2 is the mole fraction of the gaseous component dissolved in the liquid, p^s is the saturated vapor pressure of the pure liquid, and p^t is the total pressure. x_2 is extremely small for argon in water at 1 atom at room temperature. At room temperature, saturation vapor pressure of water above pure water is 17 Torr.[217]

Hence, $y_1 \approx \frac{17}{760} = 0.022$ (2.16)

Taking the flow rates of Ar, H_2, and the Ar bubbled through the water (seated at room temperature) as 350, 180, and 10 sccm, respectively, and assuming ideal gas properties of all these gases, the ratio of the partial pressure of H_2 to the partial pressure of H_2O vapor is 2×10^3. The corresponding control point, C, falls between A and E, and is effective to give us a 1% functionalization degree; therefore, the single functionalization is feasible by H_2-H_2O control at 800 K using such flow rates.

Similarly, at 300 ^oC, points A and E shift to B and F, respectively. If we functionalize the CNTs at 527 ^oC (800 K), and keep the H_2/H_2O ratio (*i.e.*, keep the flow rates) during cooling to 300 ^oC, the H_2-H_2O control point will shift to G. We will neither

lose the functionalization nor burn out the CNTs. Of course, other functionalization reactions and kinetics factors should all be considered. What will happen if we cool the f-CNTs from 527 ^{o}C to 300 ^{o}C in only Ar and H_2 without introducing the H_2O vapor? Assuming that the H_2O vapor concentration in this case is 1 ppm (as impurity in the ultra-high purity Ar and H_2), the control point at 527 ^{o}C is K, which falls below A. This means we will loose the functional groups. Although it seems that at low temperatures (*i.e.*, (<440 ^{o}C, the temperature at the cross point of HK line and BA line) the functionalization may resume even at 1-ppm-H_2O concentration, kinetics do not allow the reaction to occur—we never observe low-temperature functionalization of CNTs in the ultra-high purity Ar and H_2.

The important conclusions from the discussion above are:

1) To achieve 0.1% epoxide functional groups on f-CNTs (without considering kinetics or any other possible reactions), the H_2-H_2O control is feasible over a wide range of temperature;

2) In order to keep the functionalization, f-CNTs should not be cooled in only Ar and H_2 in the absence of H_2O.

Now there is an important issue to worry about. CNT is not the stable form of graphite, it introduces extra energy (*e.g.*, due to the curvature), the ΔG_0–T line of the oxidation reaction of a CNT to carbon dioxide should be below that of the oxidation reaction of pure graphite to carbon dioxide in the Ellingham diagram, *e.g.*, the WV line in Figure 2.19. As such, there is a risk that the WV line may fall below the H_2-H_2O control line (HC line). This simply means the CNTs get burned. In reality, introducing H_2O vapor during the cooling burns the CNTs. Therefore, the functionalization by H_2-H_2O control at relatively high temperatures is not favorable. Although funtionalization at a properly low temperatur by such a H_2-H_2O control may be thermodynamically overpowerful (*e.g.*, point G), the operation has not been successful. The reason can be very complicated.

As an alternative to the H_2-H_2O control, we can directly introduce a bit more O_2 using a H_2O_2/ H_2O solution. At room temperature, the mole fraction of H_2O_2 in the H_2O-H_2O_2 vapor for a 10 wt% aqueous solution of H_2O_2 is <0.1%.[217] The total H_2O-H_2O_2 vapor pressure is ~17 Torr. Taking the flow rates of Ar, H_2, and the Ar bubbled through the 10 wt% aqueous solution of H_2O_2 (seated at room temperature) as 500, 180, and 1 sccm, respectively, and assuming ideal gas properties of all these gases and complete decomposition of H_2O_2 in the preheating zone of the tube, the partial pressure of O_2 in the synthesis zone of the tube is instantaneously 2.5×10^{-8}. Thermodynamically, the existence of H_2 will push the partial pressure of O_2 toward 10^{-40} before any oxidation reactions of carbon occur at 300 ^{o}C; however, kinetically, various oxidation reactions of carbon can occur in parallel to the oxidation reaction of H_2.

2.5 Synthesis of VACNTs on Bulk Copper

As discussed in Section 1.5, Scenario 2—direct synthesis of VACNTs on the heat spreader—is feasible for incorporation of VACNT TIMs in electronic packaging. Bulk Cu is the most widely used heat spreader in industry. This section presents the synthesis of high-quality VACNT films on bulk Cu substrates.

A few papers have reported VACNT syntheses on various metal substrates; however, the direct VACNT synthesis on a bulk Cu substrate is still a great challenge.[135,218-223] Wang *et al*. developed a process to grow VACNTs on a copper foil surface by water-vapor-assisted TCVD.[224] However, the quality and the structure of the "VACNTs" on copper were not described clearly. Recently, Yin *et al*. reported growing MWNTs on an oxygen-free copper substrate, however, with a poor CNT alignment.[225] Implementation of VACNTs grown on copper for thermal management was reported by Fisher's research group.[8,226] A trilayered catalyst structure (6-nm Ni/10-nm Al/30-nm Ti) deposited on a copper substrate/foil was used to grow VACNTs by PECVD. Nevertheless, the VACNTs in the two references exhibited different average

diameters, diameter distributions and CNT coverage on the synthesis substrates, even though the same synthetic conditions were used. Moreover, no TEM images were given to show if the "CNTs" synthesized by the PECVD process exhibited a bamboo structure or multi-walled hollow tube structure—this is important in determining the intrinsic thermal conductivity of the "CNTs". It turned out that high reproducibility of VACNT synthesis on bulk Cu substrates by TCVD was even more challenging. Besides, fundamental understanding of the roles of the support layers underneath the catalyst layer during the VACNT synthesis on Cu is still not clear. The goals of this section are: 1) demonstration of a reproducible TCVD process to synthesize high-quality VACNTs on bulk Cu substrates; 2) providing some fundamental understanding of the TCVD synthesis on Cu.

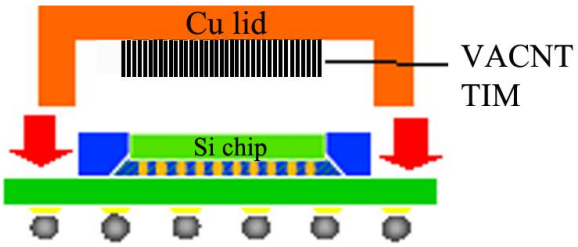

Figure 2.20 A conceptual illustration of the VACNTs grown on a Cu lid surface as TIM for microelectronic packaging.

2.5.1 Experimental

A pure Cu plate (1×1×0.1 cm^3, purchased from Speedy Metals) was abraded with SiC paper (grit 1200 and 2000 sequentially), and polished with an Al_2O_3 (100 nm) slurry. The polished Cu plate was cleaned with acetone and isopropanol sequentially at room temperature with sonication, and dried immediately with nitrogen flow. The polished Cu had an average roughness R_a=0.35-0.42 μm and a peak-to-valley height R_z=3.5-3.9 μm. R_a and R_z for the as-received Cu plate (designated as non-polished Cu) were 0.9-1.2 and

7.3-8.9 μm, respectively. The R_a and R_z values were measured on a profilometer (Tencor KLA, P15). A thin layer of Al_2O_3 was used as the support layer on the Cu substrate for VACNT synthesis. In order to study the influence of the quality of the Al_2O_3 layer on the VACNT synthesis on Cu, two different approaches of Al_2O_3 deposition were studied and compared: e-beam evaporation and ALD (refer to Section 2.3.2 for experimental details). Fe catalyst (3-3.5 nm) was deposited on top of the Al_2O_3 support layer e-beam evaporation. For comparison, VACNTs were also synthesized on Si and surface oxidized Si substrates with an Al_2O_3 support layer and the Fe catalyst layer. TCVD synthesis of VACNTs was carried out at 750 ^oC as described before. A trace amount of H_2O was introduced into the chamber as usual. Atomic force microscopy was performed in a Dimension 3100 from Veeco Instruments operating in a taping mode in air.

2.5.2 Results and Discussion

Experimental results are listed in Table 2.1. We have observed and summarized three important phenomena: 1) a thin Al_2O_3 support layer (5-20 nm) deposited by e-beam evaporation fails to grow VACNTs on either polished or non-polished Cu substrates; 2) ALD, compared with e-beam evaporation, is a much better approach of making an efficient Al_2O_3 support layer on the Cu substrates for VACNT synthesis; 3) an ultra-thin Al_2O_3 layer (5 nm) deposited by ALD is sufficient for VACNT synthesis on a surface-oxidized Si substrate but it is ineffective on a bare Si substrate. The quality of the Al_2O_3 support layer and its actual thickness account for the different results and they all depend on the Al_2O_3 deposition method and the surface roughness of the synthesis substrate.

2.5.2.1 The Discontinuity of the Al_2O_3 Support Layer by E-beam Evaporation

Generally, literature describes the conditions (thickness, deposition, and vacuum) for the deposition of an Al_2O_3 support layer on a growth substrate by e-beam evaporation; however, the continuity of the deposit has rarely been mentioned. During the e-beam

evaporation process, a continuous deposit layer forms on a substrate surface through nucleation and synthesis steps. At an early stage of deposition, heterogeneous nucleation may become rate controlling. This nucleation mechanism leads to isolated aggregates of condensate on the substrate when the deposit layer is thin.[227] This discontinuity was briefly discussed by de los Arcos *et al*.[228] In fact, the discontinuity of the deposit is the right reason why a thin layer of gold (Au) deposit on a bare Si surface by e-beam evaporation was recently employed to selectively etch Si wafers.[229]

Table 2.1 A summary of the experimental results of VACNT synthesis on various substrates with varied Al_2O_3 deposition methods and thickness.

Substrates	Al_2O_3 preparation	Al_2O_3 thickness (nm)	VACNT thicknesss (μm)[a]
non-polished Cu	e-beam	5-30	--[b]
	ALD	5, 10	--
		15, 20	<50
		25, 30	>100
polished Cu	e-beam	5-20	--
		25, 30	<50
	ALD	5	--
		10	<50
		15, 20, 25	>100
Si	e-beam	5, 10	--
		15, 20	<500
Si	ALD	5	--
		10	>100
		15	>800
		20, 25	>1200
SiO_2/Si	ALD	5, 10, 20	>1800

a. The average VACNT array thickness after 20-min synthesis on a 1-cm^2 substrate under the same TCVD conditions.
b. "--" means that a uniform VACNT film could not be grown.

In our study, under the e-beam evaporation conditions of Al_2O_3 (room temperature, 7.8×10^{-7}-1.1×10^{-6} Torr), there is no oxygen-enabled interfacial reaction between the Al_2O_3 and Cu to realize the wetting.[230-232] The poor wetting together with the surface roughness and impurity of the Cu substrate assists the heterogeneous nucleation and makes a thin Al_2O_3 deposit discontinuous. A continuous deposit forms only when the growing layer thickens enough for the aggregate to impinge on each other.[227] Therefore, when the Al_2O_3 deposit layer is too thin to become continuous, isolated nanoaggregates are formed.[228,233] In this case, the bottom Cu surface is partially exposed to the top Fe catalyst and/or the carbon source at the inter-grain voids of the Al_2O_3 layer during the TCVD process, as illustrated in Figure 2.21a, and the VACNT synthesis fails. Figures 2.22a and b show the surface status of a non-polished Cu substrate after the TCVD process of CNT synthesis.

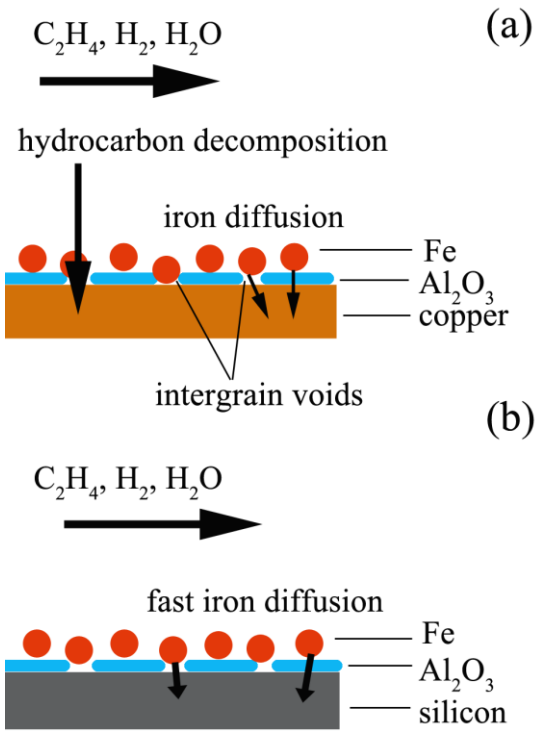

Figure 2.21 Illustrations of an ineffective support layer on a Cu (a) or Si (b) surface during a TCVD process.

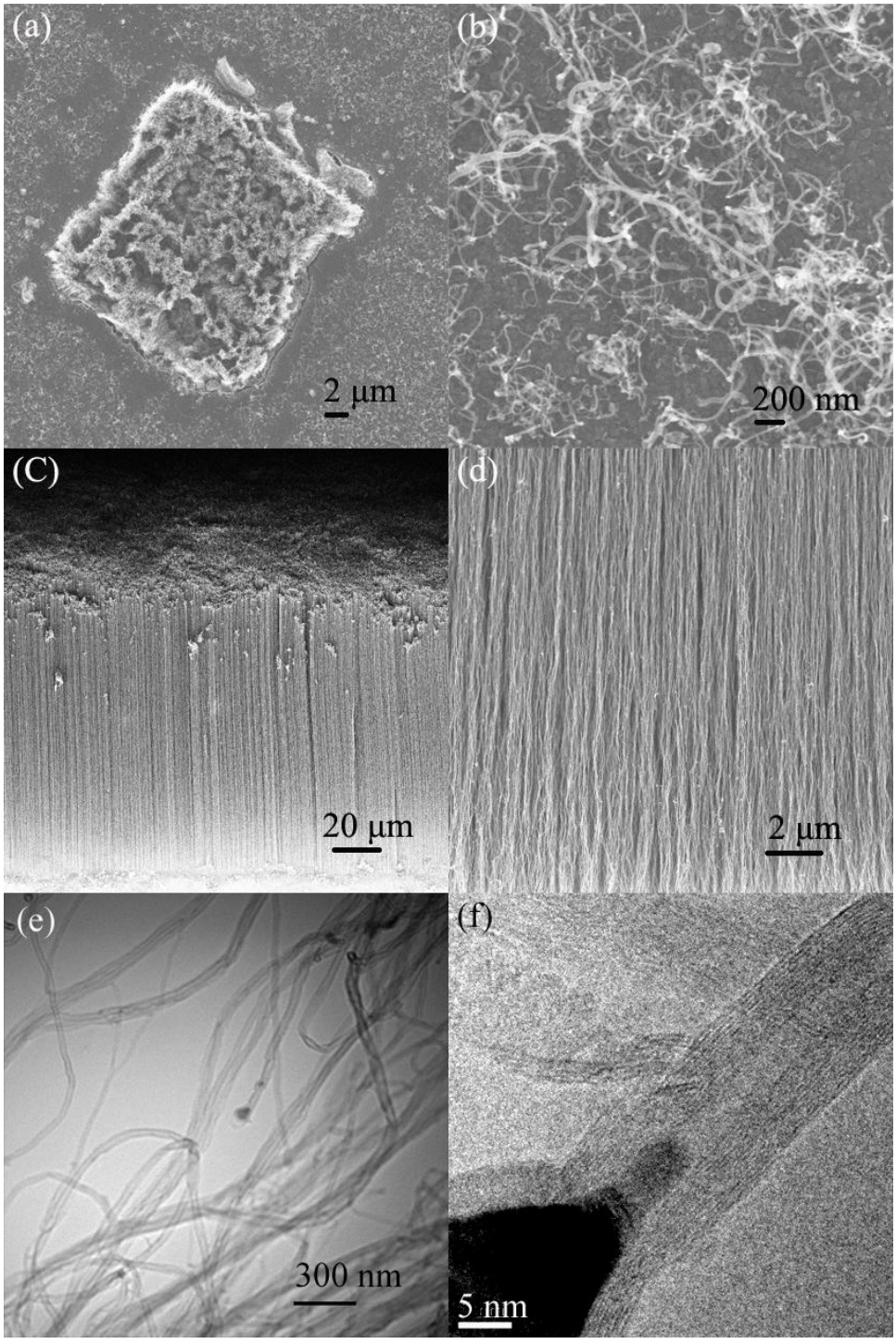

Figure 2.22 (a) and (b): Top-view SEM images of the surface of a non-polished Cu substrate (with 30 nm Al_2O_3 and 3.5 nm Fe by sequential e-beam evaporation) after a TCVD process of CNT synthesis; (c) and (d): side-view SEM images of the VACNTs synthesized on a non-polished Cu substrate (with 20 nm Al_2O_3 by ALD and 3 nm Fe by e-beam evaporation sequentially); (e) and (f): TEM images of the CNTs in (c) and (d).

There are at least two important reasons for the synthesis failure in this case. First, Cu deactivates the CNT synthesis, because bulk Cu does not catalyze decomposition of hydrocarbons,[234] and the solubility of carbon in solid Cu is extremely low—this is exactly the reason why Cu is used for single-layer graphene synthesis.[235,236] Thus, when the bottom Cu surface is exposed to the top Fe particles during the TCVD process, the local Cu-rich catalyst composition is capable of decomposing hydrocarbons, however, without giving rise to the CNT structure.[234,237] In Figure 2.23, we see that when 50-nm-Cu and 5-nm-Fe are used as the catalyst, a large amount of carbon particles are formed, with some random and sparse CNTs on the substrate surface. Second, Fe diffusion into Cu depletes or intoxicates the catalyst.[227] Fe is known to tend to diffuse into a bare Si substrate (diffusion coefficient D ~10^{-7} cm^2 s^{-1} at 1000 K) and to form chemical compound with Si. Such diffusion makes the VACNT synthesis directly on a bare Si substrate almost impossible in the absence of a surface oxidation layer as the barrier layer due to depletion or intoxication of the Fe catalyst.[183-186] Cao *et al*.[186] found that there was no detectable CNT synthesis on the Si substrate when the surface oxidation layer was thinner than 6 nm because the thin porous oxidation layer was not effective in hindering Fe diffusion into and reaction with the bottom Si substrate. In our study, a thin Al_2O_3 deposit by e-beam evaporation is discontinuous and analogous to the thin porous silicon oxide in Cao's study, as illustrated in Figure 2.21b. It is seen in Table 2.1 that a 5-nm-thick Al_2O_3 deposited by e-beam evaporation is not an effective support layer on a bare Si substrate. In the case of Cu substrate, Fe can easily diffuse into the Cu substrate not only through the thin Al_2O_3 layer but also via the inter-grain voids in the Al_2O_3 layer. The diffusion coefficient of Fe in single-crystalline Cu is higher than 10^{-12} cm^2/s at 1000 K, at least three orders of magnitude higher than that in silicon dioxide (< 10^{-15} cm^2 s^{-1}).[238, 239] It is expected that the polycrystalline Cu that has been used in this study will experience rapid Fe diffusion into the Cu due to enhanced grain boundary

diffusion rates.[240] Very recently, Fe catalyst was proved to be able to diffuse into the Al_2O_3 support layer prepared by e-beam evaporation due to its porous structure.[179]

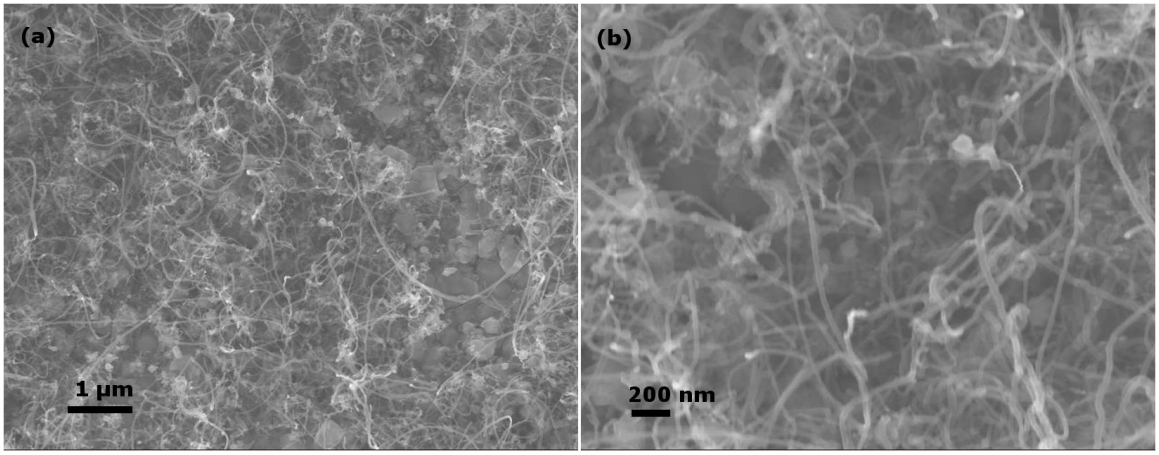

Figure 2.23 Top-view SEM images of the surface of a surface-oxidized Si substrate with 5-nm Fe and 50-nm Cu as the catalyst after the TCVD process of CNT synthesis.

A question arises as "how do we know whether a deposit layer is too thin to be continuous?" A 30-nm-thick Al_2O_3 deposited by e-beam evaporation is expected to be thick enough to be an effective support layer on the Cu substrates; however, it fails on the non-polished Cu substrates. Since the thickness during e-beam evaporation is monitored by quartz crystal microbalance and calculated automatically with reference to an atomic smooth surface, the surface roughness of the Cu substrates plays a key role in determining the actual thickness of the deposit layer. As such, an increased surface roughness increases the surface area and, consequently, reduces the actual deposit thickness. In this sense, a 30-nm-thick Al_2O_3 layer on a non-polished Cu substrate may still be too "thin"; while a smoother Cu surface should make a difference. In Table 2.1, we see that a 30-nm-thick Al_2O_3 layer is able to grow VACNTs on the polished Cu, although the synthesis rate is small. We believe that the surface roughness partially accounts for the aforementioned poor reproducibility of the VACNT syntheses on Cu substrates reported in the literature. Recently, Li *et al*. reported the instability of un-

covered Cu (*i.e.*, without surface coating by Ti/Al) surface at high temperatures, which may also account for the synthesis failure in literature.[241]

2.5.2.2 A Dense Conformal Al_2O_3 Support Layer deposited by ALD

Based on the discussion above, we postulate that a dense conformal Al_2O_3 support layer on the bulk Cu substrate would be able to realize a reproducible TCVD synthesis of VACNTs on Cu substrates. To demonstrate this, we used ALD to prepare a well-controlled Al_2O_3 layer on a Cu substrate. In comparison with e-beam evaporation, ALD, also known as atomic layer epitaxy, is a special modification of TCVD with the capability of producing films with excellent conformality and precisely controlled thicknesses.[242,243] In this study, ALD was carried out at 250 ^oC, with $Al(CH_3)_3$ and deionized water as the precursors. This process generates a uniform continuous support layer (amorphous),[243,244] resulting in highly efficient VACNT synthesis on a Cu substrate, as illustrated in Figure 2.24a. Very recently, Amama *et al*. confirmed the dense structure of Al_2O_3 by ALD (in contrast to the porous structure of Al_2O_3 by e-beam evaporation).[179] Furthermore, unlike the thickness monitoring during the e-beam evaporation, the thickness of the Al_2O_3 layer deposited by ALD is more accurate and insensitive to the surface roughness of the Cu substrates; as such, it guarantees a reproducible VACNT synthesis. It is shown in Table 2.1 that a relatively thin support layer on the Cu surface, *i.e.*, 10-nm- and 15-nm-thick Al_2O_3 on the polished and the non-polished Cu substrates, respectively, are able to support the VACNT synthesis. A thinner Al_2O_3 layer, *i.e.*, 5 nm, is not effective while a thicker Al_2O_3 layer, *i.e.*, 20 nm, results in a much higher VACNT synthesis rate. Figures 2.22c and d show a VACNT layer (>100 μm) grown on a non-polished Cu substrate with a 20-nm-thick Al_2O_3 layer deposited by ALD and a 3-nm-thick Fe layer deposited by e-beam evaporation. A high density and a good alignment of CNTs are observed.

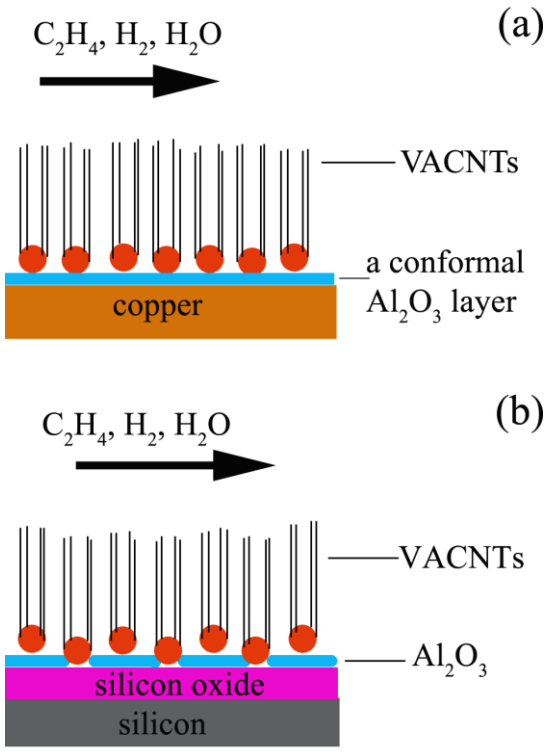

Figure 2.24 Illustrations of an effective support layer on Cu (a) or silicon dioxide (b) during a TCVD process.

In Table 2.1, we also notice that even when the support layer deposited by ALD is continuous, there is a lower limit on its effective thickness; a thicker support layer is more effective. This Al_2O_3 thickness-dependent synthesis of VACNTs on the Cu and the Si substrates is consistent with the results reported by Cao *et al.*,[186] where it was reported a monotonic increase of CNT synthesis rate with increasing surface oxide thickness on a Si substrate. A probable reason is the cracking of a relatively thin Al_2O_3 layer at high temperatures resulting in inter-grain voids within the ALD deposit. In comparison, for VACNT synthesis on the surface-oxidized Si wafers, an ultrathin (2.5-5 nm) support layer deposited by ALD is efficient. In this case, the surface SiO_2 layer (350-nm thick) serves as the major barrier layer, as illustrated in Figure 2.24b. Raman spectra (collected in LabRAM ARAMIS, Horiba Jobin Yvon, with a 532-nm-wavelength laser) of the VACNTs grown on the surface-oxidized Si wafers and those on the Cu substrates

are shown in Figure 2.25, indicating comparable VACNT qualities on the two substrates, consistent with the TEM results in Figures 2.22e and f.

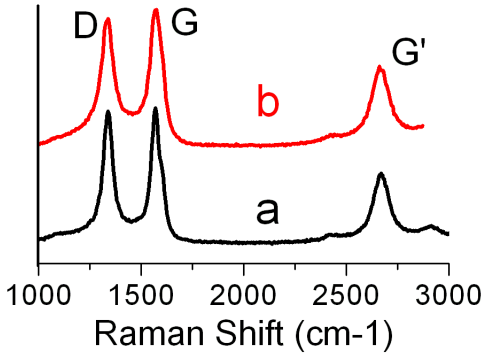

Figure 2.25 Raman spectra of the VACNTs synthesized on SiO_2/Si (a) and on Cu (b).

2.5.2.3 AFM Characterizations

The surface of a 5-nm-thick Al_2O_3 layer on a bare Si wafer surface prepared by e-beam evaporation is smooth, with a root-mean-square roughness of 0.196 nm, as shown in Figure 2.26a. Based on the nucleation-growth mechanism discussed above, the surface is expected to show lots of island-like features. However, the features are much smaller than the probe tip used and result in the large number of repeating patterns (artifacts) in the image. After a surface heat treatment for 1 hour at 750 ^oC in Ar and H_2, the size of the surface features grow, as is clearly observed in Figure 2.26b. In comparison, the surface of an equally thick Al_2O_3 layer formed by ALD is even smoother and continuous (Figure 2.26c). Its root-mean-square roughness is only 0.155 nm, which is much smaller than that formed by e-beam evaporation. With the same heat treatment as above, the surface of the ALD-prepared Al_2O_3 layer retains its smoothness, showing features much smaller than the size of the probe tip (the artifacts in Figure 2.26d). Although there might be some difference between “discontinuity” and “surface roughness”, we believe that for a 5-nm-thcik coating, a higher surface roughness reflects discontinuity.

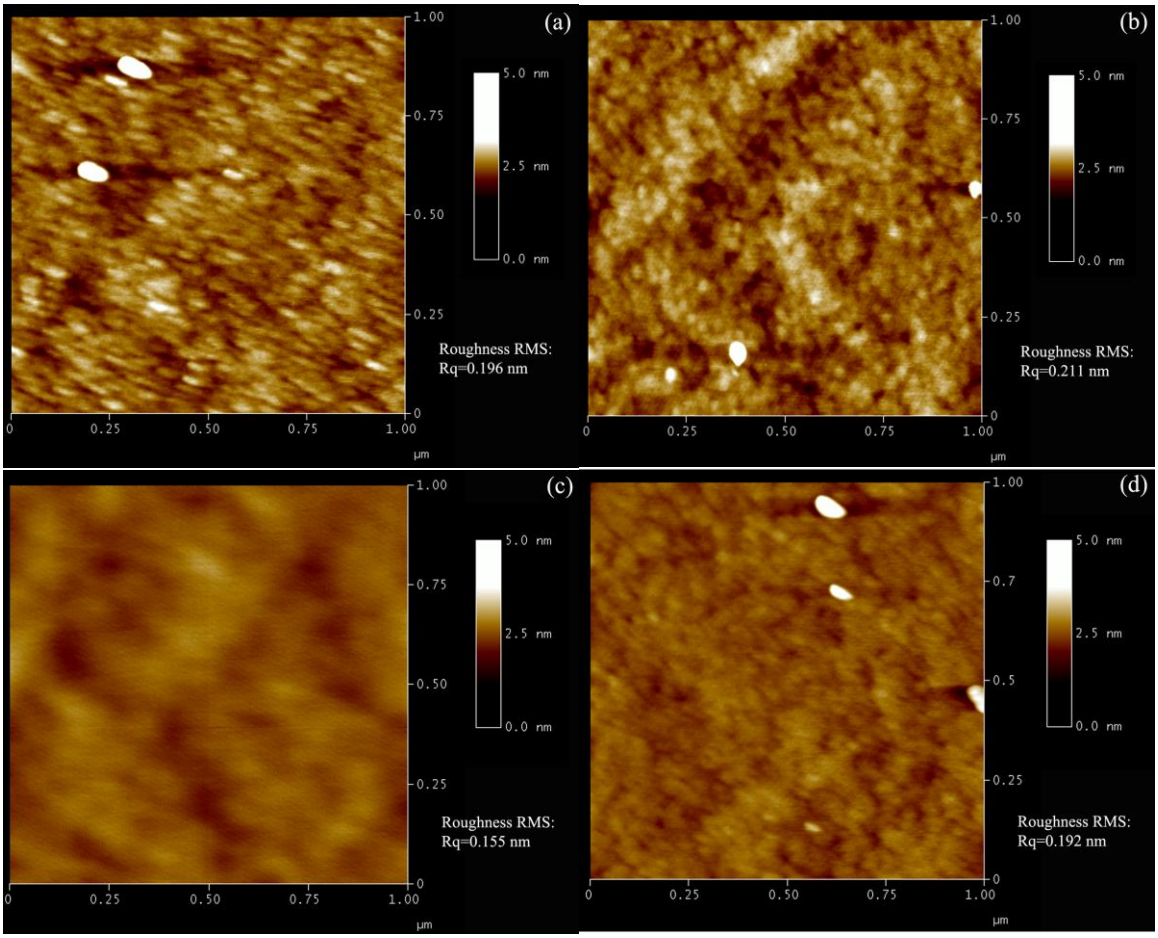

Figure 2.26 AFM images of (a) a pristine 5-nm-thick Al_2O_3 layer on a bare Si wafer surface by e-beam evaporation; (b) a 5-nm-thick Al_2O_3 layer on a bare Si wafer surface by e-beam evaporation after heat treatment for 1 hour at 750 ^oC in Ar and H_2; (c) a pristine 5-nm-thick Al_2O_3 layer on a bare Si wafer surface by ALD; (d) a 5-nm-thick Al_2O_3 layer on a bare Si wafer surface by ALD after heat treatment for 1 hour at 750 ^oC in Ar and H_2.

CHAPTER 3

POST-SYNTHESIS ANNEALING FOR DEFECT REDUCITON OF CARBON NANOTUBES

CNTs exhibit impressive potentials in many applications such as electrical interconnects,[4,5,191,245,246] TIMs,[8,226,247-253] high-performance fibers,[254-262] and so on. Although the theoretical intrinsic electrical, thermal and mechanical properties of an individual CNT are extraordinary, synthesized CNTs in reality are far from being defect-free. Presence of structural defects in a CNT has been found to shadow its promise in real-life applications.[89,99,263-269] Defect reduction is the key to realizing the true potential of individual CNTs. Conventionally a high-temperature thermal annealing process is needed for CNT defect reduction. For example, annealing of SWNTs is usually carried out above 1200 ^{o}C in vacuum.[270] Although such annealing is effective in reducing the defects of SWNT, coalescence/reconstruction of SWNTs during high-temperature annealing has been found from time to time.[271] For MWNTs, a higher annealing temperature (typically above 1900 ^{o}C) is needed.[99,272-274] However, for on-substrate applications of vertically aligned MWNTs in electronic packaging, the high-temperature thermal annealing process is not feasible because the commonly used synthesis substrates such as Si and Cu cannot sustain such high temperatures. In some cases, degradation in mechanical properties was found for high-temperature annealed MWNTs.[274] Moreover, thermal annealing is too time-consuming and costly. Therefore, finding an alternative way to fast-anneal VACNTs has become significant.

Recently, CNTs have been found to display strong microwave absorption accompanied by a rapid temperature increase to above 1550 ^{o}C.[275-277] The strong microwave absorption by CNTs has recently attracted considerable interest for both theoretical research and potential applications,[276-287] especially for CNT

functionalizations,[287] the mechanism being still open to question though. In this chapter, we report the application of microwave radiation for fast annealing of VACNTs; the annealed CNTs show great improvements in mechanical and electrical properties. What happens to CNT structure in microwave radiation and the mechanism of CNT response to microwave are discussed.

3.1 Experimental

VACNT films of ~1-mm thick were synthesized by the TCVD process with the assistance of a trace amount of hydrogen peroxide (Section 2.4.1). Microwave treatment of the synthesized VACNTs was carried out in a variable-frequency microwave (VFM) chamber (MicroCure2100, Lambda Technologies) with the following parameters: 6.425 GHz (central frequency), 1.150 GHz (bandwidth) and 0.1 s (sweep time). The microwave system could be programmed to operate at different power levels and duration. Inside the microwave chamber was a self-setup argon-filled glass chamber, in which the VACNT samples were placed. Upon microwave radiation, intensive light emitting, fast heating and outgassing were observed from the VACNT samples. VFM techniques have the advantage of being capable of overcoming the non-uniformities in temperature and arcing associated with traditional microwave processing. In our study, 500 W microwave output was able to heat the VACNT samples (the microwave-responsive CNTs) above 400 ^{o}C within a few seconds and above 800 ^{o}C within 3~5 minutes. It has been found that such highly microwave-responsive CNTs could be fast-heated to "super" high temperatures (*e.g.*, ~3000 K).[278] However, monitoring the actual temperature of the CNTs in the VFM chamber during microwave radiation is extremely challenging since infrared emissivity of CNTs at high temperatures is unknown.

In our study, thermogravimetric analysis (TGA) measurements were carried out in air, using a heating rate of 10 ^{o}C min^{-1}, up to 900 ^{o}C. In order to evaluate the mechanical properties of the CNTs, we prepared CNT fibers (10 μm in diameter) by a twisting and

densification spinning process and measured the tensile properties of the CNT fibers (Figure 3.1).[288] Briefly, the CNT fibers were produced from the MWNT forests by using tweezers to contact the sidewall and then hand-drawn at a speed of ~50 cm min^{-1}. The as-drawn fibers were physically twisted using a motorized drive at 500 rpm. The twisted fibers were passed through ethanol to provide permanent twisting. Figure 3.2 shows the SEM images of the MWNT fibers.

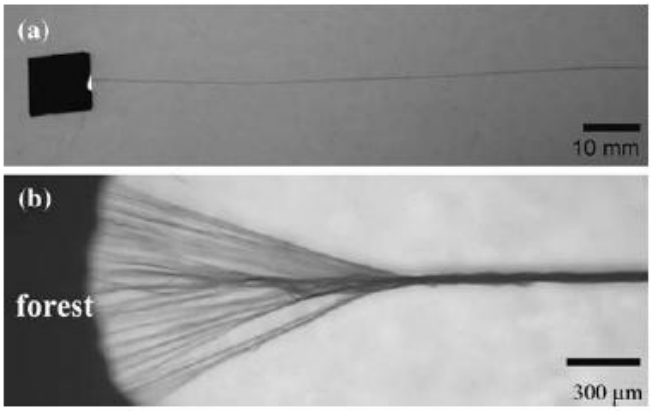

Figure 3.1 Spinning continuous MWNT fibers from the forest (a) photograph of the fiber in the process of being drawn from the 1 x 1 cm^2 forest; (b) optical image showing the nanotubes being pulled from the forest wall into a fiber.

3.2 Effect of Microwave on the Structure of CNTs

The effect of microwave radiation on the VACNTs was studied by investigating the Raman spectra of the VACNT samples treated under various microwave power outputs and duration. Raman scattering is a well-accepted characterization method for evaluating the degree of structural order of MWNTs, by using the ratio of the integrated intensity of D band (I_D) at ~1334 cm^{-1} to that of G band (I_G) at ~1570 cm^{-1}.[21] Also investigated is the ratio of the integrated intensity of D' band ($I_{D'}$, by least-square fitting Lorentzian line shapes to the asymmetric G band in the spectra) at ~1610 cm^{-1} to I_G.[289,290] Figure 3.3 shows the typical Raman spectra (in a selective regime of Raman

shift) of the control VACNT sample and the VACNT samples treated by VFM; the corresponding I_D/I_G and $I_{D'}/I_G$ are shown in Figure 3.4.

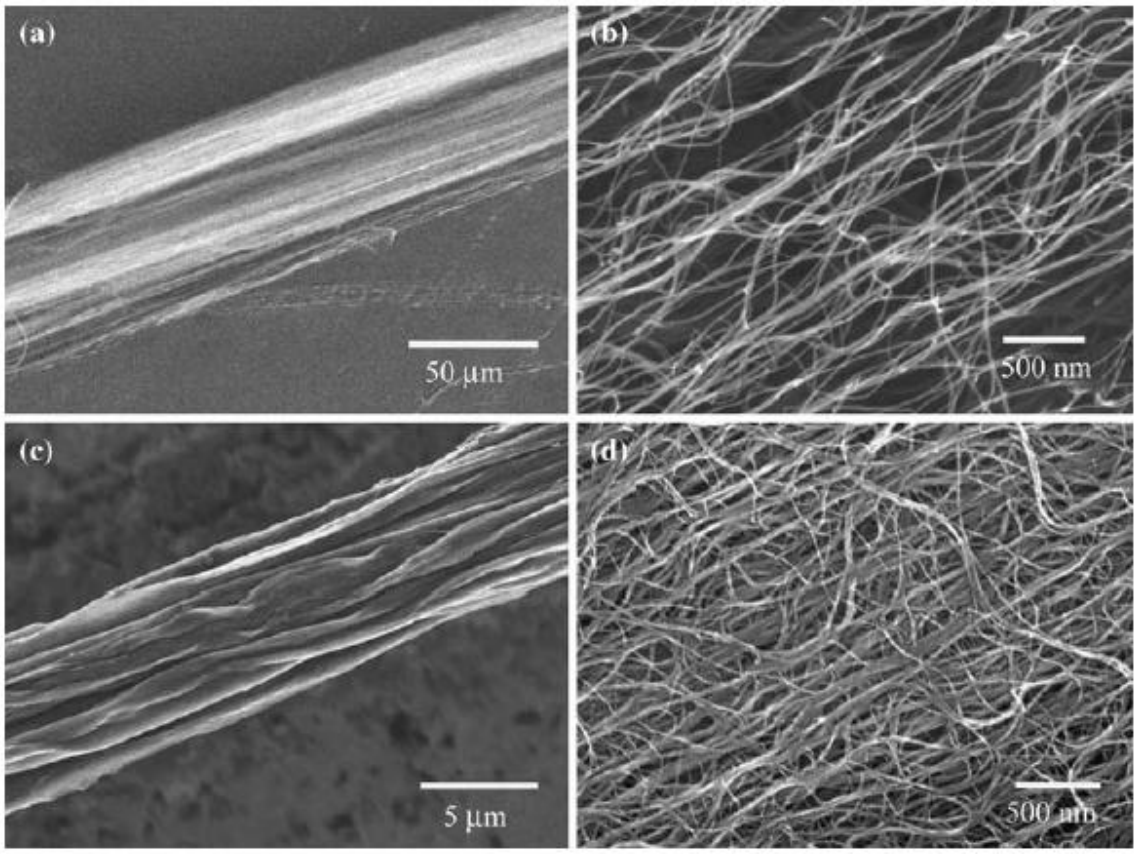

Figure 3.2 SEM images of neat MWNT fibers: (a) As-drawn aerogel fiber; (b) nanotube arrangements in the as-drawn fiber; (c) densified fiber (after passed through ethanol), and (d) nanotube arrangement in the densified fiber.

It is evident that within short duration (*i.e.*, <180 s) by 500 W microwave radiation, I_D/I_G and $I_{D'}/I_G$ decrease with increased duration, indicating an improvement in the structural order of the microwave-annealed CNTs. We postulate that what happens during the microwave annealing process is that the defective sites on the synthesized CNTs reconstruct to form graphitic structure, leading to the reduced I_D/I_G and $I_{D'}/I_G$. With extended microwave radiation duration, I_D/I_G and $I_{D'}/I_G$ rise probably due to CNT

degradation in microwave, or due to CNT oxidation given that a highly effective argon protection is difficult to achieve in the VFM chamber.[275] Such a trend was not observed distinctly for the samples treated under low-power microwave radiation (Figures 3.5 and 3.6).

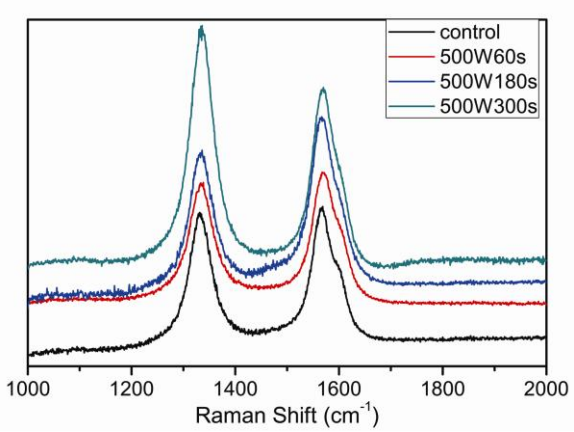

Figure 3.3 A selected regime of the typical Raman spectra of the control VACNT sample and the VACNT samples treated by VFM with 500 W of power at varied duration.

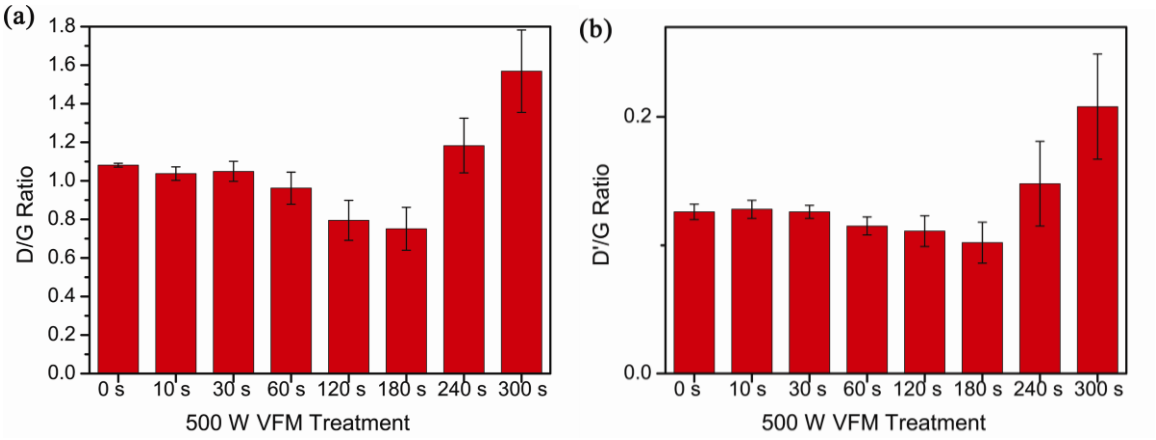

Figure 3.4 I_D/I_G (a) and $I_{D'}/I_G$ (b) of the control VACNT sample and the VACNT samples treated by VFM with 500 W of power at varied duration.

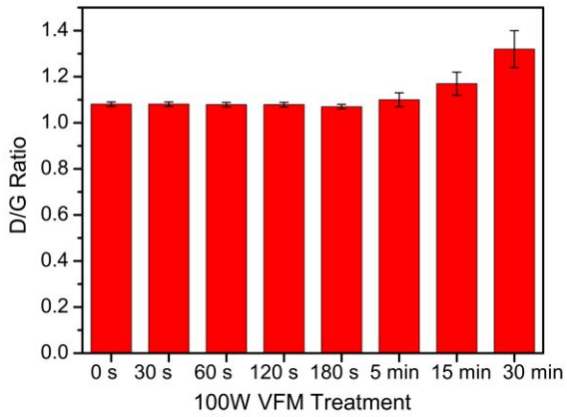

Figure 3.5 I_D/I_G of the VACNT samples treated by VFM with 100 W of power at varied duration.

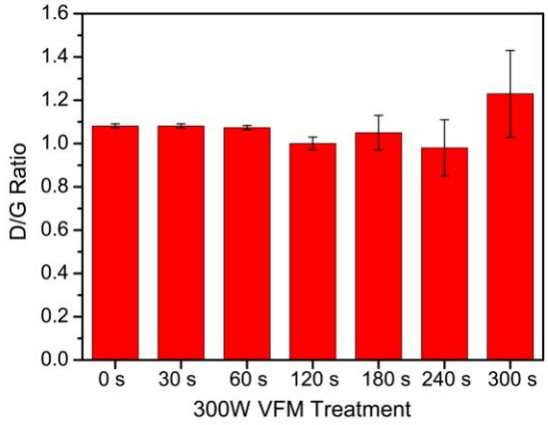

Figure 3.6 I_D/I_G of the VACNT samples treated by VFM with 300 W of power at varied duration.

Our postulation can be verified by the TGA results of the VACNTs (Figure 3.7). TGA has been used widely to study the oxidative stability of CNTs so as to evaluate CNT quality, *i.e.*, defect density and purity.[272,273,291,292] For the control VACNTs, the peak temperature of the derivative weight loss is ~675 ^{o}C, consistent with the reported values for defective (raw, un-annealed) CNTs.[273,291,293] 1- and 3-min VFM (500 W) treatments shift the peak temperature up to ~730 ^{o}C and ~740 ^{o}C, respectively, indicating an effective improvement in oxidative stability, comparable to high-temperature annealed

CNTs.[273] In comparison, a 5-min treatment causes a dramatic structural instability. The TGA results show no detectable amorphous carbon or catalyst residue, indicating high purity of our synthesized VACNTs; therefore, the oxidative stability is a reflection of the crystalline defect density of the CNT structure. Increased defect density leads to increased local reactivity to oxygen and, consequently, a lower oxidative stability. Therefore, relatively short microwave radiation duration is effective in reducing the defect density of the VACNTs, while extended duration degrades the VACNTs by introducing more defects.

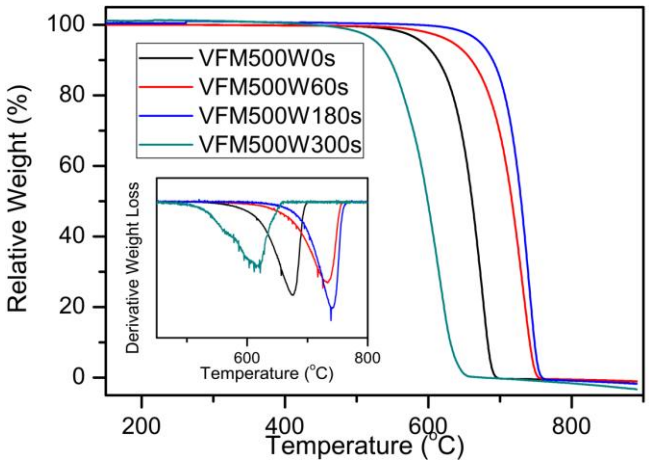

Figure 3.7 TGA results of the control VACNTs and VFM treated VACNTs; inset is the derivative weight loss plot against temperature.

A further proof comes from the XPS (SSX-100, Al K_α source) results. Figure 3.8 shows the change in the oxygen signal of the VACNTs. Increased oxygen content on the CNT surface due to extended microwave duration is evident. However, it is not observed any distinct difference in oxygen content between the control sample and the shortly treated sample probably due to the limited sensitivity of XPS; the same for the high-resolution spectra of binding energy of C1s. High-resolution transmission electron microscope images (HRTEM) are shown in Figure 3.9. No essential structural change is

observed between the control VACNTs (Figure 3.39b) and the annealed VACNTs (Figure 3.39d), while the degraded VACNTs show damaged walls (Figure 3.39e). Reconstruction of CNTs is also observed in the overtreated sample (Figure 3.39f): in contrast to the wall-to-wall distance of ~3.4 Å in the CNTs, the reconstructured allotrope shows a much smaller interlayer distance, ~2.3 Å, well matching the characteristic interlayer distance of hexagonal diamond or diamond-like carbon.[294-297] This indicates very high temperature and local pressure that the CNTs may experience in the microwave radiation. Large-scale reconstruction of the CNTs is not observed in our study, probably because the ultra-fast heating process dose not allow the large-scale reconstruction to take place kinetically.[275]

The high treatment temperature, ultra-fast heating and strong interaction between the CNTs and the microwave field result in the reduced defect density of the CNTs. First, CNTs are known to "store" hydrogen;[298,299] the C–H sites in the CNT structure can be healed up in the local presence of hydrogen under microwave radiation.[275,276] Second, the oxidized sites formed in the as-synthesized CNTs may also have been partially reduced within short treatment duration. Recently, oxygen-containing functional groups introduced to CNTs at high temperatures during CNT synthesis have been found to be unstable.[300] During the microwave treatment, the structural and the adsorbed hydrogen in the argon environment probably causes the local reduction/reconstruction of the oxygen-containing functional sites. This is the possible reason why water vapor was detected during CNT outgassing in microwave field.[275,276] With extended microwave treatment duration, the "stored" hydrogen may have been depleted, rendering the CNTs subjective to oxidation. Although the temperature that the CNTs reach in the VFM may not be as high as that used for the conventional high-temperature thermal annealing for MWNTs, CNT annealing is still possible when we take into account the special role of microwave in dramatically increasing reaction rates and the capability of inducing chemical reactions which cannot proceed by thermal heating alone.[301,302] In addition,

we note that a relatively low annealing temperature (700 ^{o}C) has been proved to be effective for CNT annealing by healing up the defective sites in CNT structures caused by acid treatment during CNT purification.[303]

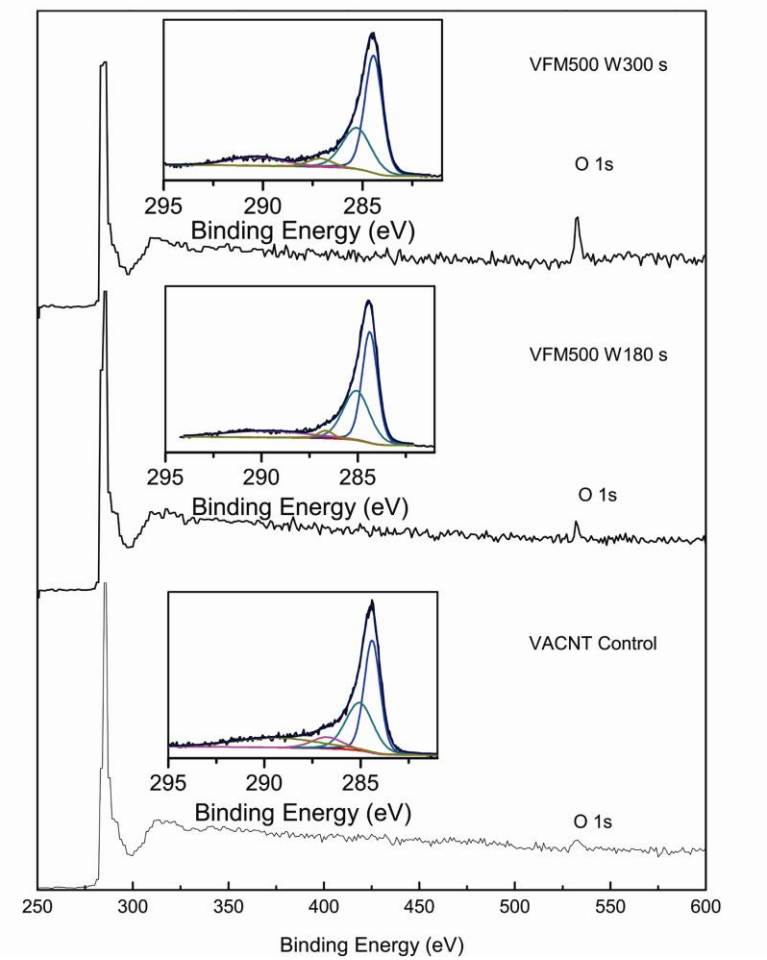

Figure 3.8 XPS surveys of the control VACNTs and the VFM treated VACNTs; insets are the corresponding high-resolution C1s spectra.

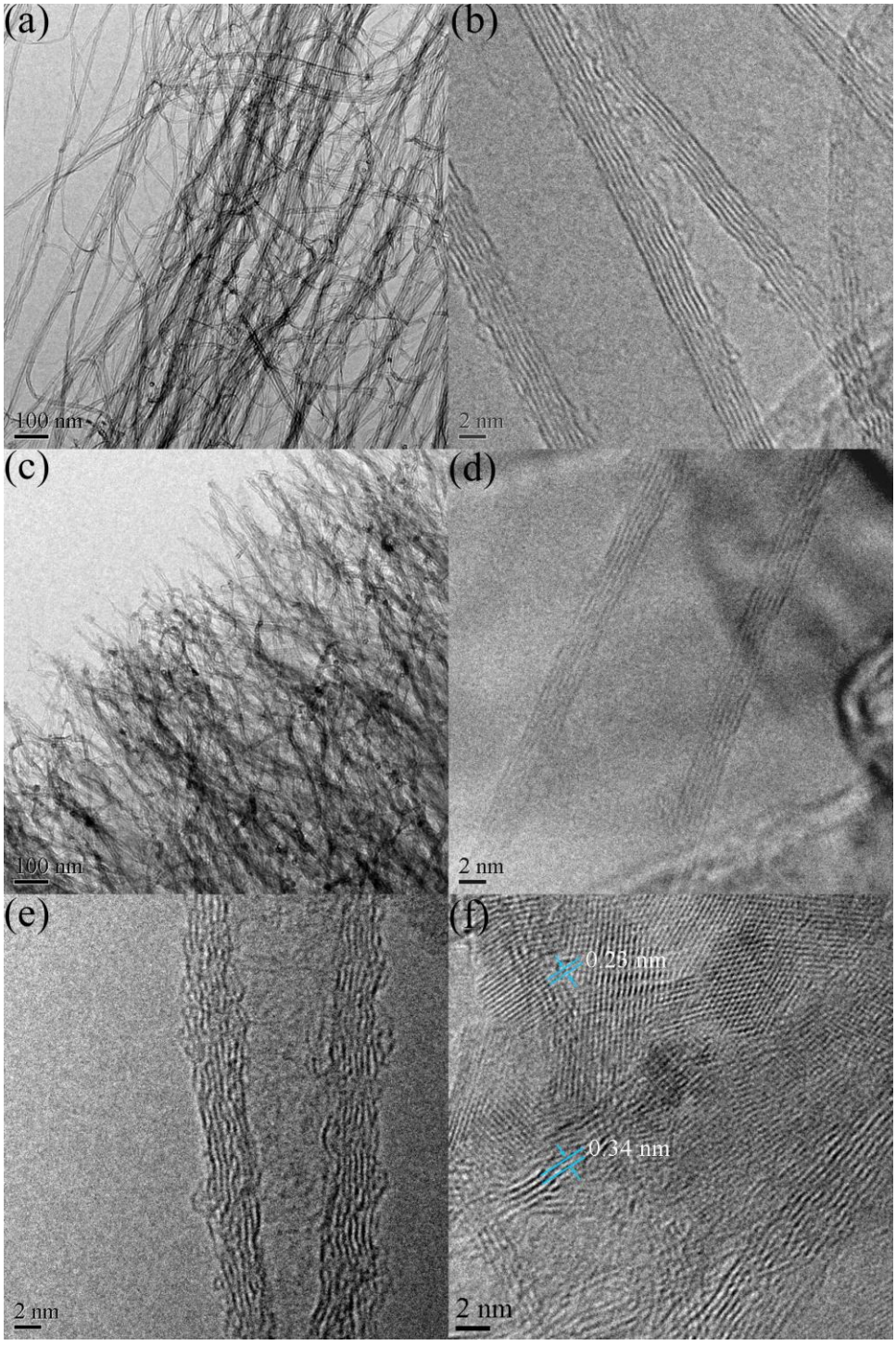

Figure 3.9 TEM images of the control VACNTs (a and b), the VACNTs treated by VFM with 500-W power for 180 s (c and d), and the VACNTs treated by VFM with 500-W power for 300 s (e and f).

Experimental data of the mechanical tests of the CNT fibers are listed in Table 3.1. The fracture strength and the modulus of the CNT fibers made of the control VACNTs (CF1 in Table 3.1) are 0.58±0.12 and 54.7±3.8 GPa, respectively, comparable to the values for CNT fibers reported by other researchers.[254,257,258,261,262,304, 305] It is evident that 3-min VFM (500 W) treatment of the VACNTs dramatically improved the fracture strength and the modulus of the as-spun CNT fibers (CF2 in Table 3.1) up to 0.79±0.08 and 89.3±22.1 GPa, respectively. The high strength is almost comparable to the record strength of 1 GPa reported by Windle's group (with 20-mm gauge length of the tested specimens),[256,258] but higher than Windle's high-performance fibers (0.44 GPa) from dog-bone CNTs.[258] The tensile strength is even comparable with the strength of super-strong CNT/polymer composite fibers (0.85 GPa).[259,261] In comparison, extended duration of microwave treatment degrades the CNTs (CF3 in Table 3.1). The mechanical property results are consistent with the Raman, TGA, XPS and TEM results except that the fibers from the degraded VACNTs possess higher strength and elastic modulus than those from the control VACNTs. A possible explanation is the enhancement in tube-tube anchoring force due to the increased number of polar groups on the CNT walls by the extended microwave treatment duration. Given the high packing density of CNTs in the spun fibers, we believe that interfacial stress transfer becomes a significant factor that determines the apparent collective Young's modulus.[306,307] For comparison, we list, in Table 3.1, the mechanical properties of CNT fibers (CF4, 10 μm in diameter) spun from VACNTs that are grown with the assistance of a trace amount of water;[288] the as-synthesized VACNTs show nearly no surface functional groups.[308] The fracture strength and modulus of CF1 are ~16% and ~580%, respectively, higher than those of CF4. Therefore, surface polar groups do account for the elastic modulus of the CNT fibers.

Besides the mechanical properties, we also measured the electrical conductivities of the CNT fibers (Figure 3.10). The electrical conductivity of CF1 and CF2 are

$6.9\pm0.7\times10^4$ and $8.3\pm1.3\times10^4$ S m^{-1}, respectively, also indicating an effective CNT quality improvement after the microwave treatment. The high electrical conductivity is comparable to the highest-known value measured for a CNT assembly to date.[309] In comparison, the electrical conductivity of CF3 is much lower, ~2×10^4 S m^{-1}.

Table 3.1 Data of the mechanical properties for the CNT fibers.

Samples[a]	CF1	CF2	CF3	CF4
Fracture strength (Gpa)	0.58 (0.12)[b]	0.79 (0.08)	0.63 (0.14)	0.50 (0.10)
Elastic modulus (Gpa)	54.7 (3.8)	89.3 (22.1)	73.5 (7.3)	8.0 (1.0)

a. CF1, CF2 and CF3 represent the fibers spun from the control VACNTs, the VACNTs after 3 min of VFM (500 W) treatment and those after 5-min VFM (500 W) treatment, respectively; CF4 represents the fibers spun from VACNTs grown with the assistance of a trace amount of water rather than hydrogen peroxide.[308]
b. The number in the brackets is the standard deviation.

3.3 Response of CNTs to Microwave Radiation

So far the mechanism of the microwave response of CNTs is still not clear. Wadhawan *et al*.[276] compared the microwave responses of raw and purified SWNTs and attributed the strong microwave absorption of the raw SWNTs to the high concentration of catalyst residue. In contrast, Imholt *et al*.[275] reported nearly no difference in the microwave response between raw and purified SWNTs. Recently, Naab *et al*.[277] found a fairly weak correlation between catalyst residue and microwave response of CNTs; instead, structural properties of CNTs seemed to play the key role. In our study, the VACNTs are pretty clean, with almost no or very little Fe residue after they are peeled off the synthesis substrate.[310] The high purity of the VACNTs, as mentioned before, can also be seen from the TGA and HRTEM results. The free-standing VACNTs, however, show no distinct difference in microwave response compared to the on-substrate VACNTs. Thus, the response of CNTs in microwave is not determined by

metal particle residue. We also notice that the VACNTs, before and after microwave annealing at varied duration (shorted than 3 min), show almost the same fast microwave response, which indicates a weak influence of structural defects on microwave response of VACNTs in the low-defect-density regime. So what determines the CNT response in a microwave field?

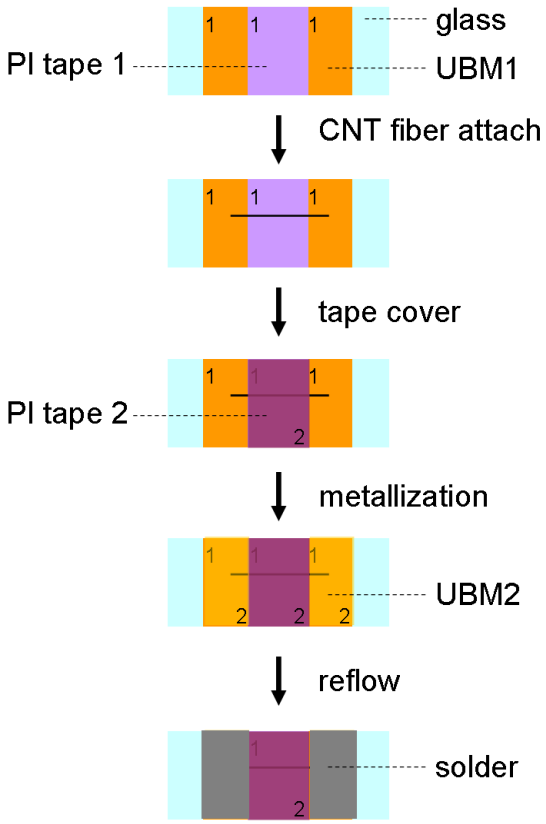

Figure 3.10 Illustration of the electrical conductivity measurement technique for an effective reduction of contact resistance. PI tape represents a double-sided polyimide tape; "UBM" represents under-bump metallurgy layer, which is Au\Ni\Ti in this study.

Generally, microwave energy absorption by materials occurs for four main mechanisms: dielectric loss, magnetic loss, Maxwell-Wagner effect, and conduction loss.

A. Dielectric loss

Dielectric loss in a microwave field (in the frequency range of MHz to GHz) is the result of orientation polarization of a material (or phase, collection, regime) by the electric component of the microwave field. Carbon materials are intrinsically non-polar and dielectric loss can be ruled out as a mechanism for microwave heating of CNTs.

B. Conduction loss

Conduction loss is the result of free charge redistribution in a microwave field. It is the main mechanism for microwave energy dissipation by materials with high D.C. conductivity. MWNTs with relatively large diameters are fully metallic. In a microwave field, oriented distribution of free charge carriers (e^-) in the CNTs is equivalent to a large dipole; the dipole reversal is a sluggish relaxation process, leading to microwave heating. Conduction loss is probably the dominating mechanism for microwave heating in the VACNTs under study.

C. Magnetic loss

Conduction loss accounts for microwave heating of carbon black (up to ~500 ^{o}C).[276] However, it may not explain why VACNTs can be heated to higher temperatures (650-2000 ^{o}C) than carbon black. Other mechanisms may need to be taken in account. Magnetic NPs have been found to exhibit a strong response to microwave radiation.[311] The presence of magnetic catalyst residue in CNTs may affect their microwave response. However, the role of magnetic catalyst residue in microwave heating of CNT is still controversial,[272,276,277,312] because quantitative analysis of the correlation between the content of the catalyst residue in CNTs and the their microwave heating was absent in the literature.

D. Interfacial effect

Two interesting phenomena call for our attention. Imholt *et al*. reported that microwave heating of CNTs was more prominent when radiated under vacuum than in air. Given that the contrast in dielectric property between CNTs and air is smaller than that between CNTs and vacuum, this interesting phenomenon may suggest Maxwell-

Wagner effect play a role. Maxwell-Wagner effect is about energy dissipation by scattering of the radiation at interfacial boundaries between two phases with contrast in dielectric property. This mechanism applies to heterogeneous materials, and therefore, may apply to VACNTs.

The second phenomenon is that the microwave heating is dramatically suppressed (<100 ^{o}C) when VACNTs are imbedded in a polymer matrix such as polyethylene and EP. We observed the heating suppression when we used microwave to assist processing of VACNT/polymer composites.[249] We note that the interfacial thermal resistance between the CNTs and the polymer matrix is high; ineffective heat dissipation by the polymer matrix off the microwave heated VACNTs—if they heated intensively by microwave—may not account for such a weak response. Moreover, the polymer materials are microwave transparent (slight absorption). Given the comparable size between the diameter of the CNTs and the radius of gyration of the polymer chains,[307] we postulate that the interfacial interaction between the CNTs and the polymer matrix suppresses the charge redistribution in CNTs under microwave radiation.

Other than the four mechanisms, it was proposed that structural properties of CNTs play the key role in microwave response.[277] For example, we synthesized vertically aligned DWNTs (Section 2.3.5). The DWNTs didn't show strong microwave response, and couldn't be heated to above 500 ^{o}C. More detailed studies of the mechanism for the microwave response of CNTs are suggested in the future.

3.4 Preparation of Graphene by Reduction of Graphene Oxide[313]

There are mainly two approaches to reducing graphene oxide (GO): thermal reduction and chemical reduction. Efficient thermal reduction usually requires temperatures of 1050 ^{o}C or above in reducing environments, because reduction at lower temperatures will still have a lot of defects remaining, leading to inferior electrical and thermal conductivities.[314-316] However, high temperature annealing suffers from

several drawbacks such as low yield (due to severe thermal decomposition),[317] and high energy consumption. GO reduction can also be achieved by chemical reduction using different reducing agents, such as hydrazine,[318,319], dimethylhydrazine,[320] hydroquinone,[321] and sodium borohydride.[322] Chemical reduction of GO can realize high throughput production, but the efficiency is lower than that of the high temperature annealing. Moreover, hydrazine and dimethylhydrazine are highly toxic and potentially carcinogenic. As an extension of the microwave treatment of CNTs, we also tried fast reduction of graphene oxide by microwave.[323] With shorter than 5 seconds of treatment, the bulk conductivity increased from 0.07 to 1×10^4 S m^{-1}, which is preferably comparable with that of the high-temperature exfoliated graphene (10^3 S m^{-1}).[324,325] In addition, the G band red-shifts to 1565 cm^{-1}, indicating the recovery of hexagonal network of carbon atoms. The I_D/I_G ratio decreases from ~1 to ~0.3, which, to the best of our knowledge, is the lowest I_D/I_G ratio of reduced GO reported up to now. Since the I_D/I_G ratio is inversely proportional to the average size of the sp^2 domains in the reduced GO structure, the microwave reduction is believed to dramatically increase the average size of the crystalline graphene domains.

CHAPTER 4

PARAMETRIC STUDY OF THE INTRINSIC THERMAL TRANSPORT PROPERTY IN VERTICALLY ALIGNED MULTI-WALLED CARBON NANOTUBES

For practical applications, collective thermal transport property of CNT aggregates (carpet, mat, yarn…) is of more interest than the intrinsic κ of individual CNTs and collective thermal transport property of 2D and 3D random CNT networks.[100] Hone *et al*. reported κ of ~250 W m^{-1} K^{-1} for a magnetically aligned SWNT film.[326] Yang *et al*. found that κ of a VACNT array by a PECVD process was only 12-17 W m^{-1} K^{-1}.[97] They attributed the low κ to the small volume filling fraction ("packing density" from here after) of CNTs in the array. Yi *et al.* measured κ of millimeter-long VACNTs.[99] At room temperature, κ was only ~25 W m^{-1} K^{-1}. The relatively low value was attributed hypothetically to a substantial amount of CNT defects. Wang *et al*. used a photothermal technique to measure the thermal conductivity of carbon nanofiber arrays and revealed a relatively low κ of ~27 W m^{-1} K^{-1}.[327] κ of 74-83 W m^{-1} K^{-1} for a VACNT array (13 μm, MWNTs with a bamboo-like structure by microwave PECVD) in the temperature range of 295-323 K was reported by Goodson *et al*. using a 3ω measurement technique.[328] However, very recently, Goodson *et al*. reported a much lower κ (<3 W m^{-1} K^{-1}) of a VACNT film along the tube-alignment (through-thickness) direction,[329] which is contradictory to their previous result. Unfortunately, no discussion was given regarding the discrepancy. In 2010, Shanov *et al*. reported an extremely low value of κ (~1 W m^{-1} K^{-1}) for their synthesized ultra-high VACNT arrays.[330] If we think about the ASTM-based steady-state thermal measurement, assuming 1 cm^2 as the area, 100 W cm^{-2} as the heat flux, 100 μm as the bond-line-

thickness of the VACNT TIM, we will get at least 100 degrees of temperature difference across the TIM—a huge temperature drop! However, in our study, we have never seen such a huge temperature drop.

The reported values of κ of VACNT arrays/films scatter over a sarcastically wide range due to the following two reasons. First, the VACNTs in literature are from different sources, and therefore, are expected to be intrinsically different in quality (defect density), structure (diameter and its distribution, wall number, and chirality of each wall), substructure (Swiss roll, Russian roll, or Bamboo), alignment, tip entanglement, packing density, adhesion to synthesis substrate, catalyst residual, *etc*. Second, different thermal measurement techniques (including laser flash technique, steady-state TIM testers based on ASTM 5470, thermoreflectance technique, photoacoustic technique, photothemal technique, 3ω technique), sampling processes, assumptions, and calculations were utilized by researchers. Although a direct comparison between such measurement results of different VACNT samples by different techniques can be seen very often in literature, it actually makes no sense at all! On the other hand, I would like to state that a reliable measurement technique should render us the feasibility of quantitative or, at least, semi-quantitative analyses of how the factors such as CNT quality, buckling, inter-tube contacts, packing density, and tube-tube interaction influence the collective thermal transport property of VACNTs. Unfortunately, no such systematic parametric study has ever been carried out with any specific measurement technique. Therefore, the reliability of the measurement results of the intrinsic κ of VACNT arrays/films in literature is open to question. Here we perform the systematic parametric study using a laser flash technique, and show that the laser flash technique is reliable in measuring the intrinsic κ of VACNT films. The parametric study may be highly important in providing researchers with necessary insights into the intrinsic thermal transport property of VACNTs, as well as into their potential application for thermal management. Currently, VACNT application for thermal management is being extensively studied in industry. In our

private communications with thermal engineers in Intel and Samsung, we all find the values in literature regarding intrinsic thermal transport property of VACNTs and resistance of VACNT TIMs are so puzzling and conflicting.

4.1 On the Basis of Laser Flash Analysis

Laser flash analysis (LFA) is a sensitive non-contact transient thermal measurement technique. It is widely used for measuring thermal diffusivity of homogeneous materials,[331-336] and in some cases, heterogeneous materials.[337] In a typical LFA setup, a laser flash lamp, a sample and an infrared detector are vertically arranged. During testing, the front face of the sample is illuminated by a pulsed laser produced by the flash lamp. Both the released energy (controlled by the filter) of flash lamp and the width of the heating pulse (100, 400, and 1000 μs for LFA 447, Netzsch Inc., the equipment used in this study) can be adjusted. The temperature on the rear surface of the sample is monitored by the infrared detector. Thermal diffusivity (α) of the sample is obtained by parametric fitting of the recorded temperature-*vs*-time history of the rear face of the sample after the laser is shone on the front face. The allowable range of α is 0.01-1000 $mm^2\ s^{-1}$ for LFA 447, with a reproducibility of approximately ±3%. κ of the sample can be calculated based on the definition: $\kappa=\alpha\rho c_p$, where ρ and c_p are mass density and specific heat, respectively. LFA technique has recently been considered a tool to measure α of VACNTs and effective α of VACNT TIMs.[251,338-342] However, the feasibility is still controversial in view of the porous structure of VACNTs, and usually large interfacial thermal resistance between CNTs and substrates. It is important to have a brief review and discussion of the basis of the LFA technique.

LFA technique was described for the first time by Parker *et al*. in 1961,[331] where a simplest relation was given

$$\alpha_{0.5} = \frac{1.37 l^2}{\pi^2 t_{0.5}} \tag{4.1}$$

where $t_{0.5}$ is the time for the rear face of the sample to reach half-maximum in its temperature rise, $\alpha_{0.5}$ the calculated thermal diffusivity using $t_{0.5}$, and l the sample thickness. The derivation of Eqn. (4.1) rests on the following approximations:

A. heat flow is 1D;

B. the pulse width of the incident laser (τ) is negligible compared with the characteristic transit duration (t_c) of the heat flux through the test sample so that the laser incidence and energy absorption is instantaneous, where t_c is defined as

$$t_c = \frac{l^2}{\pi^2 \alpha} \tag{4.2}$$

C. the penetration depth of the incident laser is very small;

D. material properties (especially α and c_p) are temperature independent, or at least, not strongly temperature dependent;

E. heat losses from the sample surfaces are negligible.

To meet approximation A, sample thickness and anisotropy in α should both be taken into account. A thin Au coating is beneficial to ensure rapid planar heat distribution upon the laser incidence. When a laser beam is shone directly on the surface of a porous VACNT film, heat distribution on the front plane is not uniform. For approximation B, the preset pulse width and sample thickness are important factors. Actually, pulses are often comparable in duration with the transit time; in those cases, corrections are needed.[333,343-345] A small penetration depth (approximation C) requires the front face of the sample be opaque to the incident light. This is an issue for measuring samples with incident light in the infrared regime. For example, Si is transparent to the infrared laser incorporated in LFA 447; in this case, an Au coating is used to make the Si surface opaque, and a thin black graphite coating is applied to the Au surface to reduce light reflectance and increase the surface emissivity. When measuring a porous sample such as a VACNT film, the laser beam can penetrate into the sample. As such, the as-measured α is, as Akoshima *et al*. pointed out, an overestimation.[346] The penetration depth, and

therefore, the accuracy of the measurement, depends upon the wavelength of the incident laser, its pulse width, and the packing density of the VACNTs. Approximation D requires the range of temperatures in a single measurement be kept as small as possible. This is one of the important reasons why materials with low thermal diffusivities are sized to be relatively thin, and also one of the reasons why in some cases α is obtained by extrapolating to zero incident laser pulse energy on the plot of apparent α values as a function of incident laser pulse energy.[341] Approximation E is not applicable to high-temperature measurement or samples with relatively high emissivity and large thickness; proper corrections are recommended.[332-334] A VACNT array has a high emissivity (>0.98) due to its sparseness and imperfect alignment of the tubes in the array.[342,347] Thus, for a thick VACNT array, *e.g.*, 1 mm,[346] heat loss by radiation is an issue and needs to be corrected.[348] In the present study, we try to provide an answer to whether and how we can use the LFA technique to measure α of VACNTs.

4.2 Experimental

4.2.1 VACNT Synthesis by a TCVD Process

VACNTs were synthesized by a water-vapor assisted TCVD process as described before. The thickness of the synthesized VACNT films can be tuned in the range from 20 to 2800 μm by tuning the growth duration. The overall packing density of the synthesized VACNT film is ~5%. Packing density (f) is defined as the volumetric percentage of the CNTs in the VACNT film, which is equal to the ratio of the mass density of the VACNT film (weighed) to the mass density of individual CNTs (calculated later).

4.2.2 Microwave Treatment

Microwave treatment of VACNT samples was carried out in a VFM chamber filled with air at normal pressure to create an extra amount of defects in the CNTs. The microwave system was programmed to operate at different power levels and duration.

4.2.3 Mechanical Bending of VACNTs

A surface-metallized VACNT film (870-μm thick) on its synthesis substrate was carefully centered on top of the bottom plane compression platen in an Instron 5548 Micro Tester. A counter Si substrate was tape-fixed to the bottom of the top platen and then moved downward slowly (50 μm min^{-1}) against the top of the VACNT sample. The top platen stopped when the preset compression ratio ($1-l'/l_0$, where l_0 is the thickness of the VACNT sample before compression, and l' is the thickness after compression) was reached, and held for 5 min before release of the force. The compression process was repeated once on the same VACNT sample. The final l' was determined under an optical microscope. Due to the elasticity of the CNTs, samples with compression ratio smaller than 40% could not be prepared reproducibly.

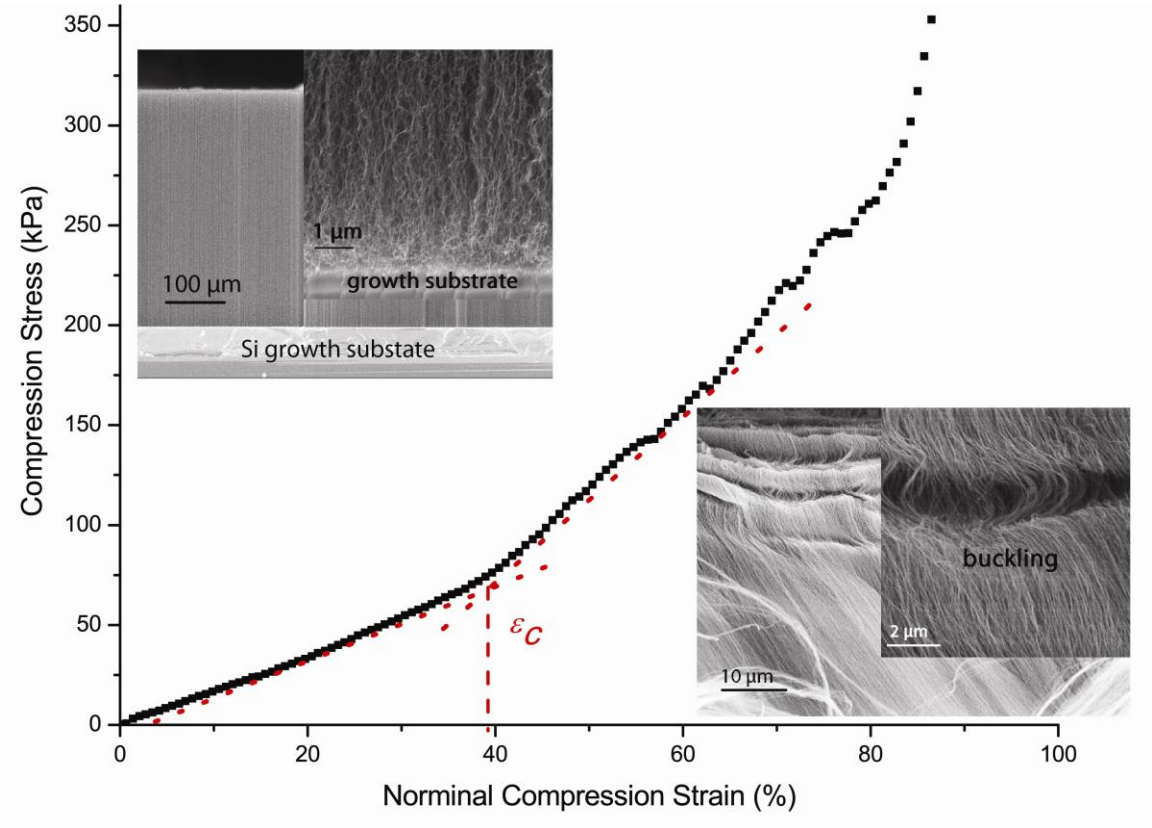

Figure 4.1 A typical stress-strain curve during compression of a VACNT film. SEM images of the VACNTs before (upper left) and after (lower right; sample tilted by 10^o in the SEM chamber) buckled are shown.

4.2.4 Mechanical Densification of VACNTs

Similar to the bending process, an on-substrate VACNT sample was tape-fixed on the bottom compression platen. A counter substrate was moved downward against the top of the VACNT sample, but stopped to hold when a ~5% (completely elastic regime) compression ratio was reached. Then the VACNT sample was bilaterally densified by 4 or 9 times.

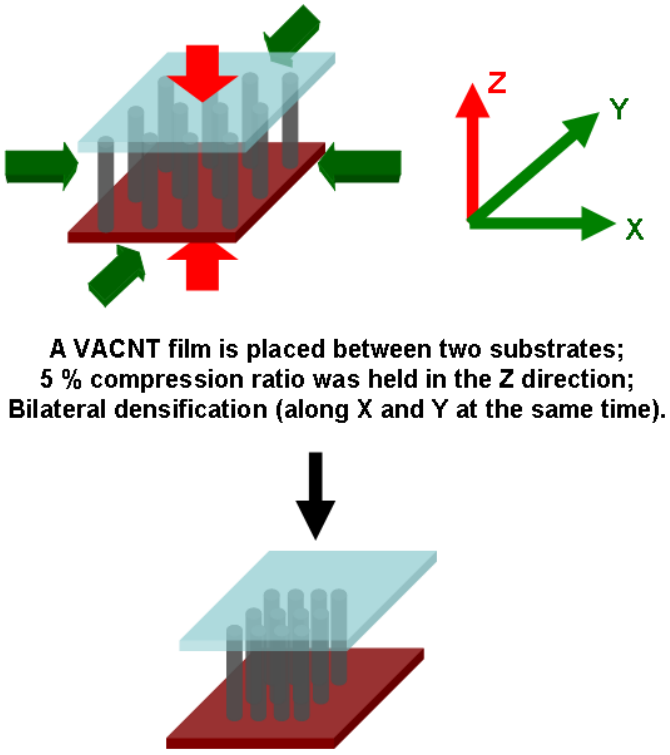

Figure 4.2 Schematic illustration of the mechanical densification process.

4.2.5 Laser Flash Measurement

Laser flash measurements of VACNT samples were carried out in a Netzsch laser flash apparatus (LFA447), with no pressure imposed during measurements. Four types of samples (1×1 cm^2 in size) were analyzed.

4.2.5.1 Type I: Free-Standing VACNT Films

A sharp and strong spike signal is evidenced in the experimental curve (Figure 4.3) due to the high porosity (packing density of CNTs ~5%) and anisotropy of α.

4.2.5.2 Type II: Surface-Metallized VACNT Films

As a modification of the type I structure, 30-nm Ti and 150-nm Au were deposited sequentially onto a free-standing VACNT film (by e-beam evaporation) to block, absorb, and distribute the energy of the incident laser beam. The metallized surface was the front surface during LFA measurement. An experimental curve with good fitting by various models is shown in Figure 4.4.

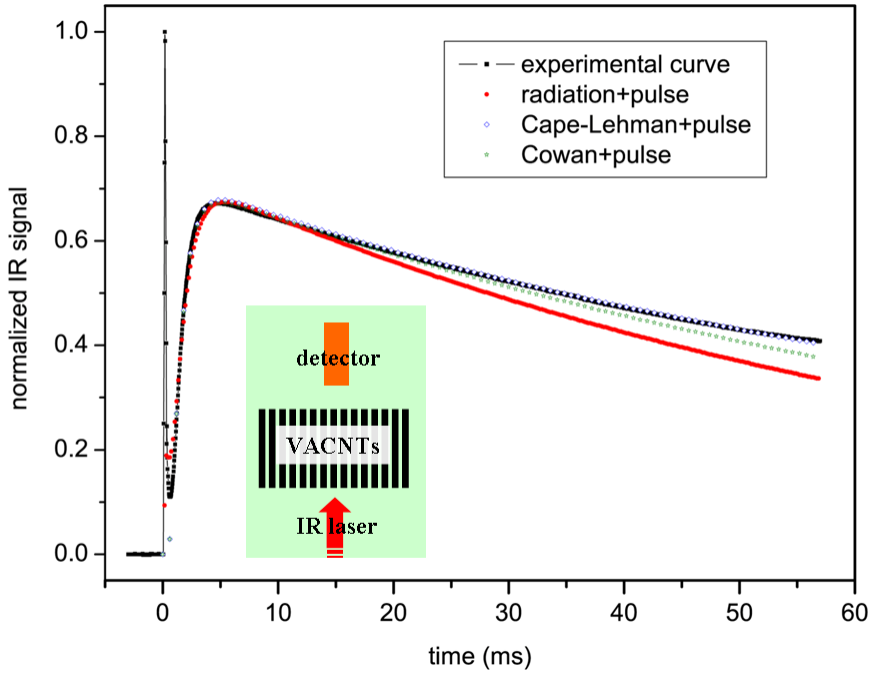

Figure 4.3 The experimental curve and fitting results for a type I sample. "Radiation + pulse", "Cape-Lehman + pulse", and "Cowan + pulse" refer to different models with correction methods of LFA; the corrections are incorporated in the commercial software on the basis of theoretical models in the literature. Inset is simplified illustration of the measurement layout.

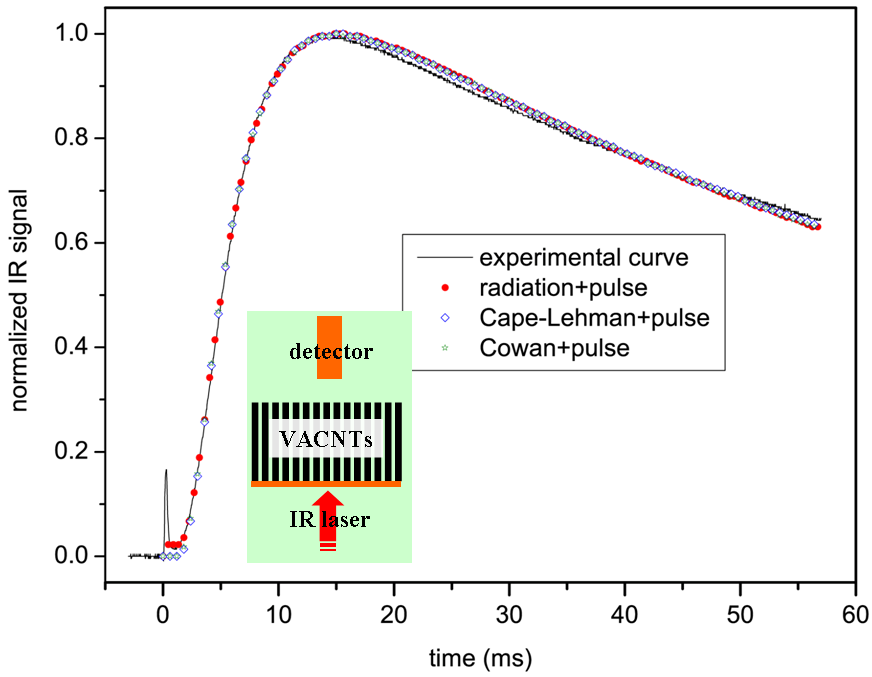

Figure 4.4 The experimental curve and fitting results for a type II sample.

4.2.5.3 Type III: BiSn-VACNT bilayer structure

The sampling process is illustrated in Figure 4.5. The VACNT array (on substrate) was surface-metallized with 30-nm Ti, 100-nm Cu, and 100-nm Au (Au\Cu\Ti as under-bump metallization layer for the solder bonding to BiSn) by sequential e-beam evaporation. The as-metallized VACNT array was pressed mildly (5 kPa) against eutectic BiSn (Bi58Sn42) (Indalloy #281, T_m=138 ^{o}C, Indium, Inc.) on a Si substrate reflowed at 170 ^{o}C. After cooling down to room temperature, the bottom Si substrate was easily removed because BiSn doesn't wet Si surface. The thickness of the bottom metallization layer (BiSn) was measured under an optical microscope. Such a bilayer sample can be treated as a single layer based on the following considerations. First, the thickness (~20 μm) and α (12.5 mm^2 s^{-1} measured by LFA, consistent with the documented data of 13.2 mm^2 s^{-1} from Indium, Inc.) of the bottom BiSn ensures an extremely short heat transport duration (t_c, BiSn=0.7l^2/α <6 μs) through the BiSn layer. This duration, in comparison

with the pulse duration (for example, τ=100 or 400 μs), is negligible. Second, the VACNT thickness can be tuned to ensure that $t_{c,VACNT}>\tau$ (finite-pulse effect), and/or $\kappa_{VACNT}/\varepsilon l_{VACNT}$>4.2 W cm^{-2} K^{-1} (radiation loss effect). A typical experimental data curve is shown in Figure 4.6.

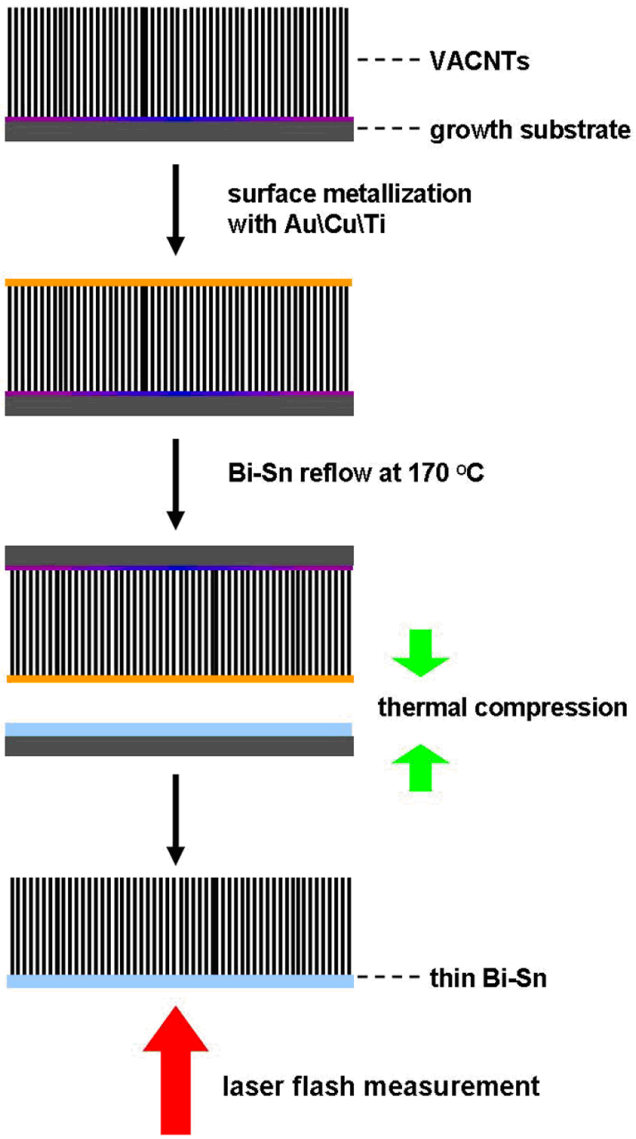

Figure 4.5 Schematic illustration of the sampling process for type III samples.

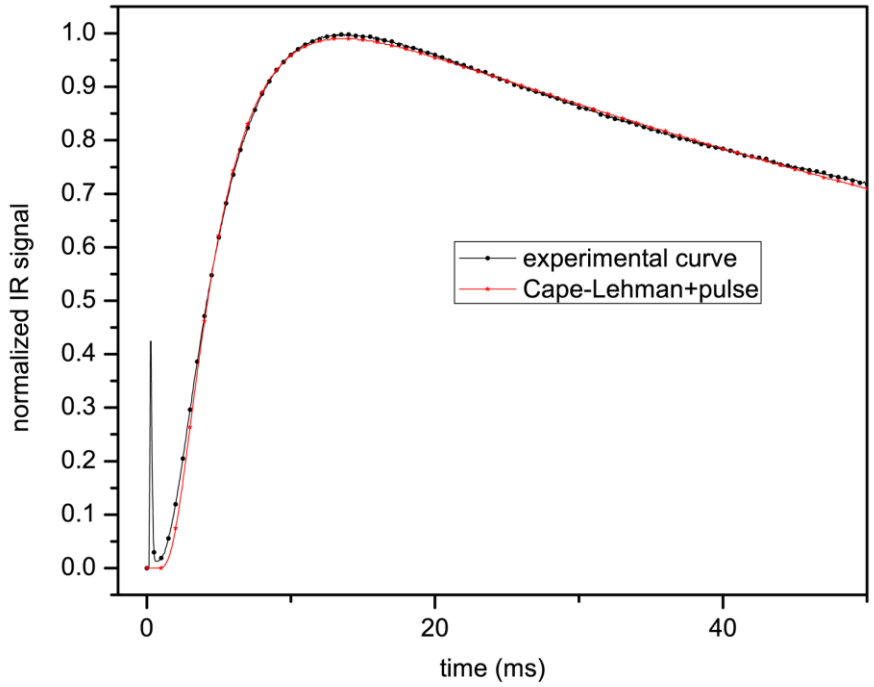

Figure 4.6 The experimental curve and fitting results for a type III sample.

4.2.5.4 Type IV: Cu-VACNT-Si Trilayer Structure

VACNTs were synthesized on a bulk Cu substrate (1-mm thick, surface finished) or a thin Cu foil (25-μm thick, surface finished) and then bonded to a Si (265-μm thick) mating substrate (the chemical bonding process will be discussed in details in Chapter 5).

4.3 Results and Discussion

4.3.1 The Importance of the Metallization Layer for Type II Samples

The experimental results of type I and II samples with various thicknesses (CNT lengths) are shown in Figure 4.7. For type I samples, the porous structure results in an overestimation of α. As predicted, α of type I samples varies greatly with the sample thickness, which should not be true. In sharp comparison, a thin metallization layer on the VACNT surface (type II) is effective in blocking the incident laser and distributing the

absorbed energy. In view of the small tube size and the inter-tube distance, the VACNT sample can be treated as a quasi-homogeneous material with respect to the incident laser. As a result, the experimental curve can be fitted very well with conventional models for homogeneous bulk materials. α is not thickness-dependent, which is in agreement with the experimental result by Yang *et al.*[97] and the theoretical prediction in the diffusive-transport-dominated regime.[349] The measured value of α is 29.45±0.52 mm^2 s^{-1}, corresponding to κ_{VACNT} of $0.27\pm0.01\times10^2$ W m^{-1} K^{-1} (calculated later). Taking into account the 5% packing density, κ of individual CNTs is calculated to be $5.4\pm0.3\times10^2$ W m^{-1} K^{-1} from the LFA results. It is noted that our preliminary measurement result on the same VACNTs by a photothermal technique was κ_{VACNT}=81 W m^{-1} K^{-1},[350] corresponding to >1600 W m^{-1} K^{-1} for the individual CNTs, which is not a reasonable value given the intrinsic defects, large diameter, and tube-tube interaction of the CNTs. Such an overestimation is probably attributed to the inaccuracy of the measurement technique used before.

It is noted that the as-measured α (Cape-Lehman+pulse correction) is a convolution of the intrinsic thermal transport property of the VACNT array, the Au\Ti coating, and the interface. In such a case, a correction on α is used based on the analysis by Maillet *et al.*:[351]

$$\frac{l_{overall}^{\ 2}}{\alpha_{con}} = \frac{l_{VACNT}^{\ 2}}{\alpha_{VACNT}}\left[1+\frac{C_{Au\backslash Ti}}{C_{VACNT}}\left(1+\frac{3R_{Au\backslash Ti}}{2R_{VACNT}}+3\frac{R_i}{R_{VACNT}}\right)\right]^2 \tag{4.2}$$

where $l_{overall}$ and l_{VACNT} are the overall thickness of the sample and the VACNT thickness, respectively, α_{con} and α_{VACNT} the convoluted thermal diffusivity (after Cape-Lehman+pulse correction, corresponding to the red-triangle data points in Figure 4.7) and the true value of the thermal diffusivity of the VACNT film, respectively, $C_{Au\backslash Ti}$ and C_{VACNT} the thermal capacitances per area of the Au\Ti coating and the VACNT film, respectively, and $R_{Au\backslash Ti}$, R_{VACNT}, and R_i the thermal resistances of the Au\Ti layer, the VACNT layer, and the VACNT/metallization interface, respectively.

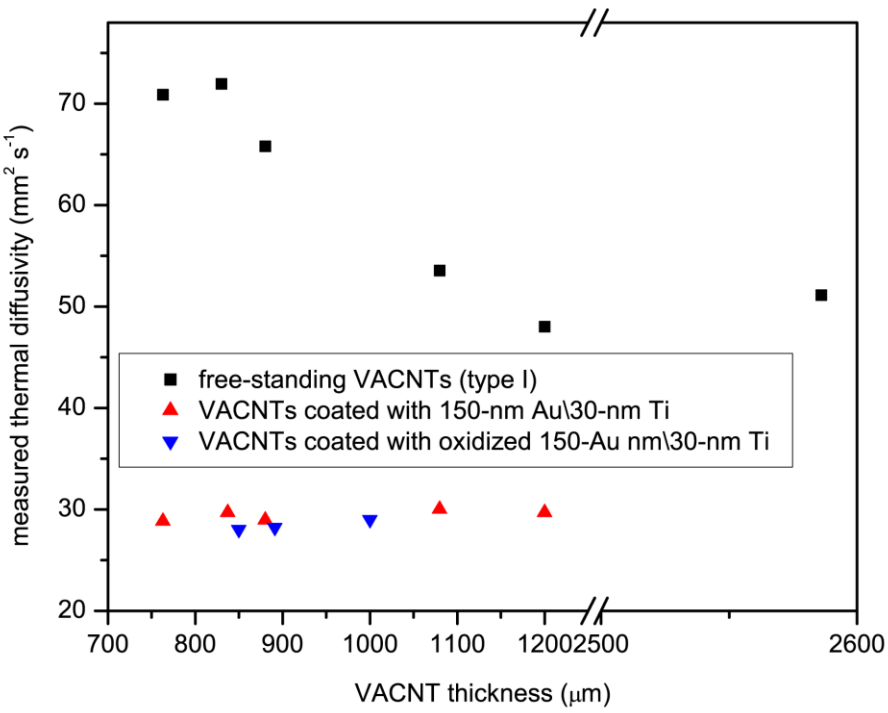

Figure 4.7 Experimental data for type I and II samples. All the data were corrected against the finite-pulse effect and heat loss (Cape-Lehman model).

C is calculated as

$$C = \rho c_p l \tag{4.3}$$

where l is the thickness of the material in study.

Taking l_{Au}=150 nm, l_{Ti}=30 nm, κ_{Au}=318 W m^{-1} K^{-1}, κ_{Ti}=21.9 W m^{-1} K^{-1}, ρ_{Au}=19.3 g cm^{-3}, ρ_{Ti}=4.51 g cm^{-3}, $c_{p,Au}$=0.129 J g^{-1} K^{-1}, $c_{p,Ti}$=0.52 J g^{-1} K^{-1}, and using a mixing rule and a series model ($\frac{l_{Au\backslash Ti}}{\alpha_{Au\backslash Ti}\rho_{Au\backslash Ti}c_{p,Au\backslash Ti}} = \frac{l_{Au}}{\kappa_{Au}} + \frac{l_{Ti}}{\kappa_{Ti}}$) for the Au\Ti coating, we get $l_{Au\backslash Ti}$=180 nm, $\rho_{Au\backslash Ti}$=16.8 g cm^{-3}, $c_{p,Au\backslash Ti}$=0.146 J g^{-1} K^{-1}, $\alpha_{Au\backslash Ti}$=39.64 mm^2 s^{-1}.

$$\rho_{CNT} = \rho_{graphite}\frac{d_{o,CNT}^2 - d_{i,CNT}^2}{d_{o,CNT}^2} = 1.3 \pm 0.01 \ \text{g cm}^{-3} \tag{4.4}$$

where $\rho_{graphite}$=2.21 g cm^{-3}, $c_{p,CNT}$=0.7 J g^{-1} K^{-1},[352] the average outer diameter of CNT $d_{o,CNT}$=14±1.2 nm, and the average inner diameter $d_{i,CNT}$=8.9±0.7 nm.

$$R_{VACNT} = \frac{l_{VACNT}}{\kappa_{VACNT}} = \frac{l_{VACNT}}{\alpha_{VACNT}\rho_{CNT}c_{p,CNT}} \quad (4.5)$$

α_{VACNT} is the solution of the equation set composed of Eqns. (4.2) and (4.5). In view of the sharp contrast in thermal diffusivity and mass density between the CNTs and the surrounding air in the porous structure, the CNTs are considered the only paths that conduct heat during the measurement. Therefore, in Eqn. (4.5), we use the mass density and the specific heat of an individual CNT instead of the effective mass density and the specific heat of a porous VACNT film.[340,353]

Now the effects of the Au\Ti coating and the CNT\coating interface can be investigated. A wide range of theoretically assumed values of α of the Au\Ti coating is covered, from 15 $mm^2\ s^{-1}$ (in the case of a porous metal film) to its theoretical value of 39.64 $mm^2\ s^{-1}$; so is the CNT\coating interfacial resistance, from 0 to 30 $mm^2\ K\ W^{-1}$. In Figure 4.8, we see that the effects of the Au\Ti coating and the CNT\coating interface on the measurement results can be neglected: the predicted deviation from the measured α is <0.3%. The deviation is smaller than the reproducibility of LFA (~3%), not to mention the propagation of errors. This theoretical analysis was tested by measuring α of the VACNT films coated with an oxidized Au\Ti layer. Oxidation of the Ti deposit in the Au\Ti coating on the VACNTs was realized by a 5-min 100-W microwave treatment, as confirmed by XPS (Figure 4.9). The average value of α is 28.41 $mm^2\ s^{-1}$ (Figure 4.7), 3.5% lower than the average α (29.45 $mm^2\ s^{-1}$) of the Au\Ti coated VACNT samples. It is more or less within the error margin of the measurement. The high reproducibility of the VACNT synthesis and sampling, and the high accuracy of the data extraction ensure a high accuracy and precision of α by the LFA technique. In comparison, α (40-280 $mm^2\ s^{-1}$) may not be determined with a compariable accuracy by other measurement techniques such as the photoacoustic technique.[226]

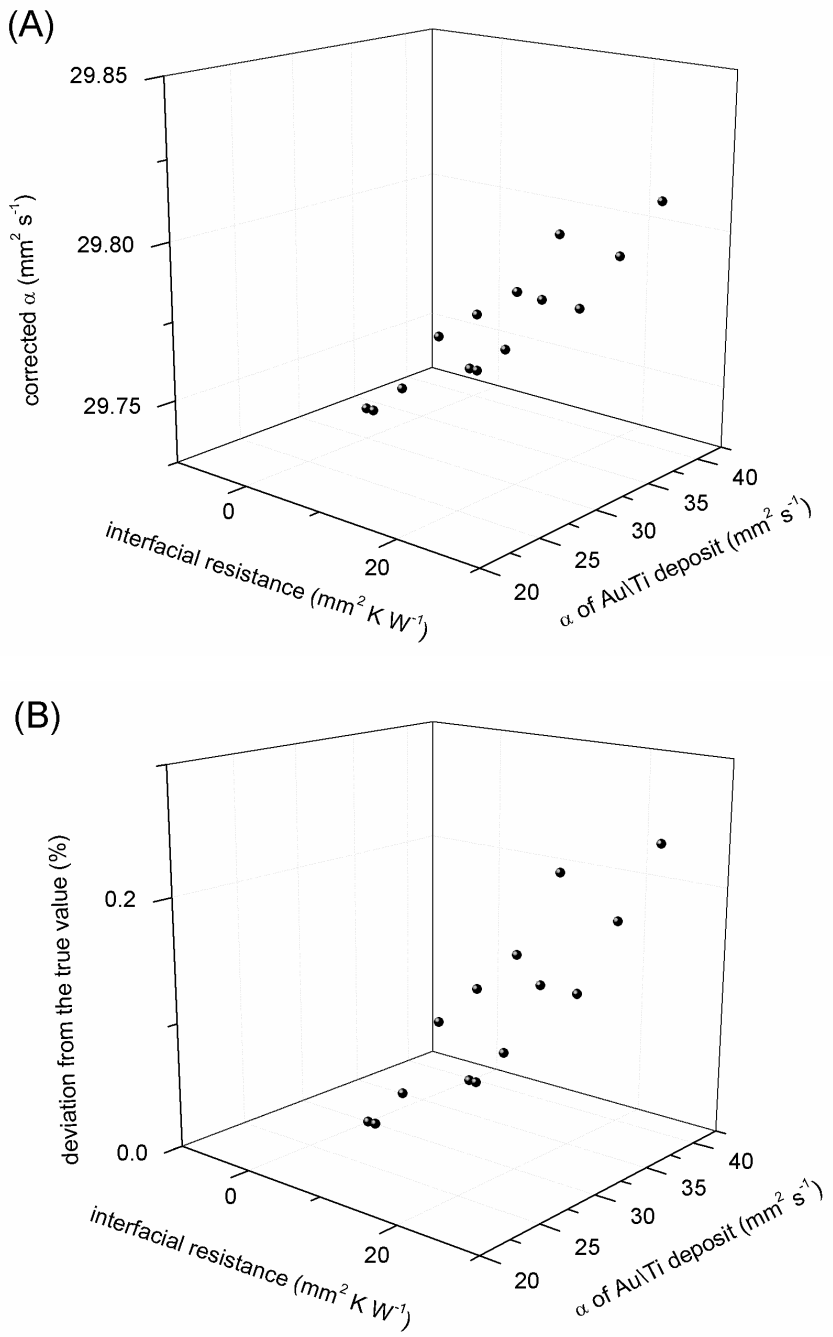

Figure 4.8 Thermal diffusivity corrections against the thermal resistance of the Au\Ti coating and the CNT\coating interfacial resistance.

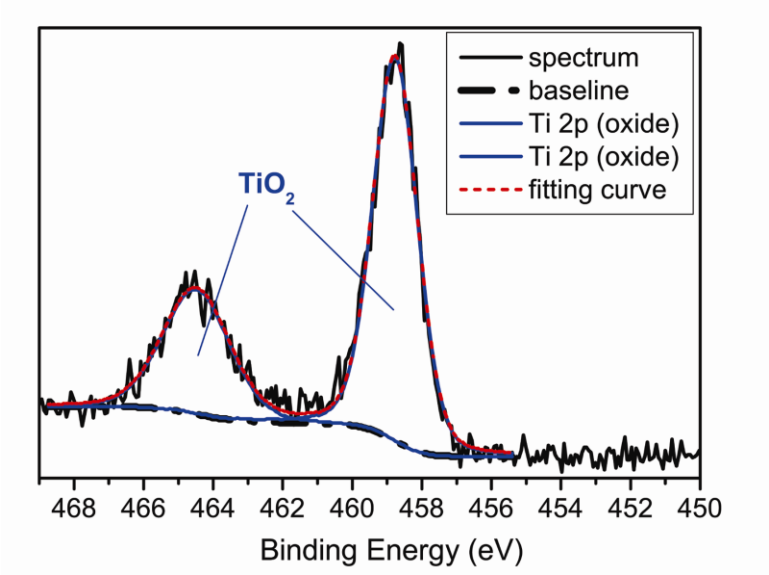

Figure 4.9 Hi-resolution X-ray photoelectron spectrum of the Ti\VACNT surface after a 5-min 100-W microwave treatment.

4.3.2 Influences of CNT Quality, Buckling, and Packing Density on the Thermal Diffusivity of VACNTs

As stated above, a reliable measurement technique should enable us to perform the systematic parametric study. Reversely, the parametric study is a good test of the reliability of the LFA technique.

4.3.2.1 Quality of CNTs

Quality of CNTs has been found to be highly important in determining the thermal properties of CNTs.[80,90,91,354,355] Most of the studies on defect-dependent thermal conductivity of CNTs have so far been focused on simulations of individual SWNTs only. Recently, Pettes and Shi presented experimental data on the defect-dependent thermal conductivity of individual CNTs,[92] where intrinsic thermal conductivities of 42-48, 179-336, and 269-343 W m^{-1} K^{-1} at room-temperature for three MWNT samples were found to be correlated well with observed defects spaced

approximately 13, 20, and 29 nm apart, respectively. Defect-dependency of the collective thermal property of VACNTs is actually of more interest but remains unexplored.

In our study, the defect density of CNTs is qualitatively evaluated by the ratio of the integrated intensity of D band (I_D) at ~1334 cm^{-1} to that of G band (I_G) at ~1570 cm^{-1} in Raman spectra. In general, the more defective the CNTs are, the higher the I_D/I_G ratio is. As can be seen in Figure 4.10, α of VACNTs decreases, as is predicted, with increased I_D/I_G ratio for categories B, C, and D. Comparing the results of categories A, B, E, and F, we find that in the regime where I_D/I_G is very close to 1, α is much more sensitive to the microwave treatment than I_D/I_G. For example, VACNTs after a 500-W microwave treatment (in air) for 1 min show an I_D/I_G value (1.05±0.02) that is very close to the value of the control samples (1.01±0.01); however, its α decreases by ~25%. This phenomenon is probably attributed to the higher sensitivity of α than I_D/I_G to CNT defect density in the low-defect-density regime. The microwave treatment, when performed in air, introduces oxygen-functionalized sites (or chemisorption of oxygen) on the CNTs. According to simulation results, when a small amount of point defects (such as vacancies, isotopic atoms, rehybridizations due to functionalizaiton, and absorption) are introduced to a single CNT, its κ drops drastically.[89,90,355,356] Due to the intrinsically large D-band in a MWNT caused by the turbostratic stacking (stacking fault) of the walls,[22,99,357] it is reasonable to believe that I_D/I_G in the Raman spectra is not sensitive to defect density in the low-defect-density regime. The low defect density of the synthesized VACNTs is reflected by the high κ value of the individual CNTs (~540 W m^{-1} K^{-1}), which is comparable with the result by Aliev *et al.* (~600 W m^{-1} K^{-1}),[342] and higher than the results by Pettes and Shi (<350 W m^{-1} K^{-1}),[92] Yang *et al.* (~200 W m^{-1} K^{-1}),[97] and Choi (<350 W m^{-1} K^{-1}) *et al.*[81]

A high-temperature annealing process (980 ^{o}C, 2 hours, Ar 350 sccm, H_2 200 sccm) reduces I_D/I_G by ~7%. Accordingly, α increases to ~34 mm^2 s^{-1}, corresponding to a 17% increase in κ for individual CNTs (to ~620 W m^{-1} K^{-1}). In comparison with the

annealing effect of a high-temperature (3000 ^{o}C) treatment on carbon fibers, where improvements by two orders of magnitude were observed (from ~40 to ~1100 W m^{-1} K^{-1} and from ~10 to ~100W m^{-1} K^{-1} for TCVD-synthesized fibers and PAN-based fibers, respectively),[357] the annealing effect presented here is not distinct. One possible reason is that the annealing temperature is not high enough to allow for a complete reconstruction of defective lattice sites. Temperatures above 1900 °C are typically used in thermal annealing of MWNTs.[273, 274]

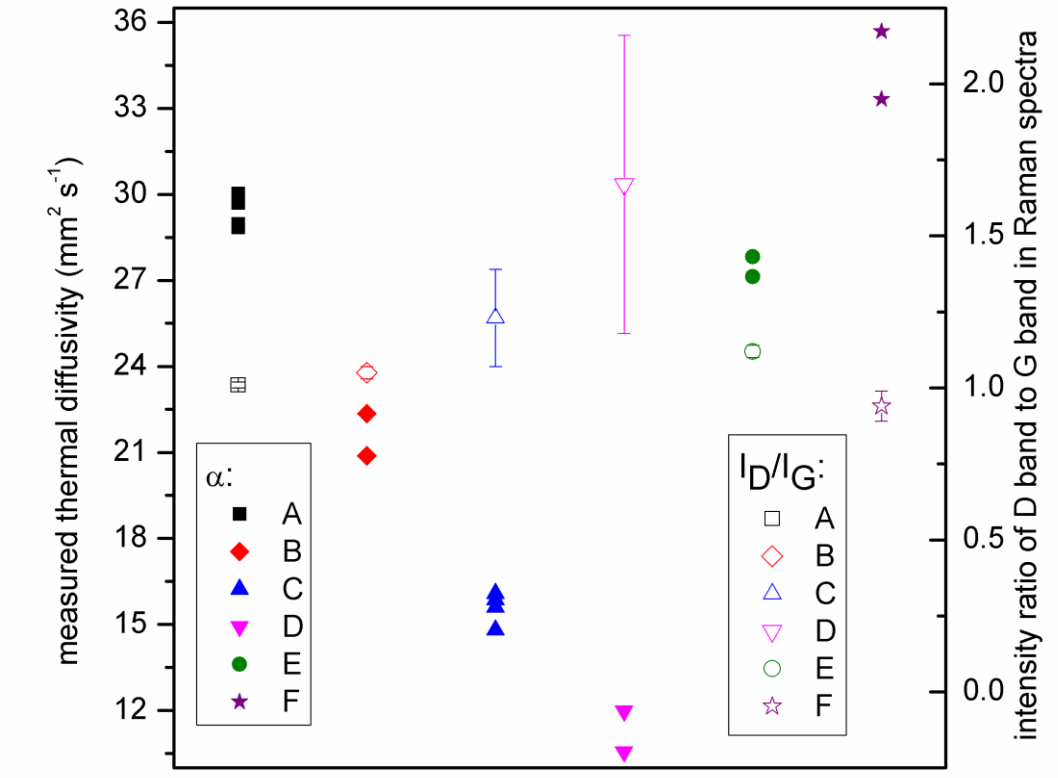

Figure 4.10 Thermal diffusivity and I_D/I_G ratio of VACNT samples (type II). Categories A, B, C, D, E, and F represent control VACNT sample, VACNTs treated by 500-W microwave for 1 min, VACNTs treated by 500-W microwave for 2 min, VACNTs treated by 500-W microwave for 5 min, VACNTs treated by 200-W microwave for 10 min, and high-temperature annealed VACNTs (980 ^{o}C, 2 hours, Ar 350 sccm, H_2 200 sccm).

4.3.2.2 Buckling of VACNTs

Buckling effect on α was studied by measuring the mechanically bent samples. A typical experimental curve from the LFA measurement for the bent samples is shown in Figure 4.11.

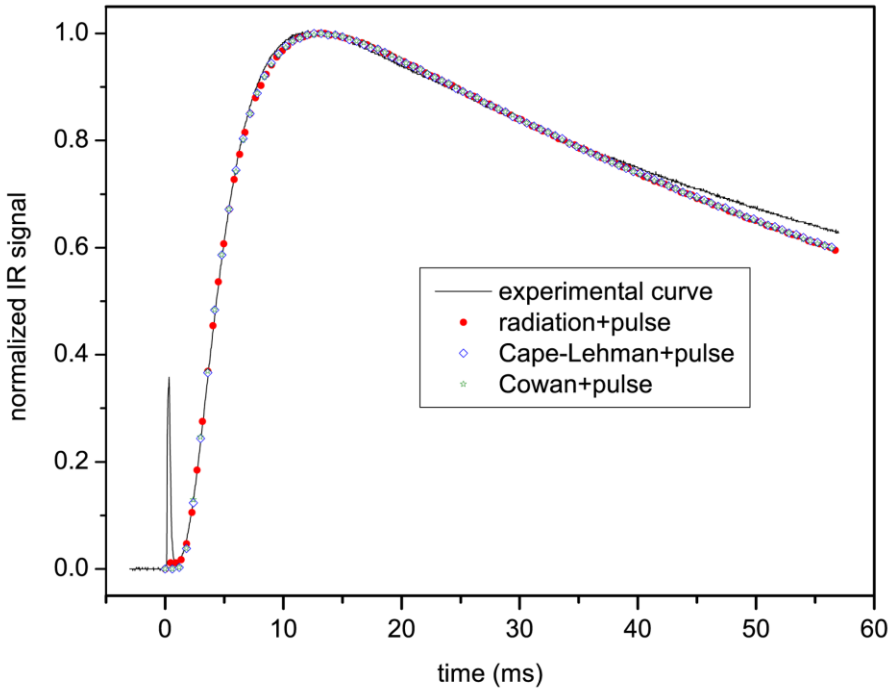

Figure 4.11 The experimental curve and fitting results for a mechanically bent sample (type II, compression ratio ~57%).

We observe a large drop of α upon compression (Figure 4.12). For example, a compression ratio of 50% results in 70% reduction in α (to ~9 mm^2 s^{-1}); a compression ratio of ~ 80% reduces α from ~30 to ~1.5 mm^2 s^{-1}. At least two reasons account for the phenomenon. First, above a critical compression ratio (named "critical strain" in literature) of ~40%, buckling associated with permanent deformation (nonreversible compression) of the film was observed. Note that a critical strain (ε_c in Figure 4.1, defined as the compression ratio above which buckling of VACNTs occurs according to

the definition in literature) of ~57% was previously reported by Cao *et al*.[358], which is higher than in our case probably because the packing density of their VACNTs (~13%) was higher than ours, and a different compression rate was used. The buckling suggests a structural breakdown of the CNTs;[358] the damaged CNT wall structure results in phonon scattering. Bending robustness of thermal conductance of short individual CNTs was observed experimentally by Chang *et al*.[359], and has recently been justified in theory by Nishimura *et al*.[360] However, it was found that when the outer shell of a MWNT broke down (disconnected), κ dropped more than 70%. Second, the bending process increases tube-tube contacts, which enhances tube-tube interaction. Tube-tube interaction has been proposed to be a negative effect on thermal transport.[100,348,361]

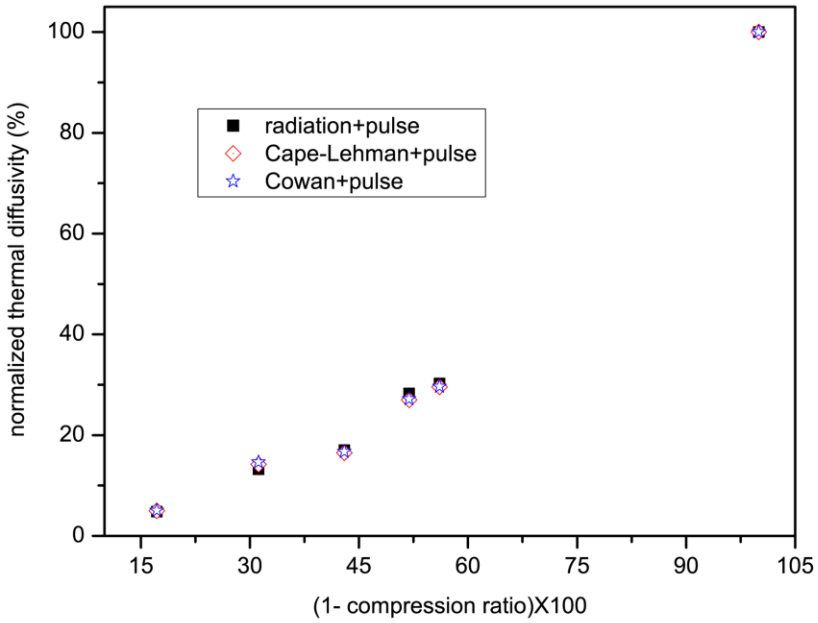

Figure 4.12 Buckling effect on the collective thermal diffusivity of VACNTs.

When measuring VACNT TIM samples, people tend to apply a certain pressure to reduce the bond-line thickness and improve the CNT/substrate contact. However, the

high compression force used in literature (*e.g.*, 0.45 MPa in Ref. 8) is very likely to permanently damage the VACNTs and result in a great reduction of thermal conductance through the VACNTs.

4.3.2.3 Packing Density of VACNTs

VACNTs with high packing densities are desired for most applications.[362,363] Figure 4.13 shows the side-view SEM images of the control VACNT film and the 9-times densified VACNT film.

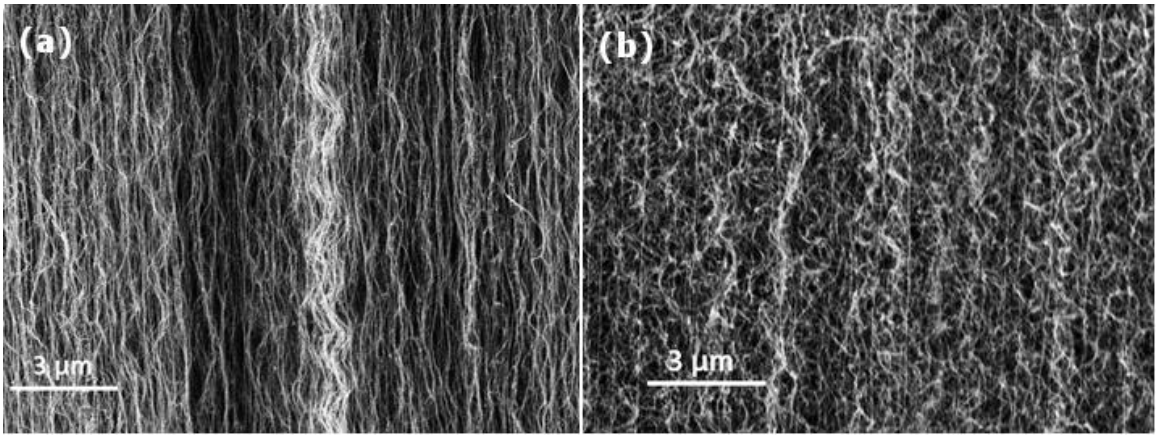

Figure 4.13 Side-view SEM images of synthesized VACNTs (a), and the VACNTs densified by 9 times (b).

In Figure 4.14, we show that α of VACNTs increases to 48.89-55.61 and 90.00-103.11 W m^{-1} K^{-1} when densified by 4 and 9 times, respectively. A higher packing density renders more channels/paths per unit area to conduct heat. When normalized to κ of individual CNTs, however, the value decreases with increased packing density, indicating a stronger tube-tube interaction upon densification. Interpretation of the negative influence of tube-tube interaction on the thermal transport is straightforward. Fundamentally, phonons are nothing more than vibrations. When vibrations of individual tubes are interfered by, for example, forces from adjacent tubes or polymer molecules on the tube surfaces, phonon scattering occurs. Tube-tube interaction (or "inter-tube

coupling") is generally dominated by van der Waals force between CNTs in a CNT bundle and a VACNT film. A decrease in thermal conductivity of CNTs due to tube-tube interaction upon bundling has also been discussed by Aliev *et al*.[348]

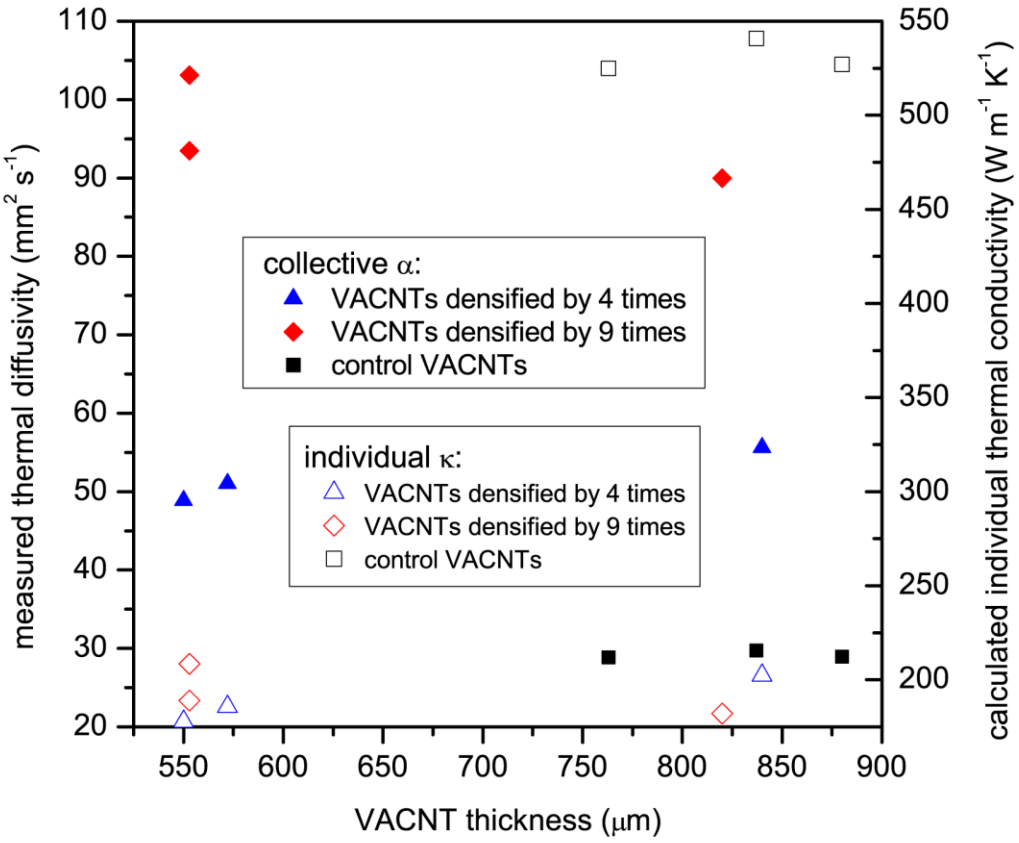

Figure 4.14 Effect of packing density on the thermal diffusivity of VACNTs.

4.3.3 Evaluation of Tip-to-Tip Contact Resistance in Layered VACNT Structures

Multi-layered VACNT films with well-defined thickness of each layer were synthesized by a TCVD process reported before.[190] Figure 4.15 shows the side-view SEM image of a synthesized multi-layered VACNT film. Array-to-array tip-to-tip thermal resistance is evaluated by extracting the VACNT-VACNT interfacial resistance from the measurement results of multi-layer VACNT samples (Table 4.1). A common

series model ($\frac{l_{total}}{\kappa_{equivalent}} = \frac{l_{total}}{\kappa_{VACNT}} + \Sigma R_i$, where R_i is the interfacial thermal resistance between two adjacent VACNT layers) is used, *i.e.*, the equivalent thermal resistance is equal to the sum of interfacial resistances between layers, and the total intrinsic resistance due to the VACNTs. The VACNT-VACNT interfacial resistance in the trilayer sample is ~2 mm^2 K W^{-1} (averaged value of the last column in Table 4.1), similar to the result (~2.1 mm^2 K W^{-1}) measured by a photoacoustic technique by Cola *et al*.[226] Normalization with respect to the actual contact area (5% in our case) leads to a tip-to-tip contact resistance of ~1×10^{-7} m^2 K W^{-1} between individual CNTs, which is on the same order of magnitude with the result (~8.4×10^{-7} m^2 K W^{-1}, after normalized to ~40% packing density) by Cola *et al*. but seems higher than side-to-side (1.2×10^{-8} m^2 K W^{-1}) and side-to-tip (1.2×10^{-9} m^2 K W^{-1}) contact resistances measured between two individual CNTs.[364] What is interesting is that the average interfacial thermal resistance shows a nonlinear increase with the number of VACNT layers (the last two columns in Table 4.1). This can probably be explained by a gradual decrease in the packing density of the VACNTs layers with growth duration.[365]

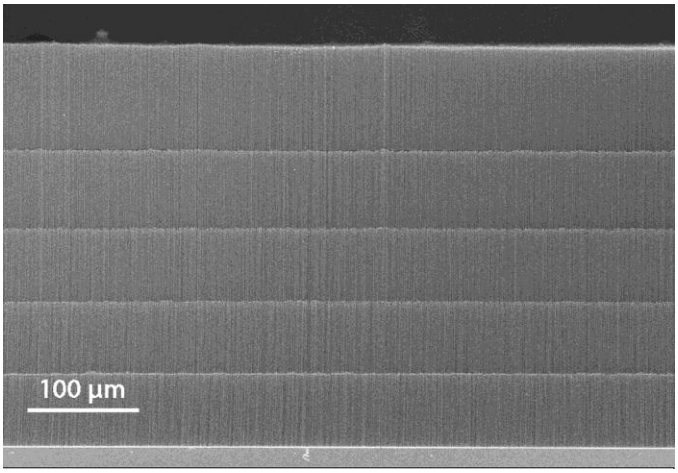

Figure 4.15 A side-view SEM image of a synthesized multi-layered VACNT film.

4.3.4 Interpretation of the Experimental Data for Type III and IV Samples

For type III samples, the as-measured α (after Cape-Lehman+pulse correction) is a convolution of the intrinsic thermal transport property of the VACNT array, the BiSn layer, and the interface. A modification method similar to that for type II is used:

$$\frac{l_{overall}^{\ 2}}{\alpha_{con}} = \frac{l_{VACNT}^{\ 2}}{\alpha_{VACNT}}\left[1+\frac{C_{BiSn}}{C_{VACNT}}\left(1+\frac{3R_{BiSn}}{2R_{VACNT}}+3\frac{R_i}{R_{VACNT}}\right)\right]^2 \tag{4.6}$$

The interfacial thermal resistance between the BiSn layer and the VACNTs is extracted from Eqn. (4.6) and listed in Table 4.2 (11-34 mm^2 K W^{-1}). The metallization layer is important in improving the bonding between the CNTs with BiSn. Without the metallization layer, the interfacial adhesion is very weak because there is essentially no bonding between CNTS and BiSn; therefore, the interfacial resistance is high (98-116 mm^2 K W^{-1}).

It is important to point out that an "effective thermal resistance/diffusivity" method based on a simple mixing rule and a series model turned out to be invalid for the type-III bilayer structure. We calculated the BiSn/VACNT interfacial thermal resistance based on a simple mixing rule and a series model (Table 4.3) but got unreasonable results. The reason is that the mass density of the VACNT film is so low that its contribution to the thermal transport, according to the calculation, becomes negligible compared with the other layer. Interpretation of experimental data for type IV samples becomes even more challenging, in which case whether or not we can fit the experimental data from the substrate-VACNT-substrate trilayer sample is greatly dependent on the substrate material in use. In Figure 4.16, we show that when a thick Cu substrate is used as the bottom layer, the experimental curve cannot be fitted properly. The large thickness of the top and/or bottom substrates in a trilayer TIM sample sabotages the accuracy of the measurement.[343] In comparison, a thin Cu foil as the bottom layer gives a satisfactory fitting curve; in this case, a conventional trilayer model

can be used to extract the equivalent thermal diffusivity of the VACNT TIM. We notice that, in the work by Shaikh *et al*.[338,339], the effective thermal resistance/diffusivity method was adopted to estimate the thermal conductivity of the VACNT array in a glass-VACNT-glass assembly. In view of the large thickness (1.6 mm) and low thermal diffusivity (0.905 mm^2 s^{-1}) of the glass slides in use, and the usually large CNT/glass interfacial thermal resistance, a series model using the equivalent mass density and the equivalent thermal diffusivity is not valid. Moreover, the main contribution to the characteristic transit duration is due to the glass layers; therefore, significant uncertainty is expected. It calls our attention that no original experimental curves and fitting curnves were given in Refs. 338 and 339.

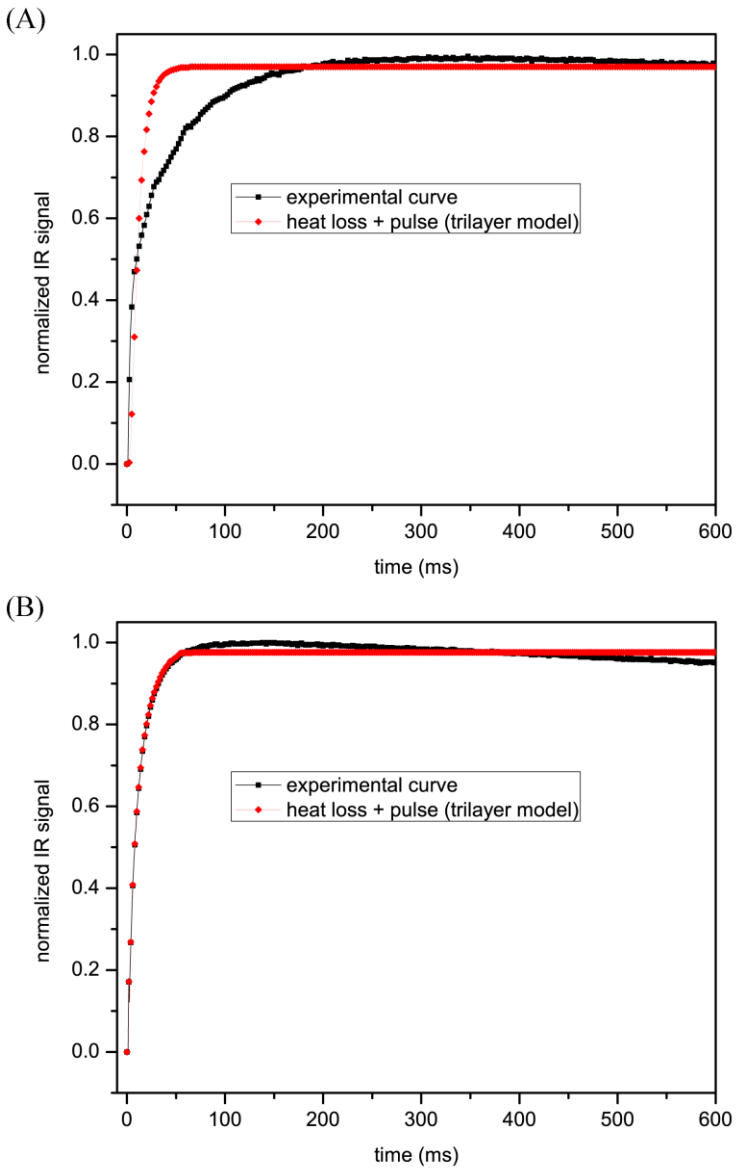

Figure 4.16 Experimental curves and fitting results for a type IV sample with a thick Cu substrate (a) or a thin Cu foil (b) as the bottom layer.

Table 4.1 Evaluation of CNT-CNT contact resistance in multi-layer VACNT samples (Type II).

$l_{overall}$ (μm)[a]	Layer No.	$\alpha_{equivalent}$ ($mm^2\ s^{-1}$)[a,b]	ρ_{CNT} ($g\ cm^{-3}$)	$c_{p,CNT}$ ($J\ g^{-1}\ K^{-1}$)	$\kappa_{equivalent}$ ($W\ cm^{-1}\ K^{-1}$)[a]	Total thermal resistance ($cm^2\ K\ W^{-1}$)	Intrinsic thermal resistance of VACNTs ($cm^2\ K\ W^{-1}$)	ΣR_i ($cm^2\ K\ W^{-1}$)[a,c]	VACNT-VACNT interfacial resistance ($\overline{R_i}$) ($cm^2\ K\ W^{-1}$)[c]
—	1	29.45[d]	1.3	0.7	0.27	—	—	—	—
1080	3	26.24	1.3	0.7	0.24	0.45	0.40	0.05	0.02
1046	3	24.67	1.3	0.7	0.22	0.47	0.39	0.08	0.03
996	7	16.88	1.3	0.7	0.15	0.65	0.37	0.28	0.05
982	7	15.71	1.3	0.7	0.14	0.69	0.37	0.32	0.05

a. As in Eqn. (4.6).
b. The measured equivalent thermal diffusivity with the Cape-Lehman correction.
c. Based on a series model of thermal resistance.
d. The average value of the measured control VACNT samples, as shown in Figure 4.7.

Table 4.2 Experimental data for type III samples and the evaluation of interfacial thermal resistance[a].

l_{VACNT} (μm)	Metallized[b]	BiSn layer thickness (μm)	α_{con} ($mm^2\ s^{-1}$)[c,d]	R_i ($cm^2\ K\ W^{-1}$)[d]
807	Y	18	26.63	0.11
632	Y	20	19.64	0.33
1090	Y	20	26.19	0.24
980	Y	18	24.77	0.34
980	N	21	18.00	0.98
1035	N	16	19.64	1.2
807	N	20	15.21	1.0

a. For the calculation in the table, the mass density of CNT and BiSn are 1.3 (calculated according to Eqn. (4.4)) and 8.56 g cm^{-3}, respectively; the specific heat of CNT and BiSn are 0.7 and 0.167 J $g^{-1}\ K^{-1}$; the thermal diffusivity of VACNTs and BiSn are 29.45 and 13.0 $mm^2\ s^{-1}$, respectively.

b. Metallized with 100-nm Au\100-nm Cu\30-nm Ti.

c. Measured thermal diffusivity of the whole sample.

d. As in Eqn. (4.6).

Table 4.3 Evaluation of the validity of "effective thermal resistance/diffusivity" method based on a mixing rule and a series model.

l_{VACNT} (μm)	BiSn layer thickness (μm)	α_{con} ($mm^2\ s^{-1}$)	Equivalent mass density ($g\ cm^{-3}$)[a]	Equivalent specific heat ($J\ g^{-1}\ K^{-1}$)[a]	Equivalent total thermal resistance ($cm^2\ K\ W^{-1}$)[a]	Thermal resistance due to BiSn ($cm^2\ K\ W^{-1}$)	Thermal resistance due to VACNTs ($cm^2\ K\ W^{-1}$)[b]		R_i ($cm^2\ K\ W^{-1}$)[c]	
807	18	26.63	0.25	0.30	4.1	0.0097	6.0	0.30	-1.9	3.8
632	20	19.64	0.33	0.27	3.8	0.011	4.7	0.24	-0.9	3.5
1090	20	26.19	0.22	0.32	6.0	0.0108	8.1	0.40	-2.1	5.6
980	18	24.77	0.22	0.32	5.7	0.0097	7.3	0.36	-1.6	5.3
980	21	18.00	0.24	0.31	7.5	0.0113	7.3	0.36	0.2	7.1
1035	16	19.64	0.19	0.34	8.0	0.0086	7.7	0.39	0.3	7.6
807	20	15.21	0.27	0.29	6.9	0.0108	6.0	0.30	0.9	6.6
807	20	15.21	0.27	0.29	6.9	0.0108	6.0	0.30	0.8	6.6

a. Equivalent mass density, specific heat and thermal resistance are calculated based on a simple mixing rule.

b. The values in the left and the right columns are calculated based on the mass density of the VACNT film and that of individual CNTs, respectively.

c. The values in the left and the right columns are calculated based on the values in the left and the right columns of the thermal resistance due to VACNTs, respectively.

CHAPTER 5

VACNT TIMS

TIMs play an important role in developing thermal solutions and have been extensively researched in the past decades.[7,8,366-383] Commonly used TIMs include polymer TIMs filled with fillers of high thermal conductivity, solder TIMs and filled phase change materials (PCMs). Although polymer based TIMs such as boron nitride (BN)/polyethyelen glycol (PEG) and BN/silicone, have their advantages in good adhesion, high compliance, easy processing and low cost, their thermal conductivities at low filler loadings are relatively low. Increasing filler loading improves the thermal conductivity of TIM itself but brings down its compliance and increases bond line thickness (BLT) in application, which consequently increases contact thermal resistance. Additionally, reliability is also an issue for polymer based TIMs because compliance of polymers degrades with operation time. In comparison, solder TIMs such as In, AuSn, InPb and InSnBi have high thermal conductivities and are now actively being pursued as TIMs. Currently, thermal resistance of a solder TIM layer (R_{TIM}, including the resistance at the two contact interfaces) is typically 5-20 mm^2 K W^{-1}. However, they have the drawbacks such as a high CTE (coefficient of thermal expansion), relatively low compliance, high cost, relatively low fatigue strength, voiding issue and sometimes complexity in processing. PCMs have high fluidity during processing making use of the latent heat of phase change during heating up, which dissipates much more heat generated by the die. However, PCMs, compared with solder TIMs, are not so popular due to a reliability issue because very often PCMs leak (flow out) from the interfaeces during operation. In general, none of the above TIMs meet the following requirements for next generation TIMs:

A. low intrinsic thermal resistance;

B. low interfacial thermal resistance with a mating substrate;

C. low CTE;

D. proper modulus to lower the thermal stress but withstand the warpage stress;

E. proper bond-line thickness to accommodate the warpage of the assembly;

F. thermal stability and chemical stability to avoid degradation with operation time.

5.1 Introduction of VACNT TIMs

The initial thrust for CNT TIMs originates from the high intrinsic thermal conductivity of individual CNTs, as well as their low CTE, flexibility, high thermal and chemical stabilities. However, researchers find that CNT/polymer composites exhibited unexpected low thermal conductivity (discussed in the next chapter and its references). Moreover, the difficulty in CNT dispersion and alignment in the polymer matrix bring more serious questions on the potential of CNT/polymer composites for thermal applications. Very soon, researchers switch to pure VACNTs as TIMs, which is still thought to be a promising research direction. VACNT TIMs have become more and more popular in not only academia but also industry, mainly attributed to the recent success on large-scale synthesis of VACNTs by various TCVD processes.[7, 8,14,226,247-249,280,328,340,350,384-387] Hu *et al*. used a 3ω method to measure the thermal contact resistance between a 13-μm thick VACNT array and the surface of a free mating substrate. The results showed that the contact resistances were 17 and 15 mm^2 K W^{-1}, respectively, under the pressure of 0.040 and 0.100 MPa.[328] Ngo *et al*. used electrodeposited Cu as a gap filler to enhance the stability and thermal transport of carbon nanofibers.[385] They reported the interfacial thermal resistance of 25 mm^2 K W^{-1} under a pressure of 0.414 MPa using a 1D reference bar method. Using a similar characterization method, Xu and Fisher reported an interfacial thermal resistance of 19.8 mm^2 K W^{-1} for a VACNT array at 0.45 MPa.[8] By using a PCM with the VACNTs, they

obtained a minimum resistance of 5.2 mm^2 K W^{-1}. Xu *et al*. used a photothermal method to evaluate the effective thermal resistance of VACNT arrays grown on Si substrates by PECVD.[280] The resistance was 12-16 mm^2 K W^{-1}, comparable to the resistance of commercially available thermal grease. Zhu *et al*. used a photothermal technique to measure the contact resistance of a VACNT/solder interface and estimate the thermal conductivity of the VACNT array.[350] The κ was 81 W m^{-1} K^{-1}. However, the VACNT/solder contact resistance was large (43 mm^2 K W^{-1}). Tong *et al*. grew a 7-μm thick VACNT array on Si and dry-attached the VACNT/Si to a glass plate. They used a transient phase sensitive photothermal technique to measure the VACNT/glass interfacial resistance to be 11 mm^2 K W^{-1}.[7] Cola *et al*. reported an overall resistance of 16 mm^2 K W^{-1} at 0.241 MPa for a Si/15-μm-VACNT/silver TIM measured by a photoacoustic technique.[226] They fabricated an interface material comprised of a metal foil with CNTs synthesized on both sides of the foil. This fabrication lowered the overall interfacial resistance to less than 10 mm^2 K W^{-1}.[248] Furthermore, they grew VACNTs on Si and Cu substrates and fabricated them to make a two-sided VACNT TIM layer. By this assembly, they reported a minimum resistance of 4 mm^2 K W^{-1}. Hu *et al*. used an IR microscopy technique to measure the thermal resistance of a VACNT-based interface with opposing VACNT arrays,[386] which is essentially the same structure with the two-sided VACNT TIM layer in Cola's work.[248] However, they found a very large thermal resistance across the array-to-array contact interface, ~140 mm^2 K W^{-1}. Panzer *et al*. used a thermoreflectance technique to measure the thermal resistance of a 28-μm-thick surface-metalized VACNT array synthesized on a Si substrate.[384] The overall resistance was 12 mm^2 K W^{-1}, dominated by the contact resistance due to the small fraction of CNTs in the array that is in contact with the mating substrate. Recenlty, Cross *et al*. reported a bonding process between a metallized VACNT film and a metallized substrate; photoacoustic measurement showed a thermal resistance as low as 1.7 mm^2 K W^{-1} for bonded VACNT films of 25-30 μm.[388]

For many of the representative work cited above, there are at least two main issues in common that inhibited real-life applications of the VACNT "TIMs": 1) the thermal contact resistance at the CNT/mating substrate interface is large and dictates the overall thermal resistance of the VACNT TIM,[389] even when a relatively high pressure was imposed; 2) the interfacial adhesion is weak. One possible reason for the large interfacial resistance is that, according to the very recent report by Panzer, the fraction of the CNTs that are physically in contact with the mating substrate is low.[384] More importantly, when heat transfers at the interface between a nanotube and a substrate, the constriction resistance is developed due to the nanometer-scale contact area and enhanced phonon-boundary scattering at the nano-contacts.[245] In the molecular scale or the atomic scale, the CNTs are not in real "contact" with the mating substrate surfaces because there is no chemical bonding or special association, which is also the reason for the weak interfacial adhesion. Thus, a challenge arises as: how can we modify the CNT/mating substrate interface to effectively reduce the thermal contact resistance and simultaneously improve the interfacial adhesion? Intuitively, we may want to "bond" the VACNTs to the mating substrates.

Various VACNT bonding/transfer processes have been developed. Zhu *et al*. proposed a solder transfer methodology for VACNTs (Figure 5.1).[191] The substrates for this process can be Cu or FR-4 boards metallized with Cu. A thin layer of solder paste, *e.g.*, SnPb and SnAgCu, is printed on the substrate surface. After reflow at a proper temperature, the solidified solder layer is polished to ~30-μm thick. The VACNTs on the synthesis substrate are then flipped to the solder coated substrate and reflowed with the assistance of flux to form electrical and mechanical connections (as illustrated in Figure 5.1). This process is straightforward to implement and overcomes the serious obstacles of integrating VACNTs into electronic packaging by offering low process temperatures and improved adhesion of VACNTs to substrates. Kordás *et al*. demonstrated a simple and scalable assembly process similar to the above solder transfer technique to fabricate

VACNT microfins onto the chip for an air cooling system with AuSn.[390] For a 1 mm^2 test chip to reach the same temperature, the applied power can be ~1 W larger when the VACNT sink is implemented than that of the situation with a bare chip. Testing indicated that the CNT fin structure allowed heat dissipation of ~30 and ~100 W cm^{-2} more power at 100 °C from a hot chip for the cases of natural and forced convections, respectively. The cooling performance of the nanotube fin structures combined with their low weight, mechanical robustness, and ease of fabrication make them possible candidates for on-chip thermal management applications. Kim *et al*. used a low temperature ceramic cement to anchor VACNTs on Si substrates with a mild curing temperature.[391] By filling the cement with Au particles, electrical conductance was enhanced, although it was not clearly determined whether the contact between the VACNTs and the Au-filled cement was Ohmic. They also demonstrated the transfer of VACNTs onto Si surface coated with a thin Au layer. The high baking temperature, *e.g.*, 800 °C, however, was not favored by electronic packaging. Sunden *et al*. reported a microwave assisted transfer of VACNTs onto thermoplastic polymer substrates.[392] Jiang *et al*. proposed a low-temperature transfer process using conductive polymer composites.[393] An ohmic contact was formed between a CNT film and a highly conductive polymer composite while a semiconductor joint was formed between a CNT film and a high resistivity polymer composite. Recently, Gan *et al*. reported a large-scale bonding of VACNTs to metal substrates with the assistance of high frequency induction heating. This technique provides a potential approach to reproducible large-scale fabrication of VACNTs for various applications.[394]

However, most of the bonding/transfer processes form “physical contact” at the interface, which means that there is no chemical bonding at the interface. Therefore, thermal conductance across the interface should be low. For example, the interfacial thermal resistance between the VACNT film and the solder layer by the solder bonding

process proposed by Zhu *et al*. is as high as 40 mm2 K W^{-1}.[350] Therefore, we introduce an improved solder bonding process, and a chemical bonding process.

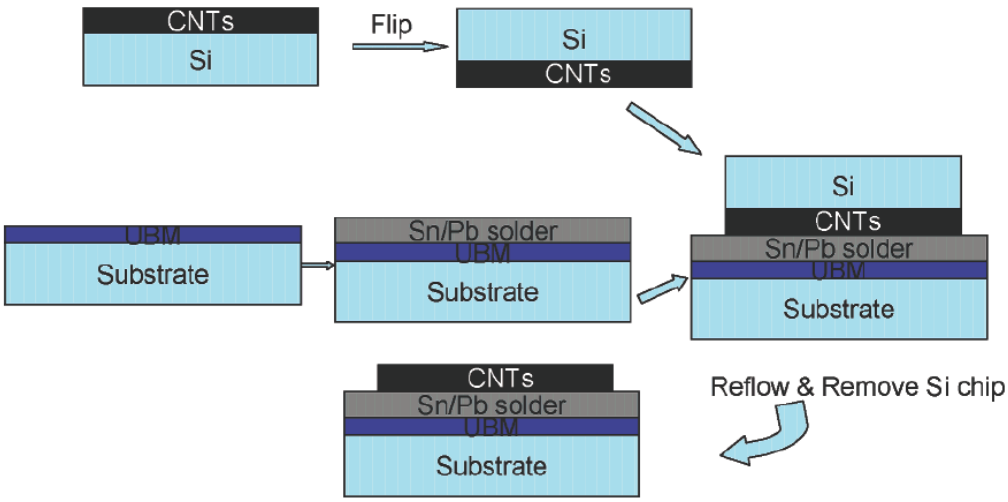

Figure 5.1 Illustration of the solder transfer methodology of VACNTs.[191]

5.2 Bonding Metallized VACNTs to Solder

Before I proceed with this section, I would like to discuss the wetting behavior between molten metals (metal melts) and graphitic carbon materials. In a prior publication, it was stated that "we believe that the open channels of nanotubes assist the adhesion between the nanotubes and the solders because of strong capillary forces that draw the solder inside the CNTs."[191] It was stated that: 1) the top end of the CNT was opended; 2) the opened channel drew the solder inside with the intimate assumption that the open end could be wetted by solder (eutectic SnPb). Since the work was published in 2005, many people have asked us about the wetting between CNTs and solders: can an open-ended CNT be wetted by solders? Let me answer the question from the following four aspects.

First, the CNTs tips might have been opended during the post-synthesis water-vapor etching because we observed the decrease in the VACNT film thickness from both

the top and the bottom sides. A couple of HRTEM images were provided to show the opened ends.[106] However, it should be noted that the growth rate of VACNTs by the water-vapor-assisted TCVD process is very high (discussed in Chapter 2); it is almost impossible to get CNTs shorter than 20 μm. As such, the long CNTs can't be dispersed well without using specific solvents and surfactants. Therefore, there is an extremely low chance to check both ends of a CNT under HRTEM.[395] Gas absorption test may be the best way to verify the opened structure, which, unfortunately, has not been carried out in our group.

Second, even if the top end was opened, it didn't necessarily contact the solder directly—we don't know where the top ends are located. The very top layer of the synthesized VACNTs is very poor in alignment (Figure 5.2c), and the CNTs are highly interwone; in other words, the CNT tips can be facing any direction randomly. In comparison, the bottom ends are very well aligned (Figure 5.2d). In order to further demonstrate the difference in the tip alignment between the bottom and the top sides of the VACNT film, we used e-beam evaporation to deposite an Au\Ni\Ti metallization layer (nominal thickness of 200, 300, and 30 nm for Au, Ni, and Ti, respectively) to the bottom and the top sides of the VACNT film. As shown in Figures 5.2a and b, due to the much better tip alignment of the bottom side of the VACNT film, the actual thickness of the metallization layer on the bottom side is much smaller than that on the top side, although their nominal thicknesses (the amount of the metal deposit) are the same. The difference in the actual thickness of the metallization layer results in completely different wetting behaviors of the CNT surfaces toward water. A thick metallization layer changes the top side of the VACNT film from being superhydrophobic to superhydrophilic due to the dramatically increased surface energy of Au compared to graphitic carbon. In a sharp contrast, the metalized bottom side of the VACNT film retains hydrophobic.

Third, even if the top end was opened, it didn't necessarily possess polar functional groups (namely oxygen-containing functional groups) to increase the surface

energy. In 2008, Kundu *et al*. reported that heating in hydrogen (above 400 ^{o}C) was effective in removing the oxygen-containing functional groups on CNTs.[300] This can be easily understood from our previous discussion on the functionalization process (Section 2.4.3). We compared the FT-IR, Raman, XPS, and contact angle (of water drops) results of the "open-ended" (*i.e.*, with water vapor during TCVD plus 5-min post-growth etching at 750 ^{o}C) VACNT surface and the "close-ended" (*i.e.*, without the post-growth etching) VACNT surface; no difference was found.

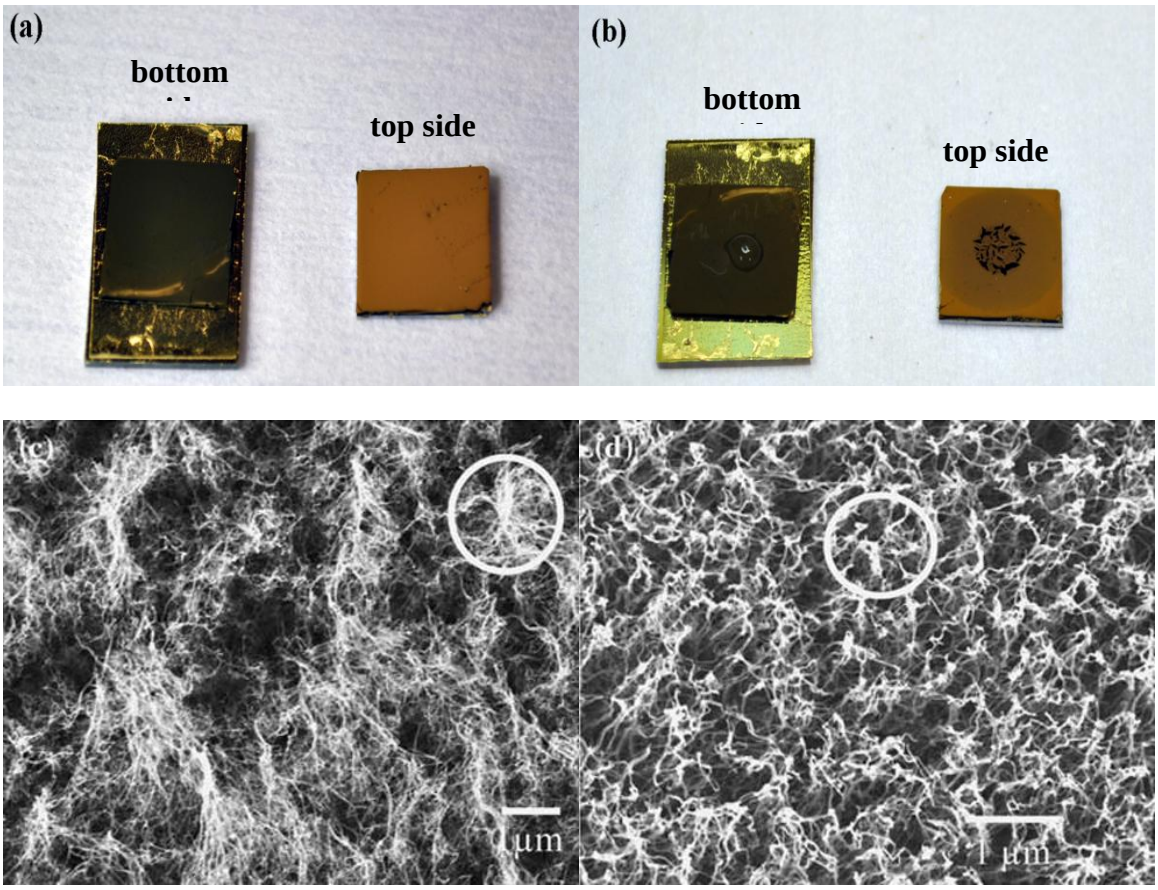

Figure 5.2 Photographs of the metalized bottom and top sides of the synthesized VACNT film (a), and their wetting behavior toward water (b); SEM images of the top (c) and the bottom (d) side of the VACNT film.

Fourth, even if the top end was opened, well-aligned, and properly functionalized, solder do not wet such CNTs. Let us look at the following experiment design (Figure 5.3). The top side of the VACNT film (assuming open-ended) was treated in O_2 plasma (RF power: 50 W; O_2: 60 sccm; CHF_3: 10 sccm; duration: 5 min; pressure: 150 torr). By such a treatment, the I_D/I_G in the Raman spectrum increases from 1.00-1.02 for the control sample surface to 1.51-1.79 for the treated surface. The control sample surface is superhydrophobic (contact angle ~140^o); while the plasma-treated surface is superhydrophilic—during contact angle measurement, the water drop wicked into the plasma-treated VACNT film instantaneously. After the plasma treatement, the top surface was patterned with 20-nm Ti by e-beam evaporation (~8.6×10^{-7} Torr), and then sequentially deposited with multilayered Sn (~1.2×10^{-6} Torr) and Au (~1.5×10^{-7} Torr). The metallized film was reflowed at 300 ^{o}C in vacuum for 10 min, and then cooled down naturally to room temperature. In Figure 5.4, we see that the AuSn dewetted from the surface without the Ti adhesion layer, and merged to the pattern area with the Ti adhesion layer. Apparently, the AuSn doesn't wet the CNTs directly; neither does SnPb in the prior study.

To understand the wetting behavior between solders and CNTs, we have to revisit the references with great cautions in mind. On the basis of surface tension, unless bonding is formed (reaction wetting) or, in some cases, oxygen is involved at the interface, there is no wetting between typical metal melts and graphitic carbon materials,[396-402] because the surface tension of most molten metals are too high relative to a graphitic surface. Dujardin *et al*. found that materials with surface tension larger than 100-200 mN m^{-1} didn't wet CNT surface;[396] in such cases, according to Young-Laplace equation (Eqn. (5.1)), opened CNT channels didn't act as "straws" to suck metal melts into the channels because the contact angle is larger than 90 ^{o}C. Zhang *et al*. studied the wetting of metal NPs on the CNT surface during e-beam evaporation, and found that Ti, Ni and Pd coatings on the CNTs were continuous or quasi-continuous

(indicating relatively good wetting), but Au, Al, and Fe coatings only formed isolated discrete particles on the CNTs.*[402]* Given that Ti, Ni, Pd have strong interaction with graphitic carbon structure,[397,398] their better wettability on the CNT surface is attributed to the low interfacial energy (γ_{sl} in Eqn. (5.2)) resulted from the quasi-bonding between carbon and Ti, Ni, and Pd.

$$\Delta p = \frac{2\gamma_{lv}\cos\theta}{r} \tag{5.1}$$

where Δp is the pressure difference, r the radius of the tube, γ_{lv} the interfacial energy between the liquid and the vapor (in most cases, air), and θ the contact angle between the wall and the liquid, which is determined by Young's equation:

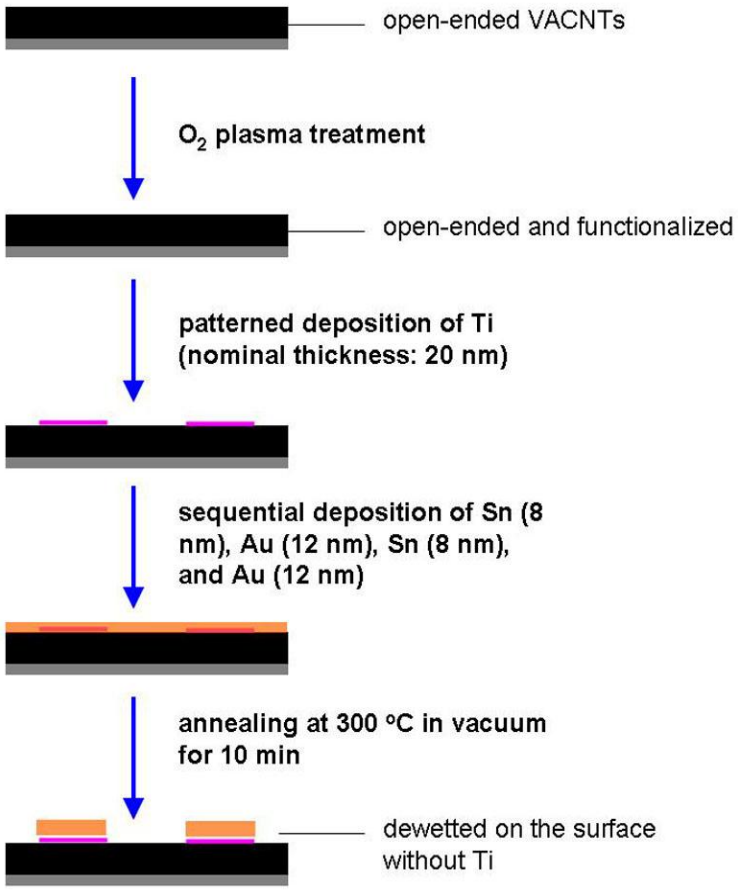

Figure 5.3 Illustration of the experiment design to study the wetting of SnAu solder on the surface of a functionalized VACNT film.

$$\cos\theta = \frac{\gamma_{sv} - \gamma_{sl}}{\gamma_{lv}} \tag{5.2}$$

where γ_{sv} is the interfacial energy between the solid and vapor, γ_{sl} between the liquid and the solid, γ_{lv} between the liquid and the vapor.

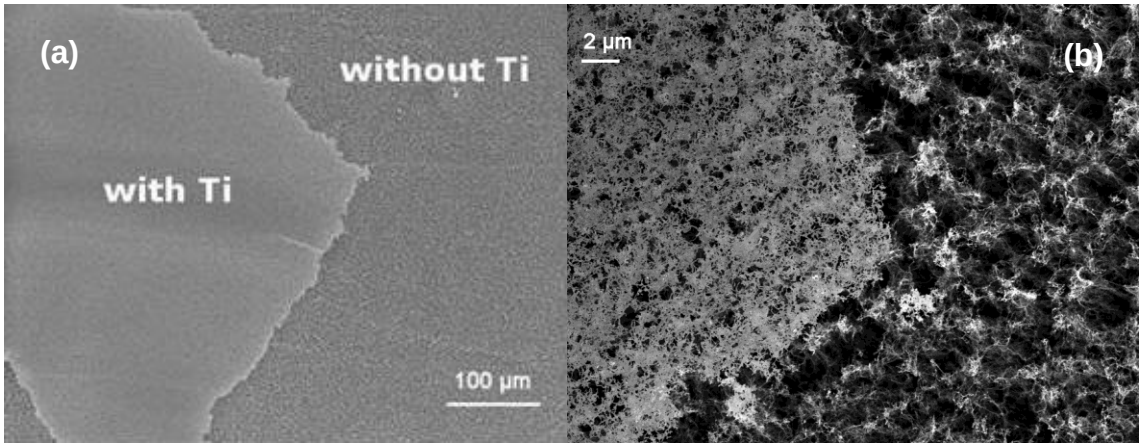

Figure 5.4 Top-view SEM images of the wettability study of SnAu solder on a functionalized VACNT surface.

Although the study by Ajayan and Iijima showing that Pb was able to wick into the open channel of CNTs seems to provide a proof of the aforementioned statement,[403] it actually is on the opposite side. In Ref. 403, it was written: "Lead particles were also often deposited on the closed caps of the tubes. The grid containing the sample was then annealed in an oven in air for about 30 min, keeping the temperature at approximately 400 ^{o}C, which is above the melting point of lead." This at least gives us two pieces of important information.

1) The Pb melt was exposed to air at 400 ^{o}C for 30 min; such conditions mean that the Pb surface was oxidized. According to the calculation by Li *et al.*, when the partial pressure of oxygen is above 10^{-24} atm,[404] Pb is oxidized. This conclusion is further supported in the widely used Ellingham diagram (Figure 5.5): the red dot refers to

the critical point of the oxidation condition of Pb at 400 ^{o}C; by connecting the red dot and the "O" dot at the upper left corner, and then extrapolating the line to cross the line of p_{O2} on the right-hand side, we get the blue dot, the value of which is the critical partial pressure of oxygen to oxidize Pb at 400 ^{o}C. Since the oxide has much lower energy than their parent metal, Dujardin *et al*. believed that it was the oxide or interfacial reaction that realized the wetting between the Pb and the CNT in Ref. 403. Recently, Lim *et al*. studied the wettability of CNTs with In and Sn.[405] They characterized the thin oxide layer between molten tin (and indium) and CNTs, and drew the conclusion that oxides formed during soldering process have played the key role in improving the wetting.

2) In Ref. 403, as described by the author, the closed end of the tube was opended by oxidation in air during the annealing. It should be noted that the CNTs were synthesized by a low-pressure process.[101] The moment when the closed end of the tube was opended, there was instantaneously a very large negative pressure between the inside and the outside of the tube, which undoubtedly assisted the wicking of the Pb melt into the CNT.[396]

Back to the previous work,[191] we recall that flux was used at the interface between SnPb and VACNTs during the reflow process. Flux is basically organic acids, with low surface energy. The flux spreads over the metal surface (solder and pad), and reacts with the surface oxide to form volatile species; as such the fresh metal surface is exposed for joining. Ideally, flux doesn't leave much residue after reflow if the reflow process has been optimized. However, when the feature size shrinks (below 50 μm), flux residue can be easily trapped due to the strong capillary force and the high viscosity of the flux residue. The flux residue has become a well-known critical issue in 3D packaing, which is why fluxless soldering has become unprecedentedly important and intensively studied in industry today.[406,407] I believe it was the flux residue that assisted the bonding of the CNTs to the solder in the prior work (Figure 5.6).

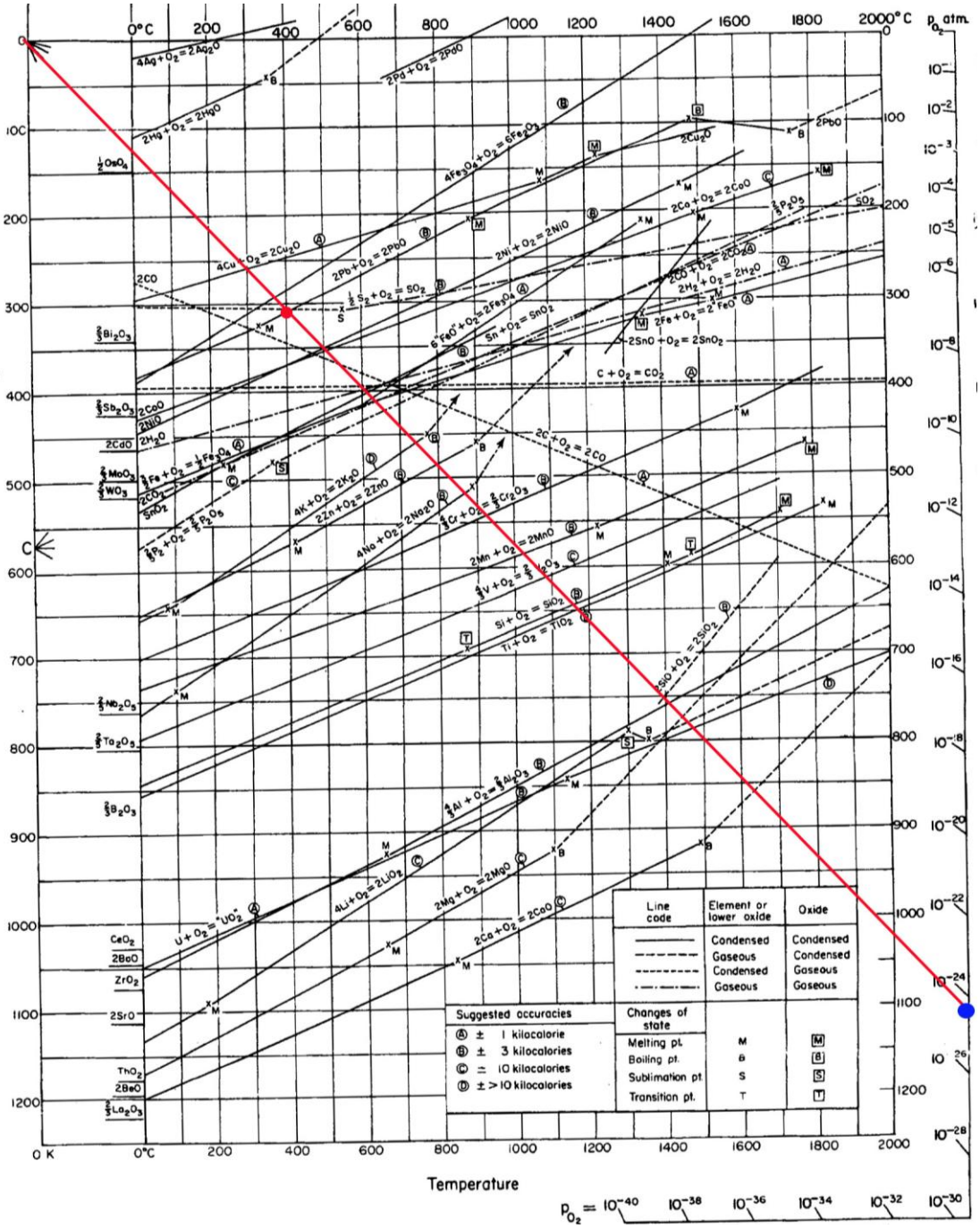

Figure 5.5 Ellingham diagram for the study of oxidation of Pb in Ref. 403.

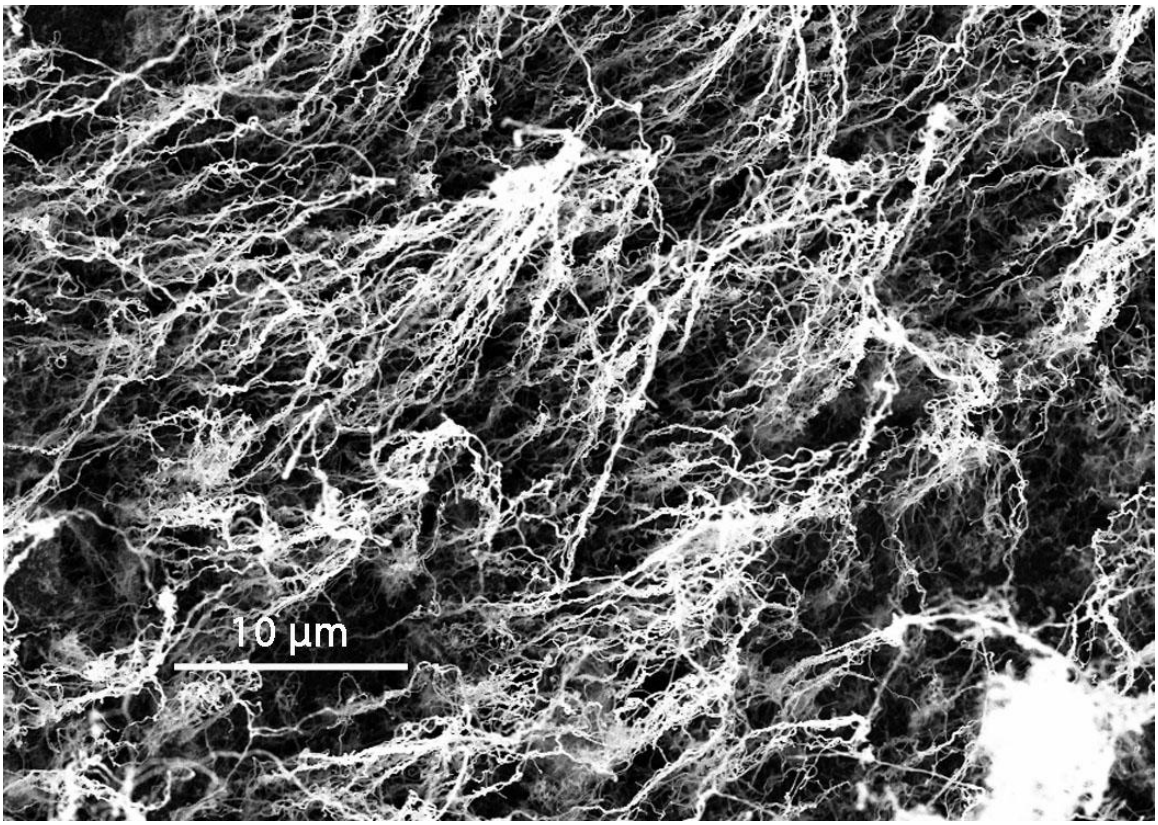

Figure 5.6 A SEM image showing the VACNTs anchored by the flux residue on a solder surface after a reflow process.

From the discussion above (the four aspects provided), I draw the following important conclusions:

1) Common pure metal metals don't wet CNTs, no matter the ends are opened or closed;

2) Although a thin metal oxide layer or flux residue at the interface may improve the bonding between CNTs and solder, the interfacial thermal resistance is high (40 mm^2 $K\ W^{-1}$);

3) An interfacial bonding/adhesion layer is highly important for reliable bonding between solder and CNTs, especially for better thermal transport across the interface.

5.2.1 Bonding VACNTs to BiSn Solder

The sampling process is illustrated in Figure 5.7. A bilayered VACNT film was synthesized, and bonded/transfered to a transfer substrate with a high-termperature adhesive tape. There are two reasons why a bilayered VACNT film was used. First, a single layer of short VACNTs with high quality and good CNT alignment is very difficult to synthesize by the water-vapor-assisted TCVD process. With the help of the first sacrificial layer (the top layer), the second layer can be short and high-quality. Second, the tip alignment on the top side of the first layer, as discussed above, is very poor; while the bottom side acts as the template to guide the tip alignment of the second layer. After the temporary transfer, the bottom of the second layer was exposed, and metallized sequentially with 30-nm Ti, 300-nm Ni, and 200-nm Au (Au\Ni\Ti as under-bump metallization layer for the solder bonding to BiSn) by e-beam evaporation. The same metallization was applied to the bonding substrate unless otherwise mentioned. The as-metallized VACNTs was pressed mildly (5 kPa) against a metallized Si substrate with eutectic BiSn (Bi58Sn42) powder (Indalloy #281, T_m=138 ^oC, Indium, Inc.) in between. No flux was needed for the bonding process. The whole structure was reflowed at 170 ^oC in air for 2 min. After cooling down to room temperature, the two layers were physically separated. The exposed top surface of the second layer was metallized and bonded to a second metallized Si substrate with the same bonding process. The thermal resistance of the TIM structure of 20-μm-BiSn/30-μm-VACNT/20-μm-BiSn (Figure 5.8) is 9-11 mm^2 K W^{-1} (measured by IR imaging technique). Note that the interfacial resistance between the VACNT and the solder in Ref. 350 is 40 mm^2 K/W. Therefore, a dramatic improvement has been achieved by introducing the Au\Ni\Ti metallization layer at the interface.

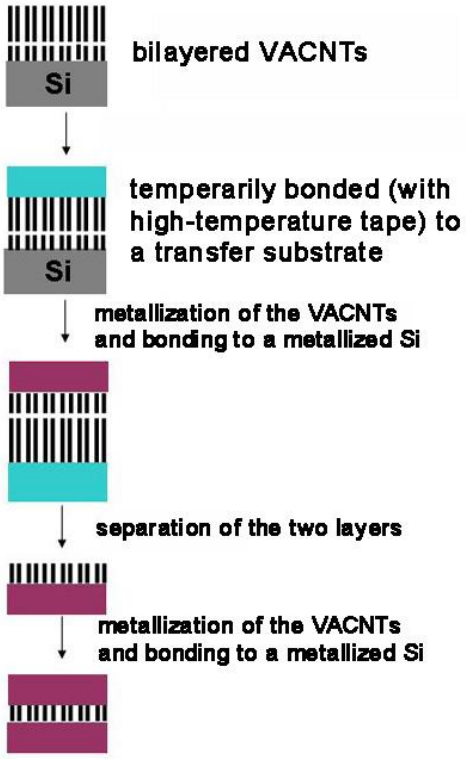

Figure 5.7 Illustration of the modified solder transfer/bonding process of VACNTs.

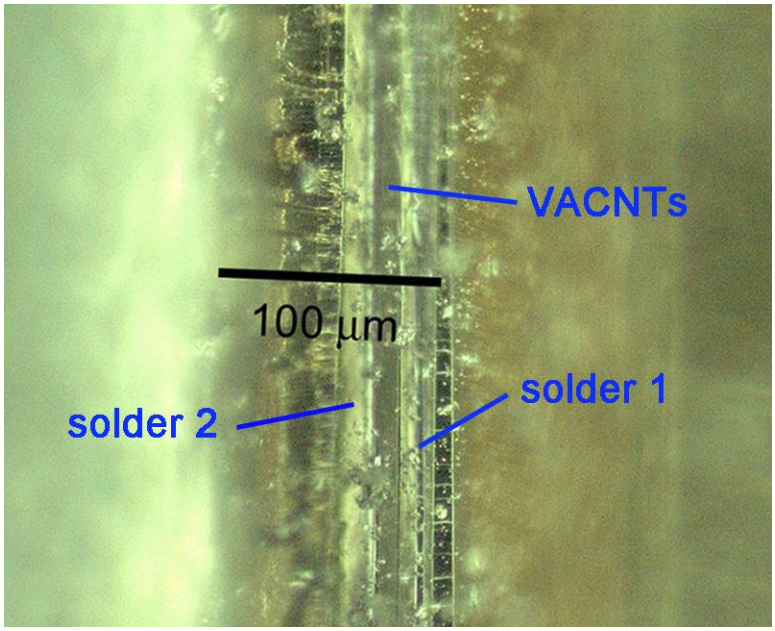

Figure 5.8 A side-view optical microscope image showing the 20-µm-BiSn/30-µm-VACNT/20-µm-BiSn interface.

5.2.2 VACNT/Solder Composite

VACNT/solder composite were prepared following the process illustrated in Figure 5.9. The thermal resistance is <3 mm^2 K W^{-1}.

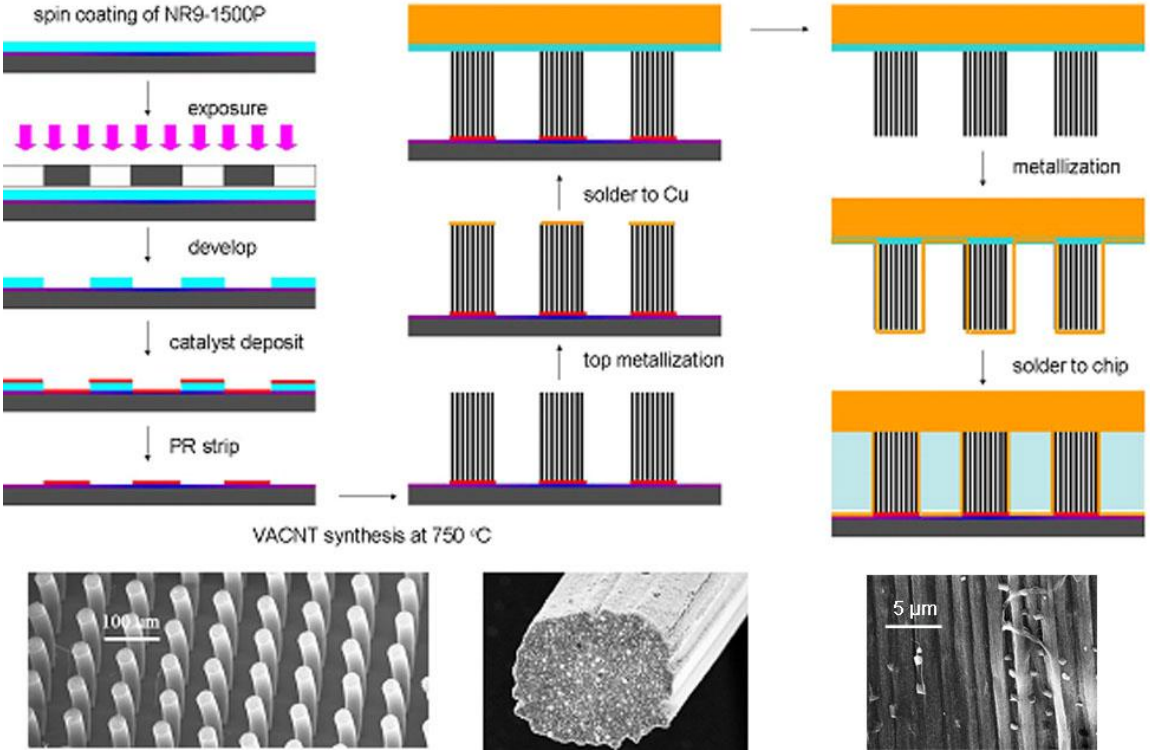

Figure 5.9 Illustration of the preparation of VACNT-BiSn composite. The bottom SEM images are the synthesized VACNT bundles, a metallized VACNT bundle, and the side-view of the prepared VACNT-BiSn composite.

5.3 Bonding VACNTs to an Gold Surface

Chemical bonding of short CNTs to a Si surface has been reported using a solution method, where CNTs were functionalized in acids and then bonded to functionalized Si surface by chemical reactions in a solution.[209,408,409] The process demonstrated the feasibility of forming chemical bonding between functionalized CNTs and a functionalized substrate. However, it has the following disadvantages: 1) The

functionalization process usually truncates the CNTs randomly and introduces high defect density to the lateral walls of the CNTs, which greatly degrades the CNTs; 2) as-assembled CNTs were not well aligned. Here we develop a novel transfer/anchoring /assembling technology to form chemical bonding between VACNTs and Au surface. The chemical assembling is a two-step process: 1) well-aligned CNTs are in situ functionalized (f-ACNTs) during the TCVD growth (discussed in Section 2.4.3); 2) f-ACNTs are then bonded to an Au surface with a self-assembled monolayer as the bridging layer at the interface.

5.3.1 Experimental

The bonding process is illustrated in Figure 5.10. Ti (5-10 nm) and Au (60-100 nm) were sequentially deposited onto a Si wafer by e-beam evaporation. The surfaces were rinsed with ethanol, dried, treated with a UV & ozone Dry Stripper (SAMCO, model: UV-1) at 0.75 L min^{-1} flow rate of the oxygen for 3 minutes, and then immediately put in a 1 mM ethanol solution of 4-mercaptobenzoic acid (MBA) for 24 hours, under a controlled nitrogen environment. After such a treatment, the Au surfaces were rinsed with ethanol to remove the redundant MBA molecules and dried with an Argon flow. The XPS survey shows the existence of the MBA molecules on the Au surface (Figure 5.11). The morphology of pristine Au surface is clearly observed both at 10 kV and 3 kV accelerating voltages (Figures 5.12a and c). In comparison, only a vague image of SAM-Au surface is obtained at 10 kV (Figure 5.12b) due to instability and relatively low electrical conductivity of the SAMs on surface. A dilute solution of $SOCl_2$ (5~10 ppm) in acetonitrile with a trace amount of pyridine (pyridine: $SOCl_2$=1:2 in mole) was used to treat the SAM-modified Au surface, to introduce reactive groups (carbonyl chloride) to the SAM structure on the Au surface. Before the surface was dried, the f-ACNT film was flipped and held onto the as-treated Au surface under a pressure of 10

kPa, and kept at 110 ^{o}C in nitrogen for 4 hours. Then the Si growth substrate was separated from the bonded f-ACNTs, leaving all the f-ACNTs attached to the Au surface.

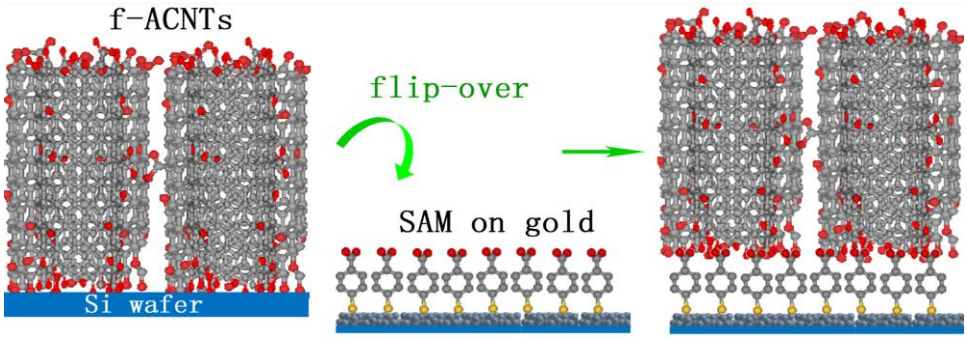

Figure 5.10 Schematic illustration of the chemical transfer process.

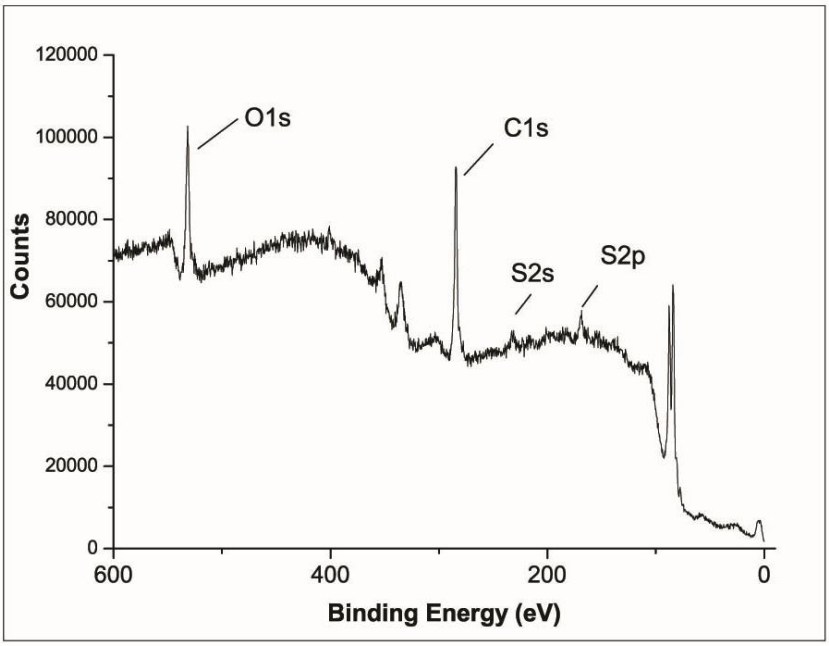

Figure 5.11 XPS spectrum of the SAM/Au surface.

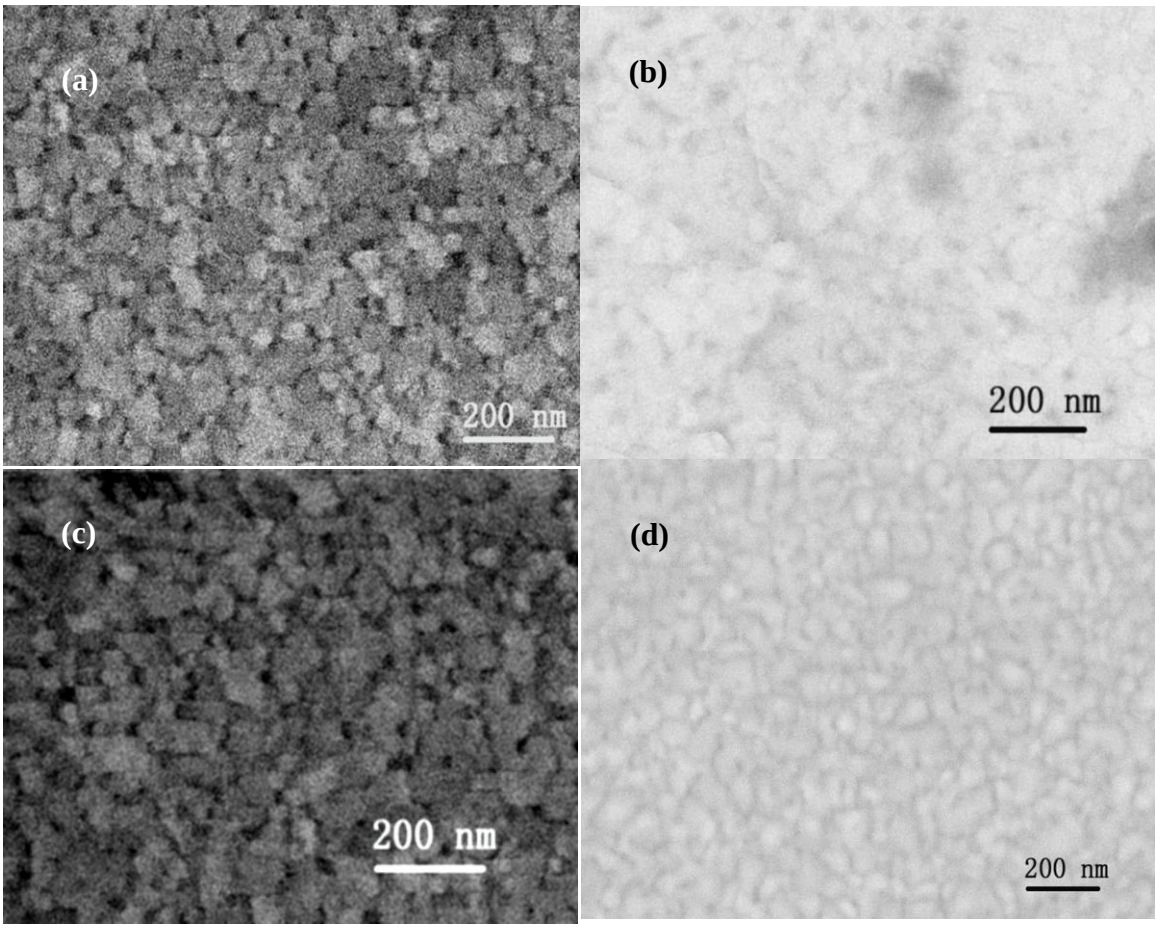

Figure 5.12 SEM images of Au surfaces before and after the SAM treatment. (a) and (c) are the Au surface at 10 and 3 kV EHT (electron high tension), respectively; (b) and (d) are the SAM-treated Au surface at 10 and 3 kV EHT, respectively.

5.3.2 Results and Discussion

The postulated major reaction during the transfer is presented in Figure 5.13. Figure 5.14a shows the chemically transferred VACNT film on the SAM-Au surface. The side-view SEM images of the anchored CNT structure are shown in Figure 5.14b. It can be seen that the aligned structure is well maintained after chemical anchoring (Figures 5.14 b and c). The bent top layer (Figure 5.14b) is due to the pressure upon the CNT film during the anchoring process. After removing the anchored CNTs off the Au surface

using tweezers, we observe that some anchored CNTs remain at the interface (Figure 5.14d). This indicates the chemically bonded interface.

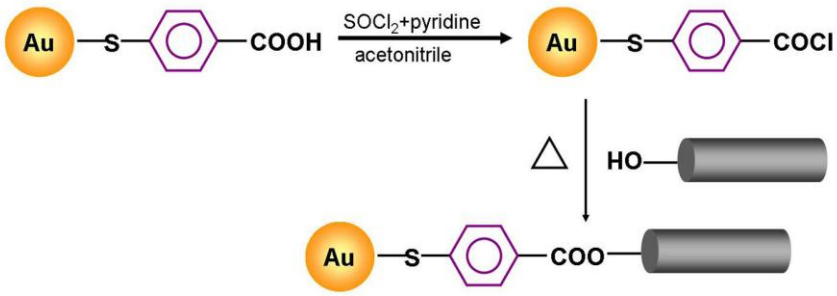

Figure 5.13 Esterification process at the interface between the f-ACNTs and the modified Au surface.

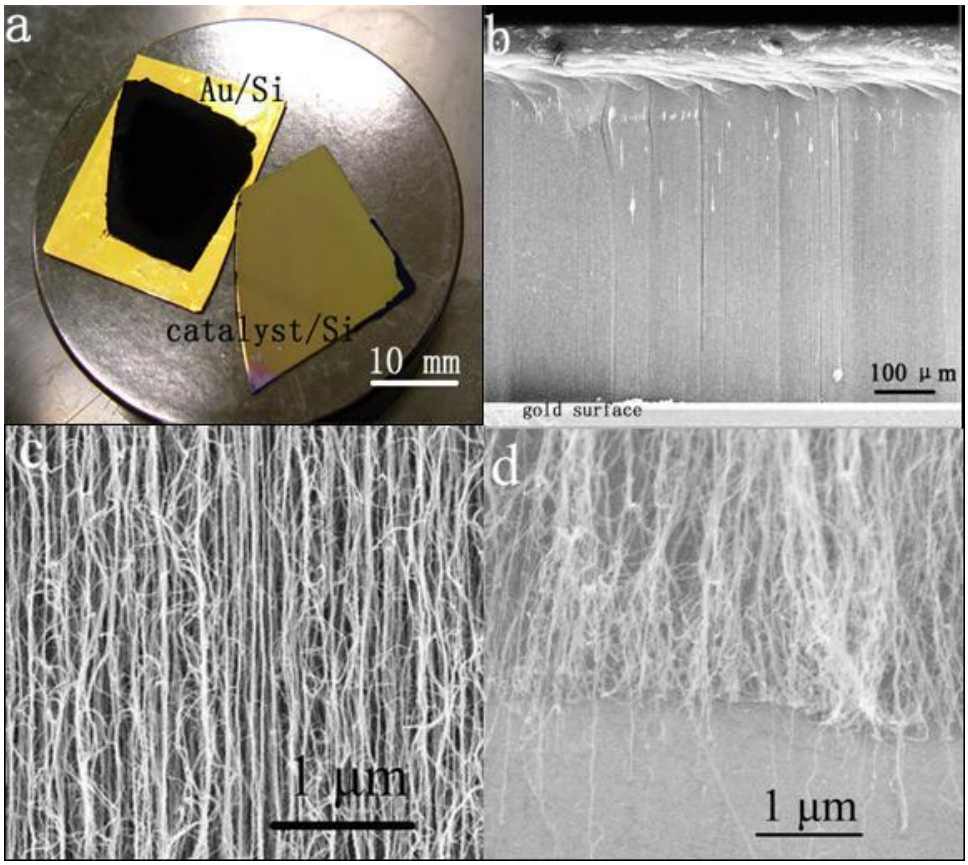

Figure 5.14 A chemically transferred VACNT film on the Au surface: (a) photograph; (b) the side-view SEM image (by 5 kPa of compressive force during transfer); (c) further enlargement of the CNT alignment after chemical transfer; (d) the anchored VACNT/Au interface after part of the transferred VACNTs were removed.

Interfacial strength was tested in Die Shear Equipment (Dage series 4000, 10 kg load cell). For the chemically transferred f-ACNT (~200 μm thick)/Au interface, the shear strength is 3.1-3.8 N cm^{-2}, ~2 times stronger than that of the pristine VACNT/Si interface (1.5-2.1 N cm^{-2}) with VACNT film of the same thickness. When a compressive force (in Instron 5548 Microtester) was applied during the transfer process, the shear strength could reach 30-110 N cm^{-2}, depending on the thickness of the VACNT film and the external compression force. We postulate that the compression force ensures more contact between the VACNTs and the Au surface so that more covalent bonds can be form between the CNTs and the Au surface, as well as stronger van der Waals forces.[107,410] Electrical performance testing of the chemically anchored VACNT films on the Au surfaces, *i.e.*, the current–voltage (I-V) response of the VACNT interconnects, was conducted on A Keithley 2000 multimeter equipped with a four-point probe station (Figure 5.15). The upper Au electrodes (150 nm, diameter: ~2.1 mm) were deposited on top of the VACNT film by e-beam evaporation. The bent top layer ensures the deposited Au doesn't penetrate into the array. The top and the bottom electrodes are connected by the chemically bonded VACNTs. Figure 5.16 shows a typical *I-V* curve of the chemically anchored CNT structure measured at room temperature. The curve is linear, suggesting that the electrical transport and the contacts are Ohmic. From the *I-V* curve, the resistance of a compact CNT bundle with a diameter of 2 mm is 0.020 Ω. The total resistance can be written as $R=R_1+R_2+R_3$, where R_1 is the top Au electrode/CNT junction resistance, R_2 the intrinsic resistance of the CNTs, and R_3 the CNT/SAM-Au surface junction resistance. Due to lack of data of R_1 and R_3, we conservatively estimate the CNT resistivity by neglecting R_1 and R_3. From the length (~730 μm) and area density (300 μm^{-2}) of the CNTs, and the average diameter of CNT (~10 nm, observed and calculated under transmission electron microscope), the resistivity of the individual CNT is estimated to ~2.0×10^{-4} Ω cm. The value is consistent with those reported in literature.[411]

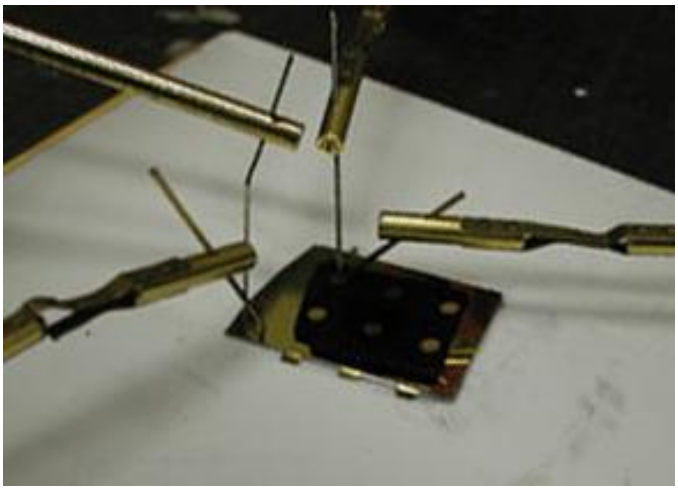

Figure 5.15 A picture of the four-probe station for electrical property testing of the anchored CNT structure.

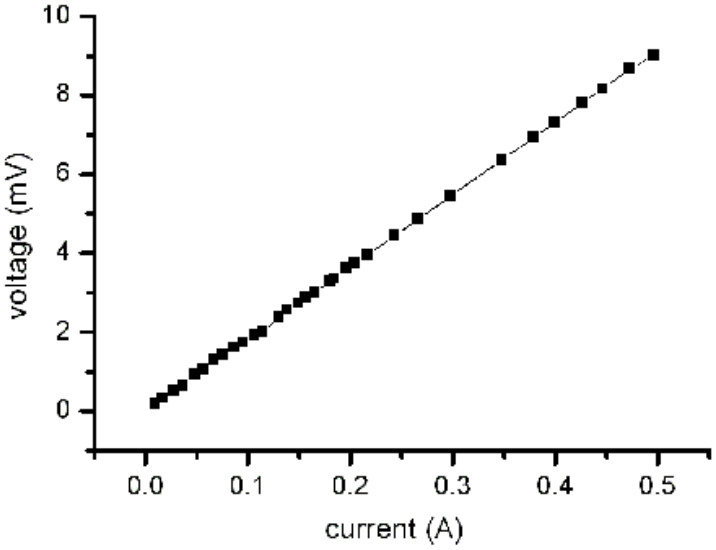

Figure 5.16 *I-V* curve of the chemically transferred CNT structure measured at room temperature.

5.4 Bonding VACNTs to a Silicon Surface

The aforementioned transfer technology has numerous benefits in that it covalently bonds the CNTs to the substrate, minimizes the damage to the CNTs during

the in situ functionalization, can be tailored to attach CNTs to a wide variety of substrates, is carried out at low temperatures and can be easily reworked. Unfortunately, the molecules that bridged CNTs to the Au surface could not survive temperatures higher than 150 ^{o}C, and it cannot be applied to Si or Cu surfaces. Besides, the operation window of the bonding process is fairly narrow—Au can be easily dissolved in the mixture of $SOCl_2$ and pyridine (discussed in Chapter 8) if the concentration is not controlled well.[308] Here we extend the concept of "chemical anchoring" to VACNT TIM assembling by using an inorganic cross-linked molecular phonon coupler (MPC) at the interface to facilitate phonon transport across the CNT/Si interface.

5.4.1 Experimental

In situ functionalized VACNT arrays of ~100-μm thick were synthesized on Cu sheets as discussed in Section 2.5. The TIM assembling process is schematically shown in Figure 5.17. Trimethoxysilane (TMS, 0.4 mL) was added into anhydrous ethanol (2 mL) followed by sequentially adding aqueous solution of hydrogen chloride (0.08 mL, 1 mol L-1) and DI water (0.07 mL). The as-prepared solution was incubated at 45 ^{o}C for 24 hours and then fumed with ammonium vapor (15 wt% ammonium hydroxide) for 5 minutes. The fumed solution was designated as solution A. Solution B was prepared by adding silicon tetrachloride (0.08 mL) and Pt(0)-1,3-divinyl-1,1,3,3-tetramethydisiloxane complex/xylene solution (0.08 mL, 2 wt%) into anhydrous xylene (2 mL). Mating substrates (Si, 1×1 cm^2) were surface-treated using UV & ozone under a 0.75 L min^{-1} flow rate of O_2 for 20 minutes). Solutions A and B were sequentially spin-coated onto the Si substrates at an angular speed of 1000 rad min^{-1} for 5 seconds and 800 rad min^{-1} for 5 seconds, respectively. Then VACNT/Cu was immediately flipped onto the mating substrate under a certain pressure (0.5-1.0 MPa). The obtained assembly was treated in the VFM chamber at 100 ^{o}C for 60 min plus at 160 ^{o}C for 30 min. The chemicals were all purchased from Sigma-Aldrich, unless otherwise mentioned.

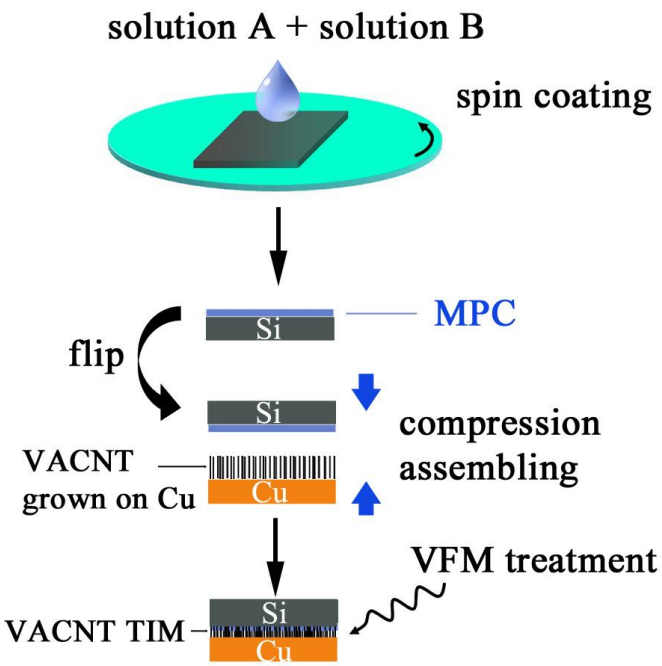

Figure 5.17 Schematic illustration of the Si/VACNT TIM/Cu assembling process.

To prove the feasibility of the hydrosilylation of the CNTs, TMS was added into the solution B (without silicon tetrachloride) and then spin-coated onto a single-sided polished Si substrate. A 100-um-thick VACNT carpet was pressed onto the as-coated Si surface and then kept at 100 ^{o}C for 60 min plus at 160 ^{o}C for 30 min in the VFM chamber with a dried nitrogen protection. After the hydrosilylation reaction, the CNTs were scratched off the Si surface, dispersed in anhydrous xylene, washed thoroughly with anhydrous xylene and dried in vacuum (~5 kPa, in a nitrogen atmosphere). The obtained products were TMS-CNT adducts.

FT-IR characterizations were performed at ambient temperature at a resolution of 2 cm^{-1}. Solution samples were spin-coated onto double-sided polished Si substrates and dried in nitrogen at room temperature to evaporate the solvents (drying of the coatings was avoided during the aforementioned TIM assembling process). 64 scans of each specimen were collected. The TMS-CNT adducts were mixed with dried KBr power and

pressed into pellets. 256 scans were collected. The thermal diffusivities of the TIM assemblies (trilayer structure, Type IV sample in Chapter 4) were measured with LFA, with no pressure imposed during measurement.

5.4.2. Results and Discussion

A thin layer of MPC was formed on a Si surface by sequential spin-coating of solution A and B. Solution A undergoes reactions analogous to those involved in a typical silica sol-gel process. The coating of pure trimethoxysilane (TMS) is rather stable, its FT-IR spectrum being shown in Figure 5.18 (spectrum a). The C-H stretching modes show up at ~2956 and 2846 cm^{-1} and display nearly no changes at elevated temperatures. The vibration mode at ~2235 cm^{-1} is attributed to Si-H groups in TMS. Spectrum b in Figure 5.18 is the spectrum of a coating of acid-treated TMS/ethanol solution, *i.e.*, solution A before fumed in ammonium vapor. The reduction in the vibration intensity ratio of the C-H groups to the Si-H groups in spectrum b, compared with spectrum a, provides evidence of consumption of the methoxy groups. The distinct shift of the main Si-H maximum from 2235 cm^{-1} in spectrum a to 2249 cm^{-1} in spectrum b indicates the loss of neighboring methoxy groups at the Si atoms and the synthesis of silane molecules, in other words, sol formation.[412] In the coating of solution A (spectrum c), the shift of the main Si-H maximum to 2254 cm^{-1}, the elimination of the C-H stretching, the appearance of a very broad band (3530-3300 cm^{-1}) due to silanol groups and a distinct split in the 1200-1000 cm^{-1} range due to Si-O stretching modes, indicate the start of formation of a cross-linked network. The vibration modes at 3057 cm^{-1} and 3157 cm^{-1} are likely due to nitrogen related intermediates.[413] After heat treatment in VFM, disappearance of the nitrogen related intermediates, reduction in the silanol stretching intensity (3530-3300 cm^{-1}) and a further split in the 1200-1000 cm^{-1} range are observed in spectrum d and are considered proofs of the network formation.

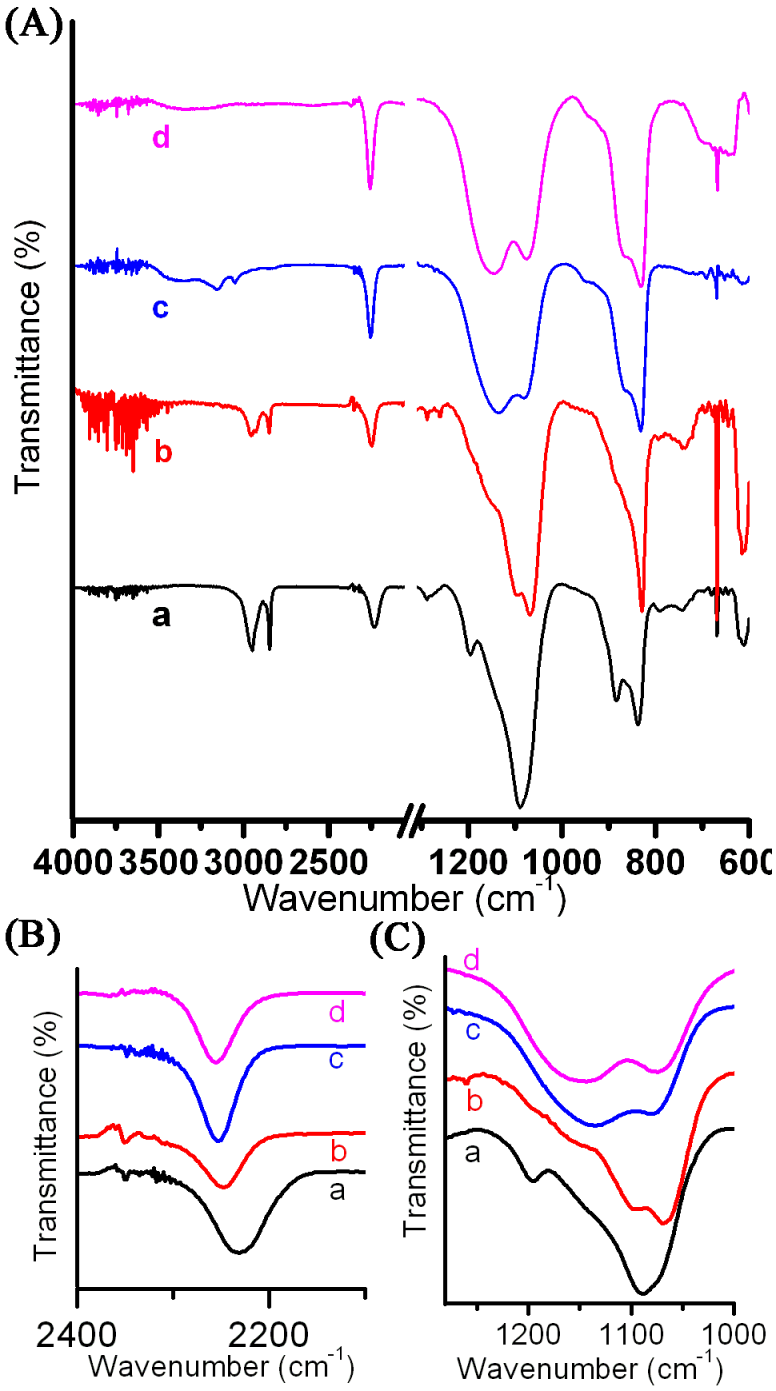

Figure 5.18 (A): FT-IR transmittance spectra of a pure TMS coating (spectrum a), a coating of solution A before fuming in ammonium (spectrum b), a coating of solution A (spectrum c), and a VFM-treated coating of solution A (spectrum d). (B), (C): enlargement of selected regions in panel (A). Spectra are shifted vertically for clarity.

The main purpose of spin-coating of solution B right after the solution A is to bond the Si-H groups to the f-ACNT surfaces by hydrosilylation reactions, in the presence of the Pt catalyst.[414] Silicon tetrachloride ($SiCl_4$) in solution B plays three significant roles in the TIM assembling. First, $SiCl_4$ is extremely sensitive to moisture; its presence protects the hydrosilylation reactions from being affected by moisture. Second, $SiCl_4$ assists the chemical bonding of the MPC to the CNT surfaces via chemical reactions of silanol groups with the surface carboxylic acid groups and hydroxyl groups on the in situ functionalized CNTs.[415,416] Third, the small $SiCl_4$ molecules easily densify the MPC layer after the weakly cross-linked network was formed in the coating of the solution A, by reactions of the highly-reactive Si-Cl groups with the remaining silanol groups.

Si-H addition to SWNTs has been investigated theoretically and experimentally.[414,417,418] It was found that the hydrosilylation was not spatially limited to the CNT ends or its defective sites. It was hypothesized that relief of the torsion strain in the small-diameter SWNTs facilitated the hydrosilylation reaction. It was also thought that larger-diameter tubes would be less reactive due to a smaller degree of π-orbital misalignment and pyramidalization.[414,419] Hence, the feasibility of hydrosilylation of large-diameter MWNTs seemed questionable. In this study, this feasibility has been proved; the hydrosilylation reaction is the right foundation of the proposed MPC-assisted TIM assembly. FT-IR spectrum of the TMS-CNT adducts in Figure 5.19 shows the presence of strong C-H stretching at 2962 and 2877 cm^{-1} due to the existence of methyl groups. This indicates the addition of TMS to the CNT surface via a hydrosilylation reaction. A further evidence for the hydrosilylation of CNTs with TMS is the distinct Si-C stretch signal at ~ 1261 cm^{-1}.[414] The hydrosilylation is also evidenced by the presence of C-H stretching from methyne groups (RCH=R')) at ~2905 cm^{-1}. The strong and wide band at 970-1240 cm^{-1} probably consists of C-O stretching, C-O-C stretching and Si-O in-plane vibration.[308,420]

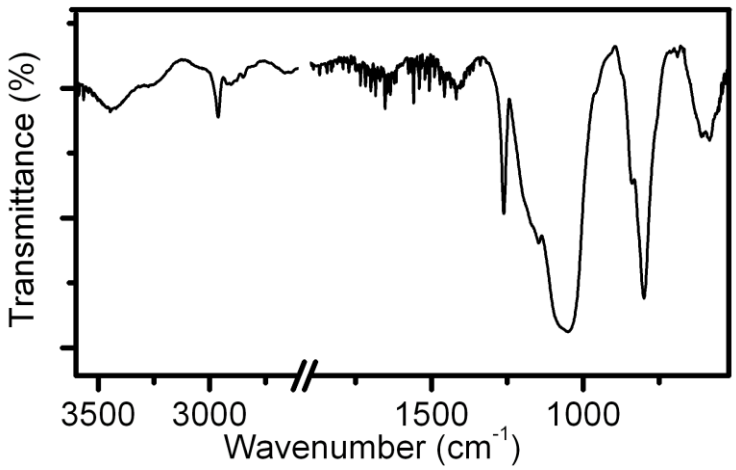

Figure 5.19 FT-IR transmittance spectrum of TMS-CNT adducts.

Upon spin-coated, the Si substrate was flipped immediately onto the VACNT synthesized on Cu accompanied by a proper compression force. Chemical reactions at the interfaces proceed in the VFM chamber. Microwave-assisted heating was employed because microwave selectively heats up the Si substrate, the CNTs and the chemicals at the interfaces. In fact, microwave radiation has attracted much interest in synthetic organic chemistry due to its special role in dramatically increasing reaction rates and the capability of inducing chemical reactions which cannot proceed by thermal heating alone. It is postulated that during the VFM treatment, chemical bonding formed between the CNTs and the mating substrate, with the MPC as the bridging agents in between.

In order to have a better observation of the status at the chemically bonded interface, we bonded a VACNT carpet to a MPC-modified Si substrate without any compression force during the assembling, removed the synthesis substrate and then peeled part of the bonded VACNTs off the mating substrate. SEM images of the as-prepared interface are shown in Figures 5.20a-c. The roots of the VACNTs anchored by the MPC at the Si surface are clearly exposed after the upper parts of the VACNTs are removed. The interfacial strength of the assembly (tested on a die shear tester) was 0.23-0.36 MPa, much stronger than the van der Waals force dominated adhesion (<0.05 MPa)

for the pressure contact assemblies (defined below). The Si surface after the die shear test is shown in Figure 5.20d.

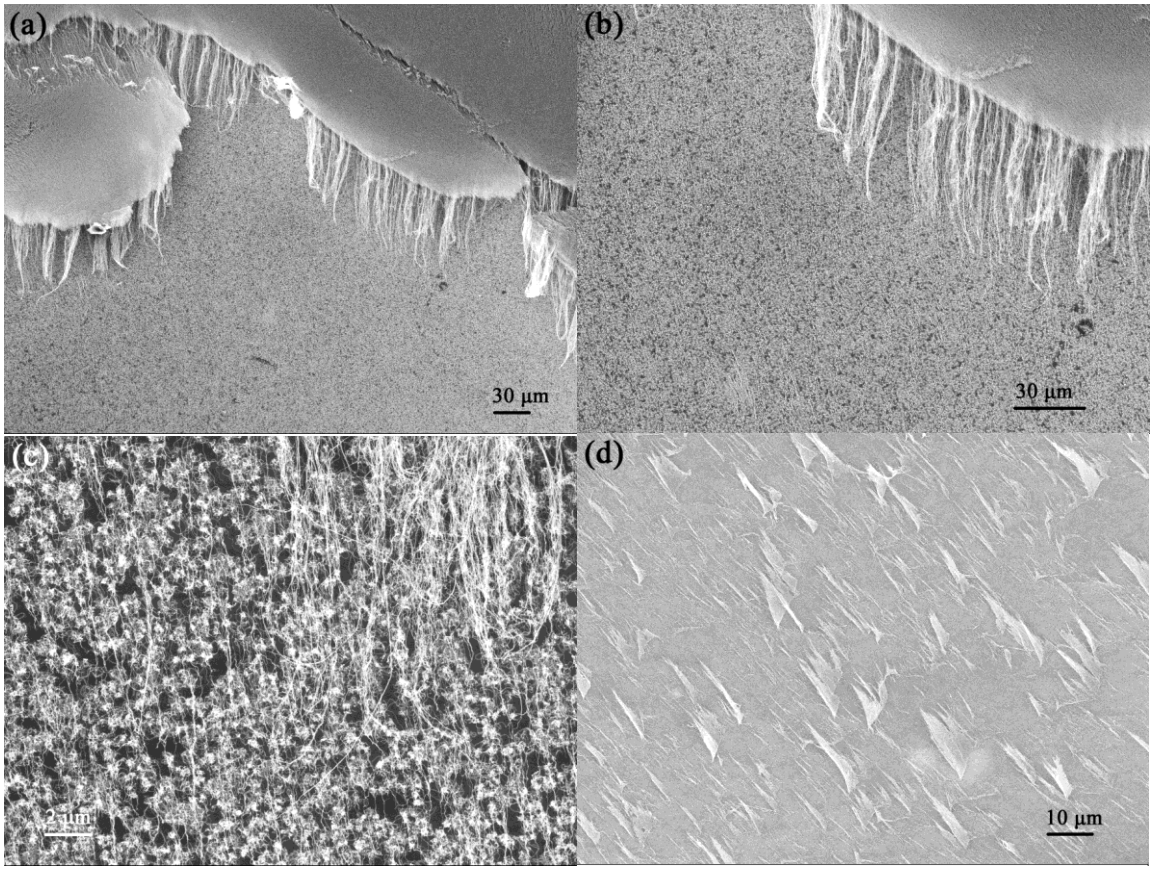

Figure 5.20 SEM images of MPC-anchored VACNTs at a Si surface (a-c) and surface status of the Si mating substrate of a MPC contact assembly after a die shear test (d).

The as-described VACNT TIM assembly is referred as the "MPC contact" assembly in the discussions on TIM properties below. We also measured the properties of "loose contact" assemblies and "pressure contact" assemblies. For the "loose contact" assembly, a Si substrate was placed on top of VACNT/Cu without pressure during assembling or thermal measurements. The "pressure contact" assembly was obtained by compressing a Si substrate (~0.4 MPa) to VACNT/Cu as in a MPC contact assembly,

however, without MPC modifications at the contact interface. The pressure contact assembly was considered almost the same as those that have been reported in the aforementioned literature papers so far.[7,226] A trilayer model was chosen to numerically fit (with energy loss) the data collected on laser flash equipment. The fitting, with an uncertainty of ~5%, gives an equivalent thermal diffusivity (α_{TIM}) of the TIM layer, in which the CNT/Si interface, the CNT/Cu interface and the intrinsic volumetric VACNT array are grouped. Figure 5.21 shows the measured α_{TIM} values of the loose contact, the pressure contact and the MPC contact assemblies. α_{TIM} of the loose contact assembly is small, ~0.461±0.112 $mm^2\ s^{-1}$, due to the strong phonon scattering at the sharp and weak CNT/Si interface. The interface modification by MPC improves α_{TIM} by an order of magnitude to ~5.292±0.953 $mm^2\ s^{-1}$. In comparison, α_{TIM} of the pressure contact assembly shows only limited improvement. Purely imposing pressures during the VACNT TIM assembly or thermal measurement increases the fraction of CNTs in "contact" with the mating substrate. However, these "contacts" are not permanent contacts or bonding in the molecular scale; the separated distance between the CNTs and the substrate surface is in the nanoscale—the regime where van der Waals forces (attractive forces) dominate. Although it is not recommended that a comparison be made directly among the results measured by different approaches, it is reasonable to believe that the pressure contact assembly in our study is equivalent to many of the aforementioned references because the intrinsic thermal conductivity of the VACNT array and the interface at CNT/substrate upon pressures are more or less the same. In this sense, the MPC contact assembly is effective in reducing the interfacial thermal resistance.

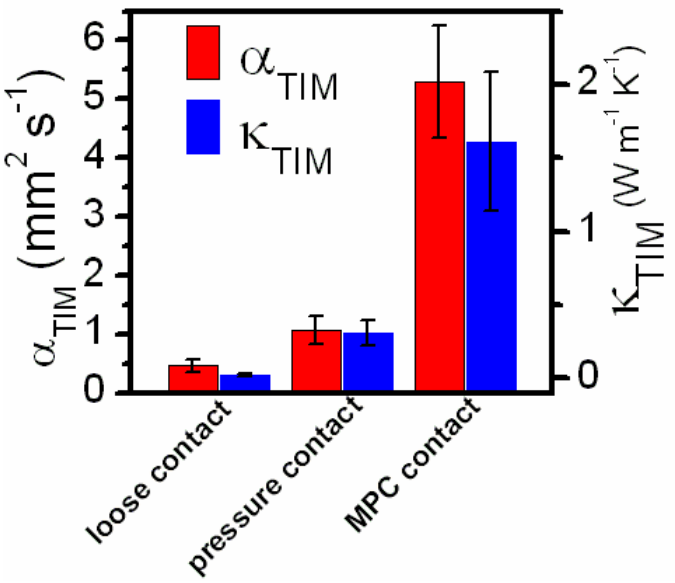

Figure 5.21 A comparison of the equivalent thermal diffusivities (α_{TIM}) and the equivalent thermal conductivities (κ_{TIM}) among the loose contact, the pressure contact and the MPC contact VACNT TIM assemblies.

In literature,[7,8,226,350] we note that the equivalent thermal conductivities of the VACNT TIM (κ_{TIM}, calculated as: $\kappa_{TIM}=l/R_{TIM}$, where l and R_{TIM} are the bond line thickness and the thermal resistance of the TIM, respectively) are smaller than 1 W m^{-1} K^{-1}. It does no harm to calculate κ_{TIM} values for our TIM assemblies according to the equation: $\kappa_{TIM}=\alpha_{TIM}\times\rho\times c_p$, where ρ and c_p are the measured mass density and the heat capacity, respectively, of the TIM layer in the assembly. The measured densities of the loose contact VACNT TIM, the pressure contact TIM and the MPC contact TIM are 0.073±0.009, 0.435±0.065 and 0.461±0.106 g cm^{-3}, respectively. These values are consistent with the theoretical estimations based on the CNT diameter and the surface coverage on the synthesis substrate. c_p of 0.66 J g^{-1} K^{-1} is used.[98] The calculation results in Figure 5.21 show a dramatic improvement in the equivalent thermal conductivity of the VACNT TIM by MPC contact assembling (1.61±0.47 W m^{-1} K^{-1}), compared with the poor conductivity of the loose contact (0.02±0.006 W m^{-1} K^{-1}) and the pressure contact (0.306±0.084 W m^{-1} K^{-1}) assemblies. The overall equivalent thermal

resistance of the MPC contact VACNT TIM is, hence, ~10 mm^2 K W^{-1}. The uncertainty of κ_{TIM} has been estimated using a standard error estimation approach:

$$\frac{\delta_{\kappa_{TIM}}}{\kappa_{TIM}} = \left[\left(\frac{\delta_{\alpha_{TIM}}}{\alpha_{TIM}} \right)^2 + \left(\frac{\delta_{\rho}}{\rho} \right)^2 \right]^{0.5} \tag{5.3}$$

CHAPTER 6

CARBON NANOTUBE/POLYMER COMPOSITES

One of the most important applications proposed for CNT/polymer composites is as TIMs with enhanced thermal conductivity and, equally importantly, reduced coefficient of thermal expansion (CTE). CNT is expected to be able to dramatically enhance the thermal conductivity of polymer composites, however, with only unsatisfactory improvement.[253,421-428] Researchers have been trying to understand such a phenomenon.[426,429-436] One important factor is structural defects in CNTs that act as scattering centers for phonons. The structural defects can come from the synthesis process, functionalization process, and dispersion process. A second factor is CNT-CNT coupling in the composite because it is impossible to have a good dispersion of CNTs without bundling them when the CNT loading is relatively high in the polymer matrix. Another widely accepted explanation is the large interfacial thermal resistance across the CNT-polymer interface. In this chapter, we focus on the interfacial effect. In Section 6.1, we study the thermal transport propery of VACNT/EP composite. By using a combined process of in situ functionalization and microwave treatment, we improve the interfacial bonding between the CNTs and the EP matrix. As such, the interfacial thermal transport between the CNTs and the EP matrix has been effectively improved. Mechanical properties of the composite have also been enhanced. We report a strong anisotropy in CTE of VACNT/EP composites and achieve an ultra-small CTE in the CNT-aligned direction by enhancing the VACNT/EP interface. In Section 6.2, the interfacial resistance between nanographite and EP is studied; from the modeling results based on effective medium theory, it is found that the interfacial thermal resistance between nanographite and EP is about one order of magnitude lower than that between CNTs and EP.

6.1 Microwave Treatment to Enhance CNT-Polymer Interface in VACNT/EP Composite

Thermal resistance at an interface—Kapitza resistance, R_K, represents a barrier to heat flow associated with the differences in phonon spectra of two phases in contact. For high structural mismatch and weak contact at an interface, R_K is large.

In thermal transport, R_K is defined by:

$$R_K = \frac{a_K}{K_m} = \frac{1}{\Lambda} \tag{6.1}$$

$$J_Q = \Lambda \Delta T \tag{6.2}$$

where J_Q, Λ, R_K, K_m, a_K and ΔT are heat flux, interfacial thermal conductance, interfacial thermal resistance, thermal conductivity of the matrix, Kapitza radius and temperature drop across the interface, respectively.

In a CNT/polymer composite system, the R_K plays a much more important role than in common composites with micro-sized fillers, not only because the interface phase accounts for as high as 15 vol% but also because the a_K is around 5-20 nm, comparable to or even larger than the tube diameter.[437,438] Experimental measurements show that the R_K in a CNT suspension is around 8×10^{-8} m^2 K W^{-1};[438] this value is of the same order of magnitude as those in other composite materials.[437] Such a large R_K arises from the weak coupling between the rigid tube structure and the soft polymer matrix.[431] For a CNT, there are four acoustic modes: a longitudinal mode, corresponding to motion of atoms along the tube axis; a twist mode, corresponding to torsion around the tube axis; two degenerate transverse modes—bending and squeezing modes, corresponding to atomic displacements perpendicular to the nanotube axis. The longitudinal and twisting modes involve only the movement of carbon atoms tangential to the tube surface and thus are expected to couple very weakly to the soft material around the tube, while the bending and squeezing modes involve out-of-plane motion and thus are more strongly coupled with the soft material around. Due to the weak coupling, sharp

contrast in the phonon spectra at the interface between the CNTs and an amorphous polymer matrix leads to strong backscattering of thermal energy waves at the interface.

Based on this theory, an effective approach to reducing R_K is to provide a stronger coupling between CNTs and a polymer matrix by covalent bonding. Therefore, proper surface functionalization of CNTs should help improve the interaction between the CNT fillers and the polymer matrix and consequently result in a significant increase in the interfacial thermal conductance,[432] as shown in Figure 6.1a. Atomistic-based modeling was conducted to calculate the R_K and found that grafting organic chains or polymer chains to the surface of CNTs with covalent chemical bonds increases the conductance across the interface.[433] R_K was found to be a function of several parameters, *e.g.*, grafting density and length of the linear chain covalently bonded to the CNT surface. Increasing chain length and grafting density lower the interfacial thermal resistance, as shown in Figure 6.1b. Some modeling and experiment have been performed to examine the conclusions.[426,434] However, conventionally, length and diameter of functionalized CNTs are not experimentally controllable. The difficulty in evaluation of dispersion and distribution is an extra issue. These problems become barriers for understanding the thermal transport in CNT/polymer systems, especially the R_K. Evaluation of the effects of surface functionalization on the R_K and, consequently on the overall effective thermal conductivity of the composite, should exclude the influence brought about by the uncontrollable length and diameter of CNTs. Therefore, in our study, we focus on VACNT/polymer composite by an infiltration process, to ensure controllable tube diameter, density, length, and dispersion/distribution in the polymer matrix. As such, the interfacial effect can be singled out. A challenge arises though: how can we functionalize the CNT surface in a VACNT film. Conventionally, people use a wet chemical method to functionalize CNT surface to increase interfacial bonding between the CNTs and the polymer matrix.[439] However, the CNT alignment gets destroyed and the surface of the CNT gets damaged. A novel approach is necessary to

enhance the VACNT-polymer interface. Appropriately, the combined process of VACNT in situ functionalization and microwave curing helps to improve VACNT-EP interfaces while maintain the well-aligned structure.

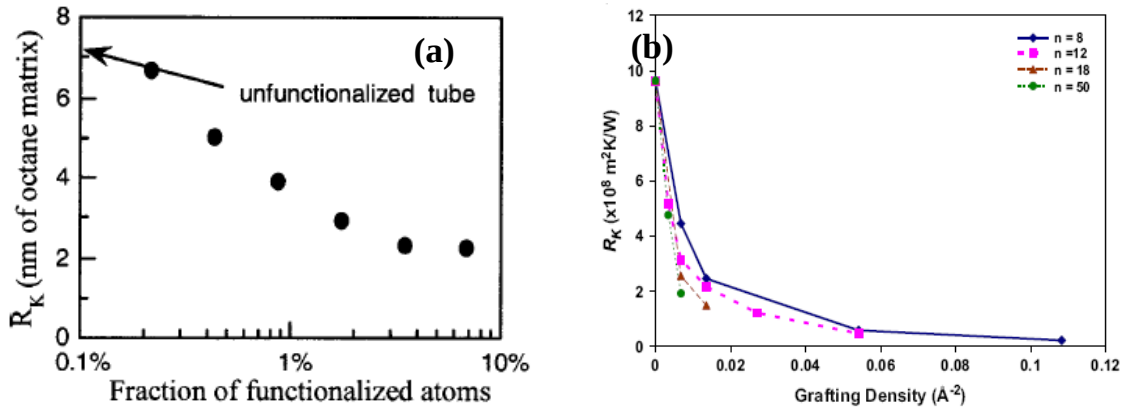

Figure 6.1 Effects of surface functionalization (a) and grafting density of organic chains (b) on the interfacial thermal resistance of CNT/polymer matrix.[433]

6.1.1 Experimental

VACNT arrays of 2-3-mm thick were synthesized as described before. The VACNT arrays were flipped onto polyimide double-sided tapes and then infiltrated with EP to prepare a VACNT/EP composite, followed by degassing under a vacuum for 40 minutes. Samples were cured thermally in a common convection oven at 155 °C for 40 minutes, or in the VFM chamber at the same set temperature. The thermal cured composite is designated as TCOM from here after, and the composite by the VFM-assisted curing as MCOM. After furnace cooling, the VACNT/EP samples were peeled off the double-sided tapes and polished to be double-sided parallel, flat and smooth and cut into pieces for specific measurements. The samples maintain vertical alignment of CNTs in the EP matrix (Figure 6.2). The EP used is bisphenol-F (EPON862), with 4-methylhexahydrophthalic anhydride and 1-cyanoethyl-2-ethyl-4-methylimidazole as the curing agent and catalyst, respectively.

CTE was measured on a thermal mechanical analyzer (TMA, TA Instruments Model 2940), at a heating rate of 5 ^{o}C min^{-1}. When measuring the through-thickness CTE (along the CNT-aligned direction), we used the bulk mode fixture and specimens of ~1-mm thick. The quartz probe was seated normal to the specimen top surface. Two different modes were used for measuring the in-plane CTE. The film mode fixture was used for thin specimens. The bulk mode fixture was used for thick specimens, where the quartz probe was seated normal to the side of the specimen, *i.e.*, normal to the CNT orientation. Storage modulus and tanδ were measured on a dynamical mechanical analyzer (DMA, TA Instruments Model 2940), at a heating rate of 5 ^{o}C min^{-1}. The single-cantilever mode was used, with the CNTs in the specimen oriented vertically, *i.e.*, along the vibration direction. A constant frequency of 10 Hz and amplitude of 10 μm was adopted. At least 5 measurements were recorded to obtain the average values in Table 6.1 and Table 6.2. Effective thermal conductivities were obtained by measuring thermal diffusivities with a LFA447, mass densities and specific heat on a differential scanning calorimeter (DSC, TA Instruments Model 2940).

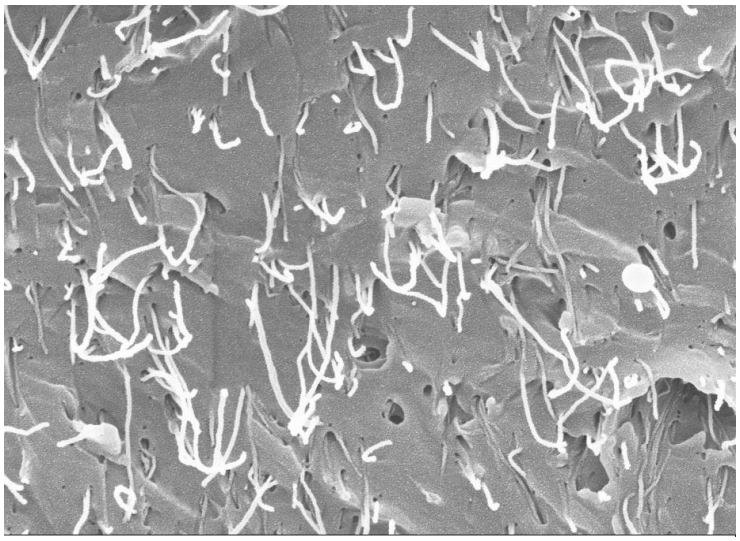

Figure 6.2 A top-view SEM image of the VACNT/EP composite.

6.1.2 Results and Discussion

6.1.2.1 Interface Enhancement

DMA measurement results for TCOM, MCOM, thermally cured EP (TEP) and microwave-assisted-cured EP (MEP) are shown in Figure 6.3 and Table 6.1. No apparent difference in glass transition temperature (T_g) and storage modulus (G') was observed between TEP and MEP, which excludes unexpected influences by the microwave radiation on the pure EP itself. The distinct differences in T_g and G' between the TCOM and the MCOM give us a hint on the enhanced CNT-EP interface in the MCOM. We note the 6 °C increase in T_g and the great enhancement in G' by the VFM treatment, compared to the pure EP and TCOM. It seems that microwave treatment plays a key role in obtaining such an ultra-low α_N of the MCOM above the T_g. During curing, microwave selectively heats up the CNTs and the polymer at the interfaces.[440] Equally important is the fast coupling between the VACNTs, functionalized sites on the VACNT surface and the reactive functional groups in the EP matrix, with the oscillating electromagnetic field.[301] It is postulated that during the curing process in the microwave field, interfacial bonding between the VACNTs and the EP matrix was dramatically improved. Consistent with the DMA results, the MCOM displays much higher thermal conductivity than the TCOM (Figure 6.4), which further verifies our postulation.

6.1.2.2 CTE

In the past twenty years, substances with low or negative thermal expansivities have attracted much interest due to their significance in electronic packaging, precision equipments, and intelligent materials, *etc*.[441-447] In electronic packaging systems, mismatch in CTE between various materials has become a critical issue for developing reliable packaging solutions. CTE values of polymer portion are much higher than those of Si, ceramic and Cu metallization. These large CTE mismatches lead to thermal stress

accumulation at contact interfaces during both packaging and device performance, which triggers component failure by, for example, warpage and rupture.[448] So far, the effective approach to reducing CTE of the polymer portion has been adding fillers of low CTE or negative CTE into polymer matrices.[445,446,448] Compared with the thermal transport properties of CNTs, there are very limited studies on CTE of CNTs and CNT/polymer composites.

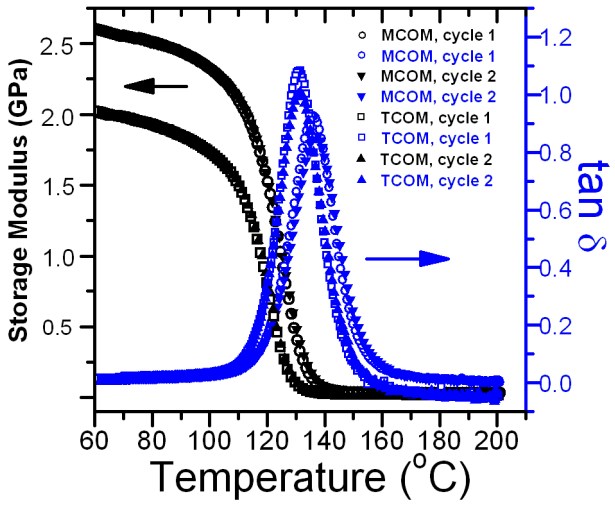

Figure 6.3 DMA results of TCOM and MCOM. Only cooling curves are included.

Table 6.1 DMA results.

Samples	T_g[a] (°C)	T_g[b] (°C)	G' [MPa] (100 °C)	G' [MPa] (50 °C)
TEP	120.72	129.9	1336	1464
MEP	120.62	128.9	1339	1489
TCOM	120.86	131.15	1732	2198
MCOM	126.9	136.19	2332	2662

a. extracted from storage modulus curves in the quasi-equilibrium cooling process;
b. extracted from tanδ peaks in the quasi-equilibrium cooling process.

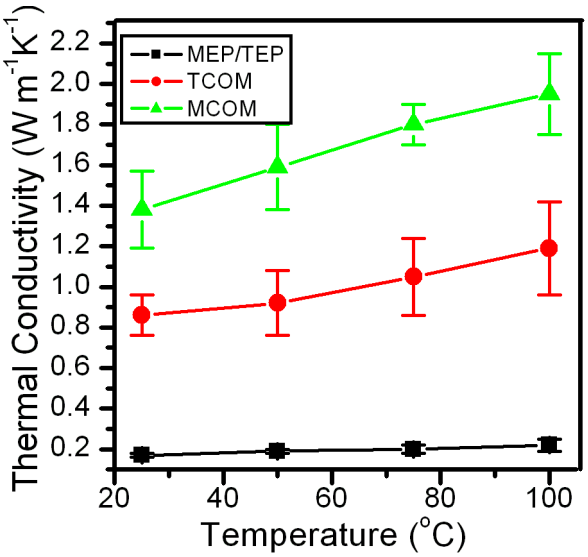

Figure 6.4 Thermal conductivities of TCOM, MCOM and EP.

Table 6.2 shows the CTE measurement results for TCOM, MCOM, TEP, and MEP. Both the TEP and the MEP samples display the typical CTE-temperature relation for amorphous polymers with CTE being much higher above T_g than below T_g. No apparent difference in CTE was observed between TEP and MEP, in consistence with their similar T_g and G' shown in Table 6.1. Both the TCOM and the MCOM samples show strong anisotropy in thermal expansion. Before their glass transitions, a more than 63% reduction in the through-thickness CTE (designated as α_N) with regard to the CTE of the EP is observed, while their in-plane CTE values (α_P) are similar to that of the EP. Unexpectedly, α_N of the MCOM above its T_g is extremely small and close to the CTE of Cu, even smaller than that below T_g, *i.e.*, a 90% reduction of the CTE of the EP above its T_g. In comparison, the TCOM, as usual, shows a large CTE increase at T_g as the turning point. One point that I would like to emphasize here is the special importance of CTE minimization of TIM composites at temperatures above their T_g, which seems to have been neglected or considered non-feasible in the past. As is known, it is the basic phenomena that polymers, upon heated, tend to have a higher positive CTE at T_g.[449]

Similar phenomena have also been observed in polymer based composites, including CNT/polymer composites. For example, Want *et al*. and Xu *et al*. observed that the CTE values of the CNT/polymer composites at temperatures above their T_g were at least 70 times of that for single crystal Si and 13 times of that for a pure Cu.[441, 447] Although semiconductor devices are expected to operate below 150 °C, the thermal non-uniformity usually referred to as hot spots, where power density could be >300 W cm^{-2}, is one factor that eventually determines the device reliability.[367,450] The hot spot issue will cause local temperature to be higher than the T_g of the TIM composite; in this case, the intensively heated part expands much more than the nearby components. How can people reduce the CTE of polymer composites above T_g to, *i.e.*, the value close to the CTE of Cu (~16 ppm K^{-1}) or Si (~ 3 ppm K^{-1})? In other words, how can we realize the principle of "1+1>2"?

Table 6.2 CTE[a] at Temperatures below and above T_g.

Samples	α_N below T_g [ppm K^{-1}]	α_N above T_g [ppm K^{-1}]	α_P below T_g [ppm K^{-1}]	α_P above T_g [ppm K^{-1}]
TEP	81	191	80	186
MEP	80	188	82	191
TCOM	30	68	81	310
MCOM	23	18	80	240

a. all values in the table were extracted from the slopes in quasi-equilibrium cooling curves.

To the best of the authors' knowledge, this is the first report so far on the ultra-low CTE above T_g for CNT/polymer composites. Obviously, the interface enhancement/bonding plays an important role. Why does the better interface lead to the ultra-low α_N above the T_g? The first possibility is the frozen, or at least partially frozen

orientation of polymer segments along the thickness direction—the CNT alignment direction. Bonded interface is the right force to freeze the polymer segments close to the interface, even above T_g. At temperatures below T_g, sideward expansion of polymer molecules contributes more to the α_P while lengthwise expansion of the molecules dominates the α_N.[449] If it is the case, the α_N of the MCOM should be smaller than that of the TCOM, while with a larger α_P. Although it looks like that α_N of the MCOM is slightly smaller than that of the TCOM, their α_P values are close. Probably radial contraction of the VACNTs in the MCOM obliterates this difference based on the better interface. At temperatures above T_g, the over-all volume expansion of the TCOM should roughly equal to that of the MCOM. Even if the polymer chains do not lose their orientations, not a big difference is expected between α_N of the MCOM and that of the TCOM. However, at temperatures above the T_g, the α_N of the MCOM is only 1/3 of the TCOM. This indicates the existence of a second mechanism that contributes to such an ultra-low α_N, as discussed below.

Molecular dynamics simulations suggest longitudinal contraction of a SWNT.[451,452] A negative radial CTE of -1.5 ppm K^{-1} in SWNTs was estimated experimentally.[453] Although it is not clear yet whether MWNTs contract longitudinally or not, it is reasonable to expect that MWNTs have much lower CTE than EP. Upon heating, there is an in-plane stretching coupled with a normal compression imposed on the polymer network due to the VACNT anchoring effects at interfaces, where the in-plane stretching comes from the radial contraction of the VACNTs while the normal compression is due to a large CTE mismatch between the VACNTs and the polymer matrix. Given that poisson's ratio of a rubbery polymer network (a crosslinked network above its T_g) is close to 0.5—indicating nearly no volume change, the in-plane stretching and the normal compression have overlapping effects in reducing α_N. Figure 6.5 illustrates such a mechanism. Below T_g, since segmental movements of polymer molecules are frozen, such stretching/compression forces cannot exert much influence on

the EP network; while above the T_g, they do. Although this overall influence may not be as strong as the interfacial anchoring effect acting on a thin polymer film by a specific substrate, where even an ultra-negative CTE was observed,[454,455] it is possible to reduce α_N to1/10 of the CTE for pure EP, or lower. This also explains why the MCOM shows a much larger α_P than its α_N, where α_P is even larger than the CTE of the EP. The even larger α_P of the TCOM is probably due to an increase in excluded volume,[440] where the weak CNT-polymer interfaces cannot exert the additional influences as in the MCOM.

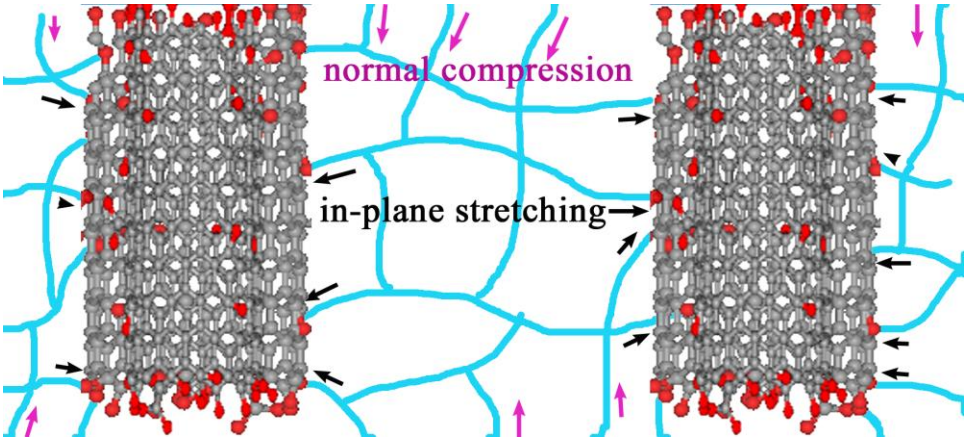

Figure 6.5 An illustration of the mechanism for the ultra-small through-thickness CTE of MCOM above its T_g. The red spots on CNT surface represent the functionalized sites on the f-ACNTs.

6.2 GNS/Polymer Interface

Graphene sheets are drawing increasing attention due to its excellent electrical, thermal and mechanical properties.[456] One potential application of graphene sheets is to incorporate them into polymer matrices to prepare high-performance composites.[320, 456] However, manufacturing graphene-based composites has been very challenging due to the difficulties in large-scale production of graphene sheets and their incorporation into polymer matrices.[320] In comparison, exfoliated graphite—especially graphite

nanosheets (GNS)—stacks of a few graphene sheets with high aspect ratio—are advantageous in terms of preparation and dispersion.[370,457-459] Recently, Sun's group reported their preparation of GNS with a high aspect ratio and incorporation of the GNS into an EP matrix.[460] The as-prepared GNS/EP composite displayed an extremely high in-plane thermal conductivity (~ 80 W m^{-1} K^{-1} at 33 vol% GNS loading). Compared with CNT/EP composites, there is no doubt that the GNS are considered more effective fillers for improving thermal conductivity. This great enhancement, hypothetically, resulted from the reduced GNS/polymer interfacial thermal resistance. However, the hypothesis is somewhat on the contrary to the results by Hung *et al*.[459] Here I give a theoretical analysis of the thermal transport behavior of GNS/polymer composites.

6.2.1 Theory and Model

Effective medium theory (EMT) is used to analyze the thermal conductivity of the GNS/EP composite in Ref. 460. EMT is commonly used to describe microstructure-property relationships in microstructurally heterogeneous materials, in particular, to calculate and/or predict the effective physical properties of a heterogeneous system. Following Nan,[437] let us consider a composite material with well-dispersed filler embedded in a polymer matrix. Assuming a homogeneous and isotropic "effective medium" with property K_0 and a perturbation in property, $K'(r)$, due to the presence of the filler, the property of the heterogeneous medium at a point denoted by the position "r" is thus expressed as: $K(r) = K_0 + K'(r)$. By using the Green function G for the homogeneous medium and the transition matrix T for the entire composite medium, the resultant effective property of the composite is expressed as: $K_e = K_0 + \langle T \rangle (I + \langle GT \rangle)^{-1}$, where I is the unit tensor and "< >" denotes spatial averaging. By neglecting the interaction between filler units at relatively low filler loading, the matrix T is simplified to be:

$$T \cong \sum_n T_n = \sum_n K_n^{'}(I - GK_n^{'})^{-1} \tag{6.3}$$

Taking the polymer matrix phase as the homogeneous reference medium and assuming perfect GNS/EP interfaces (the interfacial thermal resistance will be modeled later), we obtain the effective thermal conductivity of the composite in the Maxwell-Garnett (MG) form:

$$K_{e11} = K_{e22} = K_m \frac{2 + f[\beta_{11}(1 - L_{11})(1 + <\cos^2\theta>) + \beta_{33}(1 - L_{33})(1 - <\cos^2\theta>)]}{2 - f[\beta_{11}L_{11}(1 + <\cos^2\theta>) + \beta_{33}L_{33}(1 - <\cos^2\theta>)]} \tag{6.4}$$

$$K_{e33} = K_m \frac{1 + f[\beta_{11}(1 - L_{11})(1 - <\cos^2\theta>) + \beta_{33}(1 - L_{33}) <\cos^2\theta>]}{1 - f[\beta_{11}L_{11}(1 - <\cos^2\theta>) + \beta_{33}L_{33} <\cos^2\theta>]} \tag{6.5}$$

$$\beta_{ii} = \frac{K_{fii} - K_m}{K_m + L_{ii}(K_{fii} - K_m)} \tag{6.6}$$

$$L11 = L22 = \frac{p^2}{2(p^2 - 1)} + \frac{p}{2(1 - p^2)^{3/2}} \cos^{-1} p \tag{6.7}$$

$$L_{33} = 1 - 2L_{11} \tag{6.8}$$

where K_{e11} (=K_{e22}) and K_{e33} are the in-plane and the through-thickness effective thermal conductivities of the composite sample, respectively; f is the volumetric filler loading of the GNS; K_m is the isotropic thermal conductivity of the EP matrix; K_{f11} (=K_{f22}) and K_{f33} are the in-plane and the through-thickness thermal conductivities of the GNS unit, respectively; p reflects the aspect ratio of the GNS (the thickness over the in-plane diameter of a GNS unit) and takes, on average, 5/2000;[460,461] <$\cos^2\theta$> reflects the statistical orientation of the GNS in the EP and lies between 1/3 and 1, where <$\cos^2\theta$>=1/3 for a random orientation while <$\cos^2\theta$>=1 for a fully parallel orientation of the GNS plane relative to the surface plane of the film sample.

In Ref. 460, effective thermal diffusivity (α_e) of the composites was directly obtained in the experimental measurement. Effective thermal conductivity (K_e) was then calculated using the equation

$$K_{eii} = \alpha_{eii} \rho c_p \tag{6.9}$$

A simple mixing rule was used to calculate the mass density (ρ) and the specific heat (c_p) of the composites:

$$\rho = f\rho_f + (1-f)\rho_m \tag{6.10}$$

$$c_p = xc_{p,f} + (1-x)c_{p,m} \tag{6.11}$$

where ρ_m (0.93 g cm^{-3}) (Appendix A) and ρ_f (2.1 g cm^{-3}) are the mass densities of the EP (EPONOL resin 53-BH-35) and the graphite, respectively. $c_{p,f}$ (specific heat of graphite) of 0.70 J g^{-1} K^{-1} is taken.[462] x is the mass fraction of the GNS in the composite sample.

It is presented in Ref. 460 that at f=0.33, α_{e11} and K_{e11} are 35 mm^2 s^{-1} and 80 W m^{-1} K^{-1}, respectively. Based on these data and Eqns. (6.9)-(6.11), we calculate $c_{p,m}$ (specific heat of the EP) to be 2.91 J g^{-1} K^{-1} and thus, K_m=0.32 W m^{-1} K^{-1}. This K_m of pure EP looks unexpectedly high according to previous research experience of the author's group; however, in order to be consistent with the data in Ref. 460, let us just take this value for the effective medium analysis in this study. Based on the data of α_{e11} in Ref. 460, K_{e11} of the GNS/EP composites at various filler loading are calculated. In our modeling, K_{f11} is taken as 1500 W m^{-1} K^{-1} on the basis of the following considerations. The in-plane thermal conductivity of a single graphene sheet was estimated to be as high as ~5000 W m^{-1} K^{-1}.[463,464] Given the fact that a MWNT, which is treated as a concentrically wrapped-up GNS, possesses a similar longitudinal thermal conductivity (>3000 W m^{-1} K^{-1}) to a SWNT (~3500 W m^{-1} K^{-1}), we believe that a GNS possesses a high K_{f11} in the same order of magnitude with K_{f11} of a single graphene sheet. Previous experimental data on CNTs also showed that the longitudinal thermal conductivities of MWNT arrays were ~30 W m^{-1} K^{-1}. Since the packing densities of these MWNT arrays are ~5% and tube-tube interactions degrade the effective thermal conductivities, we estimate the equivalent longitudinal thermal conductivity of an individual MWNT to be at least 600 W m^{-1} K^{-1}. Therefore, the GNS, an unrolled form of a MWNT, should possess a K_{f11} of at least 600 W m^{-1} K^{-1}. Further information for the estimation comes from the in-plane thermal

conductivity of the commercial pyrolytic graphite sheets (PGS) provided by Panasonic, Inc. (Appendix B) As the PGS density approaches the theoretical mass density of graphite, the in-plane thermal conductivity of the PGS becomes 1500-1700 W m^{-1} K^{-1}. To be conservative, we take 1500 W m^{-1} K^{-1} in our modeling. Accordingly, K_{f33} is taken as 15 W m^{-1} K^{-1}.

6.2.2 Results and Discussion

Figure 6.6 shows a comparison between Eqn. (6.4) and the experimental data in Ref. 460. A strong influence of the GNS orientation in the EP matrix on K_{e11} is evident. $<\cos^2\theta>$=0.91 is the value with which the calculated K_{e33}/ K_{e11} at 33 vol% loading is between 1/9 and 1/10, close to the actual average orientation of the GNS in the EP matrix in Ref. 460. The model predicts higher thermal conductivity enhancement than the experimental results. Moreover, a GNS/polymer composite exhibits a very low percolation threshold (f_c<0.64%),[465] above which a continuous GNS network forms in the composite. The filler loadings under investigation are much higher than fc; in this sense, the model used here has already underestimated K_{e11}.[435] The mixing rule, percolation model and Bruggeman models will predict even higher K_{e11} than the MG model at such high filler loadings.[367] Therefore, the experimental data are still much below predictions. The deviation observed between the theoretical prediction and the experimental results probably indicates the influence of the GNS/EP interfacial resistance, consistent with the conclusion by Hung *et al*.[459] Therefore, GNS/polymer interface modification is expected to further improve K_e, in analogy to CNT/polymer composites.

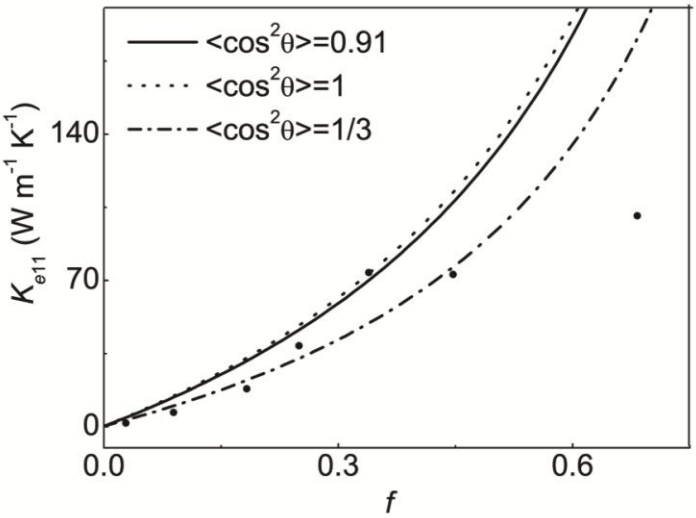

Figure 6.6 A comparison between the effective medium model (with various GNS orientations) and the experimental results (solid dots) in Ref. 460.

Meanwhile, our modeling results show distinct difference between CNT/polymer interface and GNS/polymer interface. Figure 6.7 shows schematic illustration of a modified GNS unit after the interfacial resistance, R_K, at the GNS edge is taken into account, in analogy to the methodology by Nan *et al*.[430] Nevertheless, the interfacial resistance along the through-thickness direction is neglected based on the following considerations: 1) the large aspect ratio and the flat surface of GNS enhances GNS-polymer interaction,[466] leading to a relatively negligible interfacial thermal resistance compared with that at the GNS edge; 2) since phonon acoustic mismatch is considered the main fundamental cause of the interfacial thermal resistance between GNS (or CNT) and polymer,[367] the soft-mode vibrations of GNS along its through-thickness direction, compared with the rigid-mode vibrations in its in-plane direction, can be much better coupled to the vibrations of the polymer matrix, it is reasonable to consider only the interfacial thermal resistance at the GNS edge in such a highly oriented GNS/polymer composite. As such, the effective in-plane thermal conductivity of the GNS can be expressed as:

$$K'_{f11} = K'_{f22} = \frac{B}{2R_K + B/K_{f11}} \tag{6.12}$$

where B is the average lateral size (2 μm) of a GNS unit. By replacing the K_{f11} and K_{f22} with K'_{f11} and K'_{f22}, respectively, in Eqns. (6.4) and (6.6), we get the modeling results in Figure 6.8. R_K falls in the range of 1-6×10^{-9} m^2 K W^{-1}, one order of magnitude smaller than the R_K of 8×10^{-8} m^2 K W^{-1} measured across CNT/polymer interfaces.[438] It is not difficult to understand the relatively small R_K of GNS/polymer interfaces. In polymer composites with SWNTs, due to the small tube diameter (usually <10 nm), the probability of an attachment of the ends of the CNTs to the polymer matrix (the ends have to be somehow attached to the polymer chain for effective thermal transport across the interface) is extremely low.[307] In comparison, in GNS/polymer composites, the large lateral length (usually on the order of micron) of the GNS results in a dramatically increased probability of an attachment of the GNS edge to the polymer matrix.

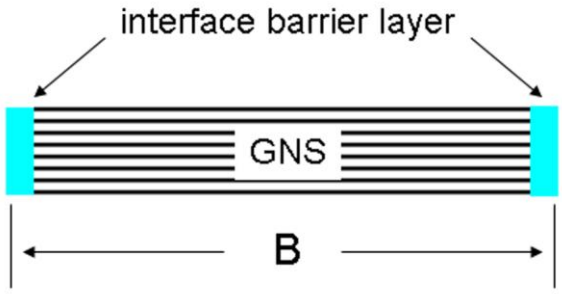

Figure 6.7 Schematic illustration of a modified GNS unit after the interfacial resistance, R_K, at the GNS edge is taken into account. A simple series model is used. B represents the lateral size of the GNS.

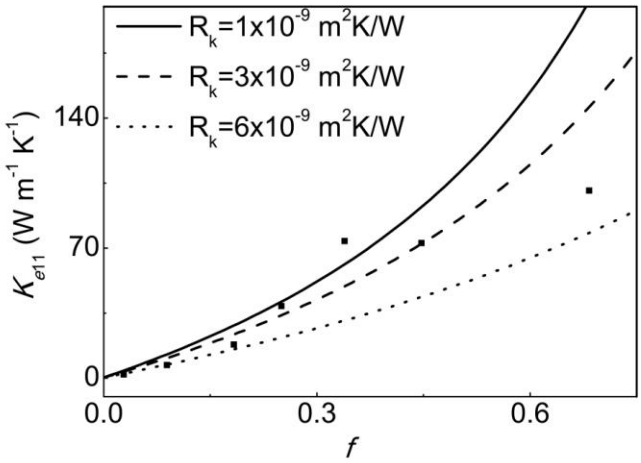

Figure 6.8 The influence of the GNS/polymer interfacial thermal resistance on the overall effective thermal conductivity of the composites (<$\cos^2\theta$>=0.91).

Figure 6.9 shows a strong influence of the aspect ratio on Ke_{11}: the higher the aspect ratio of GNS, the higher Ke_{11}. Therefore, further exfoliation of the GNS to produce higher-aspect-ratio fillers would be expected to further enhance the thermal conductivity of GNS/polymer composites. In this case, however, the interfacial thermal resistance will probably become more influential.

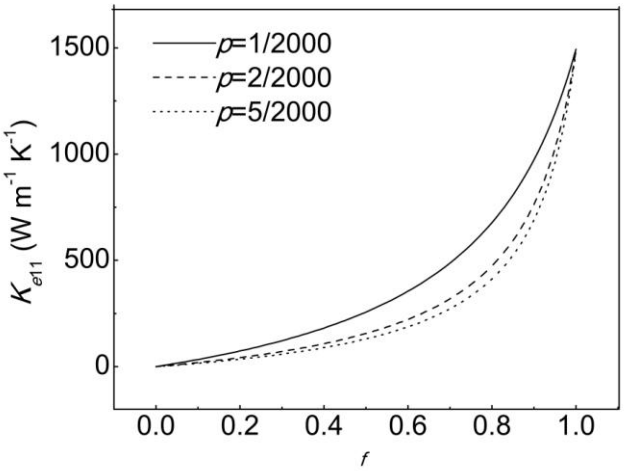

Figure 6.9 The influence of the aspect ratio of the GNS on the overall effective thermal conductivity of the composites (<$\cos^2\theta$>=0.91).

CHAPTER 7

FUTURE WORK

7.1 Synthesis of High-Quality VACNTs with a Higher Packing Density

One drawback of current TCVD synthesis of VACNTs is the relatively low CNT packing density on the growth substrate. This density limitation mainly comes from the low number density of catalyst NPs on the growth substrate. Usually, a thin layer of catalyst is deposited on a growth substrate, *e.g.*, by e-beam evaporation. The thickness of the catalyst layer after deposition is typically 0.6-3 nm for TCVD. The thin catalyst layer cracks to form NPs at high temperatures in a reducing atmosphere. A proper thickness of the catalyst layer is one prerequisite for formation and separation of catalyst particles with small distribution in diameter. For a TCVD process, density of NPs on a growth substrate typically lies between 300-1000 μm^{-2}, depending on the original thickness of the catalyst deposit, the catalyst support layer (Al_2O_3), the pressure of the chamber for TCVD, [467] and Oswald ripening during CNT growth that decreases the number density of the catalyst NPs. Therefore, in real VACNT samples by TCVD, the packing density of CNTs on the substrate is ~5% in volume or lower. Although such a surface coverage is sufficient to, in theory, provide excellent electrical or thermal conductance, defects and misalignment are unavoidable in the synthesized CNTs, which greatly degrade intrinsic properties of VACNTs. Therefore, for electrical or thermal applications, a properly higher packing density of VACNTs on substrates is desired.

In general, the CVD process and the catalyst recipe both affect the packing density of the VACNTs. In the future, systematic studies in the following two directions are worth pusuing.

First, based on the current TCVD system, fast temperature ramping can be introduced, as well as controlled chamber pressure during the TCVD.

Second, binary catalyst recipes on the packing density is worthy of being looked into, in particular, Mo-Fe, Mo-Co and Ni-Fe systems. Mo has been widely used for SWNT synthesis.[178,468,469] Yoon *et al*. reported that the addition of Mo in the Co catalyst improved the distribution of catalyst NP size on the growth substrate, and in come cases, provided an effective nucleation site for SWNTs.[178] The relatively high stability of molebdenum oxide is considered beneficial for retarding the catalyst NPs from coarsening.[468] Co-deposition of Mo and Fe is worth trying. Previous results show that the present of a small amount of Ni in the catalyst recipe can effectively retard the coarsening of the catalyst NPs, however, giving low catalysis activitiy toward ethylene. Therefore, a modified source composition together with the TCVD temperature is necessary to explore the Ni-Fe recipe.

7.2 More on Large-diameter Double-walled VACNT Array

Our prior publications showed our capabilities of synthesizing high-quality vertically aligned open-ended CNTs. An important improvement over the prior published work, according to the discussion in Section 2.3.5, is the synthesis of open-ended high-quality VACNTs yet with large inner diameter and thin walls. Large inner diameter (~5 nm) can facilitate ion transport in the tube to make the inner wall area of the open-ended tubes accessible for ion sorption. A thin wall structure undoubtedly increases the specific area of the VACNTs, as the inter-layer surface area may not be accessible to ions. As such, the large-diameter DWNT array may find an important application as electrode materials in electrochemical energy storage. So far, we have demonstrated successful synthesis of VACNTs with large inner diameters and thin walls (Figure 2.9); the synthesis will be systematically studied and optimized in the future.

7.3 Mechanism for Fast Microwave Heating of CNTs

As discussed in Chapter 3, conduction loss is probably the dominating mechanism for microwave response of the VACNTs under study. By microwave response, I refer specifically to heating rate of CNTs under microwave radiation, which can be measured in situ in the microwave apparatus. According to the widely used Drude model, the complex electrical conductivity, $\sigma(\omega)$, of a conductive material in an AC electrical field is:

$$\sigma(\omega) = \frac{\sigma_0}{1+\omega^2\tau^2} + i\frac{\sigma_0\omega\tau}{1+\omega^2\tau^2} \tag{7.1}$$

where σ_0, ω and τ are the DC conductivity of CNTs, frequency of the AC field, and mean free time of the free charge carriers in the CNTs.

σ_0 is defined as:

$$\sigma_0 = \frac{ne^2\tau}{m^*} \tag{7.2}$$

where n, and m^* are the density of free electrons (e^-) in CNTs, and the effective mass of e^-.

Therefore, both microwave frequency and the electron density affect the conduction loss. The following experiments are proposed to determine if conduction loss is the primary mechanism for microwave heating in CNTs.

1) ω can be easily tuned on the microwave apparatus so that the dependence of microwave heating on the frequency of the microwave field can be established.

2) Doping by nitrogen is an effective way of tuning the electrical conductivity of CNTs because the N-dopants increases the density of e- (n) in the CNTs without affecting the mean free time of e^- (τ_e).[470-472] In the present proposed research, synthesis of N-doped VACNTs will be carried out by the CVD process but with a slight modification. A small amount of Ar will be bubbled through a solution of water/acetonitrile at various tempertures. Acetonitrile has been used widely as an effective source of nitrogen to

synthesize N-doped multi-walled CNTs.[474,475] The dopant level can be characterized accurately by elemental analysis, electron energy loss spectroscopy, and semi-quantitatively by X-ray photoelectron spectroscopy. DC conductivity σ_0 can be easily measured with a four-point probe system. As such, doping level—conductivity—microwave response correlation will be established.

3) High-temperature annealing of the synthesized VACNTs will be carried out to improve their electrical conductivity. Microwave response of the annealed CNTs will be compared with the pristine CNTs.

Conduction loss accounts for microwave heating of carbon black (up to ~500 ^{o}C). However, it may not explain why VACNTs can be heated to higher temperatures (650-2000 ^{o}C) than carbon black. Other than the conduction loss, as mentioned in Chapter 3, effect of magnetic loss on the microwave heating of catalyst-containing CNTs is still not clear,[272,276,277,312] because even quanlitative analysis of the correlation between the content of the catalyst residue in CNTs and the their microwave heating is absent in literature. Here I propose the following strategy to study the magnetic loss effect. As shown in Figure 7.1, three types of VACNTs will be studied: pure VACNTs with no catalyst residue (Figure 7.1a)—synthesized by our current TCVD process; VACNTs coated with a controllable amount of Fe (or Ni) NPs on surface (Figure 7.1b)—prepared by deposition of the magnetic NPs; VACNTs with a controllable amount of Fe (or Ni) NPs trapped inside the tube (Figure 7.1c)—synthesized by a FCCVD process. The amount of catalyst residue can be measured accurately by ICP. Catalyst residue—microwave response correlation will be established.

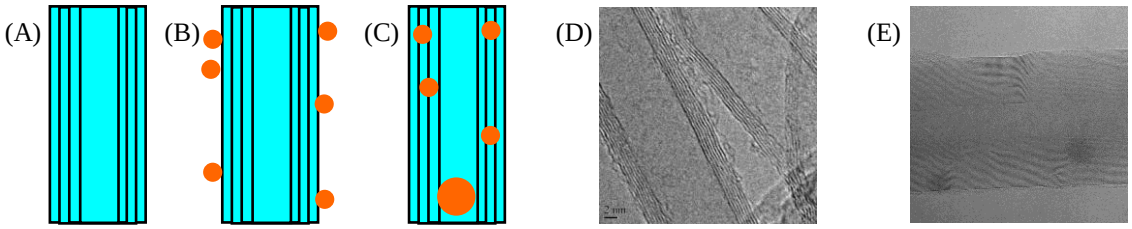

Figure 7.1 The three types (A, B, and C) of VACNTs to be studied regarding the effect of magnetic catalyst residue on microwave heating. (D) and (E) are HRTEM images of pure CNTs (A) and CNTs with Fe trapped inside the tube (in between the walls) synthesized by a FCCVD process (C), respectively.

CHAPTER 8

AN EXTRA CHAPTER ON DISCOVERY, FUNDAMENTALS AND APPLICATIONS OF ORGANIC AQUA REGIA

Recently, we reported our discovery of a series of organic mixtures that dissolve various noble metals such as Au, Ag, and Pd efficiently at room temperature.[476] By varying the composition, and reaction conditions, we were able to achieve selective dissolution of the noble metals. I named these mixtures *organicus liquor regius* as the male counterpart of *aqua regia* (female) in Latin. For the peer researchers and readers to catch the term more easily, I will use the term *organic aqua regia* (OAR) from here after. The discovery of OAR and their potential applications in many fields have attracted extensive attention.[477-479] The chapter provides a brief description of our work on, and understanding of, OAR from three aspects: discovery, fundamental chemistry, and some of the potential applications that we have already preliminarily demonstrated.

The chapter is composed of two sections. Section 8.1 describes how I discovered OAR when I was studying chemical bonding of functionalized carbon nanotubes to an Au surface, and introduces some known properties (dissolution selectivity towards metals, and dissolution kinetics) of OAR, with a touch on some of the recipes of OAR that I have already developed so far. A summary of the chemistry, strength, and issues of *aqua regia*—the most powerful solution to dissolve noble metals in history, and a tabulated comparison between OAR and *aqua regia* will be presented. A significant portion of the chapter is then devoted in Section 8.2 to some fundamental chemistry of OAR, with the focus on the Au-thionyl chloride-pyridine system. Thionyl chloride ($SOCl_2$) and its mixture with pyridine (py) have been widely used in organic chemistry for decades. We shall note that the chemistry of $SOCl_2$-py is more complex than chemists may have ever perceived. Our rigorous study on $SOCl_2$-py has provided some new

fundamental understanding of the mixture. Also discussed will be the possible mechanism for the Au dissolution by $SOCl_2$-py. A surface reaction mechanism is proposed.

8.1 Discovery of OAR

As many discoveries were, the discovery of OAR was accidental. In 2007, I was involved in developing a chemical bonding process to anchor in situ functionalized vertically aligned carbon nanotubes to a modified Au surface. The basic chemistry was to assemble a thin layer of 4-mercaptobenzoic acid molecules on the Au surface, and then form the bonding between the functional groups (*e.g.*, hydroxyl groups) on the VACNTs and the acid groups of the 4-mercaptobenzoic acid molecules via esterification (Figure 5.10). However, there were some fundamental challenges to such a bonding process. First, solid-solid reaction at the interface was very unlikely to occur given the low functionalization degree of the carbon nanotubes and the irregular surface of the carbon nanotubes (very few people talked about the irregular surface of the macroscopically well-aligned carbon nanotubes). Second, a wet chemical reaction at the interface was preferred, *e.g.*, the esterification reaction catalyzed by acid in an aqueous solution. However, the wet chemical process—if not controlled well—would damage the vertical alignment of the carbon nanotubes (at that time nearly nobody revealed the truth that a vertically aligned carbon nanotubes array/bundle could easily collapse in wettable liquids). Third, direct esterificaiton of benzoic acid with alcohol had been known to be very inefficient,[480,481] and therefore, kinetically unlikely at the interface. To address these issues, the benzoic acid group was first transformed to the benzoic acid chloride group by the reaction with $SOCl_2$ in the presence of a certain concentration of py as the catalyst. A dilute solution of $SOCl_2$ (5~10 ppm) in acetonitrile with a trace amount of py (py:$SOCl_2$=1:2 in mole) was used (illustrated in Figure 5.13).

When I was studying the functionalization (esterification) reaction, something unexpected but interesting happened one day: in the presence of py, a relatively high concentration of $SOCl_2$ resulted in efficient dissolution of Au in the organic solution at room temperature. Soon after I confirmed that Au was not soluble at all in either $SOCl_2$ or py, with and without oxygen (O_2), I realized the similarity between the organic mixtures and *aqua regia*. *Aqua regia* ("royal water") has been used for centuries as a powerful etchant to dissolve noble metals. The beauty of *aqua regia* is that the simple 1:3 mixture of concentrated nitric and hydrochloric acids can dissolve various noble metals while the noble metals are not soluble in either of the acids. The organic mixtures have exactly the same beauty with *aqua regia*: simple mixtures; therefore, I name the mixtures *organic aqua regia* (OAR). My curiosity pushed me to try other materials in the $SOCl_2$-py mixture (with and without acetonitrile); the qualitative results are listed in Table 8.1.

The discovery promises more than just the beauty and simplicity. The distinct difference between OAR and *aqua regia* is that OAR are non-aqueous, which is important. Compared with inorganic chemistry, organic chemistry provides a precise control over chemical reactivity. The ability to engineer organic reactions would probably enable selective dissolution of noble metals. With that in mind, Prof. Wong, Rongwei Zhang and I started to work on the formulation of OAR for selective dissolution of noble metals. Some preliminary results are presented here. Figure 8.1 shows the kinetic results of the dissolution of noble metals in the mixture of $SOCl_2$ and py with a volumetric ratio of 3:1. The mixture dissolves Au at a rate of 0.3 mol m^{-2} h^{-1} at room temperature, which is faster than Au dissolution in conventional cyanide leaching agents (<0.004 mol m^{-2} h^{-1}) and iodide etchants (<0.16 mol m^{-2} h^{-1}).[482,483] Ag and Pd, can also be dissolved at high dissolution rates (0.8 mol m-2 h-1 and 0.5 mol m^{-2} h^{-1}, respectively); Pt is completely inert. In a comparison, Figure 8.2 shows that a $SOCl_2$-DMF mixture dissolves Au at a rate of 0.3 mol m^{-2} h^{-1}; neither Pd nor Pt is apparently dissolved.

Table 8.1 Qualitative results of dissolution of various materials in $SOCl_2$-py mixtures.

material	dissolution (Y/N)
silver	Y
gold	Y
platinum	N
palladium	Y
copper	Y
iron	Y
nickel	Y
titanium	N
tungsten	N
tantalum	N
chromium	N
tin	Y
indium	Y
stainless steel	Y
Teflon	N
silicon	N
silicon oxide	N

Such dissolution selectivity may find many important applications such as recovery of noble metals, especially recovery of Pt. The conventional Pt recovery technologies are complicated, mainly relying on the dissolution of Pt in strong inorganic acids (*aqua regia*) and subsequent precipitation of the dissolved Pt from the solution.[484-486] However, *aqua regia* dissolves all the metals at the same time and cannot separate them out. It ends up with low-purity Pt which doesn't go back to the

product stream directly; it has to be refined, but refinery is costly. Moreover, auqa regia is notoriously dangerous to work with; it is not recyclable; it is environmentally hazardous. In comparison, OAR may provide a route to improve the recycling quality and efficiency of Pt by a selective dissolution process. The selective dissolution process removes the impurity noble metals (Ag, Au, and Pd, etc.) before the final dissolution of Pt. Besides, OAR is recyclable (simply by distillation), and dilute OAR are relatively safe and easy to handle. A thorough comparison between *aqua regia* and OAR is listed in Table 8.2. A few non-aqueous solutions for dissolving noble metals have been preliminarily investigated by other research groups,[482,487-490] however, with relatively unsatisfactory solubility,[482,488-490] selectivity,[482,488-490] efficiency,[487,489, 490] stability [490], and simplicity.[487-489]

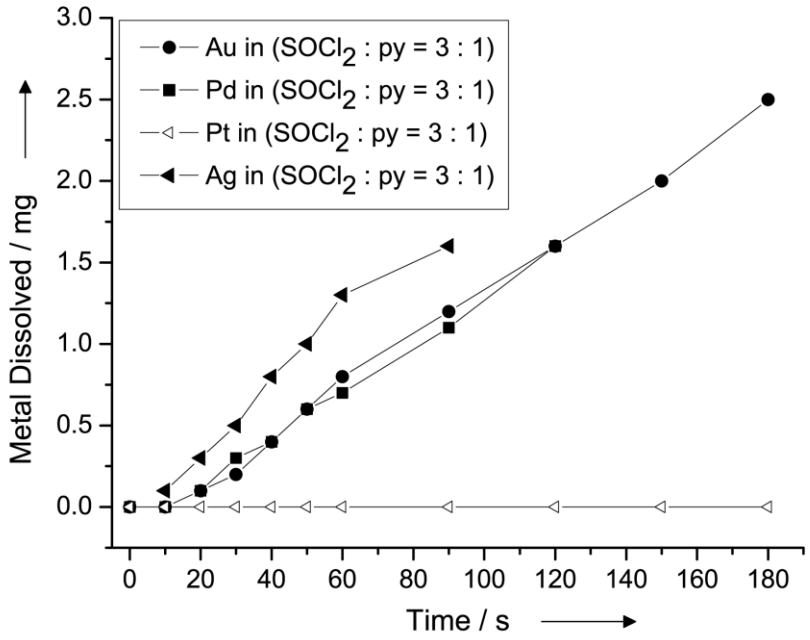

Figure 8.1 Kinetic studies of the dissolution of Au, Pd, Ag, and Pt in a 3:1 $SOCl_2$-py mixture. We deposit 250-nm-thick Au, Pd, Ag, and Pt, respectively, onto a 9-cm^2 Si substrate each, with 20-nm-thick chromium as the adhesion layer (chromium is not soluble in any organicus liquor regius we tried) to avoid the error that might be introduced due to peel-off of the noble metal metallization layer. The metalized substrates are immersed in 20 mL of $SOCl_2$-py at room temperature with mild shaking for a preset duration, taken out, rinsed thoroughly, dried, and weighed.

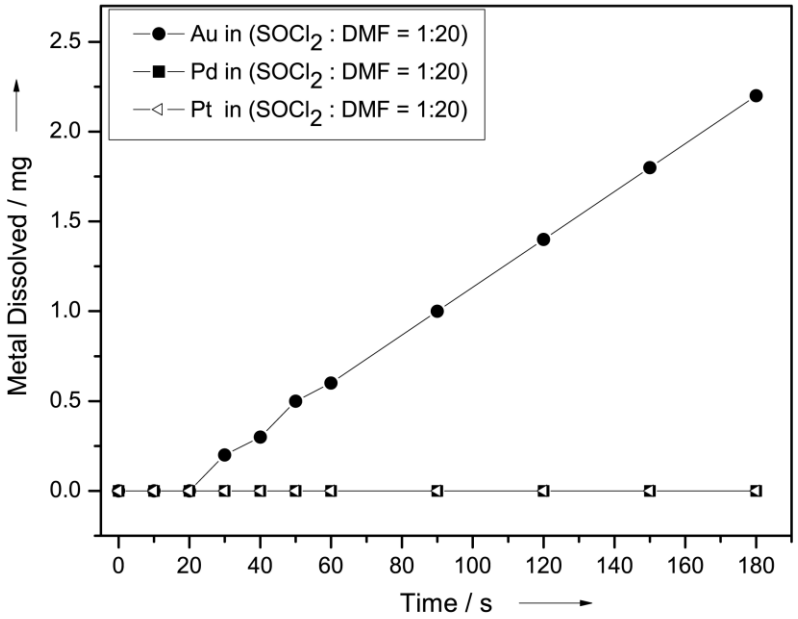

Figure 8.2 Kinetic studies of the dissolution of Au, Pd, and Pt, respectively, in a 1:20 $SOCl_2$-DMF mixture.

Table 8.2 A comparison between *aqua regia* and OAR.

	Aqua regia	OAR
composition	nitric acid + hydrochloric acid	innumerous
concentration	concentrated	customized
safety	explosive and corrosive	corrosive
recyclable	N	Y
dissolution of noble metals	indiscriminate	selective

So far, the chemicals that have been found to work as the effective basic components to compose OAR with $SOCl_2$ for dissolving Au include, but are by no means limited to, the following chemicals and their derivatives: pyrrole, pyrrolidine, pyrrolidone, isoxazole, isothiazole, pyrazole, imidazole, thiazole, oxazole, pyrazolone,

bipyrazole, pyridine, pyridazine, pyrimidine, pyrazine, triazine, indole, quinoline, purine, pteridine, phthalocyanine, N,N'-dicyclohexylcarbodiimide, N,N'-dimethylformamide (DMF), N,N'-dimethylbenzylamine, dodecyltrimethylammonium bromide, tri-p-tolyl-phosphine, *etc*. Effective dissolution of Au in a mixture of $SOCl_2$ with any of the following chemicals has not been observed: maleimide, azobisisobutyronitrile, aniline, polyaniline, phenanthroline, methylbenzyl cyanide, 2-acetyl-1-methylpyrrole, benzyltriethylammonium tetrafluoroborate.

8.2 Fundamental Chemistry of the $SOCl_2$-py Mixture and the Au-$SOCl_2$-py System

One key feature that all the aforementioned organic candidates have in common is that they more or less have charge-transfer interactions with $SOCl_2$,[491, 492] where the sulfur in $SOCl_2$ is an electron acceptor, and the nitrogen (or phosphor) an electron donor. Let me focus on the Au-$SOCl_2$-py system in this chapter.

8.2.1 $SOCl_2$-py Mixtures

Py has been known for long to be able to catalyze the synthesis of acyl chlorides (RCOCl) by the reaction between organic acids and $SOCl_2$.[493-496] So has DMF. From a bromination reaction of py in the presence of $SOCl_2$, Garcia *et al*. proposed a reaction between py and $SOCl_2$ involving the probable equilibrium among 1-(chlorosulfinyl)-pyridinium chloride (structure b in Figure 8.3), 1-(chlorosulfinyl)-4-chloro-4-hydropyridine (structure c in Figure 8.3), and further reaction products.[497] Such a proposed reaction equilibrium was used by Higashi *et al*. as the mechanism for esterification reactions between carboxylic acids and $SOCl_2$ using py as the catalyst.[495] However, no systematic spectroscopic study on the $SOCl_2$-py mixtures has been reported so far.

Indeed, there is a strong interaction between py and $SOCl_2$, which can be seen by the "white fog" formed when either of them is added to the other at room temperature. Immediate yellowing of the solution is observed when py and $SOCl_2$ are mixed fast at room temperature.

Such a strong interaction is due to the formation of a charge-transfer complex (Figure 8.4) between py and $SOCl_2$ (partial transfer of the electron density on the nitrogen to the sulphur). The charge transfer, in general, weakens the bonds within the acceptor molecule,[498] which accounts for the observed redshifts of both the asymmetric (from 446 to 427~426 cm^{-1}) and the symmetric (from 497 to 494~474 cm^{-1} depending on the ratio of $SOCl_2$ to py) Cl-S-Cl stretching in the Raman spectra of the $SOCl_2$-py mixtures (Figure 8.5). $SOCl_2$. py is observed directly in the mass spectrum of the $SOCl_2$-py mixture.[476] Nuclear magnetic resonance (NMR) data are summarizes in Table 8.3. We see the deshielding (low-field chemical shifts) of ^{14}N (ca, 5 ppm), ^{13}C (ca, 1.35 and 2.42 ppm for C-3 and C-4, respectively), and ^{1}H (ca, 0.35, 0.49 and 0.50 ppm for H-2, H-3 and H-4, respectively), and shielding (high-field chemical shift) of C-2 (ca, -1.77 ppm) relative to pure py. These chemical shifts are attributed to the charge-transfer interaction.[499] We also observe shifts and intensity changes of py-related vibration peaks in the FT-IR of the $SOCl_2$-py mixture relative to pure py and $SOCl_2$ (Figure 8.6). Such shifts are in agreement with simulation results.[476]

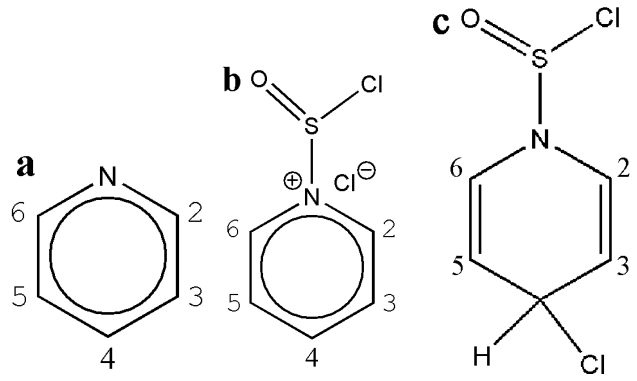

Figure 8.3 Structures of py (a), 1-(chlorosulfinyl)-pyridinium chloride (b), and 1-(chlorosulfinyl)-4-chloro-4-hydropyridine (c). The numbering of atoms is applied to the NMR analysis.

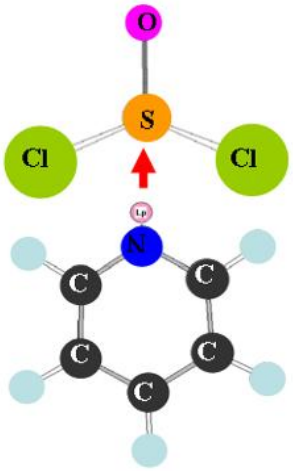

Figure 8.4 The molecular structure of the $SOCl_2$-py charge-transfer complex.

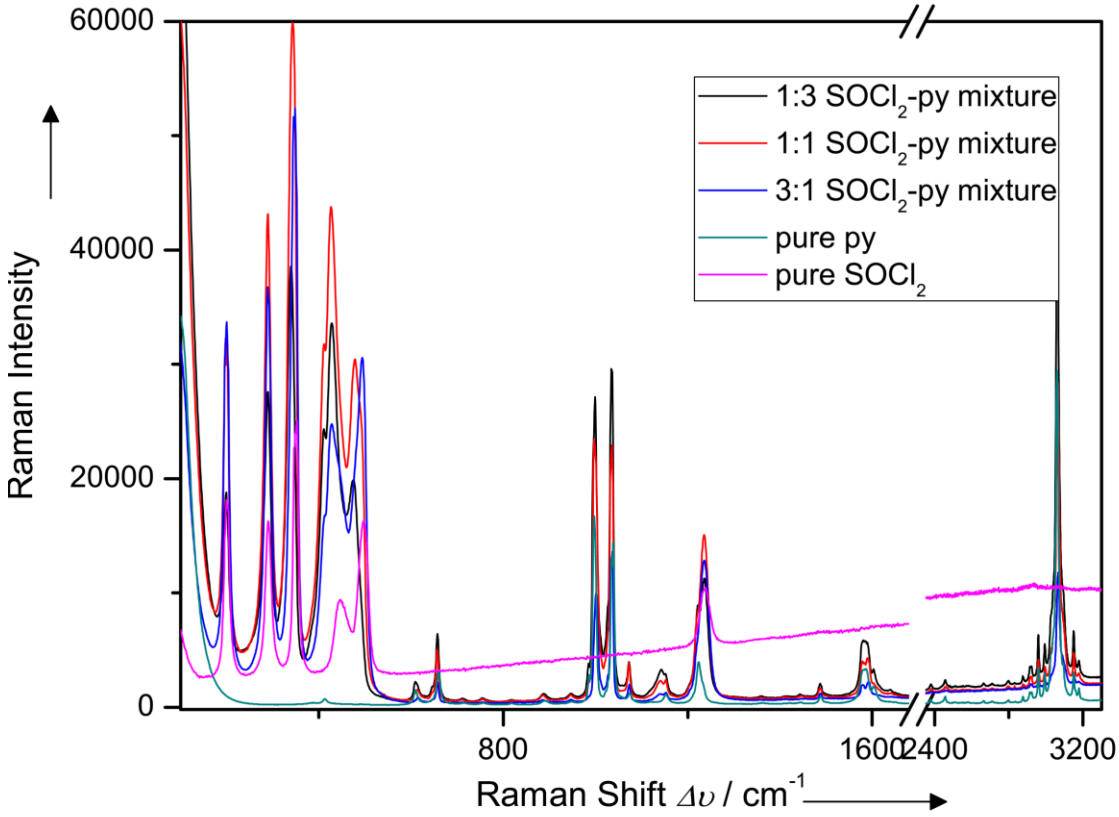

Figure 8.5 532-nm-laser-wavelength Raman spectra of py, $SOCl_2$, and their mixtures with varied ratios.

Table 8.3 Summary of solution NMR data.

δ (^{1}H) of 3:1 $SOCl_2$-py mixture	δ (^{13}C) of 3:1 $SOCl_2$-py mixture
9.68 (d, J=6.0)	148.17 (2.9)
9.50 (d, J=5.8)	138.32 (2.3)
9.28 (s)	125.15 (2.0)
9.21 (d, J=4.6)	
9.17 (d, J=4.1)	
8.94 (d, J=4.5)	
8.75 (d, J=4.2)	
8.12 (t, J=7.8)	
7.72 (t, J=6.6)	
7.52 (t, J=6.1)	
1.56 (s)	
1.18 (s)	

Left column: "s", "d" and "t" in the brackets represent "singlet", "doublet" and "triplet". The values in bold are the major chemical shifts. Right column: the values in the brackets are the half-height line-width ($v_{1/2}$).

In the Raman and the FT-IR spectra of the $SOCl_2$-py mixtures, almost all the vibration modes of pure py and pure $SOCl_2$ remain. This indicates that the parent molecules, although perturbed by the charge-transfer interaction, maintain their basic structural integrity, and that the dominating product is a molecular adduct rather than a rearrangement, elimination or dissociated product. Neither 1-(chlorosulfinyl)-pyridinium chloride nor 1-(chlorosulfinyl)-4-chloro-4-hydropyridine is identified in the NMR spectra or FT-IR spectra.[493,495-497] However, the experimental data of electrical conductivity measurement of the mixtures suggest the presence of mobile ions due to the dissociation. Therefore, 1-(chlorosulfinyl)-pyridinium chloride, though being a weak electrolyte in

$SOCl_2$ (Figure 8.7), exists as the dissociated form of the $SOCl_2$. py adduct in the solutions. Geometry optimization results show that: $SOCl_2$-py adduct (non-dissociated) is energetically more favorable than 1-(chlorosulfinyl)-pyridinium chloride, the dissociated form of the adduct, the latter being 16.8 kcal mol^{-1} higher in energy than the former. The energy difference will be lowered when put into a condense phase, depending on the dielectric constant of the solvent. This helps explain why the adduct is a weak electrolyte in $SOCl_2$.

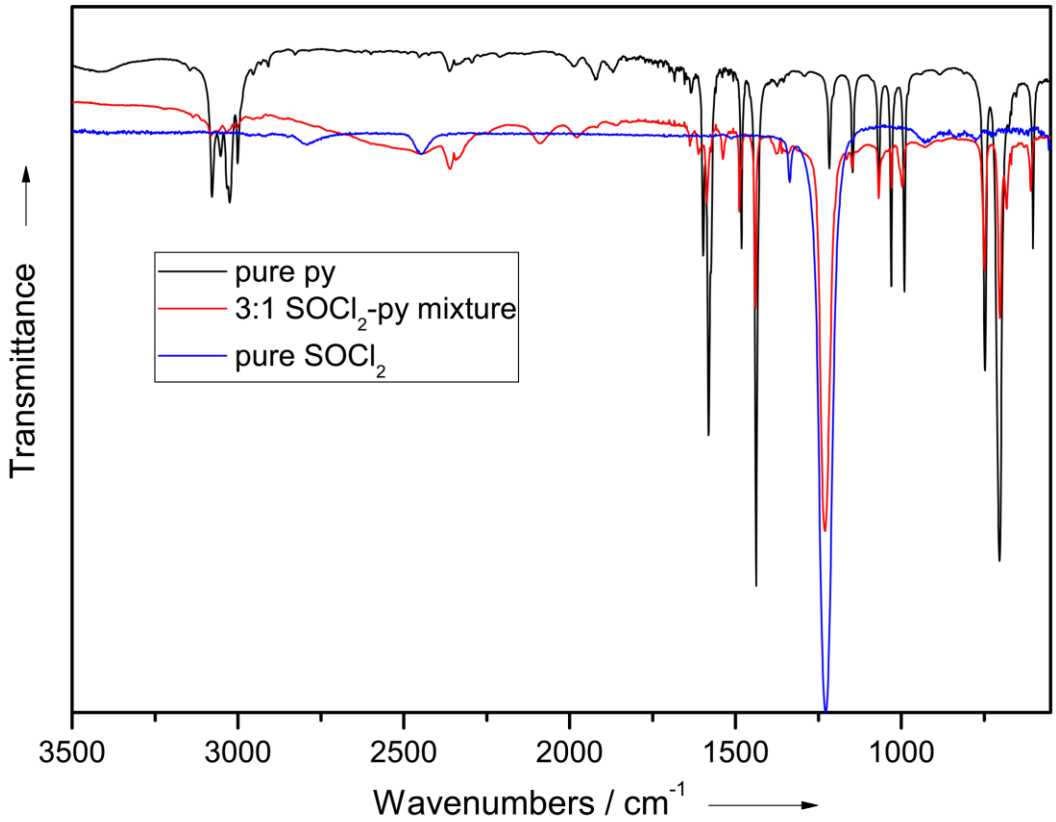

Figure 8.6 FT-IR spectra of py, $SOCl_2$, and their mixture.

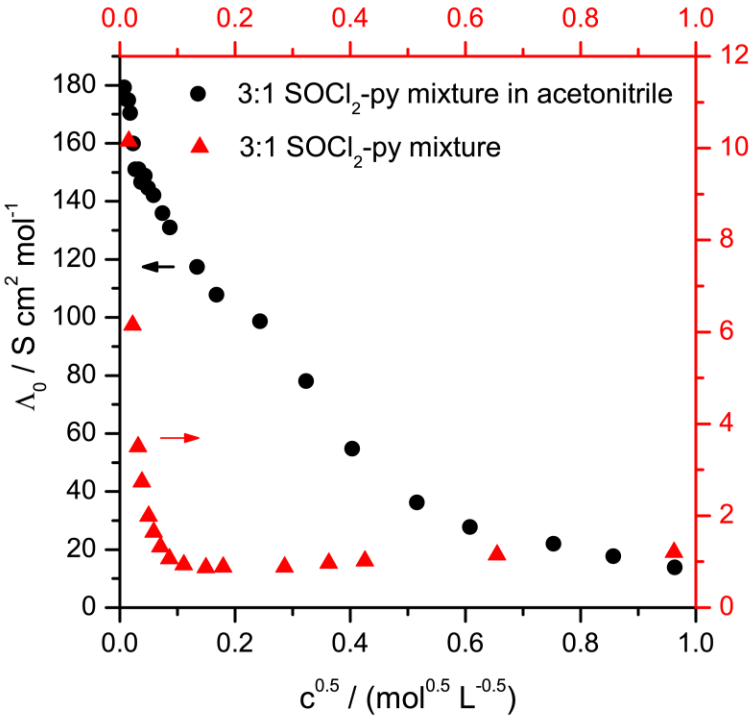

Figure 8.7 Conductivity measurement results (III): Λ-$c^{0.5}$ plot, where c is the concentration of $SOCl_2$． py adduct in the solution, and Λ the molar conductivity of the electrolyte. It is clear that $SOCl_2$． py is a weak electrolyte in $SOCl_2$ matrix; its dissociation degree increases in acetonitirle. This is in line with our prediction because $SOCl_2$ has a lower dielectric constant (9.3) and higher viscosity (0.6 cP) than acetonitrile (36.2 and 0.3442 cP, respectively).[500,501]

8.2.2 Au Dissolution in $SOCl_2$-py Mixtures

It has been confirmed that the valence state of Au after the dissolution is Au(III), in the form of $[AuCl_4]^-$. The Raman spectrum showing the $[AuCl_4]^-$ structure is shown in Figure 8.8. From the view of thermodynamics, dissolution of noble metals usually requires a strong oxidant, and simultaneously ligands that coordinate with the noble metal ion to reduce the redox potential of the metal in the solution. Obviously, Cl^- is the ligand in this case. Although even chemists may not be aware of the strong oxidizing ability of $SOCl_2$, it should be noted that Au(I)→Au(III) oxidation by $SOCl_2$ has been demonstrated under certain conditions.[502,503] $SOCl_2$ oxidizes Cu and Ag readily at room

temperature. Thus, $SOCl_2$ is a strong oxidant, and it can be the oxidant in our case. However, Au cannot be oxidized by $SOCl_2$ alone. No weight loss was detected of an Au film after it was immersed in $SOCl_2$ at room temperature or even at 70 ^oC (refluxing) for 1 week. Purging oxygen into the $SOCl_2$ bath doesn't oxidize Au, either. Py, undoubtedly, plays a very important role in the oxidative dissolution process. We believe that the charge-transfer interaction activates $SOCl_2$ to oxidize Au.

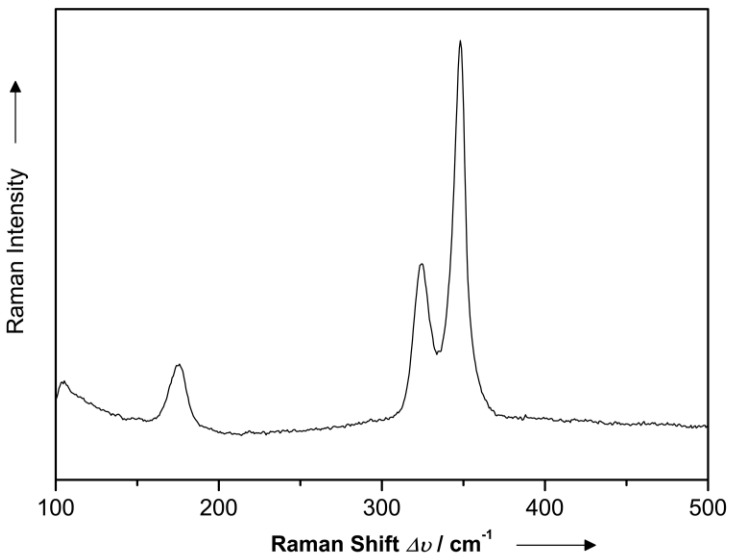

Figure 8.8 Raman spectrum of a vapor-etched Au/Si surface. Vibrations attributed to $[AuCl_4]^-$ structure are observed at 170, 324, and 348 cm^{-1}.

One drawback of thermodynamics is that it doesn't tell the reaction kinetics (in most cases, thermodynamics doesn't relate to kinetics). For example, the coordinative oxidation mechanism may not be able to explain why the dissolution rate of Au is strongly dependent on the recipe of the OAR, especially the organic component such as py, DMF, pyrrolidine, pyrrolidone, isoxazole, isothiazole, pyrazole, imidazole, *etc*. The reaction rate in different OAR can be orders of magnitude different! Moreover, Pd and Pt are less noble than Au, but are not oxidatively dissolved in many recipes of OAR. The

fundamental view of the dissolution reaction, therefore, points toward an interfacial reaction mechanism as shown in Figure 8.9.

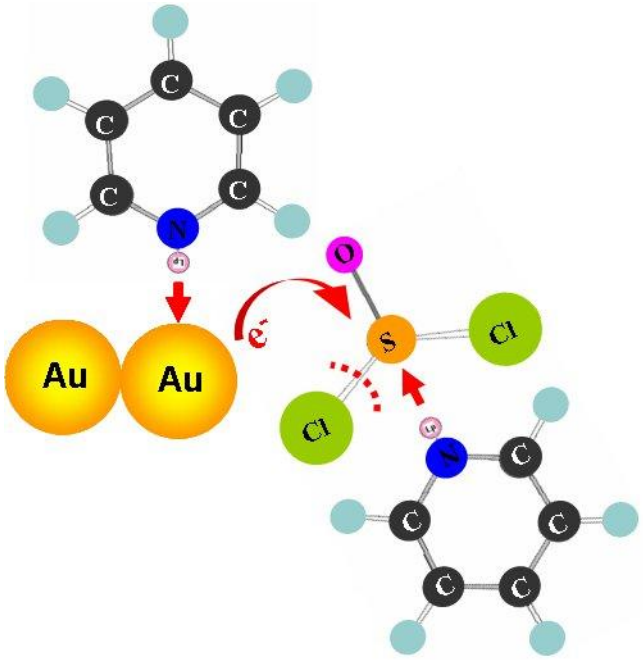

Figure 8.9 A proposed oxidative dissolution mechanism for Au in OAR.

The proposed mechanism involves two important roles by the organic component, say py, in the two major steps. First, py coordinates to the Au surface by putting the non-bonding electrons in py (according to molecular orbital theory) to the accessible and symmetry allowed atomic orbital of the metal element. As such, the work function of the noble metal is effectively reduced (this has been known for quite a while), and therefore, the surface noble metal atoms are more liable to oxidation by the oxidant, *i.e.*, activated $SOCl_2$. Second, py forms the charge-transfer complex with $SOCl_2$ to activate the oxidant; upon capture of the electrons from Au, Cl-S-Cl dissociated to generate the Cl^- as ligand. We propose that the surface coordination between Au and py, and later on, the desorption of py after electron transfer from Au to sulfur, determine the reaction rate. As such, the

electron structure and physical properties of the organic component determine its interactions with $SOCl_2$ and the Au surface, and consequently, determine the dissolution kinetics. As for Pt and Pd in OAR, I believe their solubilities are related to surface passivation. It is well known in the research field of "corrosion science" that pure Pt and Pd are thermodynamically less noble than Au but, in reality, more noble than Au. The reason is that Pt and Pd surfaces passivate against oxidants over a wide range of pH values in aqueous solutions, while Au surface doesn't. This also explains why none of Ti, Ta, Cr, and W can be dissolved in OAR. The passivation prevents the ligand and the oxidant from accessing the metal atoms. To get clearer about the mechanism for the dissolution selectivity, electrochemical characterizations and simulations are needed.

APPENDIX A

ABOUT EPONOL RESIN 53-BH-35

http://www.resins.com/Products/TechnicalDataSheet.aspx?id=4061

Sales Specification

Property	Units	Value	Test Method/Standard
Viscosity at 25°C	cP	U-Z2	ASTM D1544
Color	Gardner	6	ASTM D1544
Solids	%m/m	34-37.5	ASTM D1259

APPENDIX B

ABOUT PYROLYTIC GRAPHITE SHEETS

http://industrial.panasonic.com/www-ctlg/ctlg/qAYA0000_WW.html

Items		PGS 100µm	PGS 70µm	PGS 25µm
Thermal conductivity (W/m·K)	X,Y direction	600 to 800	750 to 950	1500 to 1700
	Z direction	15	15	(15)
Thermal diffusivity (cm^2/s)		9 to 10	9 to 10	9 to 10
Density (g/cm^3)		0.85	1.10	2.10
Specific Heat (at 50 degrees C)(J/gK)		0.85	0.85	0.85
Heat resistance (in Air)(degrees C)		400	400	400
Pull strength (MPa)	X,Y direction	19.6	22.0	30.0
	Z direction	0.4	0.4	0.1
Bending test (times) R5 180 degrees		Over 30000	Over 30000	Over 30000
Electric conductivity (S/cm)		10000	10000	(20000)

APPENDIX C

AUTHOR'S AWARDS, PUBLICATIONS, CONFERENCE PRESENTATIONS, AND PATENTS

C.1 Awards

[1] Chinese Government Award for Outstanding Self-Financed Students Abroad, 2011.

[2] ACS Student Travel Award (Division of Inorganic Chemistry), Spring Meeting, March, 2011.

[3] Finalist for 2010 GT Innovation Competition.

[4] SAIC Student Paper Competition Award Winner, Georgia Institute of Technology, November, 2010.

[5] Research Initiation Award, School of Materials Science & Engineering, Georgia Institute of Technology, April, 2009.

[6] Finalist for 2008 Motorola Graduate Student Fellowship for Research on Electronic Packaging ($1,000).

[7] Finalist for 2008 IEEE CPMT Society Ph.D. Student Fellowship (changed to CPMT student travel award after 2008).

C.2 Journal Publications

[1] **Lin W**, Xiu YH, Jiang HJ, Zhang RW, Hildreth O, Moon KS, et al. Self-assembled monolayer-assisted chemical transfer of in situ functionalized carbon nanotubes. Journal of the American Chemical Society. 2008 Jul;130(30):9636-9637.

[2] Hildreth OJ, **Lin W**, Wong CP. Effect of Catalyst Shape and Etchant Composition on Etching Direction in Metal-Assisted Chemical Etching of Silicon to Fabricate 3D Nanostructures. ACS Nano. 2009 Dec;3(12):4033-4042.

[3] Jiang HJ, Yim MJ, **Lin W**, Wong CP. Novel Nonconductive Adhesives/Films With Carbon Nanotubes for High-Performance Interconnects. IEEE Transactions on Components and Packaging Technologies. 2009 Dec;32(4):754-758.

[4] **Lin W**, Moon KS, Wong CP. A Combined Process of In Situ Functionalization and Microwave Treatment to Achieve Ultrasmall Thermal Expansion of Aligned Carbon Nanotube-Polymer Composites: Toward Applications as Thermal Interface Materials. Advanced Materials. 2009 Jun;21(23):2421-2424.

[5] Li Z, Yao YG, Lin ZY, Moon KS, **Lin W**, Wong CP. Ultrafast, dry microwave synthesis of graphene sheets. Journal of Materials Chemistry. 2010;20(23):4781-4783.

[6] **Lin W**, Moon KS, Zhang SJ, Ding Y, Shang JT, Chen MX, et al. Microwave Makes Carbon Nanotubes Less Defective. ACS Nano. 2010 Mar;4(3):1716-1722.

[7] **Lin W**, Wong CP. Comment on "The Effect of Stress Transfer Within Double-Walled Carbon Nanotubes Upon Their Ability to Reinforce Composites". Advanced Materials. 2010 Mar;22(11):1177-1179.

[8] **Lin W**, Zhang RW, Jang SS, Wong CP, Hong JI. "Organic Aqua Regia"-Powerful Liquids for Dissolving Noble Metals. Angewandte Chemie-International Edition. 2010;49(43):7929-7932.

[9] **Lin W**, Zhang RW, Moon KS, Wong CP. Synthesis of High-Quality Vertically Aligned Carbon Nanotubes on Bulk Copper Substrate for Thermal Management. IEEE Transactions on Advanced Packaging. 2010 May;33(2):370-376.

[10] **Lin W**, Zhang RW, Moon KS, Wong CP. Molecular phonon couplers at carbon nanotube/substrate interface to enhance interfacial thermal transport. Carbon. 2010 Jan;48(1):107-113.

[11] **Lin W**, Zhang RW, Wong CP. Modeling of Thermal Conductivity of Graphite Nanosheet Composites. Journal of Electronic Materials. 2010 Mar;39(3):268-272.

[12] Zhang RW, **Lin W**, Lawrence K, Wong CP. Highly reliable, low cost, isotropically conductive adhesives filled with Ag-coated Cu flakes for electronic packaging applications. International Journal of Adhesion and Adhesives. 2010 Sep;30(6):403-407.

[13] Zhang RW, **Lin W**, Moon KS, Wong CP. Fast Preparation of Printable Highly Conductive Polymer Composites by Thermal Decomposition of Silver Carboxylate and Sintering of Silver Nanoparticles. ACS Applied Materials & Interfaces. 2010 Sep;2(9):2637-2645.

[14] Zhang RW, Moon KS, **Lin W**, Duan YQ, Lotz SM, Wong CP. Interfacial Design of Anisotropic Conductive Adhesive Based Interconnects Using Molecular Wires and Understanding of Their Electrical Conduction. IEEE Transactions on Advanced Packaging. 2010 Nov;33(4):892-898.

[15] Zhang RW, Moon KS, **Lin W**, Wong CP. Preparation of highly conductive polymer composites by low temperature sintering of silver nanoparticles. Journal of Materials Chemistry. 2010;20(10):2018-2023.

[16] Zhang SJ, **Lin W**, Wong CP, Bucknall DG, Kumar S. Composites of Carbon Nanotube Fibers Prepared by Polymer Crystallization. ACS Applied Materials & Interfaces. 2010 Jun;2(6):1642-1647.

[17] Zhang SJ, **Lin W**, Yu XF, Wong CP, Cheng SZD, Bucknall DG. Surface-Induced Polymer Crystallization in High Volume Fraction Aligned Carbon Nanotube-Polymer Composites. Macromolecular Chemistry and Physics. 2010 May;211(9):1003-1011.

[18] Zhang SJ, **Lin W**, Zhu LB, Wong CP, Bucknall DG. gamma-Form Transcrystals of Poly(propylene) Induced by Individual Carbon Nanotubes. Macromolecular Chemistry and Physics. 2010 Jun;211(12):1348-1354.

[19] Shang JT, Chen BY, **Lin W**, Wong CP, Zhang D, Xu C, et al. Preparation of wafer-level glass cavities by a low-cost chemical foaming process (CFP). Lab on a Chip. 2011;11(8):1532-1540.

[20] Yang C, Gu HW, **Lin W**, Yuen MM, Wong CP, Xiong MY, et al. Silver Nanowires: From Scalable Synthesis to Recyclable Foldable Electronics. Advanced Materials. 2011 Jul;23(27):3052-3055.

[21] Zhang RW, **Lin W**, Moon KS, Liang QZ, Wong CP. Highly Reliable Copper-Based Conductive Adhesives Using an Amine Curing Agent for in Situ Oxidation/Corrosion Prevention. IEEE Transactions on Components Packaging and Manufacturing Technology. 2011 Jan;1(1):25-32.

[22] Zhang RW, Moon KS, **Lin W**, Agar JC, Wong CP. A simple, low-cost approach to prepare flexible highly conductive polymer composites by in situ reduction of silver carboxylate for flexible electronic applications. Composites Science and Technology. 2011 Feb;71(4):528-534.

[23] **Lin W**, Wong CP. Recovery of High-purity Pt from Au-Pt Core-Shell Nanoparticle Catalyst. Rare Metals, in press.

[24] Li Z, **Lin W**, Moon KS, Wilkins SJ, Yao YG, Watkins K, Morato L, Wong CP. Metal catalyst residues in carbon nanotubes decrease the thermal stability of carbon nanotube/silicone composites. Carbon. 2011 Nov;49(13): 4138-4148.

[25] **Lin W,** Wong CP. Fast etching of copper in thionyl chloride/acetonitrile solutions. Corrosion Science, 2011 Oct;53(10):3055-3057.

[26] **Lin W**, Shang JT, Gu WT, Wong CP. Collective Thermal Transport Property of Vertically Aligned Carbon Nanotubes: A Systematic Study by Laser Flash Technique. Carbon, revision submitted.

[27] Yang C, **Lin W**, Li ZY, Zhang RW, Wen HR, Gao B, Chen GH, Gao P, Yuen, MF, Wong CP. Water-borne Isotropically Conductive Adhesives: a Green Material for Flexible Printed Conductor and Interconnect. Advanced Functional Materials, in press.

[28] Yuan DJ, **Lin W**, Guo R, Wong CP, Das S. Vertically Aligned and Periodically Distributed Carbon Nanotube Bundles Grown by a Combination of Laser Interface Ablation and Metal-catalyzed Chemical Vapor Deposition. Nanotechnology, under review.

[29] Ye H, Wang XJ, **Lin W**, Wong CP, Zhang ZM. Infrared Penetration Depth of Vertically Aligned Carbon Nanotubes. Applied Physics Letters, under review.

[30] Liu Y, **Lin W**, Lin ZY, Xiu YH, Wong CP. A Combined Etching Process toward Robust Superhydrophobic SiC Surfaces. Nanotechnology, under review.

[31] **Lin W**, Wong CP. Review on Modeling of Thermal Conductivity of Polymer-based Composites, Composites Science and Technology, in preparation.

C.3 Book Chapters

[1] Lin W. and Wong C. P. (2010) Applications of Carbon Nanotubes as Electrical Interconnects and Thermal Interface Materials, Chapter 4, in Nano-Bio- Electronic, Photonic and MEMS Packaging, C. P. Wong, Y. Li and K. Moon, Ed., Springer.

[2] Lin W., Hildreth O. J. and Wong C. P. (2010) Carbon Nanotubes as Thermal Interface Materials for Electronic and Photonic Packaging, in Smart Systems Integration and Reliability, Bernd Michel, Klaus-Dieter Lang, Ed., goldenbogen.

C.4 Conference Presentations

[1] Lin W. and Wong C. P. (2011) "A Breakthrough in Highly Reliable Measurement of Thermal Transport Properties of Vertically aligned Carbon Nanotubes", IEEE 61st Electronic Components Technology Conference, June, Florida, Orlando.

[2] Lin W. (2011) "Organic Aqua Regia: Discovery and Broad Applications", ACS 241st National Meeting, March, California, Anaheim.

[3] Lin W. and Wong C. P. (2010) "Vertically Aligned Carbon Nanotubes for Thermal Interface Materials: Parameter Studies and Laser Flash Measurement". IEEE 60th Electronic Components & Technology Conference, June, Nevada, Las Vegas.

[4] Lin W. (2010) Vertically Aligned Carbon Nanotubes for Thermal Interface Materials. Invited speaker by Samsung Electronics.

[5] Lin W. and Wong C. P. (2009) "Synthesis and Assembling of Vertically Aligned Carbon Nanotubes for Thermal Interface Materials". IEEE 59th Electronic Components & Technology Conference, May, California, San Diego.

[6] Lin W. and Wong C. P. (2008) "Assembling of Carbon Nanotube Structures by Chemical Anchoring for Packaging Applications". IEEE 58th Electronic Components & Technology Conference, May, Florida, Orlando.

[7] Lin W., Jiang H. J., Wong C. P. (2008) Surface functionalized carbon nanotube film/polymer composites for thermal interface materials applications. 36th NATAS Annual Conference on Thermal Analysis and Applications, August, Atlanta.

C.5 Patents Pending

[1] Lin W, Wong CP. "Structures including carbon nanotubes, methods of making structures, and methods of using structures", Utility patent, 2010, Application serial No. 12/800,934.

[2] Lin W, Zhang RW, Wong CP. "Compositions and Methods for the Recovery of Metals", Utility patent, 2011, filing No. PCT/US2011/050317.

C.6 Research Highlights

The discovery of "*organic aqua regia*", and its important potential applications, have been highlighted both in *Nature* (2010, vol. 467, page 503), and *Science* (2010, vol. 330, page 153), featured in *Chemistry World* (2010, Vol. 7), *C&EN* (2011, March), *Chemical Processing* (2010, Dec.), *etc*.
http://www.rsc.org/chemistryworld/News/2010/September/23091001.asp
http://pubs.acs.org/cen/news/89/i14/8914notw4.html
http://www.chemicalprocessing.com/articles/2010/217.html
http://www.gatech.edu/newsroom/release.html?nid=62402
http://www.sciencedaily.com/releases/2010/10/101028152502.htm

C.7 Service as Journal Referee

CARBON
Nanotechnology
Journal of Physics D-Applied Physics
Smart Materials and Structures

Journal of Materials and Environment Science
ASME—Journal of Heat Transfer
Journal of Nanomaterials

REFERENCES

[1] Martel R, Schmidt T, Shea HR, Hertel T, Avouris P. Single- and multi-wall carbon nanotube field-effect transistors. Appl Phys Lett. 1998 Oct;73(17):2447-9.

[2] Tans SJ, Verschueren ARM, Dekker C. Room-temperature transistor based on a single carbon nanotube. Nature. 1998 May;393(6680):49-52.

[3] Kreupl F, Graham AP, Duesberg GS, Steinhogl W, Liebau M, Unger E, et al. Carbon nanotubes in interconnect applications. Microelectron Eng. 2002 Oct;64(1-4):399-408.

[4] Li J, Ye Q, Cassell A, Ng HT, Stevens R, Han J, et al. Bottom-up approach for carbon nanotube interconnects. Appl Phys Lett. 2003 Apr;82(15):2491-3.

[5] Naeemi A, Sarvari R, Meindl JD. Performance comparison between carbon nanotube and copper interconnects for gigascale integration (GSI). IEEE Electron Device Lett. 2005 Feb;26(2):84-6.

[6] Lin W, Moon KS, Wong CP. A Combined Process of In Situ Functionalization and Microwave Treatment to Achieve Ultrasmall Thermal Expansion of Aligned Carbon Nanotube-Polymer Composites: Toward Applications as Thermal Interface Materials. Adv Mater. 2009 Jun;21(23):2421-4.

[7] Tong T, Zhao Y, Delzeit L, Kashani A, Meyyappan M, Majumdar A. Dense, vertically aligned multiwalled carbon nanotube arrays as thermal interface materials. IEEE Trans Compon Packaging Technol. 2007 Mar;30(1):92-100.

[8] Xu J, Fisher TS. Enhancement of thermal interface materials with carbon nanotube arrays. Int J Heat Mass Transf. 2006 May;49(9-10):1658-66.

[9] Moore GE. Progress in Digital Integrated Electronics. International Electron Devices Meetings. 1975 1975(Dec. 2-4,): 11-3.

[10] Steinlesberger G, Engelhardt M, Schindler G, Steinhogl W, von Glasow A, Mosig K, et al. Electrical assessment of copper damascene interconnects down to sub-50 nm feature sizes. Microelectron Eng. 2002 Oct;64(1-4):409-16.

[11] Nihei M, Horibe M, Kawabata A, Awano Y. Simultaneous formation of multiwall carbon nanotubes and their end-bonded ohmic contacts to Ti electrodes for future ULSI interconnects. Jpn J Appl Phys Part 1 - Regul Pap Short Notes Rev Pap. 2004 Apr;43(4B):1856-9.

[12] Naeemi A, Meindl JD. Impact of electron-phonon scattering on the performance of carbon nanotube interconnects for GSI. IEEE Electron Device Lett. 2005 Jul;26(7):476-8.

[13] Awano Y. Carbon nanotube technologies for LSI via interconnects. IEICE Trans Electron. 2006 Nov;E89C(11):1499-503.

[14] Park M, Cola BA, Siegmund T, Xu J, Maschmann MR, Fisher TS, et al. Effects of a carbon nanotube layer on electrical contact resistance between copper substrates. Nanotechnology. 2006 May;17(9):2294-303.

[15] Nieuwoudt A, Massoud Y. Understanding the impact of inductance in carbon nanotube bundles for VLSI interconnect using scalable modeling techniques. IEEE Trans Nanotechnol. 2006 Nov;5(6):758-65.

[16] Xu T, Wang Z, Miao J, Chen X, Tan CM. Aligned carbon nanotubes for through-wafer interconnects. Appl Phys Lett. 2007 Jul;91(4).

[17] Chu RC. The challenges of electronic cooling: Past, current and future. J Electron Packag. 2004 Dec;126(4):491-500.

[18] Kenny T. DARPA NTI Project Annual Review. 2009.

[19] Hamada N, Sawada S, Oshiyama A. New One-Dimensional Conductors - Graphitic Microtubules. Phys Rev Lett. 1992 Mar;68(10):1579-81.

[20] Dresselhaus MS, Dresselhaus G, Saito R. Carbon-Fibers Based on C-60 and Their Symmetry. Phys Rev B. 1992 Mar;45(11):6234-42.

[21] Dresselhaus MS, Dresselhaus G, Saito R, Jorio A. Raman spectroscopy of carbon nanotubes. Physics Reports-Review Section of Physics Letters. 2005 Mar;409(2):47-99.

[22] Ajayan PM, Ebbesen TW. Nanometre-size tubes of carbon. Rep Prog Phys. 1997 Oct;60(10):1025-62.

[23] Reznik D, Olk CH, Neumann DA, Copley JRD. X-RAY-POWDER DIFFRACTION FROM CARBON NANOTUBES AND NANOPARTICLES. Phys Rev B. 1995 Jul;52(1):116-24.

[24] Bandow S. Radial thermal expansion of purified multiwall carbon nanotubes measured by X-ray diffraction. Jpn J Appl Phys Part 2 - Lett. 1997 Oct;36(10B):L1403-L5.

[25] Maniwa Y, Fujiwara R, Kira H, Tou H, Nishibori E, Takata M, et al. Multiwalled carbon nanotubes grown in hydrogen atmosphere: An x-ray diffraction study. Phys Rev B. 2001 Aug;64(7):4.

[26] Amelinckx S, Bernaerts D, Zhang XB, Vantendeloo G, Vanlanduyt J. A Structure Model and Growth-Mechanism for Multishell Carbon Nanotubes. Science. 1995 Mar;267(5202):1334-8.

[27] Cui H, Zhou O, Stoner BR. Deposition of aligned bamboo-like carbon nanotubes via microwave plasma enhanced chemical vapor deposition. J Appl Phys. 2000 Nov;88(10):6072-4.

[28] Sui YC, Acosta DR, Gonzalez-Leon JA, Bermudez A, Feuchtwanger J, Cui BZ, et al. Structure, thermal stability, and deformation of multibranched carbon nanotubes synthesized by CVD in the AAO template. J Phys Chem B. 2001 Mar;105(8):1523-7.

[29] Dresselhaus MS, Dresselhaus G, Avouris P. Carbon Nanotubes -- Synthesis, Structure, Properties and Applications: Springer-Verlag 2001.

[30] Odom TW, Huang JL, Kim P, Lieber CM. Atomic structure and electronic properties of single-walled carbon nanotubes. Nature. 1998 Jan;391(6662):62-4.

[31] Wildoer JWG, Venema LC, Rinzler AG, Smalley RE, Dekker C. Electronic structure of atomically resolved carbon nanotubes. Nature. 1998 Jan;391(6662):59-62.

[32] Peierl RF. Quantum Theory of Solids: Clarendon, Oxford 1995.

[33] Yao Z, Kane CL, Dekker C. High-field electrical transport in single-wall carbon nanotubes. Phys Rev Lett. 2000 Mar;84(13):2941-4.

[34] Wei BQ, Vajtai R, Ajayan PM. Reliability and current carrying capacity of carbon nanotubes. Appl Phys Lett. 2001 Aug;79(8):1172-4.

[35] Collins PC, Arnold MS, Avouris P. Engineering carbon nanotubes and nanotube circuits using electrical breakdown. Science. 2001 Apr;292(5517):706-9.

[36] Bachtold A, Strunk C, Salvetat JP, Bonard JM, Forro L, Nussbaumer T, et al. Aharonov-Bohm oscillations in carbon nanotubes. Nature. 1999 Feb;397(6721):673-5.

[37] McEuen PL, Bockrath M, Cobden DH, Yoon YG, Louie SG. Disorder, pseudospins, and backscattering in carbon nanotubes. Phys Rev Lett. 1999 Dec;83(24):5098-101.

[38] Li HJ, Lu WG, Li JJ, Bai XD, Gu CZ. Multichannel ballistic transport in multiwall carbon nanotubes. Phys Rev Lett. 2005 Aug;95(8).

[39] Naeemi A, Meindl JD. Compact physical models for multiwall carbon-nanotube interconnects. IEEE Electron Device Lett. 2006 May;27(5):338-40.

[40] Matsumura H, Ando T. Conductance of carbon nanotubes with a Stone-Wales defect. Journal of the Physical Society of Japan. 2001 Sep;70(9):2657-65.

[41] Watts PCP, Hsu WK, Kroto HW, Walton DRM. Are bulk defective carbon nanotubes less electrically conducting? Nano Lett. 2003 Apr;3(4):549-53.

[42] He Y, Zhang C, Cao C, Cheng HP. Effects of strain and defects on the electron conductance of metallic carbon nanotubes. Phys Rev B. 2007 Jun;75(23).

[43] Reyes SA, Struck A, Eggert S. Lattice defects and boundaries in conducting carbon nanotubes. Phys Rev B. 2009 Aug;80(7).

[44] Stetter A, Vancea J, Back CH. Conductivity of multiwall carbon nanotubes: Role of multiple shells and defects. Phys Rev B. Sep;82(11).

[45] Roche S, Triozon F, Rubio A, Mayou D. Electronic conduction in multi-walled carbon nanotubes: role of intershell coupling and incommensurability. Phys Lett A. 2001 Jun;285(1-2):94-100.

[46] Yoon YG, Mazzoni MSC, Choi HJ, Ihm J, Louie SG. Structural deformation and intertube conductance of crossed carbon nanotube junctions. Phys Rev Lett. 2001 Jan;86(4):688-91.

[47] Buldum A, Lu JP. Contact resistance between carbon nanotubes. Phys Rev B. 2001 Apr;63(16).

[48] Tersoff J. Contact resistance of carbon nanotubes. Appl Phys Lett. 1999 Apr;74(15):2122-4.

[49] Lee JO, Park C, Kim JJ, Kim J, Park JW, Yoo KH. Formation of low-resistance ohmic contacts between carbon nanotube and metal electrodes by a rapid thermal annealing method. Journal of Physics D-Applied Physics. 2000 Aug;33(16):1953-6.

[50] Kaushik BK, Goel S, Rauthan G. Future VLSI interconnects: optical fiber or carbon nanotube - a review. Microelectron Int. 2007;24(2):53-63.

[51] Graham AP, Duesberg GS, Seidel R, Liebau M, Unger E, Kreupl F, et al. Towards the integration of carbon nanotubes in microelectronics. 2004: Elsevier Science Sa; 2004. p. 1296-300.

[52] Moshammer K, Hennrich F, Kappes MM. Selective Suspension in Aqueous Sodium Dodecyl Sulfate According to Electronic Structure Type Allows Simple Separation of Metallic from Semiconducting Single-Walled Carbon Nanotubes. Nano Research. 2009 Aug;2(8):599-606.

[53] Tanaka T, Jin H, Miyata Y, Fujii S, Suga H, Naitoh Y, et al. Simple and Scalable Gel-Based Separation of Metallic and Semiconducting Carbon Nanotubes. Nano Lett. 2009 Apr;9(4):1497-500.

[54] Tanaka T, Jin HH, Miyata Y, Kataura H. High-Yield Separation of Metallic and Semiconducting Single-Wall Carbon Nanotubes by Agarose Gel Electrophoresis. Appl Phys Express. 2008 Nov;1(11).

[55] Tanaka T, Urabe Y, Nishide D, Kataura H. Continuous Separation of Metallic and Semiconducting Carbon Nanotubes Using Agarose Gel. Appl Phys Express. 2009 Dec;2(12).

[56] Yanagi K, Iitsuka T, Fujii S, Kataura H. Separations of Metallic and Semiconducting Carbon Nanotubes by Using Sucrose as a Gradient Medium. J Phys Chem C. 2008 Dec;112(48):18889-94.

[57] Huang SM, Cai XY, Liu J. Growth of millimeter-long and horizontally aligned single-walled carbon nanotubes on flat substrates. J Am Chem Soc. 2003 May;125(19):5636-7.

[58] Zhang YG, Chang AL, Cao J, Wang Q, Kim W, Li YM, et al. Electric-field-directed growth of aligned single-walled carbon nanotubes. Appl Phys Lett. 2001 Nov;79(19):3155-7.

[59] Chai Y, Xiao ZY, Chan PCH. Electron-shading effect on the horizontal aligned growth of carbon nanotubes. Appl Phys Lett. 2009 Jan;94(4).

[60] Lan C, Zakharov DN, Reifenberger RG. Determining the optimal contact length for a metal/multiwalled carbon nanotube interconnect. Appl Phys Lett. 2008 May;92(21).

[61] Nihei M, Horibe M, Kawabata A, Awano Y. Simultaneous formation of multiwall carbon nanotubes and their end-bonded ohmic contacts to Ti electrodes for future ULSI interconnects. 2004; 2004. p. 1856-9.

[62] Krupke R, Hennrich F, von Lohneysen H, Kappes MM. Separation of metallic from semiconducting single-walled carbon nanotubes. Science. 2003 Jul;301(5631):344-7.

[63] Liu H, Feng Y, Tanaka T, Urabe Y, Kataura H. Diameter-Selective Metal/Semiconductor Separation of Single-wall Carbon Nanotubes by Agarose Gel. J Phys Chem C. May;114(20):9270-6.

[64] Lu FSLFS, Meziani MJ, Cao L, Sun YP. Separated Metallic and Semiconducting Single-Walled Carbon Nanotubes: Opportunities in Transparent Electrodes and Beyond. Langmuir. Apr;27(8):4339-50.

[65] Voggu R, Rao KV, George SJ, Rao CNR. A Simple Method of Separating Metallic and Semiconducting Single-Walled Carbon Nanotubes Based on Molecular Charge Transfer. J Am Chem Soc. Apr;132(16):5560-1.

[66] Campidelli S, Meneghetti M, Prato M. Separation of metallic and semiconducting single-walled carbon nanotubes via covalent functionatization. Small. 2007 Oct;3(10):1672-6.

[67] Lu J, Lai L, Luo G, Zhou J, Qin R, Wang D, et al. Why semiconducting single-watted carbon nanotubes are separated from their metaltic counterparts. Small. 2007 Sep;3(9):1566-76.

[68] Maeda Y, Kimura S, Kanda M, Hirashima Y, Hasegawa T, Wakahara T, et al. Large-scale separation of metallic and semiconducting single-walled carbon nanotubes. J Am Chem Soc. 2005 Jul;127(29):10287-90.

[69] Menard-Moyon C, Izard N, Doris E, Mioskowski C. Separation of semiconducting from metallic carbon nanotubes by selective functionalization with azomethine ylides. J Am Chem Soc. 2006 May;128(20):6552-3.

[70] R&D. PcwI.

[71] Baughman RH, Zakhidov AA, de Heer WA. Carbon nanotubes - the route toward applications. Science. 2002 Aug;297(5582):787-92.

[72] Pop E, Mann D, Wang Q, Goodson K, Dai HJ. Thermal conductance of an individual single-wall carbon nanotube above room temperature. Nano Letters. 2006 Jan;6(1):96-100.

[73] Fujii M, Zhang X, Xie HQ, Ago H, Takahashi K, Ikuta T, et al. Measuring the thermal conductivity of a single carbon nanotube. Phys Rev Lett. 2005 Aug;95(6).

[74] Hone J, Whitney M, Piskoti C, Zettl A. Thermal conductivity of single-walled carbon nanotubes. Phys Rev B. 1999 Jan;59(4):R2514-R6.

[75] Hone J, Whitney M, Zettl A. Thermal conductivity of single-walled carbon nanotubes. Synthetic Metals. 1999 Jun;103(1-3):2498-9.

[76] Mingo N, Broido DA. Carbon nanotube ballistic thermal conductance and its limits. Phys Rev Lett. 2005 Aug;95(9).

[77] Osman MA, Srivastava D. Temperature dependence of the thermal conductivity of single-wall carbon nanotubes. Nanotechnology. 2001 Mar;12(1):21-4.

[78] Yu CH, Shi L, Yao Z, Li DY, Majumdar A. Thermal conductance and thermopower of an individual single-wall carbon nanotube. Nano Lett. 2005 Sep;5(9):1842-6.

[79] Berber S, Kwon YK, Tomanek D. Unusually high thermal conductivity of carbon nanotubes. Phys Rev Lett. 2000 May;84(20):4613-6.

[80] Che JW, Cagin T, Goddard WA. Thermal conductivity of carbon nanotubes. Nanotechnology. 2000 Jun;11(2):65-9.

[81] Choi TY, Poulikakos D, Tharian J, Sennhauser U. Measurement of the thermal conductivity of individual carbon nanotubes by the four-point three-omega method. Nano Letters. 2006 Aug;6(8):1589-93.

[82] Mingo N, Broido DA. Length dependence of carbon nanotube thermal conductivity and the "problem of long waves". Nano Letters. 2005 Jul;5(7):1221-5.

[83] Zhang ZM. Nano/Microscale Heat Transfer: 158-164.

[84] Yamamoto T, Nakazawa Y, Watanabe K. Control of electron- and phonon-derived thermal conductances in carbon nanotubes. New J Phys. 2007;9(245).

[85] Zhang W, Zhu ZY, Wang F, Wang TT, Sun LT, Wang ZX. Chirality dependence of the thermal conductivity of carbon nanotubes. Nanotechnology. 2004 Aug;15(8):936-9.

[86] Kim P, Shi L, Majumdar A, McEuen PL. Thermal transport measurements of individual multiwalled nanotubes. Phys Rev Lett. 2001 Nov;8721(21).

[87] Cao JX, Yan XH, Xiao Y, Ding JW. Thermal conductivity of zigzag single-walled carbon nanotubes: Role of the umklapp process. Phys Rev B. 2004 Feb;69(7):4.

[88] Maruyama S. A molecular dynamics simulation of heat conduction of a finite length single-walled carbon nanotube. Microscale Thermophys Eng. 2003 Jan-Mar;7(1):41-50.

[89] Padgett CW, Brenner DW. Influence of chemisorption on the thermal conductivity of single-wall carbon nanotubes. Nano Letters. 2004 Jun;4(6):1051-3.

[90] Bi KD, Chen YF, Yang JK, Wang YJ, Chen MH. Molecular dynamics simulation of thermal conductivity of single-wall carbon nanotubes. Physics Letters A. 2006 Jan;350(1-2):150-3.

[91] Choi TY, Poulikakos D, Tharian J, Sennhauser U. Measurement of thermal conductivity of individual multiwalled carbon nanotubes by the 3-omega method. Appl Phys Lett. 2005;87(1).

[92] Pettes MT, Shi L. Thermal and Structural Characterizations of Individual Single-, Double-, and Multi-Walled Carbon Nanotubes. Adv Funct Mater. 2009 Dec;19(24):3918-25.

[93] Benedict LX, Louie SG, Cohen ML. Heat capacity of carbon nanotubes. Solid State Commun. 1996 Oct;100(3):177-80.

[94] Yamamoto T, Watanabe K. Nonequilibrium Green's function approach to phonon transport in defective carbon nanotubes. Phys Rev Lett. 2006 Jun;96(25).

[95] Wang ZL, Tang DW, Li XB, Zheng XH, Zhang WG, Zheng LX, et al. Length-dependent thermal conductivity of an individual single-wall carbon nanotube. Appl Phys Lett. 2007 Sep;91(12).

[96] Mizel A, Benedict LX, Cohen ML, Louie SG, Zettl A, Budraa NK, et al. Analysis of the low-temperature specific heat of multiwalled carbon nanotubes and carbon nanotube ropes. Phys Rev B. 1999 Aug;60(5):3264-70.

[97] Yang DJ, Zhang Q, Chen G, Yoon SF, Ahn J, Wang SG, et al. Thermal conductivity of multiwalled carbon nanotubes. Phys Rev B. 2002 Oct;66(16).

[98] Hone J, Batlogg B, Benes Z, Johnson AT, Fischer JE. Quantized phonon spectrum of single-wall carbon nanotubes. Science. 2000 Sep;289(5485):1730-3.

[99] Yi W, Lu L, Zhang DL, Pan ZW, Xie SS. Linear specific heat of carbon nanotubes. Phys Rev B. 1999 Apr;59(14):R9015-R8.

[100] Prasher RS, Hu XJ, Chalopin Y, Mingo N, Lofgreen K, Volz S, et al. Turning Carbon Nanotubes from Exceptional Heat Conductors into Insulators. Phys Rev Lett. 2009 Mar;102(10).

[101] Ebbesen TW, Ajayan PM. Large-Scale Synthesis of Carbon Nanotubes. Nature. 1992 Jul;358(6383):220-2.

[102] Bethune DS, Kiang CH, Devries MS, Gorman G, Savoy R, Vazquez J, et al. Cobalt-Catalyzed Growth of Carbon Nanotubes with Single-Atomic-Layerwalls. Nature. 1993 Jun;363(6430):605-7.

[103] Thess A, Lee R, Nikolaev P, Dai HJ, Petit P, Robert J, et al. Crystalline ropes of metallic carbon nanotubes. Science. 1996 Jul;273(5274):483-7.

[104] Liu J, Rinzler AG, Dai HJ, Hafner JH, Bradley RK, Boul PJ, et al. Fullerene pipes. Science. 1998 May;280(5367):1253-6.

[105] Hata K, Futaba DN, Mizuno K, Namai T, Yumura M, Iijima S. Water-assisted highly efficient synthesis of impurity-free single-waited carbon nanotubes. Science. 2004 Nov;306(5700):1362-4.

[106] Zhu LB, Xiu YH, Hess DW, Wong CP. Aligned carbon nanotube stacks by water-assisted selective etching. Nano Lett. 2005 Dec;5(12):2641-5.

[107] Qu L, Dai L. Gecko-foot-mimetic aligned single-walled carbon nanotube dry adhesives with unique electrical and thermal properties. Adv Mater. 2007 Nov;19(22):3844-7.

[108] Hofmann S, Ducati C, Robertson J, Kleinsorge B. Low-temperature growth of carbon nanotubes by plasma-enhanced chemical vapor deposition. Appl Phys Lett. 2003 Jul;83(1):135-7.

[109] Nikolaev P, Bronikowski MJ, Bradley RK, Rohmund F, Colbert DT, Smith KA, et al. Gas-phase catalytic growth of single-walled carbon nanotubes from carbon monoxide. Chem Phys Lett. 1999 Nov;313(1-2):91-7.

[110] Andrews R, Jacques D, Rao AM, Derbyshire F, Qian D, Fan X, et al. Continuous production of aligned carbon nanotubes: a step closer to commercial realization. Chem Phys Lett. 1999 Apr;303(5-6):467-74.

[111] Xu YQ, Flor E, Kim MJ, Hamadani B, Schmidt H, Smalley RE, et al. Vertical array growth of small diameter single-walled carbon nanotubes. J Am Chem Soc. 2006 May;128(20):6560-1.

[112] Bower C, Zhu W, Jin SH, Zhou O. Plasma-induced alignment of carbon nanotubes. Appl Phys Lett. 2000 Aug;77(6):830-2.

[113] Choi YC, Bae DJ, Lee YH, Lee BS, Park GS, Choi WB, et al. Growth of carbon nanotubes by microwave plasma-enhanced chemical vapor deposition at low temperature. J Vac Sci Technol A-Vac Surf Films. 2000 Jul-Aug;18(4):1864-8.

[114] Devaux X, Vergnat M. On the low-temperature synthesis of SWCNTs by thermal CVD. Physica E. 2008 May;40(7):2268-71.

[115] Liu J, Czerw R, Carroll DL. Large-scale synthesis of highly aligned nitrogen doped carbon nanotubes by injection chemical vapor deposition methods. J Mater Res. 2005 Feb;20(2):538-43.

[116] Hou HQ, Schaper AK, Jun Z, Weller F, Greiner A. Large-scale synthesis of aligned carbon nanotubes using FeCl3 as floating catalyst precursor. Chemistry of Materials. 2003 Jan;15(2):580-5.

[117] Zhang XF, Cao AY, Wei BQ, Li YH, Wei JQ, Xu CL, et al. Rapid growth of well-aligned carbon nanotube arrays. Chem Phys Lett. 2002 Aug;362(3-4):285-90.

[118] Wang W, Yang KQ, Gaillard J, Bandaru PR, Rao AM. Rational synthesis of helically coiled carbon nanowires and nanotubes through the use of tin and indium catalysts. Adv Mater. 2008 Jan;20(1):179-2.

[119] Endo M, Kroto HW. FORMATION OF CARBON NANOFIBERS. J Phys Chem. 1992 Aug;96(17):6941-4.

[120] Ulmer G, Campbell EEB, Kuhnle R, Busmann HG, Hertel IV. LASER MASS SPECTROSCOPIC INVESTIGATIONS OF PURIFIED, LABORATORY-PRODUCED C60/C70. Chem Phys Lett. 1991 Jul;182(2):114-9.

[121] McElvany SW, Ross MM, Goroff NS, Diederich F. CYCLOCARBON COALESCENCE - MECHANISMS FOR TAILOR-MADE FULLERENE FORMATION. Science. 1993 Mar;259(5101):1594-6.

[122] Iijima S. GROWTH OF CARBON NANOTUBES. 1993; 1993. p. 172-80.

[123] Iijima S. Helical Microtubules of Graphitic Carbon. Nature. 1991 Nov;354(6348):56-8.

[124] Jin C, Suenaga K, Iijima S. How does a carbon nanotube grow? An in situ investigation on the cap evolution. ACS Nano. 2008 Jun;2(6):1275-9.

[125] Amelinckx S, Zhang XB, Bernaerts D, Zhang XF, Ivanov V, Nagy JB. A Formation Mechanism for Catalytically Grown Helix-Shaped Graphite Nanotubes. Science. 1994 Jul;265(5172):635-9.

[126] Norskov JK. CHEMISORPTION ON METAL-SURFACES. Rep Prog Phys. 1990 Oct;53(10):1253-95.

[127] Dupuis AC. The catalyst in the CCVD of carbon nanotubes - a review. Prog Mater Sci. 2005 Nov;50(8):929-61.

[128] Sato S, Kawabata A, Kondo D, Nihei M, Awano Y. Carbon nanotube growth from titanium-cobalt bimetallic particles as a catalyst. Chem Phys Lett. 2005 Jan;402(1-3):149-54.

[129] Lee SY, Yamada M, Miyake M. Synthesis of carbon nanotubes over gold nanoparticle supported catalysts. Carbon. 2005 Nov;43(13):2654-63.

[130] Bhaviripudi S, Mile E, Steiner SA, Zare AT, Dresselhaus MS, Belcher AM, et al. CVD synthesis of single-walled carbon nanotubes from gold nanoparticle catalysts. J Am Chem Soc. 2007 Feb;129(6):1516-7.

[131] Vollebregt S, Derakhshandeh J, Ishihara R, Wu MY, Beenakker CIM. Growth of High-Density Self-Aligned Carbon Nanotubes and Nanofibers Using Palladium Catalyst. J Electron Mater. Apr;39(4):371-5.

[132] Owens WT, Rodriguez NM, Baker RTK. CARBON-FILAMENT GROWTH ON PLATINUM CATALYSTS. J Phys Chem. 1992 Jun;96(12):5048-53.

[133] Lobo AO, Antunes EF, Palma MBS, Pacheco-Soares C, Trava-Airoldi W, Corat EJ. Biocompatibility of multi-walled carbon nanotubes grown on titanium and silicon surfaces. Mater Sci Eng C-Biomimetic Supramol Syst. 2008 May;28(4):532-8.

[134] Zhou WW, Han ZY, Wang JY, Zhang Y, Jin Z, Sun X, et al. Copper catalyzing growth of single-walled carbon nanotubes on substrates. Nano Lett. 2006 Dec;6(12):2987-90.

[135] Liu JW, Li XJ, Dai LM. Water-assisted growth of aligned carbon nanotube-ZnO heterojunction arrays. Adv Mater. 2006 Jul;18(13):1740-3.

[136] Lee CJ, Park J, Kim JM, Huh Y, Lee JY, No KS. Low-temperature growth of carbon nanotubes by thermal chemical vapor deposition using Pd, Cr, and Pt as co-catalyst. Chem Phys Lett. 2000 Sep;327(5-6):277-83.

[137] Ruban A, Hammer B, Stoltze P, Skriver HL, Norskov JK. Surface electronic structure and reactivity of transition and noble metals. Journal of Molecular Catalysis a-Chemical. 1997 Feb;115(3):421-9.

[138] Saito Y. NANOPARTICLES AND FILLED NANOCAPSULES. Carbon. 1995;33(7):979-88.

[139] Wagner RS, Ellis WC. VAPOR-LIQUID-SOLID MECHANISM OF SINGLE CRYSTAL GROWTH (NEW METHOD GROWTH CATALYSIS FROM IMPURITY WHISKER EPITAXIAL + LARGE CRYSTALS SI E). Appl Phys Lett. 1964;4(5):89.

[140] Baker RTK, Barber MA, Waite RJ, Harris PS, Feates FS. NUCLEATION AND GROWTH OF CARBON DEPOSITS FROM NICKEL CATALYZED DECOMPOSITION OF ACETYLENE. Journal of Catalysis. 1972;26(1):51-&.

[141] Kukovitsky EF, L'Vov SG, Sainov NA. VLS-growth of carbon nanotubes from the vapor. Chem Phys Lett. 2000 Jan;317(1-2):65-70.

[142] Yang RT, Yang KL. EVIDENCE FOR TEMPERATURE-DRIVEN CARBON DIFFUSION MECHANISM OF COKE DEPOSITION ON CATALYSTS. Journal of Catalysis. 1985;93(1):182-5.

[143] Baker RTK. CATALYTIC GROWTH OF CARBON FILAMENTS. Carbon. 1989;27(3):315-23.

[144] Ding F, Rosen A, Bolton K. The role of the catalytic particle temperature gradient for SWNT growth from small particles. Chem Phys Lett. 2004 Aug;393(4-6):309-13.

[145] Nielsen JR, Trimm DL. MECHANISMS OF CARBON FORMATION ON NICKEL-CONTAINING CATALYSTS. Journal of Catalysis. 1977;48(1-3):155-65.

[146] Baird T, Fryer JR, Grant B. CARBON FORMATION ON IRON AND NICKEL FOILS BY HYDROCARBON PYROLYSIS - REACTIONS AT 700DEGREESC. Carbon. 1974;12(5):591-602.

[147] Oberlin A, Endo M, Koyama T. FILAMENTOUS GROWTH OF CARBON THROUGH BENZENE DECOMPOSITION. J Cryst Growth. 1976;32(3):335-49.

[148] Hofmann S, Csanyi G, Ferrari AC, Payne MC, Robertson J. Surface diffusion: The low activation energy path for nanotube growth. Phys Rev Lett. 2005 Jul;95(3).

[149] Raty JY, Gygi F, Galli G. Growth of carbon nanotubes on metal nanoparticles: A microscopic mechanism from ab initio molecular dynamics simulations. Phys Rev Lett. 2005 Aug;95(9).

[150] Fan SS, Liu L, Liu M. Monitoring the growth of carbon nanotubes by carbon isotope labelling. Nanotechnology. 2003 Oct;14(10):1118-23.

[151] Meshot ER, Hart AJ. Abrupt self-termination of vertically aligned carbon nanotube growth. Appl Phys Lett. 2008 Mar;92(11):3.

[152] Louis B, Gulino G, Vieira R, Amadou J, Dintzer T, Galvagno S, et al. High yield synthesis of multi-walled carbon nanotubes by catalytic decomposition of ethane over iron supported on alumina catalyst. 2005: Elsevier Science Bv; 2005. p. 23-8.

[153] Boehm HP. CARBON FROM CARBON-MONOXIDE DISPROPORTIONATION ON NICKEL AND IRON CATALYSTS - MORPHOLOGICAL STUDIES AND POSSIBLE GROWTH MECHANISMS. Carbon. 1973;11(6):583-4.

[154] Homma Y, Kobayashi Y, Ogino T, Takagi D, Ito R, Jung YJ, et al. Role of transition metal catalysts in single-walled carbon nanotube growth in chemical vapor deposition. J Phys Chem B. 2003 Nov;107(44):12161-4.

[155] Alstrup I. A NEW MODEL EXPLAINING CARBON-FILAMENT GROWTH ON NICKEL, IRON, AND NI-CU ALLOY CATALYSTS. Journal of Catalysis. 1988 Feb;109(2):241-51.

[156] Hofmann S, Sharma R, Ducati C, Du G, Mattevi C, Cepek C, et al. In situ observations of catalyst dynamics during surface-bound carbon nanotube nucleation. Nano Lett. 2007 Mar;7(3):602-8.

[157] Shibuta Y, Elliott JA. A molecular dynamics study of the graphitization ability of transition metals for catalysis of carbon nanotube growth via chemical vapor deposition. Chem Phys Lett. 2009 Apr;472(4-6):200-6.

[158] Ding F, Harutyunyan AR, Yakobson BI. Dislocation theory of chirality-controlled nanotube growth. Proceedings of the National Academy of Sciences of the United States of America. 2009 Feb;106(8):2506-9.

[159] Marchand M, Journet C, Guillot D, Benoit JM, Yakobson BI, Purcell ST. Growing a Carbon Nanotube Atom by Atom: "And Yet It Does Turn". Nano Letters. 2009 Aug;9(8):2961-6.

[160] Shyu YM, Hong FCN. Low-temperature growth and field emission of aligned carbon nanotubes by chemical vapor deposition. Mater Chem Phys. 2001 Nov;72(2):223-7.

[161] Shyu YM, Hong FCN. The effects of pre-treatment and catalyst composition on growth of carbon nanofibers at low temperature. Diam Relat Mat. 2001 Mar-Jul;10(3-7):1241-5.

[162] Chen M, Chen CM, Shi SC, Chen CF. Low-temperature synthesis multiwalled carbon nanotubes by microwave plasma chemical vapor deposition using CH4-CO2

gas mixture. Jpn J Appl Phys Part 1 - Regul Pap Short Notes Rev Pap. 2003 Feb;42(2A):614-9.

[163] Qi Y, Cagin T, Johnson WL, Goddard WA. Melting and crystallization in Ni nanoclusters: The mesoscale regime. J Chem Phys. 2001 Jul;115(1):385-94.

[164] Helveg S, Lopez-Cartes C, Sehested J, Hansen PL, Clausen BS, Rostrup-Nielsen JR, et al. Atomic-scale imaging of carbon nanofibre growth. Nature. 2004 Jan;427(6973):426-9.

[165] Charlier JC, Amara H, Lambin P. Catalytically assisted tip growth mechanism for single-wall carbon nanotubes. ACS Nano. 2007 Oct;1(3):202-7.

[166] Pan ZW, Xie SS, Chang BH, Sun LF, Zhou WY, Wang G. Direct growth of aligned open carbon nanotubes by chemical vapor deposition. Chem Phys Lett. 1999 Jan;299(1):97-102.

[167] Amama PB, Pint CL, McJilton L, Kim SM, Stach EA, Murray PT, et al. Role of Water in Super Growth of Single-Walled Carbon Nanotube Carpets. Nano Lett. 2009 Jan;9(1):44-9.

[168] Han JH, Graff RA, Welch B, Marsh CP, Franks R, Strano MS. A mechanochemical model of growth termination in vertical carbon nanotube forests. ACS Nano. 2008 Jan;2(1):53-60.

[169] Liu K, Jiang KL, Wei Y, Ge SP, Liu P, Fan SS. Controlled termination of the growth of vertically aligned carbon nanotube arrays. Adv Mater. 2007 Apr;19(7):975-+.

[170] Meshot ER, Hart AJ. Abrupt self-termination of vertically aligned carbon nanotube growth. Appl Phys Lett. 2008 Mar;92(11).

[171] Stadermann M, Sherlock SP, In JB, Fornasiero F, Park HG, Artyukhin AB, et al. Mechanism and Kinetics of Growth Termination in Controlled Chemical Vapor Deposition Growth of Multiwall Carbon Nanotube Arrays. Nano Lett. 2009 Feb;9(2):738-44.

[172] Tuyen LTT, Minh PN, Roduner E, Chi PTD, Ono T, Miyashita H, et al. Hydrogen termination for the growth of carbon nanotubes on silicon. Chem Phys Lett. 2005 Nov;415(4-6):333-6.

[173] Wu J, Huang QW, Ma YF, Huang Y, Liu ZF, Yang XY, et al. Distortion of carbon nanotube array and its influence on carbon nanotube growth and termination. 2008; 2008. p. 13-7.

[174] Bedewy M, Meshot ER, Guo H, Verploegen EA, Lu W, Hart AJ. Collective Mechanism for the Evolution and Self-Termination of Vertically Aligned Carbon Nanotube Growth. J Phys Chem C. 2009 Dec 3;113(48):20576-82.

[175] Lee CJ, Kim DW, Lee TJ, Choi YC, Park YS, Lee YH, et al. Synthesis of aligned carbon nanotubes using thermal chemical vapor deposition. Chem Phys Lett. 1999 Oct;312(5-6):461-8.

[176] Suekane O, Nagasaka T, Kiyotaki K, Nosaka T, Nakayama Y. Rapid growth of vertically aligned carbon nanotubes. Jpn J Appl Phys Part 2 - Lett Express Lett. 2004 Sep;43(9A-B):L1214-L6.

[177] Li DC, Dai LM, Huang SM, Mau AWH, Wang ZL. Structure and growth of aligned carbon nanotube films by pyrolysis. Chem Phys Lett. 2000 Jan;316(5-6):349-55.

[178] Yoon YJ, Bae JC, Baik HK, Cho S, Lee SJ, Song KM, et al. Growth control of single and multi-walled carbon nanotubes by thin film catalyst. Chem Phys Lett. 2002 Nov;366(1-2):109-14.

[179] Amama PB, Pint CL, Kim SM, McJilton L, Eyink KG, Stach EA, et al. Influence of Alumina Type on the Evolution and Activity of Alumina-Supported Fe Catalysts in Single-Walled Carbon Nanotube Carpet Growth. ACS Nano. Feb;4(2):895-904.

[180] Wei YY, Eres G, Merkulov VI, Lowndes DH. Effect of catalyst film thickness on carbon nanotube growth by selective area chemical vapor deposition. Appl Phys Lett. 2001 Mar;78(10):1394-6.

[181] Yun YH, Shanov V, Tu Y, Subramaniam S, Schulz MJ. Growth mechanism of long aligned multiwall carbon nanotube arrays by water-assisted chemical vapor deposition. J Phys Chem B. 2006 Nov;110(47):23920-5.

[182] Lee CJ, Park J. Growth model of bamboo-shaped carbon nanotubes by thermal chemical vapor deposition. Appl Phys Lett. 2000 Nov;77(21):3397-9.

[183] Schwalbach P, Laubach S, Hartick M, Kankeleit E, Keck B, Menningen M, et al. Diffusion and Isomer-Shift of Interstitial Iron in Silicon Observed Via in-Beam Mossbauer-Spectroscopy. Phys Rev Lett. 1990 Mar;64(11):1274-7.

[184] Simmons JM, Nichols BM, Marcus MS, Castellini OM, Hamers RJ, Eriksson MA. Critical oxide thickness for efficient single-walled carbon nanotube growth on silicon using thin SiO2 diffusion barriers. Small. 2006 Jul;2(7):902-9.

[185] Jung YJ, Wei BQ, Vajtai R, Ajayan PM. Mechanism of selective growth of carbon nanotubes on SiO2/Si patterns. Nano Lett. 2003 Apr;3(4):561-4.

[186] Cao AY, Ajayan PM, Ramanath G, Baskaran R, Turner K. Silicon oxide thickness-dependent growth of carbon nanotubes. Appl Phys Lett. 2004 Jan;84(1):109-11.

[187] Orlanducci S, Sessa V, Terranova ML, Rossi M, Manno D. Aligned arrays of carbon nanotubes: modulation of orientation and selected-area growth. Chem Phys Lett. 2003 Jan;367(1-2):109-15.

[188] Li WZ, Xie SS, Qian LX, Chang BH, Zou BS, Zhou WY, et al. Large-scale synthesis of aligned carbon nanotubes. Science. 1996 Dec;274(5293):1701-3.

[189] Zhang WD, Wen Y, Tjiu WC, Xu GQ, Gan LM. Growth of vertically aligned carbon-nanotube array on large area of quartz plates by chemical vapor deposition. Appl Phys A-Mater Sci Process. 2002 Mar;74(3):419-22.

[190] Zhu LB, Hess DW, Wong CP. Monitoring carbon nanotube growth by formation of nanotube stacks and investigation of the diffusion-controlled kinetics. J Phys Chem B. 2006 Mar;110(11):5445-9.

[191] Zhu LB, Sun YY, Hess DW, Wong CP. Well-aligned open-ended carbon nanotube architectures: An approach for device assembly. Nano Lett. 2006 Feb;6(2):243-7.

[192] Zhu LB, Xu JW, Xiao F, Jiang HJ, Hess DW, Wong CP. The growth of carbon nanotube stacks in the kinetics-controlled regime. Carbon. 2007 Feb;45(2):344-8.

[193] Haneda M, Shinriki M, Nagao Y, Kintaichi Y, Hamada H. N2O removal by catalytic decomposition and reduction with CH4 over Fe/Al2O3. Bulletin of the Chemical Society of Japan. 2003 Dec;76(12):2329-33.

[194] Reshetenko TV, Avdeeva LB, Khassin AA, Kustova GN, Ushakov VA, Moroz EM, et al. Coprecipitated iron-containing catalysts (Fe-Al2O3, Fe-Co-Al2O3, Fe-Ni-Al2O3) for methane decomposition at moderate temperatures I. Genesis of calcined and reduced catalysts. Applied Catalysis a-General. 2004 Aug;268(1-2):127-38.

[195] Kazusaka A, Suzuki H, Toyoshima I. ZERO-VALENT IRON CATALYST DERIVED FROM FE(CO)5 SUPPORTED ON KOH-DOPED ALUMINA - HIGH-ACTIVITY FOR THE HYDROGENATION OF ETHYLENE. Journal of the Chemical Society-Chemical Communications. 1983(4):150-1.

[196] Reshetenko TV, Avdeeva LB, Ushakov VA, Moroz EM, Shmakov AN, Kriventsov VV, et al. Coprecipitated iron-containing catalysts (Fe-Al2O3, Fe-Co-Al2O3, Fe-Ni-Al2O3) for methane decomposition at moderate temperatures - Part II. Evolution of the catalysts in reaction. Applied Catalysis a-General. 2004 Aug;270(1-2):87-99.

[197] Tanaka S, Nakagawa K, Kanezaki E, Katoh M, Murai K, Moriga T, et al. Catalytic activity of iron oxides supported on gamma-Al2O3 for methane oxidation. Journal of the Japan Petroleum Institute. 2005 Jul;48(4):223-8.

[198] Mattevi C, Wirth CT, Hofmann S, Blume R, Cantoro M, Ducati C, et al. In-situ X-ray photoelectron spectroscopy study of catalyst-support interactions and growth of carbon nanotube forests. J Phys Chem C. 2008 Aug;112(32):12207-13.

[199] de los Arcos T, Garnier MG, Seo JW, Oelhafen P, Thommen V, Mathys D. The influence of catalyst chemical state and morphology on carbon nanotube growth. J Phys Chem B. 2004 Jun;108(23):7728-34.

[200] Lloyd IK, Bowen HK. IRON TRACER DIFFUSION IN ALUMINUM-OXIDE. Journal of the American Ceramic Society. 1981;64(12):744-7.

[201] Koripella CR, Kroger FA. ELECTRICAL-CONDUCTIVITY, DIFFUSION OF IRON AND THE DEFECT STRUCTURE OF ALPHA-AL2O3-FE. Journal of Physics and Chemistry of Solids. 1986;47(6):565-76.

[202] Klie RF, Browning ND, Chowdhuri AR, Takoudis CG. Analysis of ultrathin SiO2 interface layers in chemical vapor deposition of Al2O3 on Si by in situ scanning transmission electron microscopy. Appl Phys Lett. 2003 Aug;83(6):1187-9.

[203] Strausser YE, Scheibner EJ, Johannessen JS. OBSERVATIONS OF AL2O3 AND FREE SILICON AT INTERFACE BETWEEN ALUMINUM FILMS AND SIO2. Thin Solid Films. 1978;52(2):203-14.

[204] Nessim GD, Hart AJ, Kim JS, Acquaviva D, Oh JH, Morgan CD, et al. Tuning of Vertically-Aligned Carbon Nanotube Diameter and Areal Density through Catalyst Pre-Treatment. Nano Lett. 2008 Nov;8(11):3587-93.

[205] Futaba DN, Hata K, Namai T, Yamada T, Mizuno K, Hayamizu Y, et al. 84% Catalyst activity of water-assisted growth of single walled carbon nanotube forest characterization by a statistical and macroscopic approach. J Phys Chem B. 2006 Apr;110(15):8035-8.

[206] Yamada T, Maigne A, Yudasaka M, Mizuno K, Futaba DN, Yumura M, et al. Revealing the Secret of Water-Assisted Carbon Nanotube Synthesis by Microscopic Observation of the Interaction of Water on the Catalysts. Nano Lett. 2008 Dec;8(12):4288-92.

[207] Murakami Y, Chiashi S, Miyauchi Y, Hu MH, Ogura M, Okubo T, et al. Growth of vertically aligned single-walled carbon nanotube films on quartz substrates and their optical anisotropy. Chem Phys Lett. 2004 Feb;385(3-4):298-303.

[208] Zhang GY, Mann D, Zhang L, Javey A, Li YM, Yenilmez E, et al. Ultra-high-yield growth of vertical single-walled carbon nanotubes: Hidden roles of hydrogen and oxygen. Proceedings of the National Academy of Sciences of the United States of America. 2005 Nov;102(45):16141-5.

[209] Liu ZF, Shen ZY, Zhu T, Hou SF, Ying LZ, Shi ZJ, et al. Organizing single-walled carbon nanotubes on gold using a wet chemical self-assembling technique. Langmuir. 2000 Apr;16(8):3569-73.

[210] Hirsch A. Functionalization of single-walled carbon nanotubes. Angewandte Chemie-International Edition. 2002;41(11):1853-9.

[211] Sun YP, Fu KF, Lin Y, Huang WJ. Functionalized carbon nanotubes: Properties and applications. Accounts Chem Res. 2002 Dec;35(12):1096-104.

[212] Wagner CD, Zatko DA, Raymond RH. USE OF THE OXYGEN KLL AUGER LINES IN IDENTIFICATION OF SURFACE CHEMICAL-STATES BY ELECTRON-SPECTROSCOPY FOR CHEMICAL-ANALYSIS. Analytical Chemistry. 1980;52(9):1445-51.

[213] Okpalugo TIT, Papakonstantinou P, Murphy H, McLaughlin J, Brown NMD. High resolution XPS characterization of chemical functionalised MWCNTs and SWCNTs. Carbon. 2005;43(1):153-61.

[214] Felten A, Bittencourt C, Pireaux JJ, Van Lier G, Charlier JC. Radio-frequency plasma functionalization of carbon nanotubes surface O-2, NH3, and CF4 treatments. J Appl Phys. 2005 Oct;98(7).

[215] Kuznetsova A, Mawhinney DB, Naumenko V, Yates JT, Liu J, Smalley RE. Enhancement of adsorption inside of single-walled nanotubes: opening the entry ports. Chem Phys Lett. 2000 Apr;321(3-4):292-6.

[216] Kenneth WJ, Donald ER. Thermodynamics.

[217] Manatt SL and Manatt MRR. On the Analyses of Mixture Vapor Pressure Data: The Hydrogen Peroxide/Water System and Its Excess Thermodynamic Functions. Chem Eur J. 2004;10:6540-57.

[218] Wang BA, Liu XY, Liu HM, Wu DX, Wang HP, Jiang JM, et al. Controllable preparation of patterns of aligned carbon nanotubes on metals and metal-coated silicon substrates. J Mater Chem. 2003;13(5):1124-6.

[219] Hofmeister W, Kang WP, Wong YM, Davidson JL. Carbon nanotube growth from Cu-Co alloys for field emission applications. J Vac Sci Technol B. 2004 May-Jun;22(3):1286-9.

[220] Karwa M, Iqbal Z, Mitra S. Scaled-up self-assembly of carbon nanotubes inside long stainless steel tubing. Carbon. 2006 Jun;44(7):1235-42.

[221] Talapatra S, Kar S, Pal SK, Vajtai R, Ci L, Victor P, et al. Direct growth of aligned carbon nanotubes on bulk metals. Nat Nanotechnol. 2006 Nov;1(2):112-6.

[222] Gao LJ, Peng AP, Wang ZY, Zhang H, Shi ZJ, Gu ZN, et al. Growth of aligned carbon nanotube arrays on metallic substrate and its application to supercapacitors. Solid State Commun. 2008 Jun;146(9-10):380-3.

[223] Singh MK, Singh PP, Titus E, Misra DS, LeNormand F. High density of multiwalled carbon nanotubes observed on nickel electroplated copper substrates by microwave plasma chemical vapor deposition. Chem Phys Lett. 2002 Mar;354(3-4):331-6.

[224] Wang H, Feng JY, Hu XJ, Ng KM. Synthesis of aligned carbon nanotubes on double-sided metallic substrate by chemical vapor deposition. J Phys Chem C. 2007 Aug;111(34):12617-24.

[225] Yin XW, Wang QL, Lou CG, Zhang XB, Lei W. Growth of multi-walled CNTs emitters on an oxygen-free copper substrate by chemical-vapor deposition. Appl Surf Sci. 2008 Aug;254(20):6633-6.

[226] Cola BA, Xu J, Cheng CR, Xu XF, Fisher TS, Hu HP. Photoacoustic characterization of carbon nanotube array thermal interfaces. J Appl Phys. 2007 Mar;101(5).

[227] Powell CF, Oxley JH, Johan J, Blocher M. Vapor Deposition. New York: Wiley 1966.

[228] de los Arcos T, Vonau F, Garnier MG, Thommen V, Boyen HG, Oelhafen P, et al. Influence of iron-silicon interaction on the growth of carbon nanotubes produced by chemical vapor deposition. Appl Phys Lett. 2002 Apr;80(13):2383-5.

[229] Hildreth OJ, Lin W, Wong CP. Effect of Catalyst Shape and Etchant Composition on Etching Direction in Metal-Assisted Chemical Etching of Silicon to Fabricate 3D Nanostructures. ACS Nano. 2009 Dec;3(12):4033-42.

[230] Diemer M, Neubrand A, Trumble KP, Rodel J. Influence of oxygen partial pressure and oxygen content on the wettability in the copper-oxygen-alumina system. Journal of the American Ceramic Society. 1999 Oct;82(10):2825-32.

[231] Kelber JA, Niu CY, Shepherd K, Jennison DR, Bogicevic A. Copper wetting of alpha-Al2O3(0001): theory and experiment. Surf Sci. 2000 Feb;446(1-2):76-88.

[232] Park SC, Park YB. Effect of Ar+ radiofrequency plasma treatment conditions on the interfacial adhesion energy between atomic-layer-deposited Al2O3 and Cu thin films in embedded capacitors. J Electron Mater. 2008 Oct;37(10):1565-73.

[233] Pisana S, Cantoro M, Parvez A, Hofmann S, Ferrari AC, Robertson J. The role of precursor gases on the surface restructuring of catalyst films during carbon nanotube growth. Physica E. 2007 Mar;37(1-2):1-5.

[234] Rodriguez NM. A Review of Catalytically Grown Carbon Nanofibers. J Mater Res. 1993 Dec;8(12):3233-50.

[235] Deck CP, Vecchio K. Prediction of carbon nanotube growth success by the analysis of carbon-catalyst binary phase diagrams. Carbon. 2006 Feb;44(2):267-75.

[236] Deng WQ, Xu X, Goddard WA. A two-stage mechanism of bimetallic catalyzed growth of single-walled carbon nanotubes. Nano Lett. 2004 Dec;4(12):2331-5.

[237] Krishnankutty N, Park C, Rodriguez NM, Baker RTK. The effect of copper on the structural characteristics of carbon filaments produced from iron catalyzed decomposition of ethylene. Catal Today. 1997 Aug;37(3):295-307.

[238] Almazouzi A, Macht MP, Naundorf V, Neumann G. Diffusion of iron and nickel in single-crystalline copper. Phys Rev B. 1996 Jul;54(2):857-63.

[239] Kononchuk O, Korablev KG, Yarykin N, Rozgonyi GA. Diffusion of iron in the silicon dioxide layer of silicon-on-insulator structures. Appl Phys Lett. 1998 Aug;73(9):1206-8.

[240] Kaloyeros AE, Eisenbraun E. Ultrathin diffusion barriers/liners for gigascale copper metallization. Annu Rev Mater Sci. 2000;30:363-85.

[241] Li G, Chakrabarti S, Schulz M, Shanov V. Growth of aligned multiwalled carbon nanotubes on bulk copper substrates by chemical vapor deposition. J Mater Res. 2009 Sep;24(9):2813-20.

[242] Groner MD, Elam JW, Fabreguette FH, George SM. Electrical characterization of thin Al2O3 films grown by atomic layer deposition on silicon and various metal substrates. Thin Solid Films. 2002 Jun;413(1-2):186-97.

[243] Puurunen RL. Surface chemistry of atomic layer deposition: A case study for the trimethylaluminum/water process. Journal of Applied Physics. 2005 Jun;97(12).

[244] Rahtu A, Alaranta T, Ritala M. In situ quartz crystal microbalance and quadrupole mass spectrometry studies of atomic layer deposition of aluminum oxide from trimethylaluminum and water. Langmuir. 2001 Oct;17(21):6506-9.

[245] Kreupl F, Graham AP, Duesberg GS, Steinhogl W, Liebau M, Unger E, et al. Carbon nanotubes in interconnect applications. 2002: Elsevier Science Bv; 2002. p. 399-408.

[246] Nihei M, Kawabata A, Kondo D, Horibe M, Sato S, Awano Y. Electrical properties of carbon nanotube bundles for future via interconnects. Jpn J Appl Phys Part 1 - Regul Pap Short Notes Rev Pap. 2005 Apr;44(4A):1626-8.

[247] Amama PB, Cola BA, Sands TD, Xu XF, Fisher TS. Dendrimer-assisted controlled growth of carbon nanotubes for enhanced thermal interface conductance. Nanotechnology. 2007 Sep;18(38).

[248] Cola BA, Xu XF, Fisher TS. Increased real contact in thermal interfaces: A carbon nanotube/foil material. Appl Phys Lett. 2007 Feb;90(9).

[249] Lin W, Moon KS, Wong CP. A Combined Process of In-Situ Functionalization and Microwave Treatment to Achieve Ultra-Small Thermal Expansion of Aligned Carbon Nanotube/Polymer Composites: toward Applications as Thermal Interface Materials. Adv Mater. 2009;21.

[250] Lin W, Wong CP. Synthesis of Vertically Aligned Multi-Walled Carbon Nanotubes on Copper Substrates for Applications as Thermal Interface Materials. MRS 2009 Spring Meeting; 2009.

[251] Lin W, Zhang RW, Moon KS, Wong CP. Molecular phonon couplers at carbon nanotube/substrate interface to enhance interfacial thermal transport. Carbon. 2010 Jan;48(1):107-13.

[252] Biercuk MJ, Llaguno MC, Radosavljevic M, Hyun JK, Johnson AT, Fischer JE. Carbon nanotube composites for thermal management. Appl Phys Lett. 2002 Apr;80(15):2767-9.

[253] Huang H, Liu CH, Wu Y, Fan SS. Aligned carbon nanotube composite films for thermal management. Advanced Materials. 2005 Jul;17(13):1652-5.

[254] Vigolo B, Penicaud A, Coulon C, Sauder C, Pailler R, Journet C, et al. Macroscopic fibers and ribbons of oriented carbon nanotubes. Science. 2000 Nov;290(5495):1331-4.

[255] Vigolo B, Poulin P, Lucas M, Launois P, Bernier P. Improved structure and properties of single-wall carbon nanotube spun fibers. Appl Phys Lett. 2002 Aug;81(7):1210-2.

[256] Koziol K, Vilatela J, Moisala A, Motta M, Cunniff P, Sennett M, et al. High-performance carbon nanotube fiber. Science. 2007 Dec;318(5858):1892-5.

[257] Motta M, Li YL, Kinloch I, Windle A. Mechanical properties of continuously spun fibers of carbon nanotubes. Nano Letters. 2005 Aug;5(8):1529-33.

[258] Motta M, Moisala A, Kinloch IA, Windle AH. High performance fibres from 'Dog bone' carbon nanotubes. Adv Mater. 2007 Nov;19(21):3721-4.

[259] Miaudet P, Badaire S, Maugey M, Derre A, Pichot V, Launois P, et al. Hot-drawing of single and multiwall carbon nanotube fibers for high toughness and alignment. Nano Letters. 2005 Nov;5(11):2212-5.

[260] Jiang KL, Li QQ, Fan SS. Nanotechnology: Spinning continuous carbon nanotube yarns - Carbon nanotubes weave their way into a range of imaginative macroscopic applications. Nature. 2002 Oct;419(6909):801.

[261] Zhang M, Atkinson KR, Baughman RH. Multifunctional carbon nanotube yarns by downsizing an ancient technology. Science. 2004 Nov;306(5700):1358-61.

[262] Zhang XF, Li QW, Tu Y, Li YA, Coulter JY, Zheng LX, et al. Strong carbon-nanotube fibers spun from long carbon-nanotube arrays. Small. 2007 Feb;3(2):244-8.

[263] Che JW, Cagin T, Goddard WA. Thermal conductivity of carbon nanotubes. Nanotechnology. 2000, 11: 65-9.

[264] Barinov A, Gregoratti L, Dudin P, La Rosa S, Kiskinova M. Imaging and Spectroscopy of Multiwalled Carbon Nanotubes during Oxidation: Defects and Oxygen Bonding. Adv Mater. 2009 May;21(19):1916-20.

[265] Mielke SL, Troya D, Zhang S, Li JL, Xiao SP, Car R, et al. The role of vacancy defects and holes in the fracture of carbon nanotubes. Chem Phys Lett. 2004 Jun;390(4-6):413-20.

[266] Sammalkorpi M, Krasheninnikov A, Kuronen A, Nordlund K, Kaski K. Mechanical properties of carbon nanotubes with vacancies and related defects. Phys Rev B. 2004 Dec;70(24):8.

[267] Hou WY, Xiao SP. Mechanical behaviors of carbon nanotubes with randomly located vacancy defects. J Nanosci Nanotechnol. 2007 Dec;7(12):4478-85.

[268] Scarpa F, Adhikari S, Wang CY. Mechanical properties of non-reconstructed defective single-wall carbon nanotubes. J Phys D-Appl Phys. 2009 Jul;42(14):6.

[269] Liu CH, Fan SS. Effects of chemical modifications on the thermal conductivity of carbon nanotube composites. Appl Phys Lett. 2005 Mar;86(12):3.

[270] Monthioux M, Smith BW, Burteaux B, Claye A, Fischer JE, Luzzi DE. Sensitivity of single-wall carbon nanotubes to chemical processing: an electron microscopy investigation. Carbon. 2001;39(8):1251-72.

[271] Metenier K, Bonnamy S, Beguin F, Journet C, Bernier P, de La Chapelle ML, et al. Coalescence of single-walled carbon nanotubes and formation of multi-walled carbon nanotubes under high-temperature treatments. Carbon. 2002;40(10):1765-73.

[272] Paton KR, Windle AH. Efficient microwave energy absorption by carbon nanotubes. Carbon. 2008 Nov;46(14):1935-41.

[273] Bom D, Andrews R, Jacques D, Anthony J, Chen BL, Meier MS, et al. Thermogravimetric analysis of the oxidation of multiwalled carbon nanotubes: Evidence for the role of defect sites in carbon nanotube chemistry. Nano Letters. 2002 Jun;2(6):615-9.

[274] Salvetat JP, Kulik AJ, Bonard JM, Briggs GAD, Stockli T, Metenier K, et al. Elastic modulus of ordered and disordered multiwalled carbon nanotubes. Adv Mater. 1999 Jan;11(2):161-5.

[275] Imholt TJ, Dyke CA, Hasslacher B, Perez JM, Price DW, Roberts JA, et al. Nanotubes in microwave fields: Light emission, intense heat, outgassing, and reconstruction. Chem Mat. 2003 Oct;15(21):3969-70.

[276] Wadhawan A, Garrett D, Perez JM. Nanoparticle-assisted microwave absorption by single-wall carbon nanotubes. Appl Phys Lett. 2003 Sep;83(13):2683-5.

[277] Naab F, Dhoubhadel M, Holland OW, Duggan JL, Roberts J, McDaniel FD. The role of metallic impurities in the interaction of carbon nanotubes with microwave radiation. 10th International Conference on Particle Induced X-ray Emission and its Analytical Applications; 2004; Portoroz, Slovenia: Wiley Interscience; 2004. p. 601.1-.4.

[278] Ye Z, Deering WD, Krokhin A, Roberts JA. Microwave absorption by an array of carbon nanotubes: A phenomenological model. Phys Rev B. 2006 Aug;74(7).

[279] Babaei S, Solari MS. Microwave attenuation of hydrogen plasma in carbon nanotubes. J Appl Phys. 2008 Dec;104(12).

[280] Xu Y, Zhang Y, Suhir E, Wang XW. Thermal properties of carbon nanotube array used for integrated circuit cooling. J Appl Phys. 2006 Oct;100(7).

[281] Hu QT, Gan ZB, Zheng XW, Lin QF, Xu BF, Zhao AH, et al. Rapid microwave-assisted synthesis and electrochemical characterization of gold/carbon nanotube composites. Superlattices and Microstructures. May;49(5):537-42.

[282] Lin Y, Baggett DW, Kim JW, Siochi EJ, Connell JW. Instantaneous Formation of Metal and Metal Oxide Nanoparticles on Carbon Nanotubes and Graphene via Solvent-Free Microwave Heating. ACS Applied Materials & Interfaces. May;3(5):1652-64.

[283] Wu Y, Liu CH, Huang H, Fan SS. Effects of surface metal layer on the thermal contact resistance of carbon nanotube arrays. Appl Phys Lett. 2005 Nov;87(21).

[284] Kim J, So HM, Kim N, Kim JJ, Kang K. Microwave response of individual multiwall carbon nanotubes. Phys Rev B. 2004 Oct;70(15).

[285] Janowska I, Ersen O, Jacob T, Vennegues P, Begin D, Ledoux MJ, et al. Catalytic unzipping of carbon nanotubes to few-layer graphene sheets under microwaves irradiation. Applied Catalysis a-General. 2009 Dec;371(1-2):22-30.

[286] Moseenkov S, Kuznetsov V, Usoltseva A, Mazov I, Ischenko A, Buryakov T, et al. Multi-Wall Carbon Nanotubes in Microwaves. In: Trilling L, Perkins D, Dionysios D, Perlovsky L, Davey K, Landgrebe D, et al., eds. Proceedings of the 1st Wseas International Conference on Recent Advances in Nanotechnology 2009:92-5.

[287] Vazquez E, Prato M. Carbon Nanotubes and Microwaves: Interactions, Responses, and Applications. ACS Nano. 2009 Dec;3(12):3819-24.

[288] Zhang S, Zhu L, Minus ML, Chae HG, Jagannathan S, Wong CP, et al. Solid-state spun fibers and yarns from 1-mm long carbon nanotube forests synthesized by water-assisted chemical vapor deposition. 2008: Springer; 2008. p. 4356-62.

[289] Curran SA, Talla JA, Zhang D, Carroll DL. Defect-induced vibrational response of multi-walled carbon nanotubes using resonance Raman spectroscopy. J Mater Res. 2005 Dec;20(12):3368-73.

[290] de los Arcos T, Garnier MG, Oelhafen P, Mathys D, Seo JW, Domingo C, et al. Strong influence of buffer layer type on carbon nanotube characteristics. Carbon. 2004;42(1):187-90.

[291] Pang LSK, Saxby JD, Chatfield SP. THERMOGRAVIMETRIC ANALYSIS OF CARBON NANOTUBES AND NANOPARTICLES. J Phys Chem. 1993 Jul;97(27):6941-2.

[292] McKee GSB, Flowers JS, Vecchio KS. Length and the oxidation kinetics of chemical-vapor-deposition-generated multiwalled carbon nanotubes. J Phys Chem C. 2008 Jul;112(27):10108-13.

[293] Rinzler AG, Liu J, Dai H, Nikolaev P, Huffman CB, Rodriguez-Macias FJ, et al. Large-scale purification of single-wall carbon nanotubes: process, product, and characterization. Appl Phys A-Mater Sci Process. 1998 Jul;67(1):29-37.

[294] Bundy FP, Kasper JS. HEXAGONAL DIAMOND - A NEW FORM OF CARBON. Journal of Chemical Physics. 1967;46(9):3437-&.

[295] Chen LY, Chau-Nan Hong F. Diamond-like carbon composite films. Applied Physics Letters. 2003 May;82(20):3526-8.

[296] Sarangi D, Godon C, Granier A, Moalic R, Goullet A, Turban G, et al. Carbon nanotubes and nanostructures grown from diamond-like carbon and polyethylene. Applied Physics a-Materials Science & Processing. 2001 Dec;73(6):765-8.

[297] Wang ZX, Yu GQ, Ruan ML, Zhu FY, Zhu DZ, Pan HC, et al. Studies of hexagonal diamond of nano-grain in graphite surface produced by Ar+ ion bombardment. Acta Physica Sinica. 2000 Aug;49(8):1524-7.

[298] Tang YH, Lin LW, Guo C. Hydrogen storage mechanism of multiwalled carbon nanotube bundles studied by X-ray absorption spectra. Acta Physica Sinica. 2006 Aug;55(8):4197-201.

[299] Nikitin A, Li XL, Zhang ZY, Ogasawara H, Dai HJ, Nilsson A. Hydrogen storage in carbon nanotubes through the formation of stable C-H bonds. Nano Letters. 2008 Jan;8(1):162-7.

[300] Kundu S, Wang YM, Xia W, Muhler M. Thermal Stability and Reducibility of Oxygen-Containing Functional Groups on Multiwalled Carbon Nanotube Surfaces: A Quantitative High-Resolution XPS and TPD/TPR Study. J Phys Chem C. 2008 Oct;112(43):16869-78.

[301] Young DD, Nichols J, Kelly RM, Deiters A. Microwave activation of enzymatic catalysis. J Am Chem Soc. 2008 Aug;130(31):10048-9.

[302] Kappe CO. Controlled microwave heating in modern organic synthesis. Angew Chem-Int Edit. 2004;43(46):6250-84.

[303] Wang YB, Iqbal Z, Mitra S. Rapidly functionalized, water-dispersed carbon nanotubes at high concentration. J Am Chem Soc. 2006 Jan;128(1):95-9.

[304] Li YL, Kinloch IA, Windle AH. Direct spinning of carbon nanotube fibers from chemical vapor deposition synthesis. Science. 2004 Apr;304(5668):276-8.

[305] Ma WJ, Liu LQ, Yang R, Zhang TH, Zhang Z, Song L, et al. Monitoring a Micromechanical Process in Macroscale Carbon Nanotube Films and Fibers. Adv Mater. 2009 Feb;21(5):603-6.

[306] Shim BS, Zhu J, Jan E, Critchley K, Ho SS, Podsiadlo P, et al. Multiparameter Structural Optimization of Single-Walled Carbon Nanotube Composites: Toward Record Strength, Stiffness, and Toughness. ACS Nano. 2009 Jul;3(7):1711-22.

[307] Lin W, Wong CP. Comment on "The Effect of Stress Transfer Within Double-Walled Carbon Nanotubes Upon Their Ability to Reinforce Composites". Adv Mater. Mar;22(11):1177-9.

[308] Lin W, Xiu YG, Jiang HJ, Zhang RW, Hildreth O, Moon KS, et al. Self-assembled monolayer-assisted chemical transfer of in situ functionalized carbon nanotubes. J Am Chem Soc. 2008 Jul;130(30):9636-7.

[309] Tawfick S, O'Brien K, Hart AJ. Flexible High-Conductivity Carbon-Nanotube Interconnects Made by Rolling and Printing. Small. 2009 Nov;5(21):2467-73.

[310] Zhu LB, Xu JW, Xiu YH, Sun YY, Hess DW, Wong CP. Growth and electrical characterization of high-aspect-ratio carbon nanotube arrays. Carbon. 2006 Feb;44(2):253-8.

[311] Walton D, Boehnel H, Dunlop DJ. Response of magnetic nanoparticles to microwaves. Applied Physics Letters. 2004 Nov;85(22):5367-9.

[312] Lin W, Moon KS, Zhang SJ, Ding Y, Shang JT, Chen MX, et al. Microwave Makes Carbon Nanotubes Less Defective. ACS Nano. Mar;4(3):1716-22.

[313] Li Z, Yao YG, Lin ZY, Moon KS, Lin W, Wong CP. Ultrafast, dry microwave synthesis of graphene sheets. J Mater Chem.20(23):4781-3.

[314] Yang D, Velamakanni A, Bozoklu G, Park S, Stoller M, Piner RD, et al. Chemical analysis of graphene oxide films after heat and chemical treatments by X-ray photoelectron and Micro-Raman spectroscopy. Carbon. 2009;47(1):145-52.

[315] Lu G, Ocola LE, Chen J. Reduced graphene oxide for room-temperature gas sensors. Nanotechnol. 2009;20(44):445502.

[316] Jung I, Dikin DA, Piner RD, Ruoff RS. Tunable Electrical Conductivity of Individual Graphene Oxide Sheets Reduced at "Low" Temperatures. Nano Letters. 2008 Dec;8(12):4283-7.

[317] Paci JT, Belytschko T, Schatz GC. Computational Studies of the Structure, Behavior upon Heating, and Mechanical Properties of Graphite Oxide. The Journal of Physical Chemistry C. 2007;111(49):18099-111.

[318] Tung VC, Allen MJ, Yang Y, Kaner RB. High-throughput solution processing of large-scale graphene. Nat Nano. 2009;4(1):25-9.

[319] Stankovich S, Dikin DA, Piner RD, Kohlhaas KA, Kleinhammes A, Jia Y, et al. Synthesis of graphene-based nanosheets via chemical reduction of exfoliated graphite oxide. Carbon. 2007;45(7):1558-65.

[320] Stankovich S, Dikin DA, Dommett GHB, Kohlhaas KM, Zimney EJ, Stach EA, et al. Graphene-based composite materials. Nature. 2006 Jul;442(7100):282-6.

[321] Wang G, Yang J, Park J, Gou X, Wang B, Liu H, et al. Facile Synthesis and Characterization of Graphene Nanosheets. The Journal of Physical Chemistry C. 2008;112(22):8192-5.

[322] Si Y, Samulski ET. Synthesis of Water Soluble Graphene. Nano Letters. 2008;8(6):1679-82.

[323] Li Z, Yao Y, Lin Z, Moon K-S, Lin W, Wong C. Ultrafast, dry microwave synthesis of graphene sheets. Journal of Materials Chemistry. 2010;20(23):4781-3.

[324] McAllister MJ, Li JL, Adamson DH, Schniepp HC, Abdala AA, Liu J, et al. Single sheet functionalized graphene by oxidation and thermal expansion of graphite. Chemistry of Materials. 2007 Sep 4;19(18):4396-404.

[325] Schniepp HC, Li J-L, McAllister MJ, Sai H, Herrera-Alonso M, Adamson DH, et al. Functionalized Single Graphene Sheets Derived from Splitting Graphite Oxide. Journal of Physcal Chemistry B. 2006;110(17):8535-9.

[326] Hone J, Llaguno MC, Nemes NM, Johnson AT, Fischer JE, Walters DA, et al. Electrical and thermal transport properties of magnetically aligned single walt carbon nanotube films. Appl Phys Lett. 2000 Jul;77(5):666-8.

[327] Wang XW, Zhong ZR, Xu J. Noncontact thermal characterization of multiwall carbon nanotubes. Journal of Applied Physics. 2005 Mar;97(6).

[328] Hu XJ, Padilla AA, Xu J, Fisher TS, Goodson KE. 3-omega measurements of vertically oriented carbon nanotubes on silicon. J Heat Transf-Trans ASME. 2006 Nov;128(11):1109-13.

[329] Marconnett AM, Yamamoto N, Panzer MA, Wardle BL, Goodson KE. Thermal Conduction in Aligned Carbon Nanotube-Polymer Composites with High Packing Density. ACS Nano. Jun;5(6):4818-25.

[330] Jakubinek MB, White MA, Li G, Jayasinghe C, Cho WD, Schulz MJ, et al. Thermal and electrical conductivity of tall, vertically aligned carbon nanotube arrays. Carbon. Nov;48(13):3947-52.

[331] Parker WJ, Jenkins RJ, Abbott GL, Butler CP. FLASH METHOD OF DETERMINING THERMAL DIFFUSIVITY, HEAT CAPACITY, AND THERMAL CONDUCTIVITY. J Appl Phys. 1961;32(9):1679-&.

[332] Cowan RD. PULSE METHOD OF MEASURING THERMAL DIFFUSIVITY AT HIGH TEMPERATURES. Journal of Applied Physics. 1963;34(4):926-&.

[333] Heckman RC. FINITE PULSE-TIME AND HEAT-LOSS EFFECTS IN PULSE THERMAL DIFFUSIVITY MEASUREMENTS. Journal of Applied Physics. 1973;44(4):1455-60.

[334] Clark LM, Taylor RE. RADIATION LOSS IN FLASH METHOD FOR THERMAL-DIFFUSIVITY. Journal of Applied Physics. 1975;46(2):714-9.

[335] Schriemp.Jt. LASER FLASH TECHNIQUE FOR DETERMINING THERMAL DIFFUSIVITY OF LIQUID-METALS AT ELEVATED-TEMPERATURES. Review of Scientific Instruments. 1972;43(5):781-&.

[336] Blumm J, Lindemann A, Min S. Thermal characterization of liquids and pastes using the flash technique. Thermochimica Acta. 2007 Apr;455(1-2):26-9.

[337] Cernuschi F, Bison P, Moscatelli A. Microstructural characterization of porous thermal barrier coatings by laser flash technique. Acta Materialia. 2009 Jul;57(12):3460-71.

[338] Shaikh S, Li L, Lafdi K, Huie J. Thermal conductivity of an aligned carbon nanotube array. Carbon. 2007 Nov;45(13):2608-13.

[339] Shaikh S, Lafdi K, Silverman E. The effect of a CNT interface on the thermal resistance of contacting surfaces. Carbon. 2007 Apr;45(4):695-703.

[340] Xie HQ, Cai A, Wang XW. Thermal diffusivity and conductivity of multiwalled carbon nanotube arrays. Physics Letters A. 2007 Sep;369(1-2):120-3.

[341] Akoshima M, Baba T. Thermal diffusivity measurements of candidate reference materials by the laser flash method. International Journal of Thermophysics. 2005 Jan;26(1):151-63.

[342] Aliev AE, Guthy C, Zhang M, Fang S, Zakhidov AA, Fischer JE, et al. Thermal transport in MWCNT sheets and yarns. Carbon. 2007 Dec;45(15):2880-8.

[343] Cape JA, Lehman GW. TEMPERATURE AND FINITE PULSE-TIME EFFECTS IN FLASH METHOD FOR MEASURING THERMAL DIFFUSIVITY. Journal of Applied Physics. 1963;34(7):1909-12.

[344] Larson KB, Koyama K. CORRECTION FOR FINITE-PULSE-TIME EFFECTS IN VERY THIN SAMPLES USING FLASH METHOD OF MEASURING THERMAL DIFFUSIVITY. Journal of Applied Physics. 1967;38(2):465-9.

[345] Azumi T, Takahashi Y. NOVEL FINITE PULSE-WIDTH CORRECTION IN FLASH THERMAL-DIFFUSIVITY MEASUREMENT. Review of Scientific Instruments. 1981;52(9):1411-3.

[346] Akoshima M, Hata K, Futaba DN, Mizuno K, Baba T, Yumura M. Thermal Diffusivity of Single-Walled Carbon Nanotube Forest Measured by Laser Flash Method. Japanese Journal of Applied Physics. 2009 May;48(5).

[347] Mizuno K, Ishii J, Kishida H, Hayamizu Y, Yasuda S, Futaba DN, et al. A black body absorber from vertically aligned single-walled carbon nanotubes. Proceedings of the National Academy of Sciences of the United States of America. 2009 Apr;106(15):6044-7.

[348] Aliev AE, Lima MH, Silverman EM, Baughman RH. Thermal conductivity of multi-walled carbon nanotube sheets: radiation losses and quenching of phonon modes. Nanotechnology. 2010;21(3).

[349] Hou QW, Cao BY, Guo ZY. Thermal conductivity of carbon nanotube: From ballistic to diffusive transport. Acta Phys Sin. 2009 Nov;58(11):7809-14.

[350] Zhu LB, Hess DW, Wong CP. Assembling Carbon Nanotube Films as Thermal Interface Materials. Electronic Components and Technology Conference: IEEE 2007:2006-10

[351] Maillet D, Moyne C, Remy B. Effect of a thin layer on the measurement of the thermal diffusivity of a material by a flash method. International Journal of Heat and Mass Transfer. 2000 Nov;43(21):4057-60.

[352] Lin W, Zhang RW, Wong CP. Modeling of Thermal Conductivity of Graphite Nanosheet Composites. Journal of Electronic Materials. 2010 Mar;39(3):268-72.

[353] Singh R, Kasana HS. Computational aspects of effective thermal conductivity of highly porous metal foams. Appl Therm Eng. 2004 Sep;24(13):1841-9.

[354] Pan RQ, Xu ZJ, Zhu ZY, Wang ZX. Thermal conductivity of functionalized single-wall carbon nanotubes. Nanotechnology. 2007 Jul;18(28).

[355] Zhang G, Li BW. Thermal conductivity of nanotubes revisited: Effects of chirality, isotope impurity, tube length, and temperature. J Chem Phys. 2005 Sep;123(11).

[356] Pan RQ, Xu ZJ, Zhu ZY, Wang ZX. Thermal conductivity of functionalized single-wall carbon nanotubes. Nanotechnology. 2007 Jul;18(28):4.

[357] Heremans J, Rahim I, Dresselhaus MS. THERMAL-CONDUCTIVITY AND RAMAN-SPECTRA OF CARBON-FIBERS. Phys Rev B. 1985;32(10):6742-7.

[358] Cao AY, Dickrell PL, Sawyer WG, Ghasemi-Nejhad MN, Ajayan PM. Super-compressible foamlike carbon nanotube films. Science. 2005 Nov;310(5752):1307-10.

[359] Chang CW, Okawa D, Garcia H, Majumdar A, Zettl A. Nanotube phonon waveguide. Phys Rev Lett. 2007 Jul;99(4):4.

[360] Nishimura F, Takahashi T, Watanabe K, Yamamoto T. Bending Robustness of Thermal Conductance of Carbon Nanotubes: Nonequilibrium Molecular Dynamics Simulation. Appl Phys Express. 2009 Mar;2(3):3.

[361] Yan XH, Xiao Y, Li ZM. Effects of intertube coupling and tube chirality on thermal transport of carbon nanotubes. Journal of Applied Physics. 2006;99(12).

[362] Wardle BL, Saito DS, Garcia EJ, Hart AJ, de Villoria RG, Verploegen EA. Fabrication and characterization of ultrahigh-volume-fraction aligned carbon nanotube-polymer composites. Adv Mater. 2008;20(14):2707-10.

[363] Futaba DN, Hata K, Yamada T, Hiraoka T, Hayamizu Y, Kakudate Y, et al. Shape-engineerable and highly densely packed single-walled carbon nanotubes and their application as super-capacitor electrodes. Nat Mater. 2006;5(12):987-94.

[364] Yang JK, Waltermire S, Chen YF, Zinn AA, Xu TT, Li DY. Contact thermal resistance between individual multiwall carbon nanotubes. Appl Phys Lett. 2010;96(2).

[365] Bedewy M, Meshot ER, Guo HC, Verploegen EA, Lu W, Hart AJ. Collective Mechanism for the Evolution and Self-Termination of Vertically Aligned Carbon Nanotube Growth. J Phys Chem C. 2009;113(48):20576-82.

[366] Gwinn JP, Webb RL. Performance and testing of thermal interface materials. 2003; 2003. p. 215-22.

[367] Prasher R. Thermal interface materials: Historical perspective, status, and future directions. Proc IEEE. 2006 Aug;94(8):1571-86.

[368] Prasher RS. Surface chemistry and characteristics based model for the thermal contact resistance of fluidic interstitial thermal interface materials. J Heat Transf-Trans ASME. 2001 Oct;123(5):969-75.

[369] Prasher RS, Shipley J, Prstic S, Koning P, Wang JL. Thermal resistance of particle laden polymeric thermal interface materials. J Heat Transf-Trans ASME. 2003 Dec;125(6):1170-7.

[370] Yu AP, Ramesh P, Itkis ME, Bekyarova E, Haddon RC. Graphite nanoplatelet-EP composite thermal interface materials. J Phys Chem C. 2007 May;111(21):7565-9.

[371] Aoyagi Y, Leong CK, Chung DDL. Polyol-based phase-change thermal interface materials. Journal of Electronic Materials. 2006 Mar;35(3):416-24.

[372] Chung DDL. Thermal interface materials. Journal of Materials Engineering and Performance. 2001 Feb;10(1):56-9.

[373] Howe TA, Leong CK, Chung DDL. Comparative evaluation of thermal interface materials for improving the thermal contact between an operating computer microprocessor and its heat sink. Journal of Electronic Materials. 2006 Aug;35(8):1628-35.

[374] Liu ZR, Chung DDL. Calorimetric evaluation of phase change materials for use as thermal interface materials. Thermochimica Acta. 2001 Jan;366(2):135-47.

[375] Maguire L, Behnia M, Morrison G. Systematic evaluation of thermal interface materials - a case study in high power amplifier design. Microelectronics Reliability. 2005 Mar-Apr;45(3-4):711-25.

[376] Prasher RS. Rheology based modeling and design of particle laden polymeric thermal interface materials. 2005; 2005. p. 230-7.

[377] Singhal V, Siegmund T, Garimella SV. Optimization of thermal interface materials for electronics cooling applications. IEEE Transactions on Components and Packaging Technologies. 2004 Jun;27(2):244-52.

[378] Abadi P, Leong CK, Chung DDL. Factors That Govern the Performance of Thermal Interface Materials. 2009; 2009. p. 175-92.

[379] Aoyagi Y, Chung DDL. Antioxidant-based phase-change thermal interface materials with high thermal stability. 2008; 2008. p. 448-61.

[380] De Mey G, Pilarski J, Wojcik M, Lasota M, Banaszczyk J, Vermeersch B, et al. Influence of interface materials on the thermal impedance of electronic packages. International Communications in Heat and Mass Transfer. 2009 Mar;36(3):210-2.

[381] Kanuparthi S, Subbarayan G, Siegmund T, Sammakia B. An efficient network model for determining the effective thermal conductivity of particulate thermal interface materials. IEEE Transactions on Components and Packaging Technologies. 2008 Sep;31(3):611-21.

[382] Lin C, Chung DDL. Graphite nanoplatelet pastes vs. carbon black pastes as thermal interface materials. Carbon. 2009 Jan;47(1):295-305.

[383] Liu X, Zhang Y, Cassell AM, Cruden BA. Implications of catalyst control for carbon nanotube based thermal interface materials. J Appl Phys. 2008 Oct;104(8).

[384] Panzer MA, Zhang G, Mann D, Hu X, Pop E, Dai H, et al. Thermal properties of metal-coated vertically aligned single-wall nanotube arrays. J Heat Transf-Trans ASME. 2008 May;130(5).

[385] Ngo Q, Cruden BA, Cassell AM, Sims G, Meyyappan M, Li J, et al. Thermal interface properties of Cu-filled vertically aligned carbon nanofiber arrays. Nano Lett. 2004 Dec;4(12):2403-7.

[386] Hu XJ, Panzer MA, Goodson KE. Infrared microscopy thermal characterization of opposing carbon nanotube arrays. J Heat Transf-Trans ASME. 2007 Jan;129(1):91-3.

[387] Lin W, Zhang RW, Moon KS, Wong CP. Molecular phonon couplers at carbon nanotube/substrate interface to enhance interfacial thermal transport. Carbon. Jan;48(1):107-13.

[388] Cross R, Cola BA, Fisher T, Xu XF, Gall K, Graham S. A metallization and bonding approach for high performance carbon nanotube thermal interface materials. Nanotechnology. Nov;21(44).

[389] Son Y, Pal SK, Borca-Tasciuc T, Ajayan PM, Siegel RW. Thermal resistance of the native interface between vertically aligned multiwalled carbon nanotube arrays and their SiO2/Si substrate. J Appl Phys. 2008 Jan;103(2).

[390] Kordas K, Toth G, Moilanen P, Kumpumaki M, Vahakangas J, Uusimaki A, et al. Chip cooling with integrated carbon nanotube microfin architectures. Appl Phys Lett. 2007 Mar;90(12).

[391] Kim MJ, Nicholas N, Kittrell C, Haroz E, Shan HW, Wainerdi TJ, et al. Efficient transfer of a VA-SWNT film by a flip-over technique. J Am Chem Soc. 2006 Jul;128(29):9312-3.

[392] Sunden E, Moon JK, Wong CP, King WP, Graham S. Microwave assisted patterning of vertically aligned carbon nanotubes onto polymer substrates. J Vac Sci Technol B. 2006 Jul-Aug;24(4):1947-50.

[393] Jiang HJ, Zhu LB, Moon KS, Wong CP. Low temperature carbon nanotube film transfer via conductive polymer composites. Nanotechnology. 2007 Mar;18(12):4.

[394] Gan Z, Liu S, Song X, Chen M, Lv Q, Yan H, et al. Large-scale Bonding of Aligned Carbon Nanotube Arrays onto Metal Electrodes. 2009.

[395] Personal communication with Dr. Yong Ding.

[396] Dujardin E, Ebbesen TW, Hiura H, Tanigaki K. CAPILLARITY AND WETTING OF CARBON NANOTUBES. Science. 1994 Sep;265(5180):1850-2.

[397] Tao ZC, Guo QG, Gao XQ, Liu L. The wettability and interface thermal resistance of copper/graphite system with an addition of chromium. Mater Chem Phys. Jul;128(1-2):228-32.

[398] Ip SW, Sridhar R, Toguri JM, Stephenson TF, Warner AEM. Wettability of nickel coated graphite by aluminum. Mater Sci Eng A-Struct Mater Prop Microstruct Process. 1998 Mar;244(1):31-8.

[399] Gangopadhyay U, Wynblatt P. SOLID-STATE WETTING OF GRAPHITE BY PB AND PB-NI ALLOYS. Metall Mater Trans A-Phys Metall Mater Sci. 1994 Mar;25(3):607-15.

[400] Lee J, Tanaka T, Seo K, Hirai N, Lee JG, Mori H. Wetting of Au and Ag particles on monocrystalline graphite substrates. Rare Metals. 2006 Oct;25(5):469-72.

[401] Sanchez SA, Narciso J, Louis E, Rodriguez-Reinoso F, Saiz E, Tomsia A. Wetting and capillarity in the Sn/graphite system. Mater Sci Eng A-Struct Mater Prop Microstruct Process. 2008 Nov;495(1-2):187-91.

[402] Zhang Y, Franklin NW, Chen RJ, Dai HJ. Metal coating on suspended carbon nanotubes and its implication to metal-tube interaction. Chem Phys Lett. 2000 Nov;331(1):35-41.

[403] Ajayan PM, Iijima S. CAPILLARITY-INDUCED FILLING OF CARBON NANOTUBES. Nature. 1993 Jan;361(6410):333-4.

[404] Li N. Active control of oxygen in molten lead-bismuth eutectic systems to prevent steel corrosion and coolant contamination. Journal of Nuclear Materials. 2002 Jan;300(1):73-81.

[405] Lim SC, Choi HK, Jeong HJ, Song YI, Kim GY, Jung KT, et al. A strategy for forming robust adhesion with the substrate in a carbon-nanotube field-emission array. Carbon. 2006 Nov;44(13):2809-15.

[406] Kim J, Kim D, Lee CC. Fluxless flip-chip solder joint fabrication using electroplated Sn-rich Sn-Au structures. IEEE Transactions on Advanced Packaging. 2006 Aug;29(3):473-82.

[407] Lin W, Lee YC. Study of fluxless soldering using formic acid vapor. IEEE Transactions on Advanced Packaging. 1999 Nov;22(4):592-601.

[408] Sheeney-Haj-Khia L, Basnar B, Willner I. Efficient generation of photocurrents by using CdS/Carbon nanotube assemblies on electrodes. Angewandte Chemie-International Edition. 2005;44(1):78-83.

[409] Wei H, Kim S, Kim SN, Huey BD, Papadimitrakopoulos F, Marcus HL. Patterned forest-assembly of single-wall carbon nanotubes on gold using a non-thiol functionalization technique. Journal of Materials Chemistry. 2007;17(43):4577-85.

[410] Qu LT, Dai LM, Stone M, Xia ZH, Wang ZL. Carbon nanotube arrays with strong shear binding-on and easy normal lifting-off. Science. 2008 Oct;322(5899):238-42.

[411] Dai HJ, Wong EW, Lieber CM. Probing electrical transport in nanomaterials: Conductivity of individual carbon nanotubes. Science. 1996 Apr;272(5261):523-6.

[412] Marrone M, Montanari T, Busca G, Conzatti L, Costa G, Castellano M, et al. A Fourier transform infrared (FTIR) study of the reaction of triethoxysilane (TES) and

bis[3-triethoxysilylpropyl]tetrasulfane (TESPT) with the surface of amorphous silica. J Phys Chem B. 2004 Mar;108(11):3563-72.

[413] Everhart JB, Ault BS. Infrared Spectroscopic Study of the Cryogenic Thin-Film and Matrix-Isolated Complexes of Ticl4 with Nh3 and (Ch3)(3)N. Inorg Chem. 1995 Aug;34(17):4379-84.

[414] Hemraj-Benny T, Wong SS. Silylation of single-walled carbon nanotubes. Chem Mat. 2006 Oct;18(20):4827-39.

[415] Vast L, Philippin G, Destree A, Moreau N, Fonseca A, Nagy JB, et al. Chemical functionalization by a fluorinated trichlorosilane of multi-walled carbon nanotubes. Nanotechnology. 2004 Jul;15(7):781-5.

[416] Velasco-Santos C, Martinez-Hernandez AL, Lozada-Cassou M, Alvarez-Castillo A, Castano VM. Chemical functionalization of carbon nanotubes through an organosilane. Nanotechnology. 2002 Aug;13(4):495-8.

[417] Chu YY, Su MD. Theoretical study of addition reactions of carbene, silylene, and germylene to carbon nanotubes. Chem Phys Lett. 2004 Aug;394(4-6):231-7.

[418] Lu X, Tian F, Zhang QR. The [2+1] cycloadditions of dichlorocarbene, silylene, germylene, and oxycarbonylnitrene onto the sidewall of armchair (5,5) single-wall carbon nanotube. J Phys Chem B. 2003 Aug;107(33):8388-91.

[419] Niyogi S, Hamon MA, Hu H, Zhao B, Bhowmik P, Sen R, et al. Chemistry of single-walled carbon nanotubes. Accounts Chem Res. 2002 Dec;35(12):1105-13.

[420] Lin W, Wang CA, Le HL, Long B, Huang Y. Special assembly of laminated composite that mimics nacre. Mater Sci Eng C-Biomimetic Supramol Syst. 2008 Aug;28(7):1031-7.

[421] Thostenson ET, Ren ZF, Chou TW. Advances in the science and technology of carbon nanotubes and their composites: a review. Compos Sci Technol. 2001;61(13):1899-912.

[422] Borca-Tasciuc T, Mazumder M, Son Y, Pal SK, Schadler LS, Ajayan PM. Anisotropic thermal diffusivity characterization of aligned carbon nanotube-polymer composites. J Nanosci Nanotechnol. 2007 Apr-May;7(4-5):1581-8.

[423] Choi ES, Brooks JS, Eaton DL, Al-Haik MS, Hussaini MY, Garmestani H, et al. Enhancement of thermal and electrical properties of carbon nanotube polymer composites by magnetic field processing. Journal of Applied Physics. 2003 Nov;94(9):6034-9.

[424] Velasco-Santos C, Martinez-Hernandez AL, Fisher FT, Ruoff R, Castano VM. Improvement of thermal and mechanical properties of carbon nanotube composites through chemical functionalization. Chem Mat. 2003 Nov;15(23):4470-5.

[425] Liu CH, Huang H, Wu Y, Fan SS. Thermal conductivity improvement of silicone elastomer with carbon nanotube loading. Applied Physics Letters. 2004 May;84(21):4248-50.

[426] Bryning MB, Milkie DE, Islam MF, Kikkawa JM, Yodh AG. Thermal conductivity and interfacial resistance in single-wall carbon nanotube EP composites. Applied Physics Letters. 2005 Oct;87(16).

[427] Gojny FH, Wichmann MHG, Fiedler B, Kinloch IA, Bauhofer W, Windle AH, et al. Evaluation and identification of electrical and thermal conduction mechanisms in carbon nanotube/EP composites. Polymer. 2006 Mar;47(6):2036-45.

[428] Bonnet P, Sireude D, Garnier B, Chauvet O. Thermal properties and percolation in carbon nanotube-polymer composites. Applied Physics Letters. 2007 Nov;91(20).

[429] Shenogina N, Shenogin S, Xue L, Keblinski P. On the lack of thermal percolation in carbon nanotube composites. Applied Physics Letters. 2005 Sep;87(13).

[430] Nan CW, Liu G, Lin YH, Li M. Interface effect on thermal conductivity of carbon nanotube composites. Appl Phys Lett. 2004 Oct;85(16):3549-51.

[431] Shenogin S, Xue LP, Ozisik R, Keblinski P, Cahill DG. Role of thermal boundary resistance on the heat flow in carbon-nanotube composites. Journal of Applied Physics. 2004 Jun;95(12):8136-44.

[432] Shenogin S, Bodapati A, Xue L, Ozisik R, Keblinski P. Effect of chemical functionalization on thermal transport of carbon nanotube composites. Applied Physics Letters. 2004 Sep;85(12):2229-31.

[433] Clancy TC, Gates TS. Modeling of interfacial modification effects on thermal conductivity of carbon nanotube composites. Polymer. 2006 Jul;47(16):5990-6.

[434] Liu CH, Fan SS. Effects of chemical modifications on the thermal conductivity of carbon nanotube composites. Applied Physics Letters. 2005 Mar;86(12).

[435] Nan CW, Shi Z, Lin Y. A simple model for thermal conductivity of carbon nanotube-based composites. Chemical Physics Letters. 2003 Jul;375(5-6):666-9.

[436] Ju S, Li ZY. Theory of thermal conductance in carbon nanotube composites. Phys Lett A. 2006 Apr;353(2-3):194-7.

[437] Nan CW, Birringer R, Clarke DR, Gleiter H. Effective thermal conductivity of particulate composites with interfacial thermal resistance. Journal of Applied Physics. 1997 May;81(10):6692-9.

[438] Huxtable ST, Cahill DG, Shenogin S, Xue LP, Ozisik R, Barone P, et al. Interfacial heat flow in carbon nanotube suspensions. Nature Materials. 2003 Nov;2(11):731-4.

[439] Tasis D, Tagmatarchis N, Bianco A, Prato M. Chemistry of carbon nanotubes. Chem Rev. 2006 Mar;106(3):1105-36.

[440] Wang CY, Chen TG, Chang SC, Cheng SY, Chin TS. Strong carbon-nanotube-polymer bonding by microwave irradiation. Adv Funct Mater. 2007 Aug;17(12):1979-83.

[441] Wang SR, Liang ZY, Gonnet P, Liao YH, Wang B, Zhang C. Effect of nanotube functionalization on the coefficient of thermal expansion of composites. Adv Funct Mater. 2007 Jan;17(1):87-92.

[442] Mary TA, Evans JSO, Vogt T, Sleight AW. Negative thermal expansion from 0.3 to 1050 Kelvin in ZrW2O8. Science. 1996 Apr;272(5258):90-2.

[443] Roy R, Agrawal DK, McKinstry HA. VERY LOW THERMAL-EXPANSION COEFFICIENT MATERIALS. Annual Review of Materials Science. 1989;19:59-81.

[444] Numata S, Kinjo N, Makino D. CHEMICAL STRUCTURES AND PROPERTIES OF LOW THERMAL-EXPANSION COEFFICIENT POLYIMIDES. Polymer Engineering and Science. 1988 Jul;28(14):906-11.

[445] Evans JSO. Negative thermal expansion materials. Journal of the Chemical Society-Dalton Transactions. 1999(19):3317-26.

[446] Yano K, Usuki A, Okada A, Kurauchi T, Kamigaito O. SYNTHESIS AND PROPERTIES OF POLYIMIDE CLAY HYBRID. Journal of Polymer Science Part a-Polymer Chemistry. 1993 Sep;31(10):2493-8.

[447] Xu YS, Ray G, Abdel-Magid B. Thermal behavior of single-walled carbon nanotube polymer-matrix composites. Composites Part a-Applied Science and Manufacturing. 2006;37(1):114-21.

[448] Zhang ZQ, Wong CP. Recent advances in flip-chip underfill: Materials, process, and reliability. IEEE Transactions on Advanced Packaging. 2004 Aug;27(3):515-24.

[449] Boyer RF, Spencer RS. THERMAL EXPANSION AND 2ND-ORDER TRANSITION EFFECTS IN HIGH POLYMERS .2. THEORY. J Appl Phys. 1945;16(10):594-607.

[450] Mahajan R, Chiu CP, Chrysler G. Cooling a microprocessor chip. Proc IEEE. 2006 Aug;94(8):1476-86.

[451] Kwon YK, Berber S, Tomanek D. Thermal contraction of carbon fullerenes and nanotubes. Phys Rev Lett. 2004 Jan;92(1).

[452] Wei CY, Srivastava D, Cho KJ. Thermal expansion and diffusion coefficients of carbon nanotube-polymer composites. Nano Lett. 2002 Jun;2(6):647-50.

[453] Maniwa Y, Fujiwara R, Kira H, Tou H, Kataura H, Suzuki S, et al. Thermal expansion of single-walled carbon nanotube (SWNT) bundles: X-ray diffraction studies - art.no. 241402. Phys Rev B. 2001 Dec;64(24).

[454] Mukherjee M, Bhattacharya M, Sanyal MK, Geue T, Grenzer J, Pietsch U. Reversible negative thermal expansion of polymer films. Physical Review E. 2002 Dec;66(6).

[455] Kanaya T, Miyazaki T, Inoue R, Nishida K. Thermal expansion and contraction of polymer thin films. Physica Status Solidi B-Basic Solid State Physics. 2005 Mar;242(3):595-606.

[456] Geim AK, Novoselov KS. The rise of graphene. Nature Materials. 2007 Mar;6(3):183-91.

[457] Debelak B, Lafdi K. Use of exfoliated graphite filler to enhance polymer physical properties. Carbon. 2007 Aug;45(9):1727-34.

[458] Ganguli S, Roy AK, Anderson DP. Improved thermal conductivity for chemically functionalized exfoliated graphite/EP composites. Carbon. 2008 Apr;46(5):806-17.

[459] Hung MT, Choi O, Ju YS, Hahn HT. Heat conduction in graphite-nanoplatelet-reinforced polymer composites. Appl Phys Lett. 2006 Jul;89(2).

[460] Veca LM, Meziani MJ, Wang W, Wang X, Lu F, Zhang P, et al. Carbon nanosheets for polymeric composites with high thermal conductivity. Adv Mater. 2009 Mar;21:1-5.

[461] Veca LM, Lu F, Meziani MJ, Cao L, Zhang P, Qi G, et al. Polymer functionalization and solubilization of carbon nanosheets. Chemical Communications. 2009:1-3.

[462] Picard S, Burns DT, Roger P. Determination of the specific heat capacity of a graphite sample using absolute and differential methods. Metrologia. 2007 Oct;44(5):294-302.

[463] Balandin AA, Ghosh S, Bao WZ, Calizo I, Teweldebrhan D, Miao F, et al. Superior thermal conductivity of single-layer graphene. Nano Letters. 2008 Mar;8(3):902-7.

[464] Ghosh S, Calizo I, Teweldebrhan D, Pokatilov EP, Nika DL, Balandin AA, et al. Extremely high thermal conductivity of graphene: Prospects for thermal management applications in nanoelectronic circuits. Appl Phys Lett. 2008 Apr;92(15).

[465] Lu W, Lin HF, Wu DJ, Chen GH. Unsaturated polyester resin/graphite nanosheet conducting composites with a low percolation threshold. Polymer. 2006 May;47(12):4440-4.

[466] Yu AP, Ramesh P, Sun XB, Bekyarova E, Itkis ME, Haddon RC. Enhanced Thermal Conductivity in a Hybrid Graphite Nanoplatelet - Carbon Nanotube Filler for EP Composites. Adv Mater. 2008 Dec;20(24):4740-+.

[467] Di JT, Yong ZZ, Yang XJ, Li QW. Structural and morphological dependence of carbon nanotube arrays on catalyst aggregation. Appl Surf Sci. 2011 doi:10.1016/j.apsusc.2011.07.130.

[468] Hu MH, Murakami Y, Ogura M, Maruyama S, Okubo T. Morphology and chemical state of Co-Mo catalysts for growth of single-walled carbon nanotubes vertically aligned on quartz substrates. J Catal. 2004 Jul;225(1):230-9.

[469] Harutyunyan AR, Pradhan BK, Kim UJ, Chen GG, Eklund PC. CVD synthesis of single wall carbon nanotubes under "soft" conditions. Nano Lett. 2002 May;2(5):525-30.

[470] Bai L, Zhou Z. Computational study of B- or N-doped single-walled carbon nanotubes as NH3 and NO2 sensors. Carbon. 2007 Sep;45(10):2105-10.

[471] Zahab A, Spina L, Poncharal P, Marliere C. Water-vapor effect on the electrical conductivity of a single-walled carbon nanotube mat. Phys Rev B. 2000 Oct;62(15):10000-3.

[472] Wiggins-Camacho JD, Stevenson KJ. Effect of Nitrogen Concentration on Capacitance, Density of States, Electronic Conductivity, and Morphology of N-Doped Carbon Nanotube Electrodes. J Phys Chem C. 2009 Nov;113(44):19082-90.

[473] Zhu LB, Xu JW, Xiu YH, Hess DW, Wong CP. A rapid growth of aligned carbon nanotube films and high-aspect-ratio arrays. Carbon 2006: 195-9.

[474] Glerup M, Castignolles M, Holzinger M, Hug G, Loiseau A, Bernier P. Synthesis of highly nitrogen-doped multi-walled carbon nanotubes. Chemical Communications. 2003(20):2542-3.

[475] He MS, Zhou S, Zhang J, Liu ZF, Robinson C. CVD growth of N-doped carbon nanotubes on silicon substrates and its mechanism. J Phys Chem B. 2005 May;109(19):9275-9.

[476] Lin W, Zhang RW, Jang SS, Wong CP, Hong JI. "Organic Aqua Regia"-Powerful Liquids for Dissolving Noble Metals. Angewandte Chemie-International Edition.49(43):7929-32.

[477] Yeston J. Golden Selection. Science. 2010;330(6001):153.

[478] Editorial N. Dissolving precious metals. Nature. 2010;467(7315):503.

[479] http://pubs.acs.org/cen/news/89/i14/8914notw4.html.

[480] Vulakh EL, Freidlin EG, Gitis SS. REACTION OF SUBSTITUTED BENZOIC-ACIDS WITH THIONYL CHLORIDE. Zhurnal Organicheskoi Khimii. 1975;11(7):1481-6.

[481] Zuffanti S. Preparation of acyl chlorides with thionyl chloride. Journal of Chemical Education. 1948;25(9):481.

[482] Senanayake G. A review of effects of silver, lead, sulfide and carbonaceous matter on gold cyanidation and mechanistic interpretation. Hydrometallurgy. 2008 Jan;90(1):46-73.

[483] Qi PH, Hiskey JB. DISSOLUTION KINETICS OF GOLD IN IODIDE SOLUTIONS. Hydrometallurgy. 1991 Jul;27(1):47-62.

[484] Awadalla FT, Molnar RE, Riteey GM, inventors; Recovery of platinum group metals (PGM) from acidic solutions by reduction precipitation with sodium borohydride. 1992.

[485] Edwards RI, Nattrass MJ, inventors; Separation and purification of platinum and palladium. 1978.

[486] Lakewood JB, Arvada C, inventors; Separation and selective recovery of platinum and palladium by solvent extraction 1977.

[487] Raisanen MT, Kemell M, Leskela M, Repo T. Oxidation of elemental gold in alcohol solutions. Inorganic Chemistry. 2007 Apr;46(8):3251-6.

[488] Mortier T, Persoons A, Verbiest T. Oxidation of solid gold in chloroform solutions of cetyltrimethylammonium bromide. Inorganic Chemistry Communications. 2005 Dec;8(12):1075-7.

[489] Cau L, Deplano P, Marchio L, Mercuri ML, Pilia L, Serpe A, et al. New powerful reagents based on dihalogen/N,N '-dimethylperhydrodiazepine-2,3-dithione adducts for gold dissolution: the IBr case. Dalton Transactions. 2003(10):1969-74.

[490] Nakao Y. DISSOLUTION OF NOBLE-METALS IN HALOGEN HALIDE POLAR ORGANIC-SOLVENT SYSTEMS. Journal of the Chemical Society-Chemical Communications. 1992 Mar(5):426-7.

[491] Schenk PW, Steudel R. ADDUKTE DES DISCHWEFELMONOXYDS. Angewandte Chemie-International Edition. 1963;75(16-7):793-&.

[492] Korshak VV, Vinograd.Sv, Pankrato.Va. NEW WAYS TO SYNTHESIZE POLYBENZIMIDAZOLES AND POLYBENZOXAZOLES. Vysokomolekulyarnye Soedineniya Section B. 1971;13(7):550-3.

[493] Cade JA, Gerrard W. ACTION OF THIONYL CHLORIDE ON CARBOXYLIC ACIDS IN PRESENCE OF PYRIDINE. Nature. 1953;172(4366):29.

[494] Gerrard W, Thrush AM. REACTIONS IN CARBOXYLIC ACID THIONYL CHLORIDE SYSTEMS. Journal of the Chemical Society. 1953(JUL):2117-20.

[495] Higashi F, Mashimo T, Takahashi I. PREPARATION OF AROMATIC POLYESTERS BY DIRECT POLYCONDENSATION WITH THIONYL CHLORIDE IN PYRIDINE. Journal of Polymer Science Part a-Polymer Chemistry. 1986 Jan;24(1):97-102.

[496] Human JPE, Mills JA. ACTION OF THIONYL CHLORIDE ON CARBOXYLIC ACIDS IN PRESENCE OF PYRIDINE. Nature. 1946;158(4024):877.

[497] Garcia EE, Greco CV, Hunsberger IM. FACILE BROMINATION OF PYRIDINE-TYPE HETEROCYCLES AT THE BETA-POSITION. Journal of the American Chemical Society. 1960;82(16):4430-1.

[498] Steudel R, Steudel Y. Charge-transfer complexes between the sulfur molecules SO2, S2O, S-3, SONH, and SOCl2 and the amine donors NH3 and NMe3 - A theoretical study. European Journal of Inorganic Chemistry. 2007 Sep(27):4385-92.

[499] Ricca G, Severini F. A C-13 AND H-1-NMR STUDY OF THE PYRIDINE-INITIATED OLIGOMERIZATION OF MALEIC-ANHYDRIDE AND OF THE POLYMER STRUCTURE. Polymer. 1988 May;29(5):880-2.

[500] Geary WJ. The Use of Conductivity Measurements in Organic Solvents for the Characterization of Coordination Compounds. Coordination Chemistry Reviews. 1971;7(1):81.

[501] Harkness AC, Daggett Jr. HM. The Electrical Conductivities of Some Tetra-n-alkylammonium Salts in Acetonitrile. Canadian Journal of Chemistry. 1965;43(5):1215-21.

[502] Schmidbaur H, Jandik P. AU(I)-AU(II) AND AU(I)-AU(III) OXIDATION IN YLIDE COMPLEXES WITH CHLORINATING AGENTS. Inorganica Chimica Acta-Articles. 1983;74(OCT):97-9.

[503] Bovio B, Burini A, Pietroni BR. REACTIONS OF TRIMERIC 1-BENZYL-2-GOLD(I)IMIDAZOLE LEADING TO AUI CARBENE COMPLEXES - CRYSTAL-STRUCTURE OF [1-BENZYL-3-BENZOYL-IMIDAZOLIN-2-YLIDEN]CHLOROGOLD(I). Journal of Organometallic Chemistry. 1993 Jun;452(1-2):287-91.

VITA

WEI LIN

WEI was born in Fujian Province, China. He received the B.S. and M.S. degrees in Materials Science and Engineering, from Fuzhou University in 2005 and Tsinghua University in 2007, respectively. He is currently a Ph. D candidate at the School of Materials Science and Engineering, Georgia Institute of Technology. He joined Prof. C.P. Wong's research team in August, 2007. His research focuses on advanced materials and processing for electronic, photonic and bio packaging, including synthesis, functionalization, characterizations and fundamental understanding of carbon nano materials, applications of carbon nanotubes as electrical interconnects, thermal interface materials and fillers for high-performance composites, and noble metal chemistry. After graduation, he will join IBM R&D at Albany, Newyork, to work on 3D packaging of microelectronics.